A Chemical Ionisation Mass Spectrometer for Atmospheric Trace Gas Measurement: Characterisation and Deployment in Field Studies

Dissertation
zur Erlangung des Grades
„Doktor
der Naturwissenschaften“
am Fachbereich Physik, Mathematik und Informatik
der Johannes Gutenberg-Universität
in Mainz

Philipp Georg Eger
geboren in Heidelberg

Mainz, den 25.09.2019

Tag der mündlichen Prüfung: 11.12.2019

Abstract

Chemical ionisation mass spectrometers (CIMS) equipped with a radioactive ion source (usually ^{210}Po) to generate iodide ions are frequently used devices for atmospheric trace gas measurement with a broad field of application. Within the scope of this thesis a chemical ionisation quadrupole mass spectrometer (CI-QMS) with a novel electrical discharge ion source was characterised and proved to represent a promising alternative to similar instruments based on a radioactive ioniser, particularly in environments where a permission for ^{210}Po is difficult to obtain or transport is not feasible. In addition to the well-established detection of peroxyacetyl nitrate (PAN), nitryl chloride ($ClNO_2$) and peracetic acid via I^- primary ions, the instrument is capable of measuring sulphur dioxide (SO_2), hydrogen chloride (HCl), acetic acid and pyruvic acid through additional ion-molecule-reactions, unique for the radio-frequency (RF) discharge ion source. The compact design and flexibility of the CI-QMS allow for stationary, airborne and shipborne measurements with limits of detection (2σ, 1 s) of a few tens of pptv (parts per trillion by volume) for $ClNO_2$ and SO_2, which is beneficial for the investigation of chlorine- and sulphur-related chemistry in the polluted marine boundary layer. Due to a high variability in the background signal, the application as a PAN detector is limited to polluted conditions or low temporal resolution.

The CI-QMS with its discharge ion source was successfully operated in three different field studies under variable atmospheric conditions ranging from mixed urban / rural to remote forested to polluted marine environment. During the NO-TOMO campaign, which took place at a forested mountain-site in south-western Germany, generally high levels of primary and secondary pollutants (SO_2 and PAN) were measured, which reflected the influence of nearby urban conglomerations and industry on local air quality. In addition, $ClNO_2$ mixing ratios of several hundred pptv were observed at this continental site, indicating the importance of aerosol chloride transported inland from coastal regions. The IBAIRN campaign, which took place at a remote site in the Finnish boreal forest with limited anthropogenic influence, was characterised by large biogenic emissions and low nitrogen oxide (NO_x) levels. The first gas-phase measurements of pyruvic acid, a widely unexplored biogenic acid, in the boreal forest revealed its ubiquity and impact on radical chemistry in late summer. During AQABA, a shipborne campaign designed to study air quality and climate around the Arabian Peninsula, a unique dataset of $ClNO_2$, HCl and SO_2 in severely understudied regions like the Red Sea and the Arabian Gulf was collected. Mixing ratios of $ClNO_2$ ranged from the limit of detection in the Arabian Sea to several hundred of pptv over the northern Red Sea, the Gulf of Oman, the Gulf of Suez and the Suez Canal, mainly due to high nitrate radical (NO_3) production rates and the availability of particulate chloride. However, the overall production efficiency, i.e. the $ClNO_2$ yield per

NO_3 molecule formed in the reaction of nitrogen dioxide (NO_2) with ozone (O_3), remained generally low due to exceptionally high nocturnal temperatures, which shifted the equilibrium from nitrogen pentoxide (N_2O_5) towards NO_3. In combination with elevated NO_3 reactivity towards volatile organic compounds (VOCs) this resulted in the dominance of direct NO_3 losses over the heterogeneous uptake of N_2O_5 to the particle phase, with the latter representing a crucial step in the formation of $ClNO_2$. The photolysis of $ClNO_2$ and the oxidation of HCl (released by acid displacement) were determined to be important sources of chlorine radicals in polluted parts of the marine boundary layer over the Mediterranean Sea and the Arabian Peninsula, recycling NO_x and potentially enhancing oxidation rates of several hydrocarbons.

The successful long-term operation in field campaigns confirmed the suitability of the CI-QMS as an alternative to ^{210}Po-based instruments for future measurements of $ClNO_2$, SO_2, HCl, PAN and pyruvic acid in regions where observational data is lacking, in order to enhance the quality of atmospheric models and to deepen our understanding of tropospheric trace gases with an impact on air quality and climate.

Zusammenfassung

Auf Chemischer Ionisation beruhende Massenspektrometer mit einer radioaktiven Ionenquelle (üblicherweise ^{210}Po) zur Erzeugung von Iod-Ionen werden aufgrund ihres breiten Anwendungsspektrums häufig für Spurengasmessungen in der Atmosphäre eingesetzt. Im Rahmen dieser Arbeit wurde ein Chemische Ionisation - Quadrupol Massenspektrometer (CI-QMS) mit einer neuartigen Ionenquelle, die auf elektrischer Entladung basiert, charakterisiert, weiterentwickelt und in Feldmessungen eingesetzt. Insbesondere in Regionen, in denen es schwer ist, eine Messgenehmigung für ^{210}Po zu erhalten oder der Transport nicht möglich ist, stellt diese Art der Ionenquelle eine vielversprechende Alternative dar. Zusätzlich zur gut erforschten Detektion von Peroxyacetylnitrat (PAN), Nitrylchlorid ($ClNO_2$) und Peressigsäure mit Hilfe von I^- Primärionen ist das Instrument in der Lage, auch Schwefeldioxid (SO_2), Chlorwasserstoff (HCl), Essigsäure und Brenztraubensäure zu messen. Dies wird durch neu entdeckte Ionen-Molekül-Reaktionen ermöglicht, die nach derzeitigem Wissensstand einzigartig für die Entladungsquelle sind und bei der Verwendung von ^{210}Po nicht beobachtet werden. Der kompakte Aufbau des CI-QMS und die flexible Druckregelung am Gaseinlass ermöglichen sowohl stationäre als auch schiffs- und flugzeuggebundene Messungen. Nachweisgrenzen (2σ, 1 s) von einigen zehn pptv (parts per trillion by volume) für $ClNO_2$ und SO_2 eignen sich hervorragend, um die Chlor- und Schwefelchemie in der verschmutzten marinen Grenzschicht zu erforschen. Allerdings ist der Einsatz als PAN-Messgerät aufgrund erhöhter Variabilität im Hintergrundsignal auf schadstoffbelastete Regionen oder eine geringe zeitliche Auflösung begrenzt.

Das CI-QMS mit elektrischer Entladungs-Ionenquelle wurde erfolgreich in drei verschiedenen Feldstudien eingesetzt, die durch unterschiedliche atmosphärische Bedingungen gekennzeichnet waren. Während der NOTOMO-Kampagne, die auf einem bewaldeten Berg in Südwest-Deutschland stattfand, wurden trotz der eher ländlichen Lage relativ hohe Konzentrationen von primären und sekundären Luftschadstoffen wie SO_2 und PAN gemessen, was den Einfluss von Industrie, Verkehr und umliegenden Städten auf die lokale Luftqualität deutlich machte. Außerdem wurden auch $ClNO_2$ Volumenmischverhältnisse von mehreren hundert pptv beobachtet, die die Bedeutung von Chlorid in der Partikelphase unterstrichen, welches vermutlich aus Küstenregionen ins Landesinnere transportiert wurde. Die IBAIRN-Kampagne, die an einer Messstation mitten im borealen Nadelwald in Finnland stattfand, war im Gegensatz zu NOTOMO durch hohe biogene Emissionen und niedrige NO_x-Konzentrationen geprägt. Im Zuge der Kampagne wurde erstmals Brenztraubensäure, eine größtenteils unerforschte organische Säure biogenen Ursprungs, im borealen Wald gemessen. Diese Gasphasen-Messungen zeigten deutlich, dass Brenztraubensäure im Spätsommer im borealen Nadelwald allgegenwärtig ist und einen nicht zu vernachlässigenden Einfluss auf die Radikal-

chemie hat. Die AQABA-Kampagne konzentrierte sich auf Schiffsmessungen im Mittelmeer und rund um die Arabische Halbinsel mit dem Ziel, die Luftqualität und das Klima im Mittleren Osten zu erforschen. Sie lieferte einen einzigartigen Datensatz zu $ClNO_2$, HCl und SO_2 Volumenmischungsverhältnissen in der marinen Grenzschicht, insbesondere in Gebieten wie dem Roten Meer und dem Arabischen (Persischen) Golf, in denen kaum Literaturdaten vorliegen. $ClNO_2$ Volumenmischungsverhältnisse bewegten sich von der Nachweisgrenze bis zu mehreren hundert pptv im Roten Meer, im Golf von Oman, im Golf von Suez und im Suezkanal. Hauptgründe hierfür waren die hohe Produktionsrate von Nitratradikalen (NO_3) und die Verfügbarkeit von ausreichend Chlorid in der Partikelphase. Allerdings war die Produktionseffizienz bzw. die Ausbeute von $ClNO_2$ pro NO_3-Molekül, das in der Reaktion von Stickstoffdioxid (NO_2) mit Ozon (O_3) gebildet wurde, relativ niedrig, was hauptsächlich auf die außergewöhnlich hohen nächtlichen Temperaturen zurückzuführen ist. Diese führten kombiniert mit einer erhöhten NO_3-Reaktivität gegenüber flüchtigen organischen Verbindungen (VOCs) zu einer Verschiebung des chemischen Gleichgewichts von Distickstoffpentoxid (N_2O_5) hin zu NO_3. Das Resultat war die Dominanz direkter NO_3 Verluste gegenüber der heterogenen Aufnahme von N_2O_5 in Partikeln, wobei letzteres einen essentiellen Schritt für die Bildung von $ClNO_2$ darstellt. Die Messungen zeigten allerdings auch, dass die Photolyse von $ClNO_2$ und die Oxidation von (durch stärkere Säuren aus Seesalz-Aerosolen freigesetztem) HCl in verschmutzten Regionen wichtige Quellen für Chlor-Radikale darstellen, die wiederum zur Regeneration von NO_x und zu gesteigerten Oxidationsraten verschiedener Kohlenwasserstoffe beitragen können.

Das erfolgreiche Betreiben des CI-QMS in verschiedenen Messkampagnen hat dessen Eignung als Alternative zu ^{210}Po-basierten Chemische Ionisation - Massenspektrometern unter Beweis gestellt. Durch die gleichzeitige Messung von $ClNO_2$, SO_2, HCl, PAN und Brenztraubensäure bietet sich das CI-QMS für zukünftige Messungen in wenig erforschten Regionen an, um unser Verständnis von troposphärischen Spurengasen und deren Einfluss auf Luftqualität und Klima zu verbessern.

Table of contents

List of publications

During my time as a PhD student several parts of my work have been published in peer-reviewed journals. Individual chapters of my thesis are based on these first-author publications (Eger et al., 2019a,b,c). A detailed list of publications with a description of my contribution is given in the following:

Eger, P. G., Helleis, F., Schuster, G., Phillips, G. J., Lelieveld, J., and Crowley, J. N. Chemical ionization quadrupole mass spectrometer with an electrical discharge ion source for atmospheric trace gas measurement. Atmospheric Measurement Techniques, 12(3):1935–1954, 2019a. doi:10.5194/amt-12-1935-2019.

Contribution: I wrote the manuscript, developed and tested the RF discharge ion source in the laboratory, deployed the CI-QMS during the NOTOMO and IBAIRN campaigns and evaluated the field data. **Status**: The article was published in Atmospheric Measurement Techniques (AMT) as Eger et al. (2019a).

Eger, P. G., Friedrich, N., Schuladen, J., Shenolikar, J., Fischer, H., Tadic, I., Harder, H., Martinez, M., Rohloff, R., Tauer, S., Fachinger, F., Drewnick, F., Brooks, J., Darbyshire, E., Sciare, J., Pikridas, M., Lelieveld, J., and Crowley, J. N.: Shipborne measurements of $ClNO_2$ in the Mediterranean Sea and around the Arabian Peninsula during summer. Atmospheric Chemistry and Physics Discussions, 2019:1–37, 2019b. doi:10.5194/acp-2019-531.

Contribution: I wrote the manuscript, deployed the CI-QMS during the AQABA campaign and performed the data analysis presented. **Status**: The article was published in Atmospheric Chemistry and Physics Discussions (ACPD) as Eger et al. (2019b) and is accepted for final publication in ACP (in the revised version presented in this thesis).

Eger, P. G., Schuladen, J., Sobanski, N., Fischer, H., Karu, E., Williams, J., Riva, M., Zha, Q., Ehn, M., Quéléver, L. L. J., Schallhart, S., Lelieveld, J., and Crowley, J. N.: Pyruvic acid in the boreal forest: first measurements and impact on radical chemistry. Atmospheric Chemistry and Physics Discussions, 2019:1–24, 2019c. doi:10.5194/acp-2019-768.

Contribution: I wrote the manuscript, deployed the CI-QMS during the IBAIRN campaign and performed the data analysis presented. **Status**: The article was published in Atmospheric Chemistry and Physics Discussions (ACPD) as Eger et al. (2019c) and is currently in review.

Chapter 1

Introduction

Within the scope of this thesis a chemical ionisation quadrupole mass spectrometer with a novel electrical discharge ion source was characterised and deployed for trace gas measurement under variable atmospheric conditions.

1.1 Structure of the thesis

The thesis is structured as follows: In Chapter 1 a general introduction to atmospheric chemistry and physics is given and trace gases of interest, including their relevance for the troposphere, are presented to put the work into a broader scientific context. In addition, the basic principles of chemical ionisation quadrupole mass spectrometry and the main objectives of the thesis are outlined. In Chapter 2 the chemical ionisation quadrupole mass spectrometer (CI-QMS), which was developed and characterised within the scope of this thesis, is described in detail with a focus on the novel electrical discharge ion source and recently discovered detection schemes for sulphur dioxide (SO_2), hydrogen chloride (HCl) and acetic acid. Furthermore, the applicability of the instrument in various environments (remote forested, mixed urban / rural and polluted coastal) is demonstrated and advantages as well as disadvantages to similar instruments equipped with a ^{210}Po ioniser are discussed. In Chapter 3 a field study on pyruvic acid, an ubiquitous but widely unexplored biogenic acid with an impact on radical chemistry and secondary organic aerosol (SOA) formation, is presented. Measurements were performed during the IBAIRN campaign in a boreal forest environment in Finland, which was dominated by large biogenic emissions and low NO_x ($NO + NO_2$) conditions. Chapter 4 addresses the exploration of air quality and climate in the marine boundary layer over the Mediterranean Sea and around the Arabian Peninsula as part of the AQABA ship campaign, which was characterised by a mixture of different (mostly polluted) conditions. $ClNO_2$, a nocturnal NO_x reservoir and source of reactive chlorine atoms subsequent to its photolysis, was observed along the ship track and its impact on radical chemistry was quantified. Chapter 5 provides general conclusions drawn from laboratory experiments and field studies as well as suggestions for further research projects.

1.2 Chemistry and physics of the atmosphere

The atmosphere is a relatively thin layer ($\approx 1.5\,\%$ of the Earth's radius) of gas molecules surrounding our planet. Its chemical composition is crucial for life on

earth as it provides vital oxygen to animate beings and via the stratospheric ozone layer protects the surface outside the oceans from harmful solar UV radiation. The natural greenhouse effect (mainly due to water vapour) increases mean surface temperatures to above the freezing point and allows for water in its liquid form. The atmosphere also equilibrates the imbalanced solar irradiation at the equator and the poles, resulting in a global circulation, which is driven by incoming solar radiation, the Coriolis force and phase transitions of water serving as energy reservoir. In this way the atmosphere controls weather, air quality and climate.

In the last decades the exploration of physical and chemical processes taking place in the atmosphere has proceeded faster than ever. However, there are still many gaps in knowledge which need to be filled in order to extend our understanding and to mitigate the effects of climate change and air pollution for future generations. Within the scope of this thesis several atmospheric trace gases which directly or indirectly impact air quality and climate were measured with a chemical ionisation quadrupole mass spectrometer in different environments around the world to make a small contribution to this task. In this section the chemical composition and vertical structure of the atmosphere as well as the relevance of several trace gases for air quality and climate are examined.

1.2.1 Chemical composition

The atmosphere of the Earth is mainly composed of N_2, O_2 and Ar with fractional concentrations by volume (based on dry air) of 78.08, 20.95 and 0.93 % (Wallace and Hobbs, 2006). In addition to those (quasi inert) constituents, the atmosphere consists of a variety of so called trace gases with much smaller mixing ratios ranging from a few pptv (parts per trillion by volume) to several ppmv (parts per million by volume). Despite their low abundance, they are the main drivers for atmospheric chemistry and impact the radiative budget and the oxidative capacity of the atmosphere as well as the quality of the air we breathe (Schlager et al., 2012). Prominent examples are carbon dioxide (CO_2, ≈ 400 ppmv), ozone (O_3, ≈ 10–200 ppbv) and nitrogen oxides (NO_y, ≈ 10 pptv–1 ppmv). The spatial and temporal distribution of water vapour is highly variable (≈ 10 ppmv–5 %) and is mainly controlled by evaporation and precipitation with the largest concentrations found in the lower troposphere over the tropics (Wallace and Hobbs, 2006). In addition to gaseous compounds, the atmosphere also contains aerosol particles like water droplets, dust, sea salt or soot and secondary organic aerosol (SOA) formed from gaseous precursors (Schneider et al., 2006; Seinfeld and Pandis, 2016).

1.2.2 Anthropogenic emissions

The atmosphere can be considered as a large photochemical reactor where emitted trace gases (both anthropogenic and biogenic) are dispersed, transported and steadily interact with radicals, aerosols and solar radiation. Since the beginning of industrialisation humankind is emitting gases into the atmosphere which signif-

icantly alter its chemical composition. Fortunately, toxic gases like, for example, CO (emitted in combustion processes) do not accumulate in the atmosphere due to a self-cleaning mechanism involving oxidising agents like OH, which transform most pollutants into water-soluble products that can be removed from the atmosphere via dry and wet deposition (Lelieveld et al., 2004). Nevertheless, particularly the emission of NO_x, non-methane hydrocarbons (NMHCs) and particulate matter (PM_{10}, $PM_{2.5}$) can have an unfavourable impact on air quality and human health, substantially increasing premature mortality (Lelieveld et al., 2015). Furthermore, continuously rising emissions of anthropogenic greenhouse gases (characterised by absorption bands in the infrared region) already led to an exceptional increase in atmospheric CO_2 and CH_4 levels compared to pre-industrial times, resulting in a substantial radiative forcing and thus global warming (Hartmann et al., 2013). To emphasise that within the last 200 years human activities have become a significant global geophysical force, the current epoch is more frequently referred to as the "Anthropocene" (Crutzen, 2006). If greenhouse gas emissions cannot be limited globally within the next decades, life on earth will drastically change with rising surface temperature and sea level, increasing frequency and intensity of extreme weather events, a loss of biodiversity and migration of millions of people (Butchart et al., 2010; Stocker et al., 2013).

1.2.3 Vertical structure

Atmospheric pressure continuously decreases with height above ground as the pressure at any height z is proportional to the weight of the air in the vertical column above that level. The pressure decrease can be approximated by the barometric height formula (Eq. 1.1) which is based on the hydrostatic equilibrium ($\frac{\partial p}{\partial z} = -g\rho$) and the assumption of an isothermal atmosphere (Wallace and Hobbs, 2006).

$$p = p_0 \exp\left(-\frac{Mg}{RT}\, z\right) \tag{1.1}$$

The scale height of $z_0 = \left(\frac{RT}{Mg}\right) \approx 8\,\text{km}$ in Eq. (1.1) defines the point at which the pressure drops below the fraction $1/e \approx 0.37$ and represents the height of a homogeneous atmosphere, where M denotes the molar mass of air, g is the gravitational constant and R the universal gas constant. Based on predominant temperature gradients the atmosphere can be divided into four layers depicted in Fig. 1.1, which are known as the troposphere, the stratosphere, the mesosphere and the thermosphere. In the following, the thermal structure of the atmosphere is briefly outlined, with explanations based on the textbook of Wallace and Hobbs (2006).

In the troposphere ($\approx$0–13 km, up to 17 km in the tropics) temperature almost linearly decreases with height (expect for inversions) due to the heating of the surface and adiabatic expansion of rising air parcels with transformation of latent and sensible heat into potential energy. The troposphere is usually well mixed, contains more than 99 % of the total atmospheric water vapour and hence determines most of our weather. The temperature decreases with height at an average

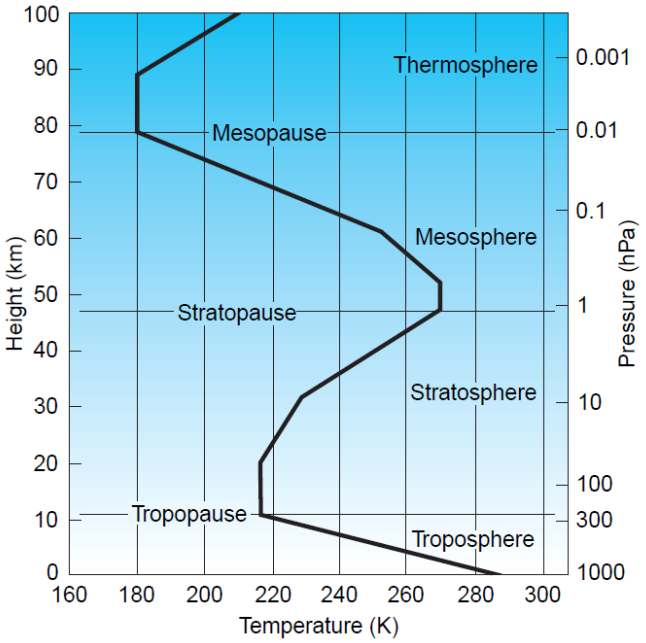

Figure 1.1: A typical mid-latitude vertical temperature profile, as represented by the U.S. Standard Atmosphere, taken from Wallace and Hobbs (2006).

lapse rate of $\Gamma = -\frac{\partial T}{\partial z} \approx 6.5\,\mathrm{K\,km^{-1}}$, which varies due to condensation of water vapour. In practise, air masses at different heights are often compared by their potential temperature, i.e. the temperature that an air parcel would attain if adiabatically brought to standard pressure (1000 hPa). The potential temperature can be calculated via Eq. (1.2) (with isentropic exponent κ, specific heat capacity at constant pressure, c_p, and at constant volume, c_v) and is conserved for dry adiabatic expansion or compression.

$$\Theta = T\left(\frac{p_0}{p}\right)^{\left(\frac{\kappa-1}{\kappa}\right)} \quad \text{with} \quad \kappa = \frac{c_p}{c_v} \tag{1.2}$$

In the stratosphere ($\approx$10–50 km), the lapse rate is reversed, i.e. temperature increases with height, mainly due to the absorption of highly-energetic UV radiation by the ozone layer according to the Chapman reactions (Chapman, 1930). In contrast to the troposphere, the stratosphere is generally stable and turbulent vertical mixing is inhibited. However, the tropopause between troposphere and stratosphere is not an insurmountable barrier for trace gases but allows to a certain extent for vertical transport in both directions (e.g. stratospheric injection of sulphur during volcanic eruptions and down-mixing of HCl which has been formed in the stratosphere). Of particular interest for the climate on Earth (greenhouse effect and optical properties of clouds) is the upper troposphere–lower stratosphere region (UTLS, 8–25 km, depending on latitude), which can be explored by aircraft measurements (Hoor et al., 2010; Schlager et al., 2012).

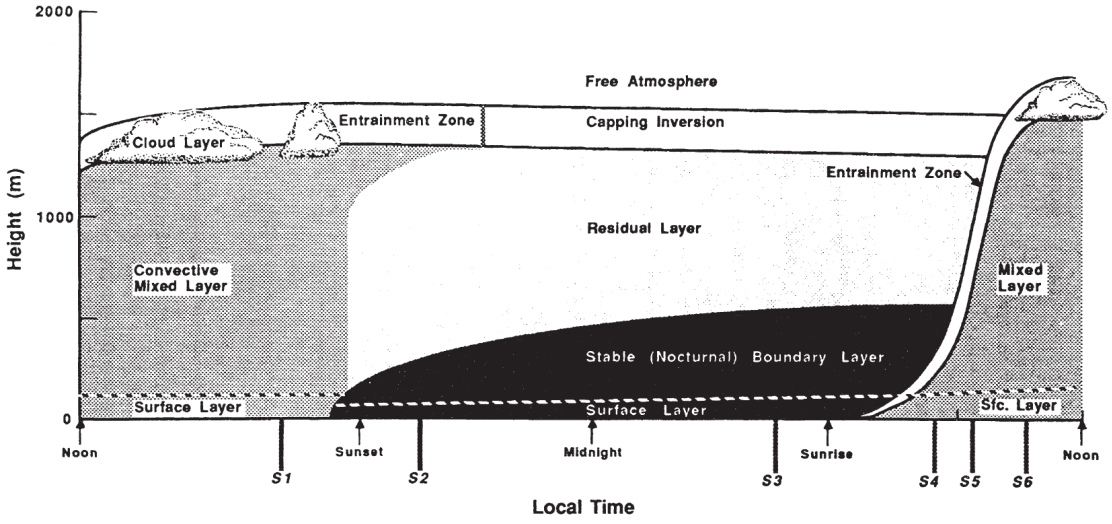

Figure 1.2: Diurnal evolution of the planetary boundary layer in high pressure regions over land, taken from Stull (1988).

The temperature in the mesosphere ($\approx$ 50–85 km) decreases as altitude increases due to declining O_3 concentrations and vertical mixing takes place, while in the thermosphere temperatures rise again due to the absorption of solar UV radiation by O_2 and N_2 (Finlayson-Pitts and Pitts Jr, 1999). The transition from mesosphere to thermosphere marks the end of the turbosphere, from where on different gaseous compounds are not well-mixed anymore.

In this thesis the focus is set on processes taking place in the planetary boundary layer (PBL), i.e. the lowermost part of the troposphere ($\approx$ 1 km), which is directly affected by interaction with the surface and by human activities (Stull, 1988). This layer plays a key role for air quality and is characterised by strong vertical turbulent mixing with wind speeds ranging from zero at the surface to the velocity of the geostrophic wind at its upper boundary. In this layer also the removal of primary and secondary pollutants via dry and wet deposition takes place, which is mainly dependent on boundary layer height, surface properties and solubility. During day-time, the PBL usually consists of a convective mixed layer (as illustrated in Fig. 1.2), whereas during night-time turbulence vanishes and it can partition into a stable nocturnal boundary layer (where emissions from the surface can accumulate) and a residual layer on top (Stull, 1988). After sunrise, a new convective mixed layer starts to form with an entrainment zone at the top where air from the free troposphere is mixed into the boundary layer. This dynamic diurnal cycle is particularly reflected in the volume mixing ratio of trace gases, which have been emitted by sources close to the ground and are dispersed within a variable mixed layer volume (e.g. biogenic emissions from the boreal forest, see Chapter 3).

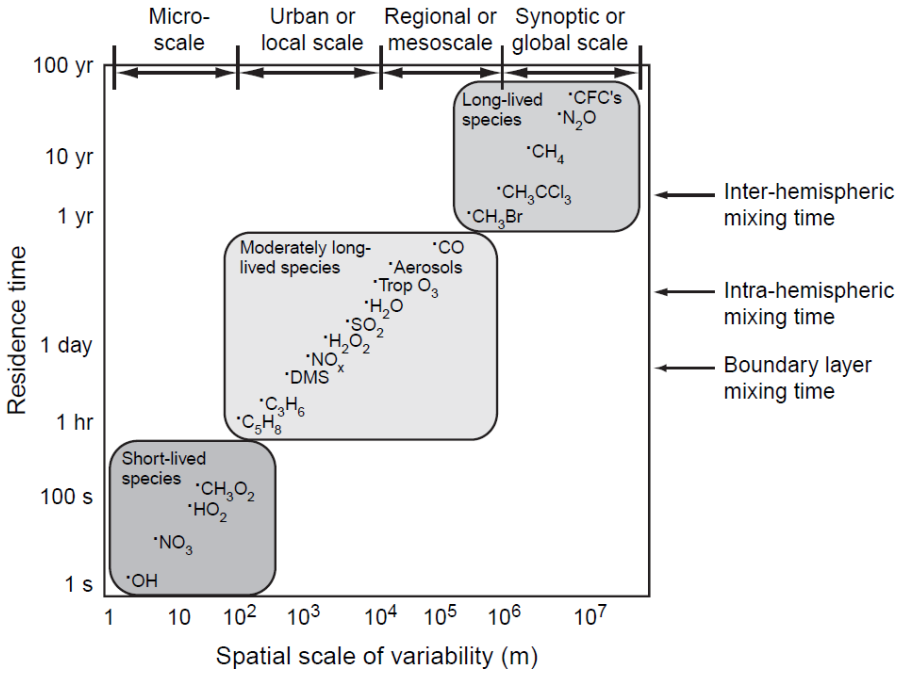

Figure 1.3: Spatial and temporal (expressed by residence time τ) scales of variability for some atmospheric constituents, taken from Wallace and Hobbs (2006).

1.3 Trace gases in the troposphere

To gain a better insight into the complex mechanisms influencing air quality and climate, it is crucial to understand the role of different trace gases. Although these trace gases are present at low volume mixing ratios (typically pptv to ppmv), they can be highly reactive and play a key role in tropospheric chemistry (Wallace and Hobbs, 2006). Some of them are directly emitted (from anthropogenic and biogenic sources), others are chemically or photochemically produced from precursors. The main emission sources are fossil fuel combustion, biomass burning, gas and oil production, agriculture, vegetation, oceans and soils while the main sinks are oxidation by OH (and other radicals), photolysis and deposition (Schlager et al., 2012). Anthropogenic trace gases include carbon monoxide (CO), carbon dioxide (CO_2), NO_x, SO_2, methane (CH_4) and several volatile organic compounds (VOCs), whereas the most abundant biogenic trace gases are isoprene, monoterpenes and dimethylsulfid (DMS).

The spatio-temporal distribution of atmospheric trace gases is determined by an interplay of sources and sinks, transport, mixing, chemical reactions and interaction with solar radiation, aerosols and clouds (Schlager et al., 2012). We can differentiate between short-lived and long-lived trace gases with a residence time τ, i.e. the time after which the initial concentration has decreased to $1/e \approx 0.37$. τ ranges from less than one second to several decades (see Fig. 1.3), depending on the strength and distribution of sources and sinks (Wallace and Hobbs, 2006). Assuming steady state (i.e. loss and production rates are in balance), τ can be

calculated from $\tau = (k_{\text{loss}})^{-1}$ with loss rate k_{loss}. Long-lived species like CO_2, CH_4 and nitrous oxide (N_2O) with lifetimes from several years to decades (Fig. 1.3) are typical greenhouse gases which impact the radiation balance of the atmosphere and the Earth's climate by absorbing long-wave radiation from the ground (Wallace and Hobbs, 2006). A prominent example are hydro-chloro-fluoro-carbons (HCFCs) with a residence time of about 100 a, which are responsible for the large ozone hole discovered over Antarctica during spring time in the 1980s (Solomon, 1988). Although emissions have stopped more than two decades ago thanks to the Montreal Protocol, the stratospheric ozone layer has hardly recovered due to the long lifetime of the HCFCs. In contrast, short-lived trace gases like the hydroxyl radical (OH) and the nitrate radical (NO_3) are very reactive and control the oxidation capacity of the atmosphere (Lelieveld et al., 2004; Liebmann et al., 2018) by transforming chemical compounds into water-soluble gases, which can be removed from the atmosphere via wet and dry deposition. Some trace gases like CO, O_3 and SO_2 directly affect air quality and human health due to their toxicity; others are involved in new particle formation, e.g. SO_2 after oxidation to sulphuric acid (Wallace and Hobbs, 2006). In the following sections several trace gases relevant for this work will be described in more detail.

1.3.1 Nitrogen oxides

Nitrogen oxides, commonly referred to as NO_x ($NO + NO_2$), play a crucial role in atmospheric chemistry as they influence the concentration of tropospheric hydroxyl radicals (OH) and are involved in the formation of tropospheric ozone (O_3) (Crutzen, 1970; Logan, 1983), hereby affecting air quality. NO_x is mostly emitted in the form of NO in combustion processes (industry and vehicles) with the highest concentrations (see Fig. 1.4) found in densely populated and industrialised areas (Beirle et al., 2003; Krotkov et al., 2016; Seinfeld and Pandis, 2016). A mechanism for NO formation at high temperatures (e.g. combustion or lightening) was first postulated by Zeldovich and Raizer (1966) and involves reactions (R 1.1–1.3) where $M = \{N_2, O_2\}$ denotes a collision partner needed for momentum conservation.

$$O_2 + M \longrightarrow O + O + M \quad \text{(R 1.1)}$$
$$O + N_2 \longrightarrow NO + N \quad \text{(R 1.2)}$$
$$N + O_2 \longrightarrow NO + O \quad \text{(R 1.3)}$$

Due to a subsequent and fast cooling the back reactions are usually suppressed and the emitted NO can be further oxidised to NO_2 via Reaction (R 1.4) (Finlayson-Pitts and Pitts Jr, 1999).

$$NO + O_3 \longrightarrow NO_2 + O_2 \quad \text{(R 1.4)}$$

The spatial and temporal distribution of NO_x is dependent on the interplay between chemical reactions and transport from the emission source. It can be oxidised to other reactive nitrogen species (referred to as NO_y) which includes NO_x,

Table 1.1: Global tropospheric NO_x emissions [Tg N a^{-1}] (Ciais et al., 2013).

$\sum$ Anthropogenic	37.5
Fossil fuel combustion and industrial processes	28.3
Agriculture	3.7
Biomass and biofuel burning	5.5
$\sum$ Natural	11.3
Soils	7.3
Lightening	4
Total	48.8

NO_3, N_2O_5, HNO_3, $ClNO_2$, peroxyacetyl nitrates, alkyl nitrates and particulate nitrate (Singh, 1987). Apart from transformation into reservoir species like peroxy acetyl nitrate (PAN, see below), the most important tropospheric sink of NO_x is the oxidation to HNO_3 (Reaction R 1.5), which is permanently removed from the atmosphere via deposition (Logan, 1983).

$$NO_2 + OH \longrightarrow HNO_3 \qquad \text{(R 1.5)}$$

Global annual tropospheric NO_x emissions from 2000–2010 were estimated as 48.8 Tg N a^{-1}, whereby fossil fuel combustion and industrial processes (including vehicles) represent the major source of NO_x, contributing more than 50 % to the total emissions (Ciais et al., 2013) (Table 1.1). Other anthropogenic sources are agriculture and biomass or biofuel burning. The remaining 23 % can be attributed to biogenic sources, which are mainly lightening and microbial activity in soils (Zörner et al., 2016). For comparison, in pre-industrial times total NO_x emissions were only 13.1 Tg N a^{-1} of which 10.5 Tg N a^{-1} originated from natural sources (Galloway et al., 2004). Future predictions are highly uncertain and strongly dependent on the policy decisions of industrialised nations and especially rapidly developing countries. Figure 1.5 (lower panel) illustrates that NO_x emissions in Europe and the United States have been decreasing within the last decade and also in China the maximum has been exceeded, whereas emissions in India are still rising (Krotkov et al., 2016; Gurjar et al., 2016; Miyazaki et al., 2017).

1.3.2 Volatile organic compounds

Volatile organic compounds (VOCs) denote a large group of gaseous species with high vapour pressure (including isoprene, terpenes, alkanes, alkenes, alcohols, esters, carbonyls and acids), which are emitted into the atmosphere from both the biosphere and anthropogenic activity (Atkinson and Arey, 2003). They have a significant influence on reactive atmospheric chemistry via photochemical ozone production in the presence of NO_x (see below) and on the formation, composition and climate impact of aerosols (Wallace and Hobbs, 2006). From several thousands of individual VOCs, only a fraction has been studied in detail and sources and sinks are often not fully constrained. Global annual emissions are estimated as 1300 Tg

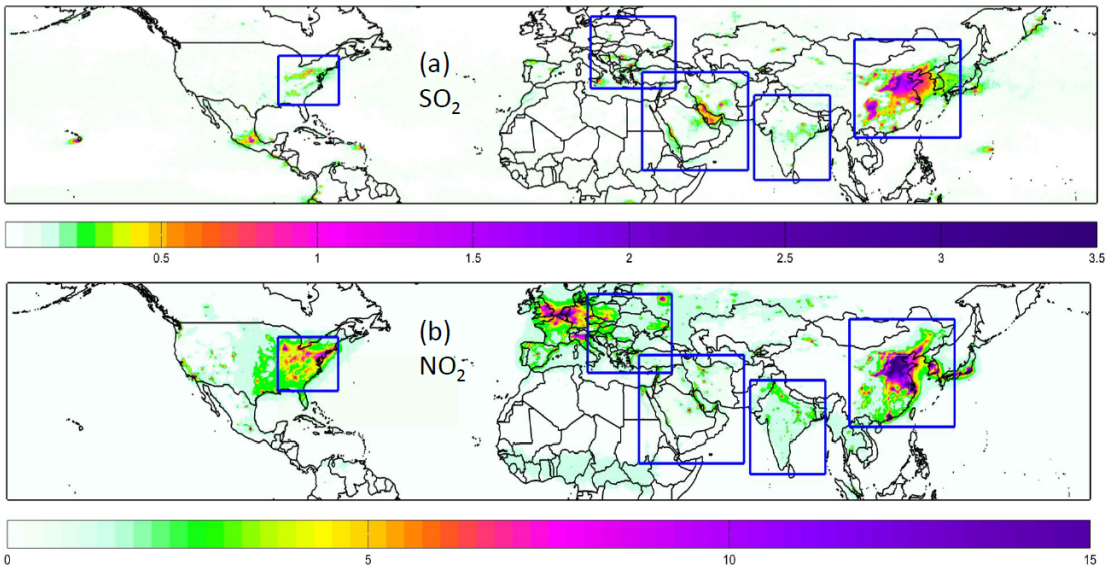

Figure 1.4: OMI-derived maps of (a) PBL SO_2 in Dobson units (DU) and (b) tropospheric NO_2 columns in 10^{15} molecules cm^{-2} for the years 2005–2007, with enhanced pollution levels around major cities and industrial centres, taken from Krotkov et al. (2016).

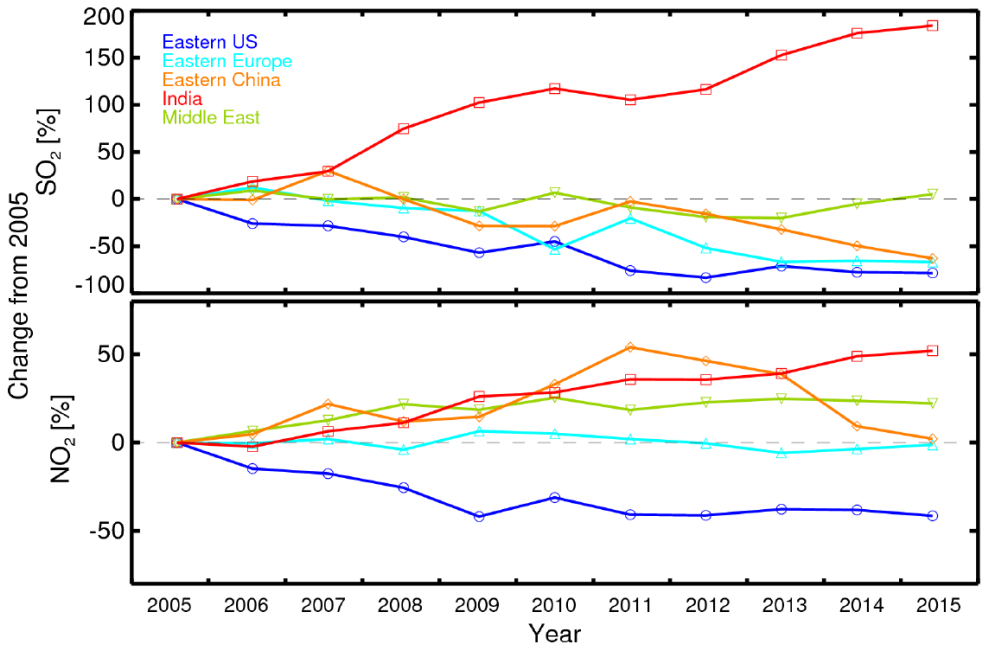

Figure 1.5: Percent change in OMI annual average columns since 2005: SO_2 (top) and NO_2 (bottom) over the world's most polluted regions, taken from Krotkov et al. (2016).

C a^{-1} (Goldstein and Galbally, 2007) which is about an order of magnitude larger than total NO_x emissions (see previous section). On a global scale, biogenic VOCs like isoprene and monoterpenes are the dominant components with mixing ratios up to several ppbv observed in vegetated areas (e.g. tropical and boreal forests) and a strong dependence on seasonality, temperature and light (Guenther et al., 1995; Kesselmeier and Staudt, 1999). Anthropogenic VOCs are mainly formed in incomplete combustions (e.g. vehicles) or other industrial processes like roadworks and fabrication of dissolvents and refrigerants (Reimann and Lewis, 2007).

For this work the focus lies on the group of organic acids (see Chapter 3), which are highly variable in their occurrence (due to their relatively short lifetimes) and are not only found in the atmosphere but also in the biosphere, lithosphere and hydrosphere (Kesselmeier and Staudt, 1999). They contribute to aerosol acidity and the formation of secondary organic aerosols (SOA), hence affecting air quality and climate (Hallquist et al., 2009). Whereas in remote areas (see IBAIRN field study) mostly biogenic organic acids like acetic and formic acid (mixing ratios up to several ppbv) dominate, in polluted areas anthropogenic compounds like sulphuric and nitric acid (involved in the formation of acid rain) play a major role (Kesselmeier and Staudt, 1999). With the chemical ionisation quadrupole mass spectrometer presented in this work, acetic acid ($CH_3C(O)OH$), peracetic acid ($CH_3C(O)OOH$) and pyruvic acid ($CH_3C(O)C(O)OH$) can be detected. Acetic acid has mostly biogenic sources (vegetation, wood) (Talbot et al., 1990) but can also be emitted from biomass burning and industrial combustion or can be produced photochemically. Pyruvic acid originates from both direct biogenic emission and photochemistry involving precursors like isoprene (Chapter 3). In contrast, peracetic acid is photochemically produced in the reaction of peroxy radicals with HO_2 (see below) and competes with PAN formation at high temperatures and low-NO_x conditions (Crowley et al., 2018).

1.3.3 Photostationary state

The photodissociation of NO_2 into NO and $O(^3P)$ by radiation with $\lambda < 420\,\text{nm}$ is a key reaction in the troposphere, as the produced oxygen atom immediately recombines with O_2 to form O_3. In turn, the ozone reacts with NO to form NO_2 and O_2. Thus, during daytime reactions (R 1.6–1.8) represents a closed cycle without any net ozone production (red cycle in Fig. 1.6). More precisely, NO and NO_2 are in a photostationary state, i.e. NO_2 production via NO and NO_2 losses through photolysis are in balance, such that the rate of O_3 concentration change is small in comparison to its rates of formation and removal (Seinfeld and Pandis, 2016).

$$NO_2 + h\nu \longrightarrow NO + O(^3P) \quad \text{(R 1.6)}$$

$$O(^3P) + O_2 + M \longrightarrow O_3 + M \quad \text{(R 1.7)}$$

$$NO + O_3 \longrightarrow NO_2 + O_2 \quad \text{(R 1.8)}$$

The steady-state (ss) ozone concentration is then determined by the ratio between source and sink reactions in Eq. (1.3).

$$[O_3]_{ss} = \frac{J_{NO2}\,[NO_2]}{k_{NO+O3}\,[NO]} \tag{1.3}$$

$$\phi = \frac{J_{NO2}\,[NO_2]}{k_{NO+O3}\,[NO][O_3]} \tag{1.4}$$

To illustrate deviations from the photo-stationary state, the Leighton Ratio ϕ (Eq. 1.4) was introduced (Leighton, 1961), which is equal to unity at high NO_x levels but deviates positively from unity when some chemical process other than the reaction between NO and O_3 converts NO to NO_2. This condition is fulfilled in the presence of peroxy radicals (HO_2, RO_2) formed in the oxidation of VOCs or CO by OH. Following the exemplary reaction schemes (R 1.9 and R 1.10), NO can be transformed into NO_2 without consuming O_3 (blue cycle in Fig. 1.6) which leads to a net photochemical production of ozone (Lelieveld and Dentener, 2000), influencing air quality (Lelieveld et al., 2002; Kampa and Castanas, 2008).

$$\begin{array}{lcl}
OH + O_2 + CO & \longrightarrow & CO_2 + HO_2 \\
HO_2 + NO & \longrightarrow & NO_2 + OH \\
NO_2 + h\nu & \longrightarrow & NO + O(^3P) \\
O(^3P) + O_2 + M & \longrightarrow & O_3 + M \\
\hline
\text{netto: } CO + 2\,O_2 & \longrightarrow & CO_2 + O_3
\end{array} \tag{R 1.9}$$

$$\begin{array}{lcl}
RH + OH & \longrightarrow & R + H_2O \\
R + O_2 + M & \longrightarrow & RO_2 + M \\
RO_2 + NO & \longrightarrow & RO + NO_2 \\
NO_2 + h\nu & \longrightarrow & NO + O(^3P) \\
O(^3P) + O_2 + M & \longrightarrow & O_3 + M \\
\hline
\text{netto: } RH + OH + 2\,O_2 & \longrightarrow & RO + O_3 + H_2O
\end{array} \tag{R 1.10}$$

1.3.4 Photochemistry and PAN

Despite mixing ratios of only a few pptv, the hydroxyl radical (OH) is the most important oxidising agent in the troposphere, transforming emitted (partially toxic) trace gases into water soluble compounds that can be removed via deposition (Lelieveld et al., 2016). It is primarily formed in the photolysis of ozone ($\lambda < 310$ nm, Reactions R 1.11–1.13), whereby the excited oxygen atom subsequently reacts with water vapour to form two OH radicals (representing a sink for tropospheric O_3). However, the yield for this reaction is only about 10 %; most

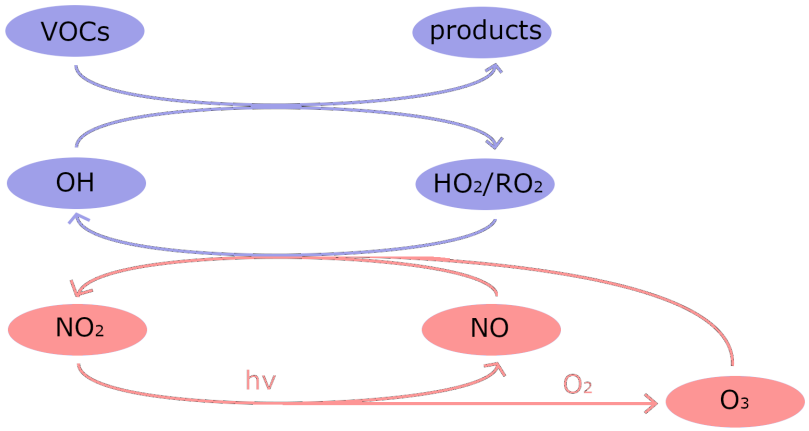

Figure 1.6: Scheme of the photostationary state (red cycle), which can be disturbed by peroxy radicals (HO_2 / RO_2), formed from the OH-initiated oxidation of VOCs (blue cycle), resulting in a net ozone (O_3) production.

of the excited $O(^1D)$ fall back to the ground state and recombine with O_2 to form O_3 again (Seinfeld and Pandis, 2016).

$$O_3 + h\nu \longrightarrow O(^1D) + O_3 \quad \text{(R 1.11)}$$

$$O(^1D) + H_2O \longrightarrow 2\,OH \quad \text{(R 1.12)}$$

$$O(^1D) + M \longrightarrow O(^3P) + M \quad \text{(R 1.13)}$$

As mentioned before, the reaction of OH with CO and VOCs forms hydroperoxy (HO_2) and organic peroxy (RO_2) radicals which can further react with NO to form NO_2 without consuming O_3. In addition, formed $CH_3C(O)O_2$ radicals are precursors for secondary pollutants like peroxy acetyl nitrates (PANs, $RC(O)O_2NO_2$) (Roberts, 1990). PAN, which can be measured by the instrument presented in this thesis, is the most abundant ($\approx 90\,\%$) of this group of PANs (including PPN, PiBN, mPAN and others) and can reach levels up to several ppbv. It is also a toxic component of the photochemical smog (also referred to as Los Angeles smog), which is characterised by the reaction scheme (R 1.14) (Haagen-Smit, 1952; Taylor, 1969).

$$VOCs + NO + h\nu \longrightarrow O_3 + PAN + HNO_3 + particles \quad \text{(R 1.14)}$$

In addition, it is a reservoir species for NO_x (Reaction R 1.15) with an atmospheric lifetime of a few hours at high temperatures up to several days or weeks at low temperatures (e.g. in the upper troposphere) (Roberts, 1990). In this way NO_x is transported to remote areas (Singh and Hanst, 1981) and when temperatures rise again, can be released (Reaction R 1.16) far away from the emission source,

enhancing local ozone production (Williams et al., 1997).

$$\mathrm{CH_3C(O)O_2 + NO_2 + M \longrightarrow CH_3C(O)O_2NO_2 + M} \quad \text{(PAN)} \quad \text{(R 1.15)}$$
$$\mathrm{CH_3C(O)O_2NO_2 + M \longrightarrow CH_3C(O)O_2 + NO_2 + M} \quad \text{(R 1.16)}$$
$$\mathrm{CH_3C(O)O_2 + HO_2 \longrightarrow CH_3C(O)OOH + O_2} \quad \text{(PAA)} \quad \text{(R 1.17)}$$
$$\mathrm{\longrightarrow CH_3C(O)OH + O_3} \quad \text{(R 1.18)}$$
$$\mathrm{\longrightarrow OH + CH_3CO_2 + O_2} \quad \text{(R 1.19)}$$
$$\mathrm{CH_3C(O)OOH + OH \longrightarrow CH_3C(O)O_2 + H_2O} \quad \text{(R 1.20)}$$

At low-NO_x conditions $CH_3C(O)O_2$ reacts with HO_2 (instead of NO_2) to form peracetic acid (PAA, Reaction R 1.17) and acetic acid (R 1.18) or recycles OH via Reaction (R 1.19). PAA represents an intermediate sink for HO_2 and $CH_3C(O)O_2$ and is measured by the instrument presented in this thesis (along with acetic acid). Major sinks for PAA are the reaction with OH (R 1.20) and wet deposition. Except for high temperatures or under very low NO_x conditions, PAN mixing ratios are usually greater than that of PAA (Crowley et al., 2018).

1.3.5 Nocturnal chemistry: NO_3 and N_2O_5

In the presence of O_3, NO_2 can further react to the nitrate radical (NO_3, Reaction R 1.21) (Atkinson, 2000), which is an important oxidising agent, especially during night-time.

$$\mathrm{NO_2 + O_3 \longrightarrow NO_3 + O_2} \quad \text{(R 1.21)}$$
$$\mathrm{NO_3 + h\nu \longrightarrow NO_2 + O} \quad \text{(R 1.22)}$$
$$\mathrm{NO_3 + h\nu \longrightarrow NO + O_2} \quad \text{(R 1.23)}$$
$$\mathrm{NO_3 + NO \longrightarrow 2\,NO_2} \quad \text{(R 1.24)}$$
$$\mathrm{NO_3 + NO_2 + M \longleftrightarrow N_2O_5 + M} \quad \text{(R 1.25)}$$
$$\mathrm{NO_3 + VOCs \longrightarrow products} \quad \text{(R 1.26)}$$

During day, NO_3 is rapidly photolysed (Reactions R 1.22 and R 1.23) or reacts with NO (R 1.24) so that its mixing ratios are usually below the detection limit (Brown et al., 2003; Crowley et al., 2010). Only after sunset the lifetime increases so that N_2O_5 can be formed in the reaction of NO_3 with NO_2 (Reaction R 1.25) as illustrated in Fig. 1.7. The equilibrium between NO_3 and N_2O_5 is strongly temperature-dependent, with N_2O_5 formation favoured by high NO_2 mixing ratios and low temperatures (Platt et al., 1980). NO_3 can also react with VOCs (Reaction R 1.26) (Ng et al., 2017) to form e.g. alkyl nitrates (Fig. 1.7), which reduces the rate of formation of N_2O_5.

1.3.6 Reactive chlorine: $ClNO_2$ and HCl

The heterogeneous uptake of gaseous N_2O_5 to the aerosol phase represents an important atmospheric sink of NO_x (Chang et al., 2011) via conversion to HNO_3

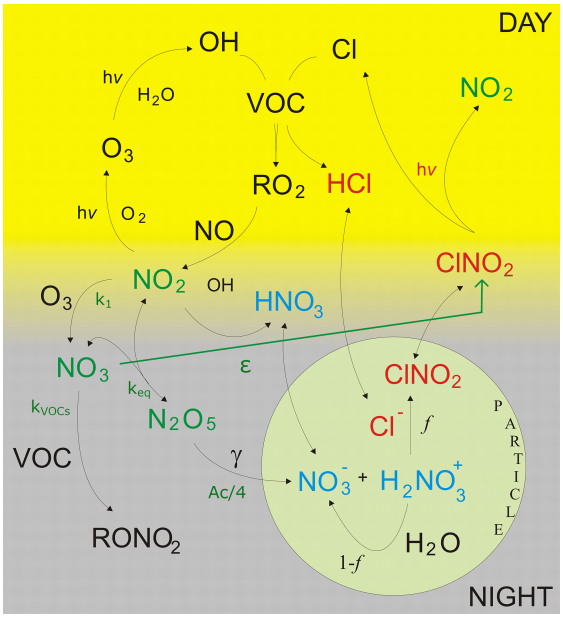

Figure 1.7: Reactive nitrogen chemistry during day and night and reactions involved in the formation of $ClNO_2$, with uptake coefficient γ, $ClNO_2$ yield f and $ClNO_2$ production efficiency ϵ (see Sect. 4.3.2). Adapted from Phillips et al. (2016).

(Reaction R 1.27) and subsequent removal from the boundary layer via deposition. In the presence of aerosol chloride, nitryl chloride ($ClNO_2$) can be formed along with HNO_3 (NO_3^-) (Reaction R 1.28) (Behnke et al., 1997; Finlayson-Pitts et al., 1989) according to Fig. 1.7.

$$N_2O_5\,(g) + H_2O\,(aq) \longrightarrow 2\,HNO_3\,(aq) \qquad (R\,1.27)$$

$$N_2O_5\,(g) + Cl^-\,(aq) \longrightarrow ClNO_2\,(g) + {NO_3}^-\,(aq) \qquad (R\,1.28)$$

$$ClNO_2 + h\nu \longrightarrow Cl + NO_2 \qquad (R\,1.29)$$

$ClNO_2$ has a lifetime of more than 30 hours in the nocturnal marine boundary layer (Osthoff et al., 2008) but is rapidly photolysed during daytime (Reaction R 1.29), releasing NO_2 (which is hereby recycled) and reactive chlorine atoms. These Cl atoms can increase oxidation rates of several VOCs (Fig. 1.7) and compete with OH-induced reactions during early morning hours (Phillips et al., 2012). $ClNO_2$ has been measured at a continental site in Germany during NOTOMO (Sect. 2.7.2) and in a mostly polluted marine environment during the AQABA ship campaign (Chapter 4).

Another relevant Cl-containing species is hydrogen chloride (HCl) which is directly emitted from waste incineration and other industrial processes or released from sea salt aerosols via acid displacement (Wang et al., 2019). On a global scale acid displacement is the dominant source of HCl, especially in polluted coastal regions (see AQABA campaign, Chapter 4) where it is displaced by HNO_3 and H_2SO_4 (Reactions R 1.30 and R 1.31), themselves originating from anthropogenic NO_x and SO_2 emissions. HCl is rapidly removed from the atmosphere via wet

deposition or can further partition into fine mode aerosols, hereby representing an important source of chloride transported inland from coastal regions, which enhances continental $ClNO_2$ production rates (Wang et al., 2019), like indicated for the NOTOMO campaign (Sect. 2.7.2).

$$HNO_3 + NaCl \longrightarrow HCl + NaNO_3 \quad \text{(R 1.30)}$$

$$H_2SO_4 + 2\,NaCl \longrightarrow 2\,HCl + Na_2SO_4 \quad \text{(R 1.31)}$$

1.3.7 Sulphur emissions and particle formation

Sulphur is mostly inserted into the atmosphere in the form of SO_2 originating from combustion of fossil fuels (coal and mineral oil). Natural sources of SO_2 are volcanos and microbial activity in oceanic algae releasing dimethylsulfid (DMS, CH_3SCH_3) which is further oxidised to SO_2 (Wallace and Hobbs, 2006). SO_2 has a tropospheric lifetime of several hours to days and is a primary pollutant affecting air quality and climate through formation of sulphate aerosol (Seinfeld and Pandis, 2016). The fate of SO_2 is either deposition or oxidation to H_2SO_4 by OH following Reactions (R 1.32–1.35), whereby the OH is recycled in (R 1.34) (Finlayson-Pitts and Pitts Jr, 1999).

$$SO_2 + OH + M \longrightarrow HSO_3 + M \quad \text{(R 1.32)}$$

$$HSO_3 + O_2 \longrightarrow SO_3 + HO_2 \quad \text{(R 1.33)}$$

$$HO_2 + NO \longrightarrow NO_2 + OH \quad \text{(R 1.34)}$$

$$SO_3 + H_2O + M \longrightarrow H_2SO_4 + M \quad \text{(R 1.35)}$$

H_2SO_4 has a tropospheric residence time of minutes to hours as it is rapidly deposited to aerosols or droplets (Roedel, 2000). It initiates secondary aerosol formation, influences aerosol acidity and is involved in the occurrence of acid rain (Singh and Agrawal, 2007). In addition, it is a crucial component of the so called “winter smog” (also referred to as ”London smog”), with negative effects on human health. Sulphuric acid further acts as cloud condensation nuclei and affects cloud properties, with sulphate aerosol contributing to a radiative forcing of minus $0.4\,W\,m^{-2}$ (Myhre et al., 2013). Global SO_2 emissions in the year 2011 are estimated as ≈ 100 Tg (SO_2) a^{-1} (Klimont et al., 2013), mainly from anthropogenic sources (indicated by satellite observations in Fig. 1.4a). In the last two decades de-sulphurisation in the industrial sector has contributed to a substantial enhancement in air quality in western Europe and the U.S. (Krotkov et al., 2016; Kharol et al., 2017) and to an embanking of acid rain caused by SO_2. More recently China has also reduced its SO_2 emissions (Klimont et al., 2013), whereas in India they are still rising (see Fig. 1.5). In addition, international shipping remains a major emission source (Corbett and Fischbeck, 1997), significantly contributing to the properties of marine aerosol and clouds and to air pollution in coastal regions (Coggon et al., 2012). The role of SO_2 in the polluted marine boundary layer around the Arabian Peninsula has been studied during the AQABA ship campaign (see Appendix A).

1.4 Mass spectrometry for trace gas measurement

Mass spectrometers (MS) are versatile analytic devices which produce (predominantly single-charged) ions out of a gaseous sample, separate them by their mass-to-charge ratio (m/z) and thus provide information about the composition of the sample. In the field of atmospheric science they are widely used for the simultaneous detection of atmospheric trace gases with mixing ratios in the order of pptv and for aerosol composition measurements. In the following, the basic principles of mass spectrometry will be outlined along with details on chemical ionisation and quadrupole mass analysers, based on a textbook on mass spectrometry by Gross (2011). MS consist of three basic elements: ion generation, separation and detection, the latter two performed under high-vacuum conditions to avoid collisions with nitrogen or oxygen atoms and to guarantee a long lifetime of the detector. Depending on the field of application several ways of ionisation, separation and detection are implemented. Ionisation can be realised thermally or by firing at the sample with high-energetic electrons, ions or photons, resulting in a different degree of fragmentation of the product ions. The most common ionisation methods are electron ionisation (EI), chemical ionisation (CI), photoionisation and thermal ionisation. After being generated, the ions are accelerated by pressure differences and electrical potentials (with kinetic energy of the ions according to Eq. 1.5) and focussed by ion guides. Separation can be realised by different analysers, including magnetic sector field, linear quadrupole, ion trap, Fourier-Transform, ion mobility and Time-of-Flight MS. After passing the analyser, ions reach the detector where the electrical signal is amplified and digitalised for further analysis.

$$E_{\mathrm{kin}} = eU = \frac{1}{2}\,mv^2 \tag{1.5}$$

The intensity of the signal is then derived from the height or more accurately the area of the peak at a specific m/z. In this work a linear quadrupole analyser in combination with a chemical ionisation technique using iodide anions was applied, which is explained in more detail in the following sections.

1.4.1 Linear quadrupole analysers

Since it has been discovered that two- and three-dimensional quadrupole electrical fields can be used for mass analysis (Paul and Steinwedel, 1953), quadrupole mass spectrometers have become versatile instruments frequently used in literature (Dawson, 1976, 1986). Main advantages compared to other methods are high transmission and temporal resolution (about 1 s), low ion acceleration voltages and a light, compact and low-cost design for flexible application (Gross, 2011). A review on developments in the field of quadrupole mass analysers is presented by Douglas (2009).

Linear quadrupole analysers consist of four parallel hyperbolically or cylindrically shaped rod electrodes stretched in z-direction (Fig. 1.8), whereby two opposite electrodes are held at the same potential (DC with superimposed AC voltage). In

the following the working principle is outline based on Gross (2011). When ions travel the quadrupole in z-direction, they experience an attracting force from the electrode with the opposite charge. By applying periodical voltages to the rods, attraction and repulsion in x- and y-direction will alternate in time, based on the field potential Φ (Eq. 1.6) whereby $(x, y) = (0,0)$ is the centre of the quadrupole and r_0 is the field radius (10 mm for the MS used in this thesis), i.e. the distance from the centre to an electrode. U denotes a DC voltage and V an AC voltage with frequency ω, which is typically in the order of 1 MHz (1.44 MHz for the MS used in this thesis) and thus a radio-frequency (RF).

$$\Phi(x, y, t) = \left(\frac{x^2 - y^2}{r_o^2}\right)(U + V\cos(\omega t)) \tag{1.6}$$

The equations of motion in x- and y-direction are expressed in terms of Mathieu differential equations (Mathieu, 1868) with dimensionless parameters a, q and τ (Eq. 1.7–1.11):

$$\frac{d^2x}{d\tau^2} + (a_x + 2q_x \cdot cos(2\tau)) \cdot x = 0 \tag{1.7}$$

$$\frac{d^2y}{d\tau^2} + (a_y + 2q_y \cdot cos(2\tau)) \cdot y = 0 \tag{1.8}$$

$$a_x = -a_y = \frac{4eU}{m_i r_0^2 \omega^2} \tag{1.9}$$

$$q_x = -q_y = \frac{2eV}{m_i r_0^2 \omega^2} \tag{1.10}$$

$$\tau = \frac{\omega t}{2} \tag{1.11}$$

For a given set of a, q and ω only ions with a specific m/z can traverse the quadrupole on stable trajectories in the x-y-plane and reach the detector. The stability of the trajectory of an ion with a specific m/z is defined by the amplitude of the RF voltage V and the ratio U/V. This can be illustrated by means of a stability diagram, where a is plotted against q. Typically quadrupole mass analysers are operated in stability region I, which is illustrated in Fig. 1.9. To vary the accepted m/z range of stable ions, both voltages are increased at a constant DC-to-RF ratio along the load line of $a/q = 2U/V = \text{const}$. To achieve a better mass resolution, the ratio a/q is increased but this can be realised only to a certain extent without significantly decreasing the transmission (Gross, 2011).

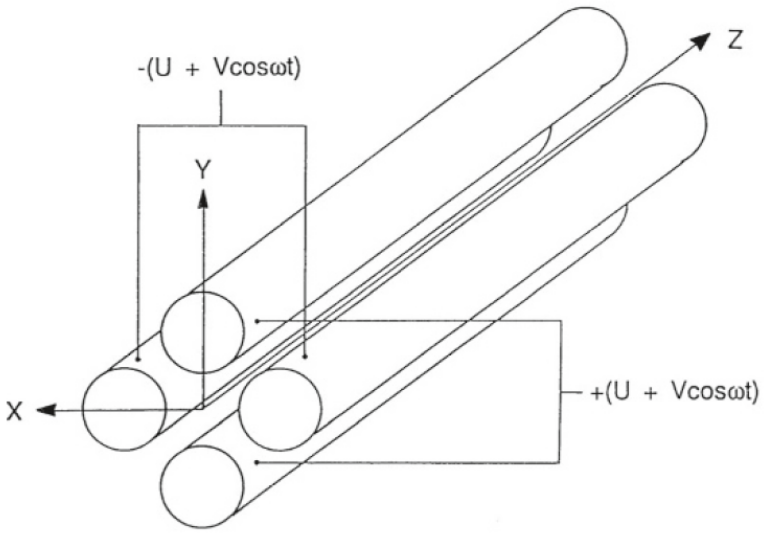

Figure 1.8: Schematic drawing of a linear quadrupole analyser, taken from Gross (2011).

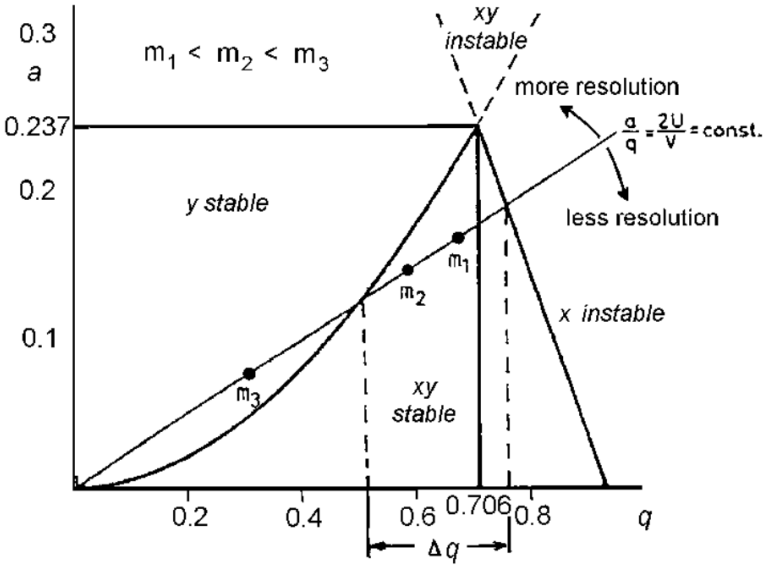

Figure 1.9: Detail of the upper half of region I of the stability diagram for a linear quadrupole analyser, figure taken from Gross (2011).

1.4.2 Chemical ionisation

Chemical ionisation (CI) is a soft ionisation method introduced by Munson and Field (1966) which is similar to electron ionisation (EI) but has the advantage of generally causing less fragmentation. In contrast to EI, the analyte is not directly ionised by highly-energetic electrons but via ion-molecule reactions, whereby in the first step reagent ions are formed from electron ionisation of the reagent gas molecules, which in the second step transfer charge to the analyte (e.g. via electron attachment or adduct formation). Depending on the choice of reagent ions, CI provides a higher sensitivity and selectivity compared to EI and does not require a high vacuum ($< 10^{-4}$ Pa) in the ion source region (Gross, 2011; Huey, 2007). In general, both positive and negative ions can be generated via CI but – due to a higher selectivity towards compounds with high electron affinity (e.g. halogens) – in this work we focus on the application in negative ion mode (NCI). In combination with a quadrupole mass analyser, chemical ionisation mass spectrometers (CIMS) are particularly suitable for airborne measurements (Aufmhoff et al., 2012) as they are characterised by high sensitivity, selectivity, flexibility and an easy handling (Huey, 2007). The choice of reagent ions strongly depends on selectivity and sensitivity to trace gases of interest and consideration of potential interferences. A review on the application of I^- and SF_6^- for the CIMS measurement of reactive nitrogen species is presented by Huey (2007). I^- ions are known to react very selectively with, for example, peroxyacyl-radicals and are unreactive with most abundant trace gases like O_3 and NO_2 so that ions are sufficiently stable on the time scale of the reaction process. In addition, I^- has a large m/z and one of the largest mass defects which facilitates identification of product ions if the mass resolution is high.

Iodide ions are commonly generated in a stream of N_2 and trace amounts of CH_3I by the bombardment with alpha-radiation of a ^{210}Po ioniser (Slusher et al., 2004; Phillips et al., 2012) and dissociative attachment of thermal electrons to CH_3I (Reaction R 1.36, where the star depicts an excited state).

$$CH_3I + e^- \longrightarrow (CH_3I^-)^* \longrightarrow I^- + CH_3 \qquad \text{(R 1.36)}$$

Advantages of ^{210}Po ionisers are high stability and generally low chemical background signals whereas the main disadvantages are restrictions concerning its use and transport. Alternative ion sources for I^- generation are, however, rarely used as they often suffer from elevated chemical background signals across the mass spectrum. In this thesis an electrical RF discharge ion source is applied to generate primary ions by chemical ionisation from a stream of CH_3I / N_2, similar to an radioactive ion source. The main difference is the formation of additional primary-ions including IO_x^- and $I(CN)_x^-$ that result in a more complex mass spectrum and extension of the established detection scheme, as explained in detail in Chapter 2.

1.4.3 Mass resolution and sensitivity

Two peaks are considered separate from each other when the valley between them is less than 10 (or 50) % of the intensity of the smaller peak. The mass resolution R is then defined by Eq. (1.12) where m is the mass which is measured and Δm is the detectable mass difference (Gross, 2011). To separate, for example, N_2 with 28.0161 atomic mass units (amu) and CO with 27.9949 amu a resolution of $R \approx 1320$ would be required. In practise, Δm is often derived from the full width at half maximum (FWHM) of a single peak. Quadrupole mass spectrometers usually provide unit resolution, i.e. $\Delta m = 1$, which means that two peaks with a difference of one mass unit can just be separated (e.g. $R = 20$ at m/z 20 and $R = 200$ at m/z 200) (Douglas, 2009). If higher resolving power is needed, ToF-MS are preferred, which combine high mass resolution with an unlimited mass range and fast scanning rates for a complete mass spectrum (Lee et al., 2014).

$$R = \frac{m}{\Delta m} \tag{1.12}$$

For CIMS instruments, the concentration of the trace gas $[P]$ is usually calculated from Eq. 1.13, where $[P^-]$ is the background-corrected signal of the analyte (in Hz) and $[R^-]$ is the reagent ion signal (Huey, 2007). This equation is valid under the assumption that the concentrations of neutral species and reagent ions are stable during the ionisation process (i.e. less than a few percent of the reagent ions are consumed).

$$[P] = \frac{[P^-]}{[R^-]\, kt} \tag{1.13}$$

As the effective rate constant k and the effective reaction time t are difficult to determine (e.g. due to multiple product ions), the effective sensitivity S [Hz pptv^{-1}] is usually derived from calibrations with a known amount of the analyte $[P]_c$ (Eq. 1.14).

$$S := kt = \frac{[P^-]_c}{[R^-]_c\, [P]_c} \tag{1.14}$$

The instrument sensitivity depends on numerous parameters, including ionisation efficiency, duty cycle ($\approx 100\,\%$ for a quadrupole analyser in single ion monitoring mode), ion transmission and efficiency of the detector. By normalising $[P^-]$ by $[R^-]$, drifts in ion source intensity can be accounted for (Huey, 2007). The sensitivity for individual trace gases can be optimised by adjusting pressure, flows and electrical potentials in CDC, octupole and quadrupole (see Sect. 2.2). Since H_2O can compete with the reagent ion (decreasing the sensitivity) or provide a third body to stabilise the ion-molecule-cluster (increasing the sensitivity), a correction factor (c_{RH}) needs to be applied to eliminate the relative humidity dependence of the signal. In the case of $ClNO_2$ detection with iodide primary ions (see Sect. 2.6) the concentration is calculated via Eq. 1.15.

$$[ClNO_2] = \frac{[ICl NO_2{}^-] \times c_{RH}}{[I^-] \times S_{ClNO2}} \tag{1.15}$$

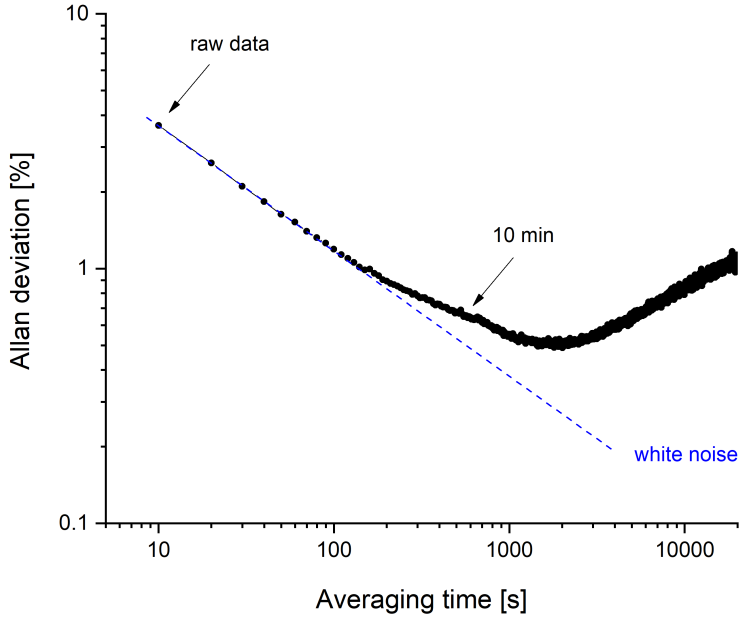

Figure 1.10: Allan deviation plot (1σ) for the CI-QMS primary ion signal during the AQABA campaign.

1.4.4 Limit of detection and total measurement uncertainty

The detection limit (LOD) is the smallest amount of an analyte than can still be distinguished from the background signal. For the field studies presented in this thesis we define the LOD as 2 times the standard deviation (2σ, 95 % confidence) when measuring a blank. Assuming Poisson white noise, the standard deviation of a signal is given by $\sigma_P = \sqrt{P}$), where P denotes the number of counts. This implies that the LOD can be enhanced when integrating over a longer period and thus collecting more ions. In reality, the signal will drift over time due to fluctuations in temperature, ion transmission, detector efficiency etc. and the noise will deviate from $\sqrt{P}$ for $t \to \infty$. The instrument precision can be derived from the stability of the primary ion signal, as exemplary illustrated by an Allan deviation plot in Fig. 1.10 for the primary-ion signal (I^-) during AQABA (Chapter 4). The precision relative to the signal for raw data (10 s temporal resolution) is a few percent, whereas when averaging over 5–10 min (as usually done for stationary measurements) it decreases to $< 1\,\%$. Averaging over an even longer period, however, hardly improves the precision, as it is no longer determined by pure white noise.

The total measurement uncertainty depends on how precisely product ions of interest and primary ions can be measured (which is a function of the chosen integration time, see Fig. 1.10). It also depends on the uncertainty associated with the subtraction of the background signal, which may vary (e.g. during field studies where it is recorded $\approx$ once per hour) due to chemical interferences or memory effects. Finally, the uncertainty of the calibration standard (which depends on the

calibration method and data from manufacturers of gas bottles, permeation sources etc.) largely contributes to the total measurement uncertainty (see Sect. 2.6), including the uncertainty of the humidity correction. Further sources of uncertainty are fluctuations in ion transmission or detection efficiency (which are usually eliminated by monitoring the primary ion signal), wall losses (especially for sticky molecules), and chemical interferences (from unidentified molecules). The overall uncertainty can be derived from $\sigma_{\text{total}} = \sqrt{\sum_i (\sigma_i)^2}$, where σ_i are the single uncertainties. To give an example, the total uncertainty of the $ClNO_2$ measurement during AQABA was equal to $30\,\% \pm 6\,\text{pptv}$, which could mainly be attributed to the uncertainty of the calibration method (involving thermal dissociation cavity ring-down spectroscopy, TD-CRDS) and drifts between consecutive background measurements.

1.5 Objectives of the thesis

As pointed out in Sect. 1.3, trace gases like NO_x, VOCs, O_3, PAN and SO_2 are key components in the troposphere with a large impact on climate, air quality and human health. As Fig. 1.11 illustrates, the trace gases measured by the instrument presented in this thesis are linked to each other through complex chemical and physical processes, involving emission of anthropogenic (NO_x, SO_2, VOCs) and biogenic (VOCs) trace gases and interaction with solar radiation, radicals and aerosols. In the following this reaction scheme is briefly outlined (for more details

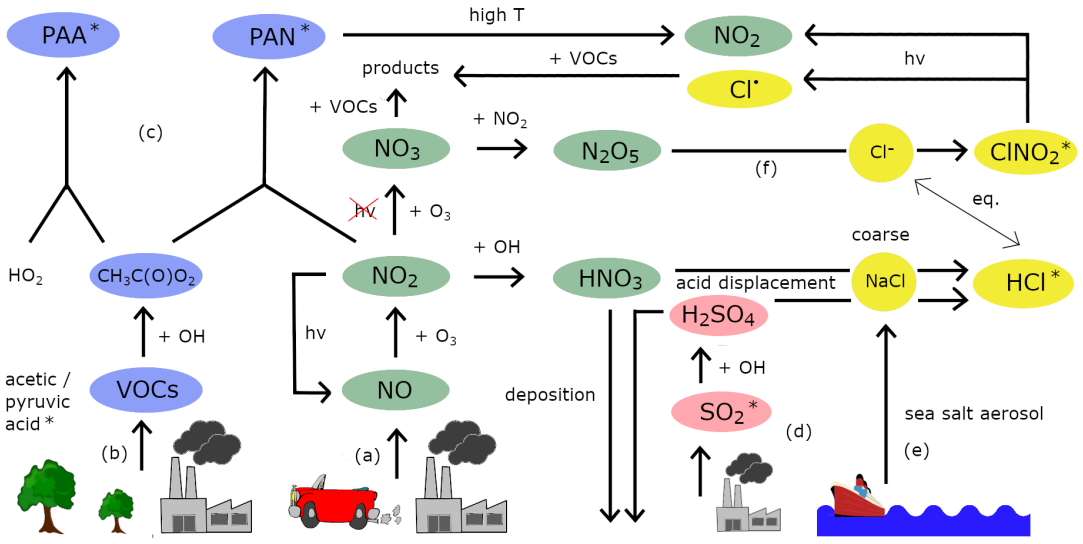

Figure 1.11: Simplified scheme of sources, sinks and interactions between measured trace gases (marked by a star, *). Important pathways are highlighted by letters a–f.

on individual trace gases see previous sections), whereby trace gases detectable by the CI-QMS are highlighted with a star (*) and different pathways are marked by letters (a–f) according to Fig. 1.11:

(a) The dominant atmospheric source of NO_x is the emission of NO from industry and vehicles and its subsequent reaction with O_3 to NO_2. During the day, NO_2 can be further oxidised by OH, resulting in the formation of HNO_3, which is deposited to the surface. In the absence of sunlight NO_2 forms NO_3, which can further react to N_2O_5, a precursor for $ClNO_2$* and HNO_3.

(b) In addition, VOCs can be emitted from both the biosphere (e.g. acetic* and pyruvic acid*, see Chapter 3) and from anthropogenic sources. They represent important precursors for peroxy radicals (HO_2 and $CH_3C(O)O_2$).

(c) Under low-NO_x conditions (see IBAIRN campaign) these peroxy radicals mainly react with HO_2 to generate PAA*. In more polluted environments (see NOTOMO campaign) they will favourably react with NO_2 to form PAN*, which is a reservoir species for NO_x at low temperatures but will rapidly decompose at high temperatures (see AQABA, Chapter 4).

(d) Combustion of sulphur-containing fossil fuels produces SO_2* which can be oxidised to sulphuric aicd. H_2SO_4 can partition into the aerosol phase, form SOA and act as a cloud condensation nuclei.

(e) In the presence of sea salt aerosol released from the oceans, HCl* can be displaced by HNO_3 and H_2SO_4, especially in the polluted marine environment (see AQABA campaign).

(f) Gas-phase HCl is also in equilibrium with particulate chloride in fine mode aerosol particles, which can take up N_2O_5 to form NO_3^- and $ClNO_2$*, depending on the particulate chloride concentration. During day $ClNO_2$ is photolysed releasing NO_2 and Cl-radicals, with the latter being highly reactive towards several hydrocarbons and competing with OH-induced reactions in the early morning.

Measuring the above mentioned trace gases thus provides important information on reactive chlorine, sulphur, nitrogen and organic chemistry and reveals the relevance of individual pathways in different environments. It enables us to close observational gaps in regions where little or no literature data is available and provides input for atmospheric chemistry models, ultimately extending our understanding of the atmosphere.

A widely used method to measure trace gases with high temporal resolution, sensitivity and low detection limit is chemical ionisation quadrupole mass spectrometry (CI-QMS) which has been briefly outlined in the previous section. The instrument, which is presented in detail in Chapter 2, is a technical evolution of an existing instrument formerly used to measure PAN, PAA and $ClNO_2$ (Phillips et al., 2012, 2013). Within the scope of this thesis it was further developed, extensively characterised in the laboratory and applied in several field studies (Chapter 2–4). It offers the possibility to sensitively measure a mixture of anthropogenic (e.g. SO_2) and biogenic (e.g. acetic acid and pyruvic acid) trace gases including

Figure 1.12: Overview of measurement sites during NOTOMO (Chapter 2), IBAIRN (Chapters 2 and 3) and AQABA (Chapter 4). The (approximate) route of the ship between southern France and Kuwait during AQABA is indicated by the white line. The map was created with Google Earth.

important reservoir species (e.g. $ClNO_2$, HCl, PAN and PAA) and secondary pollutants (e.g. PAN). To enable detection of this unique package of trace gases, the instrument was equipped with a novel electrical discharge ion source (replacing the polonium ioniser commonly used in literature), which expanded the established ion detection scheme (see Chapter 2). Due to its compact design and flexible inlet it is suitable for stationary measurements as well as for usage on moving platforms like ships and aircraft.

1.6 Overview of field studies

From 2015–2017 the instrument was applied in three different field studies around the globe: NOTOMO (Germany, 2015), IBAIRN (Finland, 2016) and AQABA (Mediterranean Sea and Arabian Peninsula, 2017). The measurement sites in Germany and Finland as well as the ship track through the Mediterranean Sea, the Red Sea, the Arabian Sea and the Arabian Gulf are highlighted on the map in Fig. 1.12. Within these field studies different aspects of atmospheric chemistry and the relevance of the above mentioned trace gases in various environments are explored.

1.6.1 NOTOMO campaign

The NOTOMO (NOcturnal chemistry at the Taunus Observatory: insights into Mechanisms of Oxidation) camapign (see Chapter 2) took place at the Taunus Observatory (50° 13' 25" N, 8° 26' 56" E, 825 m above sea level) at the summit of the "Kleiner Feldberg" in south-western Germany. The measurement site is surrounded by coniferous forest (mainly spruce) and shrubs and known for its relatively remote character in central Germany, with only a few main roads and some small towns within 5 km distance (Crowley et al., 2010). In the following a short introduction is presented, a more detailed description is given elsewhere (Crowley et al., 2010; Sobanski et al., 2017). There are two mountains of similar height located to the north-east and south-east (Großer Feldberg at 878 m and Altkönig at 798 m above sea level) and the nearby area in the north-west to north-east sector can be described as rural, forested and relatively sparsely populated. However, the site is regularly impacted by air pollution from the south-east to south-west sector, which originates from the heavily populated and industrialised Rhein-Main area, including dense traffic systems and urban centres such as Frankfurt, Wiesbaden and Mainz. In addition, the heavily populated and industrialised Ruhr area is located about 130 km to the north-west. Due to its unique character the measurement site is perfectly suited for studying the interaction of biogenic emissions from the forest with anthropogenic emissions from industry, agriculture and urban conglomerations, resulting in partially high levels of NO_x, O_3, PAN and SO_2 (see Sect. 2.7.2).

1.6.2 IBAIRN campaign

Besides rain forest and temperate forest, the boreal forest is one of the largest terrestrial biomes on Earth and characterised by strong emissions of biogenic VOCs including isoprene, monoterpenes and organic acids (Kesselmeier and Staudt, 1999; Rinne et al., 2005; Hakola et al., 2012). It has a significant impact on the Earth's climate as it serves as a global carbon reservoir (Bradshaw and Warkentin, 2015). In addition, it influences the atmosphere via surface albedo, evapotranspiration and formation of cloud condensation nuclei and SOA from gaseous biogenic precursors (Kulmala et al., 2004; Bonan, 2008; Sihto et al., 2011). The IBAIRN (Influence of Biosphere–Atmosphere Interactions on the Reactive Nitrogen budget) campaign aimed on deepening our understanding of sources and sinks of several biogenic VOCs and their impact on reactive nitrogen chemistry. In contrast to atmospheric conditions experienced during NOTOMO, the IBAIRN measurement site (see Chapters 2 and 3) was only occasionally impacted by anthropogenic emissions (with the nearest city Tampere ≈ 50 km to the south-west). Measurements were performed at the "Station for Measuring Forest Ecosystem-Atmosphere Relations II" (SMEAR II) in Hyytiälä (61.846 °N, 24.295 °E, 180 m above sea level) in southern Finland (Hari and Kulmala, 2005), which is located within the boreal forest (dominated by Scots pine and Norway spruce), in an area characterised by large biogenic emissions and low NO_x concentrations (Williams et al., 2011; Crow-

ley et al., 2018; Liebmann et al., 2018). In this work, measurements of SO_2, HCl, PAN and organic acids are reported with a focus on pyruvic acid and its impact on radical chemistry during late summer (see Chapter 3).

1.6.3 AQABA campaign

The Middle East is a rapidly developing region that is already subject to severe air pollution and weather extremes and is likely to be heavily impacted by future climate change with increasing frequency and intensity of droughts, heatwaves and associated Aeolian dust and pollutant emissions (Lelieveld et al., 2009, 2012, 2016). The region is characterised by large emissions of NO_x and SO_2 (see Fig. 1.13), mainly from oil and gas industry (Khatib, 2014), shipping and urban conglomerations, as well as dust particles from the deserts, which interact with pollutants (Abdelkader et al., 2015). High levels of solar irradiation, VOCs and NO_x combine to result in an active photochemistry, especially during summer, and severe photochemical air pollution with O_3 levels regularly exceeding 100 ppbv (Lelieveld et al., 2009). The AQABA (Air Quality and climate change in the Arabian Basin) campaign (see Chapter 4) was designed to investigate the factors that cause the high levels of air pollution around the Arabian Peninsula and especially in the Arabian (Persian) Gulf region. With a ship track covering the Suez Canal, the Red Sea, the Gulf of Aden, the Arabian Sea, the Gulf of Oman and the Arabian Gulf, the intension of this study was to close gaps in knowledge in an area where observational data is lacking. The campaign took place in summer when temperatures and photochemical activity are highest and provided CI-QMS measurements of SO_2, HCl and $ClNO_2$ and secondary pollutants like PAN, which is, however, expected to play a minor role during summer due to its thermal instability. For this work the focus was set on $ClNO_2$ formation, resulting from the interaction of pollutant emissions from ships and petrochemical activity with chloride-containing aerosol, and the impact of reactive chlorine chemistry in the marine boundary layer around the Arabian Peninsula.

Besides the Arabian Gulf (see Fig. 1.13), the eastern Mediterranean is another region, where elevated concentrations of primary and secondary pollutants are frequently reported, especially during summer (Dayan et al., 2017). To study this in more detail, the ship track during AQABA also included the eastern Mediterranean Sea, which is regularly impacted by long-range transport of trace gases from continental Europe and high tropospheric O_3 concentrations (Lelieveld et al., 2002). In particular megacities and Mediterranean harbours are regional hotspots of air pollution, with elevated NO_x concentrations and SO_2 levels regularly exceeding several ppbv (Kanakidou et al., 2011; Schembari et al., 2012). To expand the data coverage in the Mediterranean and Middle East region, SO_2, HCl, PAN and $ClNO_2$ were measured along the ship track between southern France and Kuwait.

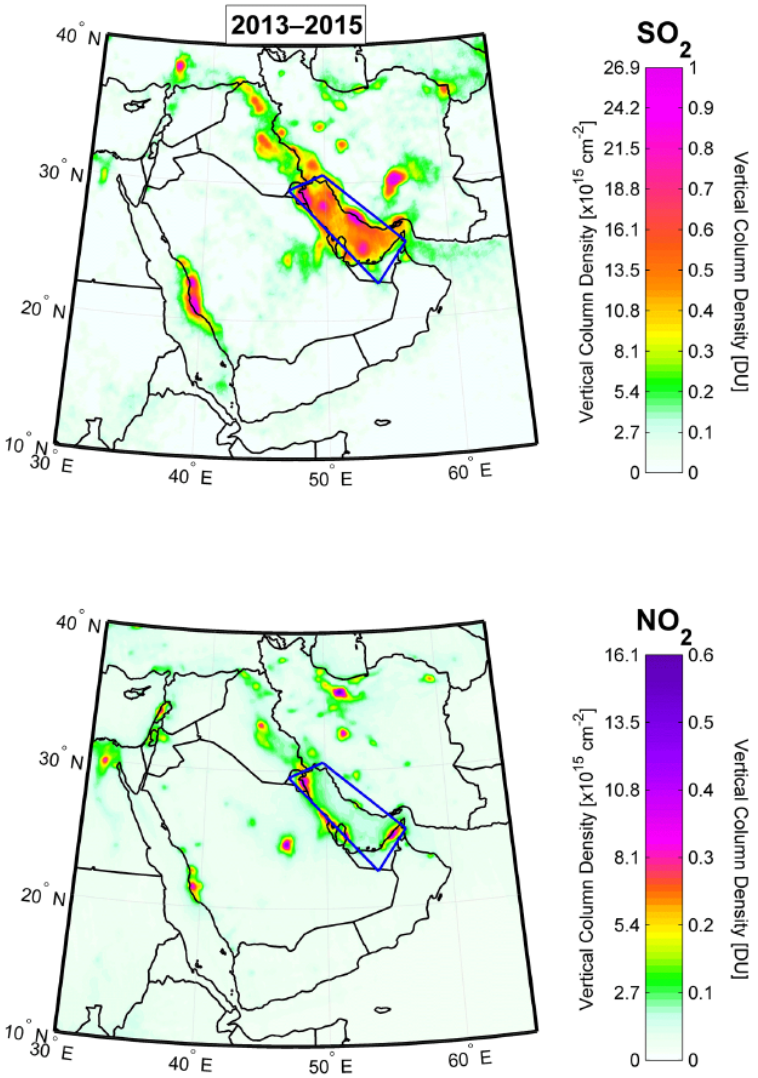

Figure 1.13: 3-year average OMI SO_2 (top) and tropospheric NO_2 (bottom) regional maps over the Middle East for 2013–2015, taken from Krotkov et al. (2016). The blue box outlines the Arabian (Persian) Gulf region with high SO_2 and NO_2 levels due to oil and gas operations.

Chapter 2

Characterisation of a chemical ionisation quadrupole mass spectrometer with an electrical discharge ion source and application in field studies

Philipp G. Eger[1], Frank Helleis[1], Gerhard Schuster[1], Gavin J. Phillips[1,2], Jos Lelieveld[1], and John N. Crowley[1]

[1]Atmospheric Chemistry Department, Max-Planck-Institut für Chemie, 55128 Mainz, Germany
[2]Department of Natural Sciences, University of Chester, Chester CH2 4NU, UK

This chapter is based on the manuscript "Chemical ionization quadrupole mass spectrometer with an electrical discharge ion source for atmospheric trace gas measurement" published in Atmospheric Measurement Techniques (AMT) as Eger et al. (2019a). It summarises the instrumental development in the laboratory with a focus on advantages and disadvantages of an electrical discharge ion source for chemical ionisation mass spectrometry. The applicability for trace gas measurement is examined in three field studies under different atmospheric conditions.

Summary

We present a chemical ionisation quadrupole mass spectrometer (CI-QMS) with a radio-frequency (RF) discharge ion source through N_2 / CH_3I as a source of primary ions. In addition to the expected detection of PAN, peracetic acid (PAA) and $ClNO_2$ through well-established ion-molecule reactions with I^- and its water cluster, the instrument is also sensitive to SO_2, HCl and acetic acid ($CH_3C(O)OH$) through additional ion chemistry unique to our ion source. We present ionisation schemes for detection of SO_2, HCl and acetic acid along with illustrative datasets from three different field campaigns underlining the potential of the CI-QMS with an RF discharge ion source as an alternative to ^{210}Po. The additional sensitivity to SO_2 and HCl makes the CI-QMS suitable for investigating the role of sulphur and chlorine chemistry in the polluted marine and coastal boundary layer.

2.1 Introduction

Chemical ionisation mass spectrometry using iodide anions (commonly referred to as I-CIMS) is a widely used technique to measure various atmospheric trace gases with high temporal resolution and low detection limit. The potential of I-CIMS for atmospheric trace gas measurement was established in laboratory stud-

ies (Huey et al., 1995) on chlorine nitrate ($ClONO_2$), which plays a central role in polar stratospheric O_3 depletion (Molina et al., 1987), and dinitrogen pentoxide (N_2O_5), which, through its heterogeneous hydrolysis on cloud droplets and aerosols, acts as a sink of gas-phase NO_x ($NO + NO_2$) (Lelieveld and Crutzen, 1990; Dentener and Crutzen, 1993). The first applications of I-CIMS for monitoring atmospheric composition were for measurement of N_2O_5, peroxyacyl nitric anhydride (PAN, $CH_3C(O)O_2NO_2$) and other peroxycarboxylic nitric anhydrides (Huey, 2007). Since then it has been recognised that several classes of organic and inorganic trace gases can be detected sensitively by I-CIMS including organic and inorganic acids, organic nitrates, halogen-nitrates and di-halogens (Phillips et al., 2013; Lee et al., 2014; Neuman et al., 2016; Priestley et al., 2018). Our instrument has previously been deployed with a radioactive ion source (^{210}Po) to investigate the atmospheric chemistry of nitryl chloride ($ClNO_2$), PAN and peracetic acid (PAA, $CH_3C(O)OOH$) (Phillips et al., 2012, 2013, 2016; Crowley et al., 2018).

PAN (and other peroxycarboxylic nitric anhydrides) are formed in the atmosphere via the reaction of NO_2 with peroxyacyl radicals ($RC(O)O_2$) generated during the photo-oxidation of volatile organic compounds (VOCs). Slusher et al. (2004) reported the first detection of PAN, PPN (peroxypropionic nitric anhydride), MPAN (peroxymethacrylic nitric anhydride) and PiBN (peroxyisobutyric nitric anhydride) using thermal decomposition chemical ionisation mass spectrometry (TD-CIMS) with iodide ions. The most abundant, PAN, is of great importance owing to its role in transportation of NO_2 from source regions to remote areas (Moxim et al., 1996). The detection of PAN and its analogues via I-CIMS requires thermal dissociation (generally at temperatures close to 100 °C) to the peroxy radical, which then reacts with I^- primary ions to form the carboxylate anion, which is then detected. Compared to gas chromatographic methods for detection of peroxycarboxylic nitric anhydrides, the I-CIMS technique allows faster measurements with comparable sensitivity and selectivity (Slusher et al., 2004; Roiger et al., 2011) enabling eddy covariance flux measurements (Turnipseed et al., 2006; Wolfe et al., 2009). Although the bond dissociation energy of the peroxycarboxylic nitric anhydrides is similar, Zheng et al. (2011) report lower sensitivity for APAN (peroxyacrylic nitric anhydride), PiBN, PnBN (peroxy-n-butyric nitric anhydride) and CPAN (peroxycrotonyl nitric anhydride) and Mielke and Osthoff (2012) report lower sensitivity for MPAN compared to PPN and PAN. Peroxycarboxylic nitric anhydrides have been measured using I-CIMS in various locations including boreal forests (Phillips et al., 2013), pine forests (Turnipseed et al., 2006; Wolfe et al., 2009), urban areas (Slusher et al., 2004; LaFranchi et al., 2009; Wang et al., 2017b) and the Arctic (Roiger et al., 2011).

Detection of PAA by I-CIMS was reported by Phillips et al. (2013) who performed the first combined measurement of PAN and PAA in a boreal forest in Finland. PAA acts as a significant sink for $CH_3C(O)O_2$ and HO_2 under low-NO_x conditions and can compete with PAN formation, especially at high temperatures (Crowley et al., 2018). As for PAN, PAA was detected as the acetate anion at a mass-to-charge ratio (m/z) of 59. Unlike other TD-CIMS instruments that de-

scribe an absence of a residual signal when NO is added to the inlet (e.g. Warneke et al. (2016)), the I-CIMS deployed by Phillips et al. (2013) and the instrument presented in this study are very sensitive to PAA at m/z 59. Furgeson et al. (2011) also describe an interference at m/z 59 that is not titrated by NO and suggest detection of PAA, which is produced in their photochemical source used for PAN generation. In addition, Veres et al. (2015) report a very similar mechanism to PAA detection for the detection of pernitric acid (PNA). Differences in the sensitivities of various I-CIMS instruments to PAA at m/z 59 are likely to be associated with different de-clustering potentials. At m/z 59, the I-CIMS deployed by Phillips et al. (2013) was insensitive to acetic acid. A wide range of organic acids can be detected as an I^- cluster with the parent molecule (Le Breton et al., 2012; Lee et al., 2014) using time-of-flight mass spectrometers (I-CIMS-TOF), which have a high mass resolution and exploit the iodine mass defect for the identification of the elemental composition of the organic trace gases detected.

$ClNO_2$ is formed in the heterogeneous reaction of N_2O_5 on chloride-containing particles and surfaces during the night (Behnke et al., 1997). The daytime photolysis of $ClNO_2$ results in the release of chlorine atoms, which enhance oxidation rates of organic trace gases, especially during early morning hours (Phillips et al., 2012; Riedel et al., 2012a). Nitryl chloride has been observed by I-CIMS as $ICl NO_2^-$ and ICl^- in the polluted marine boundary layer (Osthoff et al., 2008; Riedel et al., 2012a), close to the coast, for example in Hong-Kong (Wang et al., 2016) and London (Bannan et al., 2015) but also inland in continental North America (Thornton et al., 2010; Mielke et al., 2011; Faxon et al., 2015), rural continental Europe (Phillips et al., 2012) and northern China (Tham et al., 2016).

Most I-CIMS systems in operation for atmospheric measurement use a radioactive ion source (usually ^{210}polonium, an α-emitter) to generate the primary iodide ions from methyl iodide (CH_3I). Although this type of ion source is well-established and known for its high stability and low chemical background, important and sometimes unsurmountable obstacles to its use are the safety regulations for the shipment, storage and operation of radioactive devices containing polonium. Potential alternatives are corona discharge and X-ray ion sources, as commonly used in atmospheric pressure chemical ionisation mass spectrometers (AP-CIMS) (Jost et al., 2003; Skalny et al., 2007; Kürten et al., 2011; Zheng et al., 2015), though the former have not been used for iodide ion generation.

We have developed a CI-QMS instrument (chemical ionisation quadrupole mass spectrometer) with an electrical discharge ion source that generates iodide ions without the use of a radioactive ioniser. Although this instrument was originally intended for measurement of PAN, PAA and $ClNO_2$, we discovered that a wider variety of gas-phase species, including SO_2, HCl and acetic acid could be detected. In the following we show that the instrument is suitable for measurement (at the tens of pptv level) of trace gases connected with sulphur and chlorine chemistry, for example in the anthropogenically influenced marine boundary layer. Its deployment as a PAN detector is limited to environments where PAN mixing ratios regularly exceed 100 pptv or when high temporal resolution is not necessary.

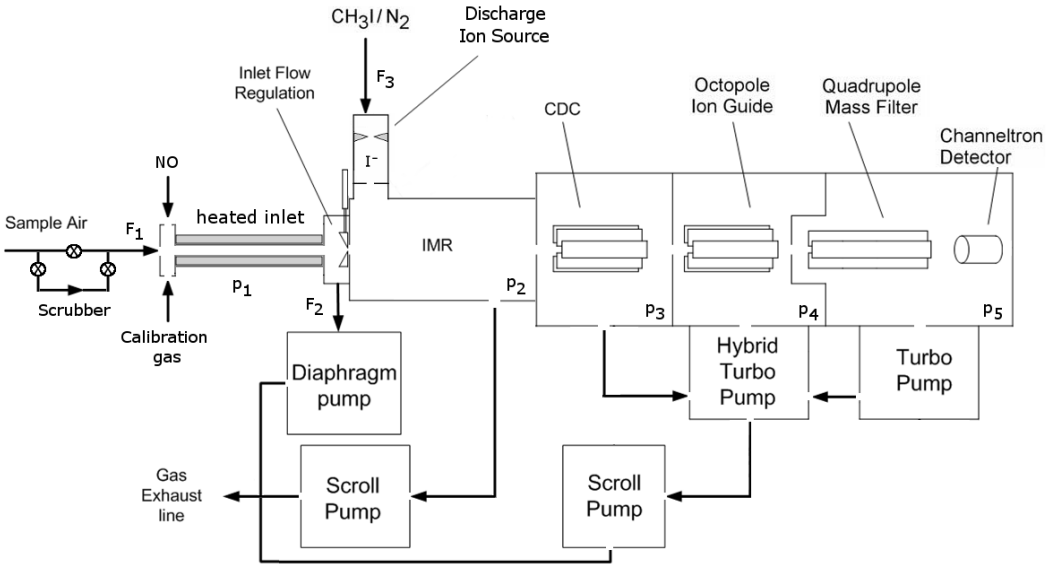

Figure 2.1: Schematic diagram of the CI-QMS. The air is sampled through the TDR (heated inlet) and enters the IMR after optional bypassing through the scrubber and mixing with calibration gas or nitrogen oxide (NO) for PAN background measurement. Ions are guided to the detector via the CDC, OCT and QMF. Typical flows (F) and pressures (p) are $F_1 = 2.2\,\mathrm{slm}$, $F_2 = 1.0\,\mathrm{slm}$, $F_3 = 0.8\,\mathrm{slm}$, $p_1 =$ ambient pressure, $p_2 = 24\,\mathrm{mbar}$, $p_3 = 0.6\,\mathrm{mbar}$, $p_4 = 6 \times 10^{-3}\,\mathrm{mbar}$, and $p_5 = 9 \times 10^{-5}\,\mathrm{mbar}$.

2.2 Instrumentation

Our chemical ionisation quadrupole mass spectrometer (CI-QMS) is based on the thermal dissociation technique described by Slusher et al. (2004) and Zheng et al. (2011) and was originally constructed in collaboration with Georgia Tech as a prototype THS Instruments product. A schematic diagram of the instrument in its present form is given in Fig. 2.1. The major modification, forced by issues of the restricted use of polonium on some platforms, is replacement of the ^{210}Po-ioniser with an electrical discharge ion source (see Fig. 2.2). The instrument as sketched in Fig. 2.1 consists of a thermal dissociation region (TDR), discharge ion source (DIS), ion molecule reactor (IMR), collisional dissociation chamber (CDC), octupole ion guide (OCT), quadrupole mass filter (QMF) and detector (DET). The four different vacuum chambers are separated by critical orifices and pumped by a combination of scroll pumps and turbo-molecular pumps. The CI-QMS is built into an aircraft rack (HALO, Gulfstream G 550) to facilitate airborne operation. A description of the various parts of the instrument as identified in Fig. 2.1 is given in the following.

2.2.1 Thermal dissociation region (TDR)

During standard operation a flow (F_1) of 2.2 L (standard temperature and pressure, STP) min^{-1} (slm) is sampled through the instrument inlet (see Fig. 2.1).

Ambient air entering the TDR first passes through a 2 μm pore size membrane filter (Pall Teflo) to efficiently remove particles. The thermal decomposition of PAN takes place in a 20 cm length of perfluoroalkoxy (PFA) tubing (9.3 mm internal diameter, ID) enclosed in a snugly fitting stainless steel shell heated to 200 °C. A gas temperature of 160–170 °C was measured inside the heated section of tubing. The last 4 cm long section of PFA in front of the orifice to the IMR is not actively heated but the gas temperature still remains at $\approx$ 130 °C, suppressing PAN recombination. Due to space restrictions inside the aircraft rack, the oven is curved over a 90° bend; however no significant reduction in sensitivity due to a loss of $CH_3C(O)O_2$ on the PFA walls could be observed when compared to a straight TD inlet. A bypass flow of 1 slm (F_2) decreases the inlet residence time and therefore optimises the peroxyacyl radical transmission. However, as PAN is calibrated in situ with a photochemical source (see Sect. 2.2.7), the fractional transmission of $CH_3C(O)O_2$ does not need to be known. A total of 1.2 slm (F_1 minus F_2) of the inlet flow enters the IMR via a constant-pressure orifice (see Sect. 2.2.3) and mixes with the 0.8 slm flow (F_3) of CH_3I/N_2 passing through the ion source. For ground-level deployment, the TDR is held at ambient pressure resulting in a residence time of $\approx$ 200 ms at 1 bar. For application in an aircraft, the arrangement of TDR and constant-pressure orifice can be switched so that a constant pressure of $p_1 = 100$ hPa is established in the TDR, resulting in a 40 ms residence time. With this mode of operation, measurements can be made at altitudes up to $\approx$ 15 km depending on aircraft inlet configuration.

2.2.2 Discharge ion source (DIS)

The radio-frequency (RF) discharge ion source represents the major difference to I-CIMS instruments commonly described in the literature. It consists of two tungsten needles, their tips placed at a distance of approximately 6 mm (adjustable) from each other (see Fig. 2.2); changing this distance by a few millimetres did not have a large effect on the overall ion count rate. The vacuum fittings through which the needles enter the discharge volume can optionally be evacuated to eliminate an air leak into the ion source. A 2.5 kV voltage (20 kHz) applied across the tungsten needles leads to the formation of a stable glow discharge (3 mA). An RF discharge was chosen for its advantages for operation in negative ion mode and because it is easier to handle with regard to electric field geometry and polarity. The discharge between the tungsten needles can be observed by eye or spectroscopically through a quartz viewing port; a photograph of the glow and the dispersed N_2 emission spectrum due to the $C^3\Pi_u \rightarrow B^3\Pi_g$ transition (Lofthus and Krupenie, 1977; Bayram and Freamat, 2012) is shown in Fig. B.1 of the supplementary information. The line intensities increase with the voltage applied ($\approx$ factor of 2.5 from 1500 to 3000 V), but the relative intensities do not change significantly. From the relative line intensities we calculate that the N_2 molecules have a vibrational temperature of $\approx$ 3000 K (Svarnas, 2013).

In normal operation, a flow of 0.8 slm (F_3) of 2 ppmv methyl iodide (CH_3I) in nitrogen passes through the ionisation region. In order to prevent the backflow

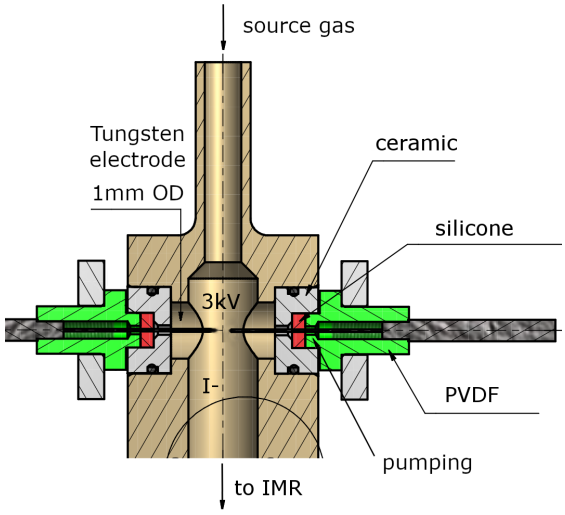

Figure 2.2: Schematic drawing of the RF discharge ion source. The high voltage and the distance between the tips of the tungsten electrodes are variable, as described in the text. A transformer, which is supplied with up to 200 V AC from the internal V25 unit, applies temporarily fluctuating potentials to both electrodes. The body of the ion source (coloured in light brown) is made of stainless steel. PVDF is polyvinylidene fluoride. The region around the electrodes can optionally be pumped as described in the text.

of air from the IMR into the discharge region, the flow through the ionisation region is kept high (0.8 slm) and passes through a 0.9 mm aperture before entering the IMR. Similar to the α radiation of a ^{210}Po-ioniser, I^- ions are formed via dissociative electron attachment to CH_3I. In contrast to typical corona discharge ion sources with a current of a few μA (see, e.g. Kürten et al. (2011)) our glow discharge operates at ≈ 3 mA, which leads to highly energetic electrons and ions in the ionisation region and a more complex mass spectrum (see Sect. 2.3).

2.2.3 Ion molecule reactor (IMR)

Under standard operating conditions for ground-level measurements, a flow of 1.2 slm of the air to be analysed (F_1 minus F_2) is mixed with the 0.8 slm flow of CH_3I / N_2 (F_3) entering the IMR from the ion source. The IMR is evacuated by a dry scroll vacuum pump (ULVAC DISL-101, 100 L min^{-1}) and is held at a constant pressure of 24 mbar (p_2). For operation above the boundary layer, an extra 50 cm^3 (STP) min^{-1} (sccm) flow of humidified air is added just in front of the IMR to ensure that sufficient water vapour is present to form $I^-(H_2O)$ clusters. The role of $I^-(H_2O)$ and other primary-ion clusters with water is discussed in Sect. 2.5.

The constant pressure within the IMR is achieved by use of a variable orifice consisting of two metal plates, one with a hole shaped like the 2-D projection of a bike saddle and one with a circular hole, the relative position of which (i.e. the degree of overlap of the holes) is controlled by a stepper motor. The saddle form was chosen as it results in a roughly linear relationship between stepper motor

position and mass flow through the orifice, enabling rapid and precise adaptation to changes in ambient pressure even during steep ascents or dives of an aircraft.

The temperature in the IMR is above ambient owing to the inflow of heated gas through the TDR. The exact residence time for trace gases to react with primary ions in the IMR is not accurately known, as the mixing of the gas flows and temperature evolution in the IMR are not well characterised. Based on the mass flow rate into the IMR and its volume ($\approx 100\,\mathrm{cm}^3$) and disregarding ion drift due to the potential applied between the IMR and the CDC, we calculate an approximate reaction time of $\approx 70\,\mathrm{ms}$.

2.2.4 Collisional dissociation chamber (CDC) and octupole ion guide (OCT)

The CDC region consists of an octupole ion guide to accelerate and collimate the effusive ion beam entering from the IMR. It is separated from the IMR by a critical orifice (0.8 mm diameter) and held at a pressure of 0.6 mbar (p_3), by the Holweck stage of a turbo-molecular pump (Leybold Turbovac 90 i, $90\,\mathrm{L\,s^{-1}}$ with an Agilent IDP-3 scroll pump, $50\,\mathrm{L\,min^{-1}}$ as a backup pump). A potential difference of typically 20 V is applied in the CDC, which results in the de-clustering of weakly bound adducts (often with H_2O), a simplified mass spectrum and a higher sensitivity to the product ion of interest. The de-clustering voltage can be varied independently for each ion of interest, thus optimising sensitivity for individual trace gases. An example of the variable de-clustering potential during operation of the CI-QMS in the selected ion monitoring mode (e.g. to measure the $I^-(H_2O)$ cluster or differentiate between acetic and peracetic acid) is given below. An additional octupole ion guide in the subsequent vacuum chamber (6.0×10^{-3} mbar, p_4) further collimates the ion-beam and guides it to the detector region. This octupole ion guide is evacuated by the turbo-molecular stage of the Leybold Turbovac 90 i.

2.2.5 Quadrupole mass filter (QMF) and detector (DET)

A radio-frequency generator (Balzers QMH 410-3, 1.44 MHz) provides a combination of direct and alternating voltage to the quadrupole rods (10 mm) so that ions with a specific m/z are forced on stable trajectories and reach the detector. These ions are then detected with a channel electron multiplier (ITT Ceramax 7550 M). The detector chamber is pumped to a pressure of 9.0×10^{-5} mbar (p_5) by a turbo-molecular pump (Varian V70LP, $70\,\mathrm{L\,s^{-1}}$).

2.2.6 Scrubber

To determine the instrumental and chemical background the sampled air is automatically and periodically bypassed into a scrubber (see Fig. 2.1) consisting of a 20 cm long stainless steel oven filled with steel wool and heated to 120 °C. The trace gases discussed in this work are all destroyed efficiently by the hot metal surfaces whilst leaving the relative humidity unaffected.

2.2.7 Photochemical PAN source

For in situ PAN calibration we use a photochemical source based on the method of Warneck and Zerbach (1992) but with a phosphor-coated Pen-Ray mercury lamp (Jelight, broad emission centred at 285 nm) as described by Flocke et al. (2005). Typically, 50 sccm of acetone (200 ppmv in synthetic air, Air Liquide) and 5 sccm of NO (1 ppmv in N_2, Air Liquide) are mixed in a quartz glass reactor (150 mL volume, actively cooled by a fan) at 1050 mbar forming PAN (Reactions R 2.1–2.4).

$$CH_3C(O)CH_3 + h\nu\,(O_2) \longrightarrow CH_3O_2 + CH_3C(O)O_2 \quad \text{(R 2.1)}$$

$$CH_3O_2 + NO\,(O_2) \longrightarrow HCHO + HO_2 + NO_2 \quad \text{(R 2.2)}$$

$$CH_3C(O)O_2 + NO\,(O_2) \longrightarrow CH_3O_2 + CO_2 + NO_2 \quad \text{(R 2.3)}$$

$$CH_3C(O)O_2 + NO_2 + M \longrightarrow CH_3C(O)O_2NO_2 + M \quad \text{(R 2.4)}$$

$$CH_3C(O)O_2 + HO_2 \longrightarrow CH_3C(O)OOH + O_2 \quad \text{(R 2.5)}$$

$$\longrightarrow CH_3C(O)OH + O_3 \quad \text{(R 2.6)}$$

The calibration source converts NO almost stoichiometrically to PAN (conversion $> 95\,\%$) and results in a mixing ratio of about 4 ppbv of PAN in the TDR. The PAN source is continuously operated and its 55 sccm output drains into the exhaust line, periodically switching into the main flow during scrubbing. The conversion efficiency of NO to PAN was checked using thermal dissociation cavity ring-down spectroscopy as described previously (Phillips et al., 2013). The PAN source also generates both PAA and acetic acid (R 2.5–2.6), which, as described below, are also detected by the CI-QMS.

2.2.8 Electronics and data acquisition

The vast majority of the instrument's electronics are controlled by a "V25" system developed in-house. The V25 handles the interplay between single components such as flow controllers, pressure gauges, magnetic valves, thermocouples, heaters, MS potentials and RF generators. All command sequences and measurement cycles (background, calibration, etc.) can be customised and fully automated for operation in aircraft or in remote locations. During measurement campaigns we usually focus on specific trace gases and operate in selected ion monitoring mode, typically monitoring between 3 and 10 different values of m/z to increase the temporal resolution. Different m/z values can be adjusted in a few milliseconds by variation of the direct voltage and the amplitude of the alternating voltage applied to the quadrupole rods. The integration time of the detector for a single channel is usually set to 10 ms for primary ions and 100 ms for product ions, which represents a compromise between high signal-to-noise ratio (S/N) and high temporal resolution. For each m/z monitored, the integrated signal is calculated by summing up eight individual channels, resulting in a total integration time (for one product ion) of about 800 ms. Higher-frequency measurements are possible at the cost of a reduction in the signal-to-noise ratio. The counts for each channel and the integrated counts as well as the most important system parameters are saved on

Table 2.1: Ion source configurations (i-v) according to Fig. 2.3 and primary ions observed.

	Ion source	Source gas	Inlet gas	Primary ions (most abundant first)
i	^{210}Po	CH_3I/N_2	Air	$I^-(H_2O)_n$
ii	^{210}Po	CH_3I/Air	Air	$I^-(H_2O)_n$, $O_2^-(H_2O)_n$, CO_3^-
iii	RF discharge	CH_3I/N_2	Air	$I^-(H_2O)_n$, $I(CN)_2^-$, CNO^-, NO_3^-, IO_3^-
iv	RF discharge	CH_3I/N_2	N_2	$I^-(H_2O)_n$, $I(CN)_2^-$, $IH(CN)^-$
v	RF discharge	I_2/N_2	Air	$I^-(H_2O)_n$, IO_3^-, IO_4^-, IO_2^-, NO_3^-

Notes: "Air" refers to synthetic hydrocarbon-free air. Number of water clusters $n = \{0,1\}$.

an internal PC card and can additionally be collected and monitored online using customised LabView software. To identify additional traces gases of interest, the whole mass spectrum (m/z 1–256) is occasionally scanned and recorded, which takes about 1–2 minutes.

2.2.9 Size, weight and power consumption

The CI-QMS is situated in a compact aircraft rack (65 cm × 55 cm × 140 cm, HALO, Gulfstream G 550) with a total weight of 135 kg and a power consumption of 0.9 kW with the vacuum pumps as the main power consumers. The two vacuum scroll pumps require 230 V AC input whereas all the other components are operated with 24 V DC from an AC/DC converter that either can be supplied with 230 V AC or 115 V AC (three phases, 400 Hz, for aircraft operation).

2.3 Primary-ion spectra

The deployment of an RF discharge source for iodide ion production leads to a more complex primary-ion mass spectrum when compared to use of ^{210}Po; consequently, a wider variety of trace gases can be detected. Here we compare both ion sources with respect to sensitivity and achievable detection limits of a number of trace gases. Figure 2.3 illustrates the primary-ion spectrum with a discharge ion source under various conditions and compares it to that obtained using ^{210}Po. The absolute ion count rates for both ion sources are comparable, i.e. up to $(6 \pm 2) \times 10^6$ Hz for I^-. Details of the configurations (i–v) and primary ions observed are summarised in Table 2.1.

The primary-ion mass spectrum obtained by passing $CH_3I\,/\,N_2$ through the ^{210}Po-ioniser (370 MBq, configuration i) at typical relative humidity (50 % at 25 °C) and low de-clustering voltage (0–2 V) in the CDC is dominated by I^- and $I^-(H_2O)$ at m/z 127 and 145, with no other significant ion peaks present at > 0.1 % relative signal strength to I^-. The background signal for all trace gases of interest, i.e. PAN and PAA at m/z 59 and $ClNO_2$ at m/z 208 and 210 is consequently negligible and the detection limits are correspondingly low (a few pptv in 1 s integration time).

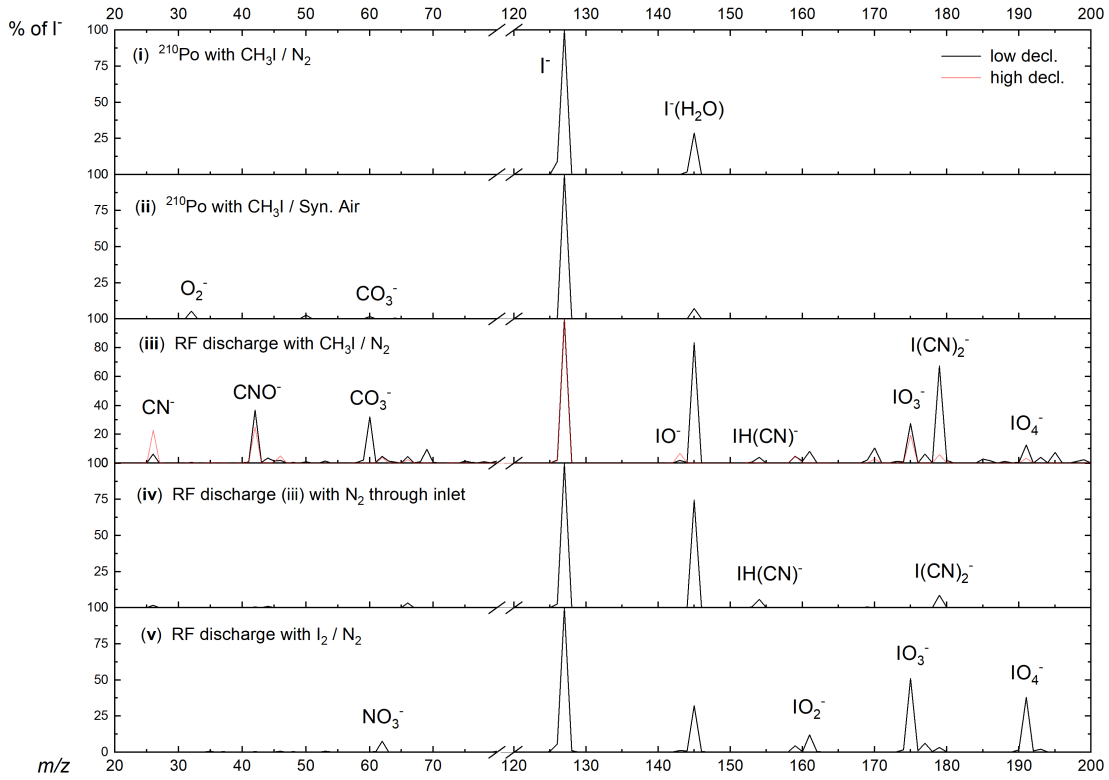

Figure 2.3: Primary-ion spectra (using I_2/N_2 (v) or CH_3I/N_2 (iii–iv) and using either pure synthetic air (iii) or N_2 (iv) for the inlet gas) obtained using the RF discharge (iii–v) or ^{210}Po (i–ii) as an ion source. The integrated counts (eight channels) for each m/z normalized to the highest peak present are shown, which is I^-. For this reason, true peak shapes are not visible. A description of the different configurations can be found in Table 2.1.

With RF discharge and CH_3I/N_2 as an ion source gas (configuration iii, applied in all the field measurements we discuss below), the primary-ion mass spectrum is more complex with additional ions such as CNO^- (m/z 42, 37 % of I^- at low de-clustering), CO_3^- (m/z 60, 32 % of I^-), NO_3^- (m/z 62, 5 % of I^-), IO_3^- (m/z 175, 28 % of I^-) and $I(CN)_2^-$ (m/z 179, 67 % of I^-). With the de-clustering voltage set to 20 V (the best S/N ratio for most molecules of interest), the background count rate compared with ^{210}Po is elevated by at least 1 order of magnitude for m/z 59, which is used to monitor PAN and PAA. The high chemical background is assumed to originate from CH_3I breakdown in the discharge ion source and formation of O_2^- in the ion source and IMR. When pumping the region around the ion source needles the formation of NO_3^- (m/z 62) can be reduced by a factor of 2 but the other ions still show similar ion count rates. This observation suggests that a small amount of O_2 entering the ion source can form additional NO_3^-. According to manufacturer's specifications the nitrogen supply (N_2 6.0, Westfalen AG) can contain up to 0.5 ppmv O_2 and H_2O, which can also result in the formation of NO_3^- in the ion source.

To examine the influence of oxygen in the IMR on the primary ions formed we switched the main gas flow (i.e. that which does not pass through the RF discharge) from ambient air to pure nitrogen (configuration iv). In this case, apart from I^-, only CN^- (m/z 26, 2 % of I^- at low de-clustering), $IH(CN)^-$ (m/z 154, 6 % of I^-) and $I(CN)_2^-$ (m/z 179, 9 % of I^-) remained. While these conditions are unrealistic for atmospheric measurements they clearly indicate that the presence of additional primary ions containing O atoms and the elevated chemical background on m/z of interest are highly dependent on the amount of O_2 present in the IMR. With pure N_2 in the inlet (configuration iv), background signals at m/z 59, 188, 207 and 208 could be lowered by about an order of magnitude. The use of N_2 results in a drastically reduced sensitivity to SO_2, as the primary ion used to detect it (IO_3^-, see Sect. 2.4.2) is no longer abundant. This is illustrated in Fig. B.2 of the supplementary information where we plot the dependence of the IO_3^- signal (m/z 175) on the fractional pressure of O_2 in the inlet and the signal at m/z 207 (ISO_3^-) used to monitor SO_2 (see Sect. 2.4.2). Clearly, detection of SO_2 is not possible without the presence of O_2 and is not available when using ^{210}Po as an ion source.

In an attempt to improve the detection limit for PAN by lowering the background signal on m/z 59, I_2, produced from a flow of nitrogen over iodine crystals (configuration v), was used instead of CH_3I. This resulted in a significant reduction of background signals, especially on m/z 59 and the disappearance of all the ion peaks containing C and N atoms with just IO_3^- (m/z 175, 51 % of I^-), IO_4^- (m/z 191, 38 % of I^-), IO_2^- (m/z 159, 12 % of I^-) and NO_3^- (m/z 62, 8 % of I^-) remaining. However, use of I_2 was accompanied by a drastic lowering of the sensitivity to PAN, despite comparable I^- ion counts at m/z 127. The decrease in sensitivity can be traced back to equilibrium between I^-, I_2 and I_3^-.

$$I^- + I_2 + M \rightleftarrows {I_3}^- + M \qquad \text{(R 2.7)}$$

An equilibrium constant (K_{eq}, in bar^{-1}) of $K_{eq} = [I_3^-]/([I^-][I_2]) = \exp(11300/T)$ for reaction (R 2.7) (based on the Gibbs free energy of $-94.14\,kJ\,mol^{-1}$; NIST (2016)) and an estimate (based on its saturation vapour pressure) of the concentration of I_2 of $\approx 2 \times 10^{-7}$ bar) results in the complete dominance (by several orders of magnitude) of $[I_3^-]$ compared to $[I^-]$ in the IMR. While the presence of large concentrations of I_3^- may explain the large signal at m/z 127 following de-clustering, we conclude that the reaction between I_3^- and $CH_3C(O)O_2$ is very inefficient or does not lead to $CH_3CO_2^-$ formation. I_2 does not represent a feasible alternative to CH_3I for PAN measurement and HCl detection is not possible. However, we can still detect SO_2 via IO_x^- primary ions and also acetic acid presumably due to (IO_x^-) clusters with $CH_3C(O)OH$.

In another experiment performed with the ^{210}Po source, synthetic air instead of nitrogen was flowing over the polonium ioniser (configuration ii), simulating a huge leak of oxygen into the source. Besides I^- and $I^-(H_2O)$, O_2^- (m/z 32, 5 % of I^-), $O_2^-(H_2O)$ (m/z 50, 3 % of I^-) and CO_3^- (m/z 60, 2 % of I^-) were present but ions like IO_x^- and $I(CN)_x^-$ that are probably responsible for the detection of SO_2 and HCl (see below) were not observed as they are unique to the RF discharge ion

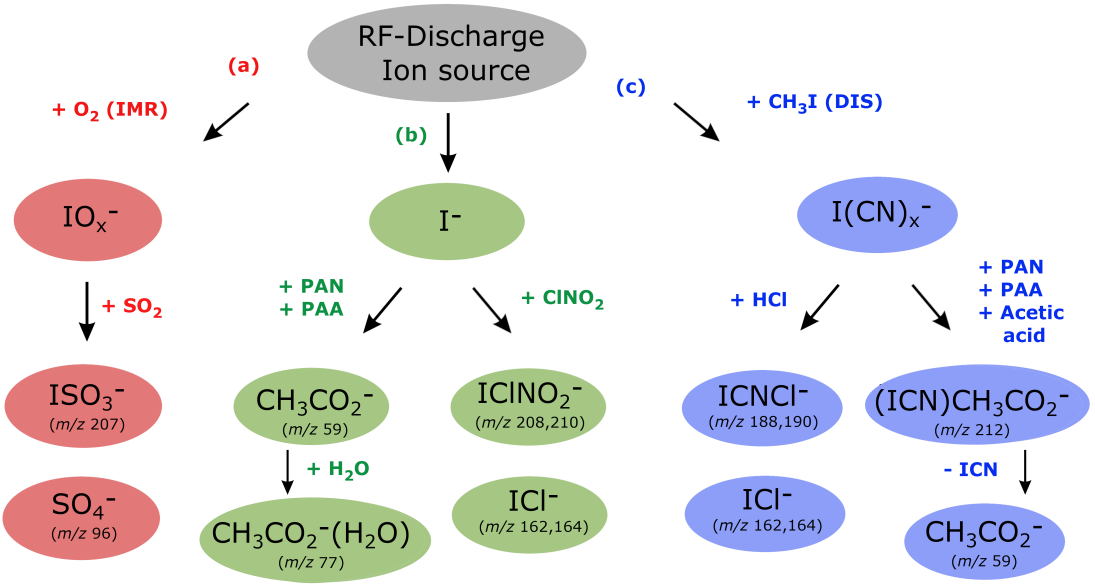

Figure 2.4: Ion detection schemes for SO_2, PAN, PAA, acetic acid, $ClNO_2$ and HCl using the RF discharge ion source.

source. In combination with the experiment where the housing around the tungsten needles was evacuated, we conclude that a leak of O_2 into the discharge region might increase O_2^- and NO_3^- but is not responsible for the complex primary-ion spectrum observed with our discharge ion source. No change in the ion spectrum was observed when the linear steel tubing between ion source and IMR was replaced by tubing with a 90° bend. This result precludes an important role for ion formation via highly energetic radiation from the ionisation region reaching the IMR interacting with O_2. The diffusion of oxygen from the IMR into the ion source is also very unlikely due to a high-volume flow between the ion source and IMR and the use of a small aperture. We conclude that the role of O_2 in the formation of primary ions containing I, O, C and N atoms in the IMR is most likely related to its role as a trapper and carrier of electrons, possibly as excited O_2^- anions.

2.4 Detection schemes and calibration methods

Figure 2.4 shows which trace gases we can detect with our instrument using the RF discharge ion source. The middle branch (b) represents ionisation via I^- and its water cluster ion and is the same as ^{210}Po-based ion generation schemes frequently used for detection of PAN (Slusher et al., 2004), PAA (Phillips et al., 2013) and $ClNO_2$ (McNeill et al., 2006). The outer branches (a and c) are unique to our CI-QMS using the discharge ion source and can be attributed to the presence of different primary ions. The presence of H, C and N atoms from CH_3I / N_2 breakdown in the discharge region leads to the existence of the right-hand branch (c) that disappears when CH_3I is replaced by I_2 (see Sect. 2.3, configuration v).

The usual presence of oxygen inside the IMR is responsible for the existence of the left-hand branch (a) and is not available with configuration (iv) in which nitrogen was used for the main gas flow instead of synthetic air. For the combined detection of PAN, $ClNO_2$, SO_2, HCl, peracetic and acetic acid, configuration (iii) was used in all of our field measurements. In the following we discuss in detail the ion-molecule reactions involved in the detection of these trace gases and also outline how the CI-QMS is calibrated and which sensitivities and detection limits can be achieved.

2.4.1 PAN, PAA and acetic acid

PAN, PAA and acetic acid are all detected as $CH_3CO_2^-$ at m/z 59. Depending on the relative humidity and the de-clustering potential in the CDC, clusters of $CH_3CO_2^-$ with H_2O are observed at m/z 77. Sensitivities and product yields for the detection of these three molecules are summarised in Table 2.2. The detection mechanism for PAN using I^- primary ions is the same as that reported when using ^{210}Po as an ion source (Slusher et al., 2004). PAN is thermally decomposed inside the TDR into a peroxy radical ($CH_3C(O)O_2$) and NO_2 via Reaction (R 2.8).

$$CH_3C(O)O_2NO_2 + M \longrightarrow CH_3C(O)O_2 + NO_2 + M \quad \text{(R 2.8)}$$

$$CH_3C(O)O_2 + I^-(H_2O)_n \longrightarrow CH_3C(O)O^-(H_2O)_n + IO \quad \text{(R 2.9)}$$

$$CH_3C(O)OOH + I^-(H_2O)_n \longrightarrow CH_3C(O)O^-(H_2O)_n + HOI \quad \text{(R 2.10)}$$

The rate coefficient for the thermal decomposition of PAN (at 453 K and 1 bar) is $\approx 2000\,s^{-1}$ (Atkinson et al., 2006; IUPAC, 2019), so that $> 99.99\,\%$ of PAN should be thermally dissociated within 200 ms. This could be confirmed by measurement of the signal due to a stable PAN source whilst varying the inlet temperature. The $CH_3C(O)O_2$ product reacts with I^- in the IMR to form $CH_3CO_2^-$ (m/z 59) via Reaction (R 2.9) involving clusters with water vapour. The detection of PAA with I^- primary ions is believed to be direct, via Reaction (R 2.10) (Phillips et al., 2013). When using the RF discharge ion source there is also an additional pathway for PAN and PAA detection, involving $I(CN)_2^-$ primary ions, resulting in the formation of $I(CN)CH_3CO_2^-$ which is observed at m/z 212 when de-clustering is switched off. With de-clustering this ion fragments to m/z 59. However, the sensitivity is relatively low and the selectivity is not improved as acetic acid is also detected at this m/z (see Table 2.2).

The separation of PAN from PAA and acetic acid signals when sampling air masses which contain both trace gases can be achieved by cooling the TDR to prevent formation of $CH_3C(O)O_2$ and thus detection of PAN (Phillips et al., 2013) or by adding NO to the TDR in order to remove $CH_3C(O)O_2$ (Reaction R 2.11).

$$CH_3C(O)O_2 + NO \longrightarrow CH_3 + CO_2 + NO_2 \quad \text{(R 2.11)}$$

The latter method has the advantage of being more rapid as NO can be switched in and out of the TDR in a matter of seconds whereas cooling of the inlet may take minutes. Generally we add NO (100 ppmv in nitrogen, Air Liquide) to the TDR

Table 2.2: Product yield, sensitivity and limit of detection of the CI-QMS for PAN, PAA, acetic acid, $ClNO_2$, SO_2 and HCl.

Reactant	Product	m/z	$(\text{yield})_{\text{Dis}}$	S^a_{Dis}	$\text{LOD}^b_{\text{Dis}}$	S_{Pol}	LOD_{Pol}
PAN	$CH_3CO_2^-$	59	98	1.04	34[c]	17	3
	$I(CN)CH_3CO_2^-$	212	2				
PAA	$CH_3CO_2^-$	59	98	0.22[d]	194[d]	5.7	4
Acetic acid	$CH_3CO_2^-$	59	95	0.62	57		
	$CH_3C(O)OH^-$	60	3				
	$I(CN)CH_3CO_2^-$	212	2				
$ClNO_2$	$I^{35}ClNO_2^-$	208	30	0.60	12	3.5	3
	$I^{37}ClNO_2^-$	210	10				
	$I^{35}Cl^-$	162	45				
	$I^{37}Cl^-$	164	15				
SO_2	ISO_3^-	207	8	0.09	56		
	ISO_4^-	223	2				
	SO_3^-	80	10				
	HSO_3^-	81	17				
	SO_4^-	96	19				
	HSO_4^-	97	30				
	SO_5^-	112	9				
	HSO_5^-	113	5				
HCl	$I(CN)^{35}Cl^-$	188	18	0.14	135		
	$I(CN)^{37}Cl^-$	190	6				
	$I^{35}Cl^-$	162	6				
	$I^{37}Cl^-$	164	2				
	$^{35}Cl^-$	35	51				
	$^{37}Cl^-$	37	17				

Notes: Parameters are reported for RF discharge (Dis) and ^{210}Po (Pol) ion sources. [a]Sensitivity S (in Hz pptv^{-1}) at 50 % RH (25 °C), normalised to 10^6 Hz I^- and de-clustering set to 20 V. [b]Limit of detection (LOD, 2σ, 1 s integration time, in pptv). [c]The LOD is calculated from background signal at m/z 59 and does not include the worsening in detection limit incurred when acetic acid and PAA are present at the same m/z as described in the text. [d]Without de-clustering applied.

at a mixing ratio of 0.23 ppmv (3.7×10^{12} molecule cm^{-3}). Given the approximate residence time of ca. 200 ms in the TDR (calculated from the volume of the TDR and the volumetric flow rate) and the rate coefficient for Reaction (R 2.11) of 1.4×10^{-11} cm^3 molecule^{-1} s^{-1} at 453 K (Atkinson et al., 2006; IUPAC, 2019) we calculate that more than 99.99 % of the $CH_3C(O)O_2$ is removed by titration with NO. When NO is added, we therefore measure only PAA (or the sum of PAA and acetic acid, depending on de-clustering potential; see below). The signal due to PAN is then calculated by subtracting the interpolated signal during NO addition. The use of the RF discharge source also results in sensitivity to acetic acid at m/z 59, which is not observed using ^{210}Po as an ion source. Rather, detection of acetic acid has been reported at m/z 187 ($ICH_3C(O)OH^-$) (Lee et al., 2014). Our instrument is relatively insensitive for acetic acid at m/z 187 and, without de-clustering, we measure acetic acid mainly as $(CNO)CH_3C(O)OH^-$ (m/z 102) and $I(CN)CH_3CO_2^-$ (m/z 212).

When monitoring m/z 59 using the discharge ion source, the background signal during NO addition consists of both PAA and acetic acid. To differentiate between them we make use of the fact that the relative sensitivity to PAA and acetic acid at m/z 59 depends on the de-clustering potential applied in the CDC. We find that acetic acid is only detected at m/z 59 when a de-clustering voltage of about 20 V is applied, whereas PAA is detected at m/z 59 both with and without de-clustering, albeit with different sensitivity. The difference is related to the fact that for PAA the product ion is formed directly in Reaction (R 2.10), whereas acetic acid is believed to initially form a cluster with $I(CN)_2^-$ (R 2.12) and only dissociate to $CH_3CO_2^-$ when the 20 V de-clustering voltage (ΔU) is applied (R 2.13).

$$CH_3C(O)OH + I(CN)_2^- \longrightarrow HCN + I(CN)CH_3CO_2^- \quad (m/z\ 212) \quad \text{(R 2.12)}$$

$$I(CN)CH_3CO_2^- + \Delta U \longrightarrow ICN + CH_3CO_2^- \quad (m/z\ 59) \quad \text{(R 2.13)}$$

ICN^-, $IH(CN)^-$ and $I(CN)_2^-$ are all potential primary ions for detection of acetic acid, though $I(CN)_2^-$ is the most abundant. When NO is added, the mixing ratio of acetic acid can be calculated by subtracting the signal without de-clustering from the signal with de-clustering. Unfortunately, the chemical background without de-clustering at m/z 59 is a factor of 2.5 higher than with de-clustering and the sensitivity is reduced, which increases the LOD for detection of PAA significantly (see Table 2.2).

Results of combined PAA and acetic acid measurements from the CYPHEX field campaign and speciation via changing the CDC parameters can be found in (Derstroff et al., 2017). An exemplary time series showing the different measurement modes of the CI-QMS (scrubber, ambient, NO addition) and the differences in detection of PAA and acetic acid when applying a de-clustering voltage is provided in Fig. B.3 of the supplementary information.

An enhancement in sensitivity to acetic acid at m/z 59 when using the RF discharge ion source compared to ^{210}Po, is illustrated by the signals obtained from the photochemical source used to generate PAN, which also generates unquantified amounts of both PAA and acetic acid (Sect. 2.2.7, Reactions R 2.5 and R 2.6).

When using the RF discharge ion source and 20 V de-clustering voltage, the signal ratio of PAN / (PAA + acetic acid) at m/z 59 is ≈ 0.2. In contrast, using ^{210}Po as an ion source the ratio is ca. 0.9. As the relative sensitivity (m/z 59) to PAN and PAA is similar, this change in ratio reflects enhanced instrument sensitivity to acetic acid when using the discharge ion source with de-clustering. This represents a significant disadvantage of the RF discharge source for PAN detection compared to ^{210}Po. Not only is the instrumental background at m/z 59 higher, the presence of acetic acid in ambient air samples means that a larger and more variable chemical background signal has to be subtracted to calculate the PAN mixing ratio, which increases the limit of detection and overall uncertainty significantly.

Calibration of PAN, PAA and acetic acid

The in situ calibration of PAN is described in Sect. 2.2.7. The overall uncertainty of the calibration, based on the uncertainty in dilution, the mixing ratio of the NO calibration cylinder (1 ppmv) and the conversion efficiency from NO to PAN is $\approx 10\,\%$.

For PAA, two methods, both using a diffusion source containing a commercially available 39 % solution of PAA in acetic acid, have been used to calibrate the CI-QMS. In the first, we use simultaneous CI-QMS and wet-chemical peroxide-specific detection of PAA based on the horseradish peroxidase / catalase / p-hydroxyphenyl fluorescence measurement technique (Lazrus et al., 1986) in which organic peroxides (and peracids) are converted to H_2O_2 (AL2021, Aero-Laser GmbH). The wet-chemical method is calibrated via standard H_2O_2 solutions and the overall uncertainty (related to scrubbing efficiency of PAA) is 13 %. As the AL2021 is not always available during campaigns, we developed a second approach in which PAA undergoes transformation to I_3^-(aq), which can be quantified using aqueous-phase absorption spectroscopy (Awtrey and Connick, 1951; Friedrich, 2015). Based on uncertainty in the scavenging of PAA into an acidified, aqueous solution, uncertainty associated with the absorption cross section of I_3^- and the reproducibility of I_3^- signals when sampling from a constant source of PAA, we estimate the total uncertainty of the I_3^- method to be $\approx 30\,\%$.

For the calibration of acetic acid we use a permeation source (7.33 ng min^{-1} at 30 °C, Metronics) with an uncertainty of 8 %. Additionally, we sampled the output of a diffusion source of pure liquid acetic acid simultaneously using the CI-QMS (41.2 ppbv after dilution) and an infrared absorption spectrometer measuring CO_2 (LI-COR) following the stoichiometric, thermal oxidation of acetic acid to CO_2 (Veres et al., 2010). The uncertainty of this calibration method is $\approx 10\,\%$. Within combined uncertainty, both methods indicated the same sensitivity of the CI-QMS to acetic acid.

2.4.2 Sulphur dioxide

The "standard" use of ^{210}Po-ionisation does not allow for the sensitive detection of SO_2 using I^- ions. As outlined in Sect. 2.3, additional primary ions (IO_x^-) formed

with our RF discharge ion source enable SO_2 detection as, for example, ISO_3^- (m/z 207). In addition, ISO_4^-, SO_4^- and SO_5^- are also formed and the relative yields are listed in Table 2.2. Although the underlying ion-molecule reactions resulting in their formation are not fully characterised, based on the observation of IO_3^- and IO_4^- in the primary-ion mass spectrum we propose the following scheme (Reactions R 2.14–2.17).

$$SO_2 + IO_3^- \longrightarrow O_2 + ISO_3^- \qquad (m/z\ 207) \qquad \text{(R 2.14)}$$

$$SO_2 + IO_4^- \longrightarrow O_2 + ISO_4^- \qquad (m/z\ 223) \qquad \text{(R 2.15)}$$

$$SO_2 + IO_3^- \longrightarrow IO + SO_4^- \qquad (m/z\ 96) \qquad \text{(R 2.16)}$$

$$SO_2 + IO_4^- \longrightarrow IO + SO_5^- \qquad (m/z\ 112) \qquad \text{(R 2.17)}$$

As written, reactions (R 2.14) and (R 2.16) involving the IO_3^- anion are exothermic with reaction enthalpies of ≈ -250 and $-113\,\mathrm{kJ\,mol^{-1}}$, respectively. The enthalpies of formation used to derive these values were taken from the literature: $\Delta H_f^{298}(SO_2) = -287\,\mathrm{kJ\,mol^{-1}}$ (Chase, 1998), $\Delta H_f^{298}(IO) = 126\,\mathrm{kJ\,mol^{-1}}$ (Goos et al., 2005) and $\Delta H_f^{298}(SO_4^-) = -738\,\mathrm{kJ\,mol^{-1}}$ (NIST, 2016) or calculated from other thermodynamic properties. The formation enthalpy for IO_3^- ($\Delta H_f^{298}(IO_3^-) = -211\ \mathrm{kJ\,mol^{-1}}$) was calculated from its electron affinity ($453.5\,\mathrm{kJ\,mol^{-1}}$; Wen et al. (2011)) and the formation enthalpy of IO_3 ($242\,\mathrm{kJ\,mol^{-1}}$; Goos et al. (2005)). The formation enthalpy for ISO_3^- ($\Delta H_f^{298}(ISO_3^-) = -752\,\mathrm{kJ\,mol^{-1}}$) was calculated from the SO_3–I^- bond strength ($161\,\mathrm{kJ\,mol^{-1}}$; Hao et al. (2005)) and the formation enthalpies of I^- ($-195\,\mathrm{kJ\,mol^{-1}}$; Goos et al. (2005)) and SO_3 ($-396\,\mathrm{kJ\,mol^{-1}}$; Goos et al. (2005)). In the absence of thermodynamic data for IO_4^-, we cannot assess the reaction enthalpies for Reactions (R 2.15) and (R 2.17). The iodine-containing ISO_3^- (m/z 207) is most specific and suitable for monitoring SO_2 with good sensitivity.

Calibration of SO_2

SO_2 is calibrated by the addition of a small flow of SO_2 from a gas cylinder (1 ppmv in synthetic air, Air Liquide). The true mixing ratio of SO_2 flowing from the bottle into the absorption cell at 1 bar pressure was determined via UV-absorption spectroscopy using a white-cell and diode array set-up (Wollenhaupt et al., 2000) and an absorption spectrum (290–320 nm) from the literature (Bogumil et al., 2003). The mixing ratio that was determined in this manner was found to agree within 10 % of the manufacturers specifications. The linearity of the CI-QMS signal with the SO_2 mixing ratio (up to 60 ppbv) is shown as Fig. B.4a in the supplementary information.

2.4.3 Nitryl chloride

The scheme for detection of $ClNO_2$ using I^- ions generated using ^{210}Po is well-established (Osthoff et al., 2008; Thornton et al., 2010). Both ICl^- (m/z 162 and 164) and $IClNO_2^-$ (m/z 208 and 210) are formed (Reactions R 2.18 and R 2.19),

the latter generally preferred to monitor $ClNO_2$ in ambient air owing to potential interference through reactions of other chlorine-containing trace gases forming ICl^-.

$$ClNO_2 + I^- \longrightarrow ICl{NO_2}^- \qquad (m/z \text{ 208 and 210}) \qquad \text{(R 2.18)}$$

$$ClNO_2 + I^- \longrightarrow ICl^- + NO_2 \qquad (m/z \text{ 162 and 164}) \qquad \text{(R 2.19)}$$

The same ions are observed during operation with the RF discharge ion source with similar product yields for ^{210}Po as the ones for the RF discharge reported in Table 2.2.

Calibration of $ClNO_2$

$ClNO_2$ was calibrated by passing Cl_2 (50 ppmv in nitrogen, Air Liquide) over $NaNO_2$ (30 g) and NaCl (10 g) crystals in a glass flask (Thaler et al., 2011). The $ClNO_2$ generation efficiency was found to be improved by moistening the crystals by adding 2–3 drops of water. The gas mixture exiting the glass flask, which contains unreacted Cl_2, NO_2 and $ClNO_2$, was diluted in 5 slm air and sampled simultaneously with the CI-QMS and a cavity ring-down spectrometer that detects both NO_2 and $ClNO_2$ after thermal decomposition at 420 °C to NO_2 (Thieser et al., 2016). $ClNO_2$ thermograms (Sobanski et al., 2016; Thieser et al., 2016) indicate that, under the flow and pressure conditions of these calibrations, $ClNO_2$ is thermally decomposed to NO_2 at 420 °C (Reaction R 2.20), but there is no significant loss at 200 °C, the TDR temperature of the CI-QMS.

$$ClNO_2 + M \longrightarrow Cl + NO_2 + M \qquad \text{(R 2.20)}$$

The total uncertainty ($\approx 25\,\%$) associated with the calibration derives from uncertainty in the NO_2 cross section used to calculate NO_2 mixing ratios in the cavity ring-down spectrometer and the assumption that all $ClNO_2$ is detected as NO_2.

2.4.4 Hydrogen chloride

Using the discharge ion source we detect HCl as Cl^-, ICl^- and $I(CN)Cl^-$, presumably via Reaction (R 2.21–2.23).

$$HCl + I(CN)_2{}^- \longrightarrow HCN + I(CN)Cl^- \qquad (m/z \text{ 188 and 190}) \qquad \text{(R 2.21)}$$

$$HCl + ICN^- \longrightarrow HCN + ICl^- \qquad (m/z \text{ 162 and 164}) \qquad \text{(R 2.22)}$$

$$HCl + CN^- \longrightarrow HCN + Cl^- \qquad (m/z \text{ 35 and 37}) \qquad \text{(R 2.23)}$$

Reactions (R 2.22) and (R 2.23) are weakly exothermic with reaction enthalpies of ≈ -25 and -73 kJ mol^{-1}, respectively. If available, the enthalpies of formation used to derive these values were taken from Goos et al. (2005), $\Delta H_f^{298}(HCl) = -92\,kJ\,mol^{-1}$, $\Delta H_f^{298}(HCN) = 130\,kJ\,mol^{-1}$, $\Delta H_f^{298}(Cl^-) = -234\,kJ\,mol^{-1}$, $\Delta H_f^{298}(CN^-) = 61\,kJ\,mol^{-1}$, and Refaey and Franklin (1977), $\Delta H_f^{298}(ICl^-) = -155$ kJ mol^{-1}. $\Delta H_f^{298}(ICN^-) = 92\,kJ\,mol^{-1}$ was calculated from the electron affinity

of ICl (130 kJ mol^{-1}, Miller et al. (2012)) and ΔH_f^{298}(ICN) = 222 kJ mol^{-1} (Goos et al., 2005). The $I(CN)_2^-$ ion is stable in an aqueous solution (Chadwick et al., 1980), but la lack of thermodynamic data for it and for $I(CN)Cl^-$ precludes calculation of the energetics of Reaction (R 2.21).

As $I(CN)Cl^-$, formed by reaction of dicyanoiodate anion with HCl in Reaction (R 2.21), is the most abundant and specific product ion, HCl is generally monitored at m/z 188. In the absence of interferences, the ratio of signals at m/z 188 to m/z 190 and m/z 162 to m/z 164 should be determined by the natural relative abundance of the ^{35}Cl and ^{37}Cl isotopes, which is $\approx$3.13. Plots of the relative ion signals at m/z 188 versus m/z 190 and m/z 162 versus m/z 164 obtained during the CYPHEX campaign are given in Fig. B.5 of the supplementary information. The tight correlation and the slope of 3.09 for the ratio m/z 162 to m/z 164 is very close to the expected value, indicating that to a good approximation, only one trace gas containing one Cl atom was measured. In contrast, the ratio of m/z 188 to m/z 190 is significantly lower than expected, and the correlation displays more scatter. This low ratio indicates that m/z 190 suffers from interference from another trace gas. A likely candidate is HNO_3, detected as $IHNO_3^-$ at m/z 190 (Lee et al., 2014). The signals at m/z 188 and m/z 162 are correlated very well ($R^2 = 0.96$) indicating that they both represent HCl only, as no significant $ClNO_2$ was present during CYPHEX.

Calibration of HCl

A bottle of gaseous HCl diluted in N_2 (60 ppmv) was used to calibrate the CI-QMS during laboratory operation. The concentration of HCl was determined using UV-absorption spectroscopy (184.95 nm) using a cross section of 2.39 $\times$ 10^{-19} cm^2 molecule^{-1} (Bahou et al., 2001) as described by (Zimmermann et al., 2016). Once the sensitivity of the CI-QMS to HCl was established using bottled gas, the output of a laboratory-built permeation source was measured by comparing signals in the CI-QMS at m/z 188. The permeation source consisted of a few ml of concentrated HCl-solution welded into a short length (4 cm) of 6.35 mm (OD) PFA tubing, housed in 20 cm of 12.7 mm (OD) PFA tubing (at 30 °C) through which 50 sccm of air flows. The permeation rate measured was 5.2×10^{-5} sccm with an uncertainty of $\approx$10 %. The linearity of the CI-QMS signal with the HCl mixing ratio was characterised in the laboratory ($R^2 = 0.99$) and is shown as Fig. B.1b in the supplementary information.

2.5 Dependence of sensitivity on relative humidity

The CI-QMS sensitivity for the trace gases discussed here is dependent on the amount of water vapour present in the IMR, which will vary with ambient relative humidity (RH). Broadly speaking, we observe a positive dependence of the sensitivity (see Fig. 2.5) on relative humidity between 0 and 20 % at 25 °C, with a flattening of the curve between 20 and 80 % RH. This effect is generally explained

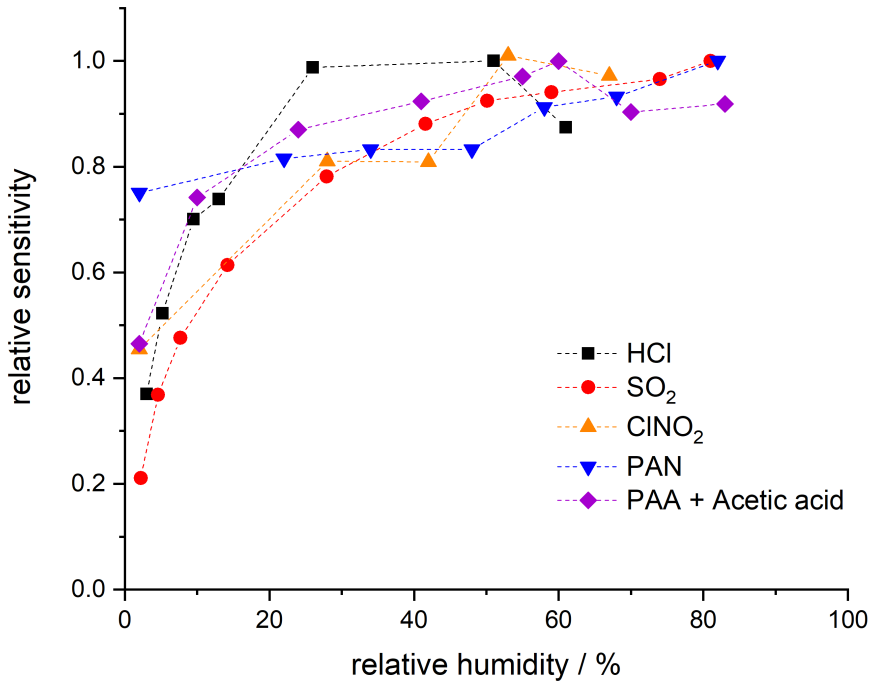

Figure 2.5: Dependence of the ion signal on the relative humidity (at 25 °C and 1 bar) of the air sampled. For PAA + acetic acid on m/z 59 only a combined humidity dependence is given as their contributions to the signal could not reliably be quantified.

by the reactions proceeding predominantly through clustered primary ions, e.g. $I^-(H_2O)$, which is observed at m/z 145. Under weak de-clustering conditions, the product ions are also clustered with H_2O, confirming the participation of $I^-(H_2O)$. For the IO_3^- and $I(CN)_2^-$ primary ions used to detect SO_2 and HCl, the water clusters $IO_3^-(H_2O)_n$ and $I(CN)_2^-(H_2O)_n$ are not observed or are very weak, even without de-clustering. We observe that the concentration of IO_3^- and $I(CN)_2^-$ in the primary-ion spectra is however dependent on the presence of H_2O, which explains the RH dependence of the sensitivity of detection for SO_2 and HCl. All ambient measurements of the trace gases discussed here are therefore corrected for RH effects using calibration curves based on data such as those displayed in Fig. 2.5.

2.6 Sensitivity, detection limits and total uncertainty

The total uncertainty of the measurement of any of the trace gases listed above is determined mainly by the uncertainty associated with the calibration method (and its reproducibility) but may also be influenced by, for example, scrubbing efficiency and drifts between background measurements (variable for different field campaigns). The response of the CI-QMS to any one trace gas may also vary over a period from days to a few weeks due to drifts in temperature, resolution of the mass spectrometer and degradation of the detector. The sensitivity (i.e.

signal in Hz per pptv of trace gas) depends on the rate coefficient for the reaction between primary ions and trace gases and the yield of product ions. The sensitivity may also depend on relative humidity (abundance of H_2O clusters) and de-clustering potential (breakup of weak bonds). The limit of detection (LOD) is mainly dependent on variability in the background signal for the respective m/z and can be calculated as 2 times the standard deviation when using synthetic (i.e. hydrocarbon-free) air or when passing the air through the scrubber (as usually performed during field measurements). In the text below (summarised in Table 2.2), we report sensitivities (in $\mathrm{Hz\,pptv^{-1}}$) and limits of detection (LOD, 2σ, in pptv) obtained under typical measurement conditions (configuration iii from Sect. 2.3) and, when applicable, compare them to values obtained using ^{210}Po as an ion source.

2.6.1 PAN, PAA and acetic acid

When using ^{210}Po as an ion source, an LOD of 3 pptv PAN (1 s) is achievable, which is adequate for e.g. airborne operation (Roiger et al., 2011) or flux measurements (Wolfe et al., 2009). The use of the RF discharge for PAN detection results in an increase in background signal (from a few hertz when using ^{210}Po to several hundred hertz when using the RF discharge ion source) even in hydrocarbon-free synthetic air. The LOD calculated from twice the standard deviation of a background measurement during the NOTOMO campaign is 34 pptv (1 s). The total uncertainty calculated from measurement precision, background subtraction (signal drifts, interpolation) and uncertainty in the calibration method is $15\,\% \pm 27$ pptv. However, the uncertainty of the PAN measurement is highly dependent on the levels and variability of PAA and acetic acid present in the air as their signal has to be interpolated and subtracted. In ambient air masses, the larger part of the signal at m/z 59 with the RF discharge is due to acetic acid which sometimes displays variability on the timescale of minutes. In this case the uncertainty of the background interpolation and therefore the overall uncertainty of the PAN measurement is drastically increased. This is essentially a selectivity problem, which limits deployment of the instrument for PAN measurements to more polluted regions where PAN mixing ratios regularly exceed 100 pptv and/or high time resolution is not necessary. As described above, the selectivity to PAN can be improved by switching off de-clustering (no acetic acid detection at m/z 59), which comes with a significant reduction in sensitivity (see below).

In order to differentiate between PAA and acetic acid, the de-clustering voltage has to be modulated between 20 V and 2 V. At the lower voltage, only PAA is detected but the resultant high chemical background and worsened sensitivity were found to lead to a poor limit of detection of a few hundred pptv (1 s) (see Table 2.2) which is about a factor of 100 higher than with use of ^{210}Po (4 pptv in 1 s). At the higher potential the LOD would be much better but the sensitivity to acetic acid at m/z 59 reduces the selectivity of the measurement. The total uncertainty calculated from measurement precision, background subtraction (signal drifts, interpolation) and uncertainty in the calibration method is $20\,\% \pm 39$ pptv.

The LOD for acetic acid at m/z 59 is 57 pptv (1 s) but the selectivity is reduced due to the PAA contribution. The total uncertainty calculated from measurement precision, background subtraction (signal drifts, interpolation) and uncertainty in the calibration method is $15\,\% \pm 45$ pptv.

2.6.2 SO_2

The sensitivity of the CI-QMS to SO_2 reported in Table 2.2 is dependent on the relative humidity (see Sect. 2.5) and is especially dependent on the de-clustering voltage, the best signal-to-noise ratio being found at 20 V. Although HSO_4^- (m/z 97) has the highest sensitivity of all product ions, we generally monitor the ISO_3^- ion (m/z 207) as the background signal is lower and the detection limit improved. Figure B.6 of the supplementary information displays the correlation between both m/z over a period of 4 weeks during the NOTOMO campaign. The correlation coefficient ($R^2 = 0.95$) is large, from which we conclude that both m/z can be used to calculate SO_2 mixing ratios. The detection limit for m/z 207 is 56 pptv (1 s) (based on noise in background measurements during the NOTOMO field campaign), which is sufficient to monitor SO_2 in lightly polluted areas. At a lower temporal resolution and when monitoring only ISO_3^- and I^-, the LOD can be improved to a few pptv (e.g. in 10 min). The total uncertainty, calculated from measurement precision, background subtraction (signal drifts, interpolation) and uncertainty in the calibration method is $20\,\% \pm 23$ pptv.

2.6.3 $ClNO_2$

Very good detection limits have been reported (Osthoff et al., 2008; Thornton et al., 2010; Phillips et al., 2012) for the measurement of $ClNO_2$ via I-CIMS using ^{210}Po ionisation, a result of low background signal at m/z 208 ($ICl NO_2^-$) and an efficient reaction with I^-. Using ^{210}Po, Phillips et al. (2012) achieved an LOD ($2\,\sigma$) of 3 pptv (1 s), which can be compared to the value of 12 pptv (see Table 2.2) obtained with the RF discharge ion source, the difference stemming from a higher chemical background signal. With an averaging interval of 5 min the LOD can be reduced to 2–3 pptv. $ClNO_2$ can also be detected as ICl^- (m/z 162 and 164), which provides higher sensitivity compared to $ICl NO_2^-$ (see Table 2.2) but can suffer from a significant interference due to HCl, which is likely to be present in air masses containing $ClNO_2$. For example, 1 ppbv HCl contributes a signal at m/z 162 which is equivalent to 60 pptv $ClNO_2$ at this m/z. Monitoring $ClNO_2$ at m/z 208 is more specific, with an equivalent signal due to 1 ppb HCl of less than 10 pptv, which can be accounted for when measuring HCl in parallel (at m/z 188, see above). It should be noted that the interference at m/z 162 is not unique to the RF discharge but has also been observed when using a ^{210}Po-ioniser (Phillips et al., 2012). The total uncertainty for $ClNO_2$ measurement, calculated from precision, background subtraction (signal drifts, interpolation) and uncertainty in the calibration method, is $30\,\% \pm 6$ pptv.

2.6.4 HCl

Sensitivities and product yields for several ions connected to HCl detection are reported in Table 2.2. As ICl^- (m/z 162 and 164) suffers from a $ClNO_2$ interference (see above) and Cl^- (m/z 35 and 37) could possibly arise from other Cl-containing species, the more specific ion $I(CN)Cl^-$ (m/z 188 and 190) is used to monitor HCl. The LOD for m/z 188 is 135 pptv (1 s), which can be further improved by extended averaging if high time resolution is not required. The total uncertainty calculated from measurement precision, background subtraction (signal drifts, interpolation), scrubbing efficiency (it takes more time to remove HCl in the scrubber than e.g. SO_2) and uncertainty in the calibration method is $20\,\% \pm 72$ pptv.

2.7 Application in the field

Our CI-QMS instrument has been deployed in different ground-based field campaigns including ones at coastal (CYPHEX, 2014), forested (IBAIRN, 2016) and mountain sites (NOTOMO, 2015) in Europe. In the following we present subsets of the data from these campaigns in order to indicate how the instrument with an RF discharge ion source (configuration iii in Sect. 2.3) performs in the field.

2.7.1 CYPHEX 2014

During CYPHEX (Cyprus Photochemistry Experiment, summer 2014), located at a coastal site on the eastern Mediterranean island of Cyprus, we measured chemically aged air masses with origins in continental Europe (Meusel et al., 2016; Derstroff et al., 2017). A time series of SO_2 and HCl for a 3-week period of the campaign is shown in Fig. 2.6. SO_2 was detected for the first time using the CI-QMS during CYPHEX in which observations of covariance between the signal at m/z 207 and particulate sulphate provided the first clues to the identity of the mass peak as ISO_3^- and indications of sensitivity to SO_2. As we had not anticipated CI-QMS sensitivity to SO_2, calibration was performed post-campaign. We observed SO_2 mixing ratios as high as 11 ppbv, the plume-like nature of which strongly suggests nearby point sources such as ship traffic or air masses originating from power plants in continental Europe. Our measurements are consistent with other observations in the coastal Mediterranean boundary layer. Bardouki et al. (2003) found SO_2 mixing ratios up to 3 ppbv in Crete (August 2001) and Schembari et al. (2012) report average daily mean values of several ppbv in different western Mediterranean harbours measured in the summers of 2009 and 2010. Kanakidou et al. (2011) conclude that megacities can be hotspots of air pollution in the eastern Mediterranean, with average SO_2 mixing ratios of 1 ppbv measured in Crete (1997–1999), 8 ppbv in Istanbul (1998–2008), 10–15 ppbv in Athens (1995–1997) and 48 ppbv in Cairo (1999–2000), where about 70 % originates from industrial activities.

Similar to SO_2, the measurement of HCl was unexpected, the isotopic ratio of 3:1 for the signals at m/z 162 and 164 (ICl^-) providing evidence that the trace

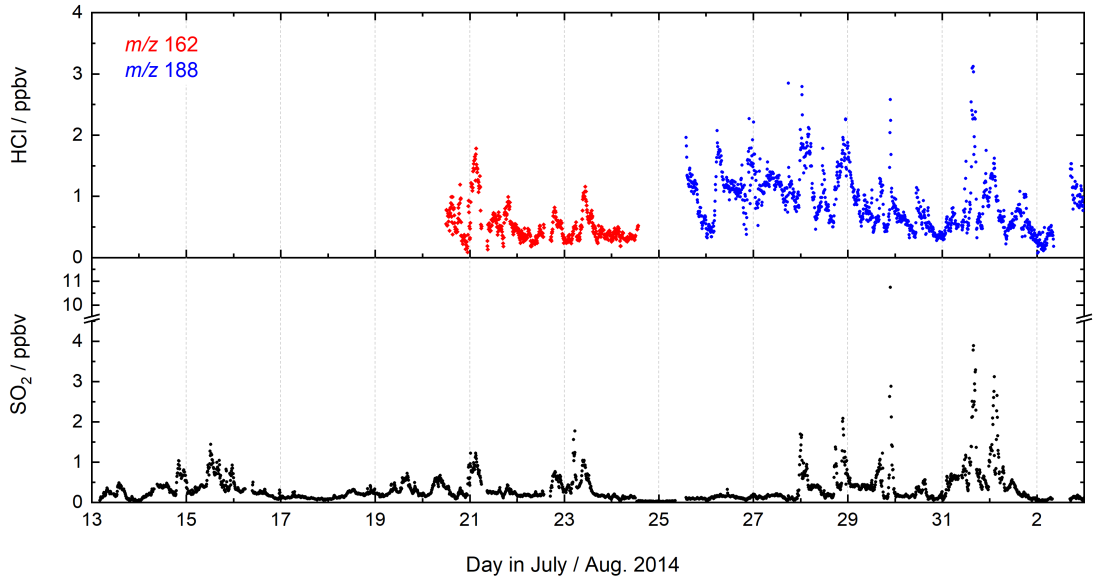

Figure 2.6: CI-QMS time series of SO_2 and HCl mixing ratios during the CYPHEX field campaign in Cyprus.

gas measured contained one Cl atom. The identification of HCl was confirmed during the campaign, in which a permeation source was built and used to periodically supply HCl to the CI-QMS. Calibration of the permeation source ensued post-campaign as described in Sect. 2.4.4. HCl mixing ratios up to 3 ppbv were observed which could be attributed to the release of HCl from sea salt aerosols when polluted air masses from continental Europe reached the coastal site. The covariance between HCl and SO_2 in Fig. 2.6 suggests that an acid displacement mechanism involving SO_2 oxidation to H_2SO_4 and transfer of H_2SO_4 to aqueous sea salt aerosol was involved. The median value of the HCl mixing ratio for the CYPHEX campaign was 790 pptv, which can be compared with reports of median values of 600–700 pptv HCl over the Atlantic near Europe and values of up to 6 ppbv in the polluted coastal boundary layer on the Isles of Shoals, 10 km off the southern Maine coast, USA, with an average of 600 pptv (July–August 2004) (Keene et al., 2007, 2009).

2.7.2 NOTOMO 2015

The mountain-site campaign NOTOMO (NOcturnal chemistry at the Taunus Observatory: insights into Mechanisms of Oxidation, summer 2015) took place in a rural location in south-western Germany with significant urban influence (Sobanski et al., 2017). A time series of SO_2, $ClNO_2$ and PAN mixing ratios and the signal at m/z 59 (contributions from acetic and peracetic acid) is displayed in Fig. 2.7. During NOTOMO, SO_2 was monitored as ISO_3^- (m/z 207) and HSO_4^- (m/z 97), and a very good correlation between both signals ($R^2 = 0.95$) within a period of 4 weeks confirmed that both ions reliably represent the same molecule

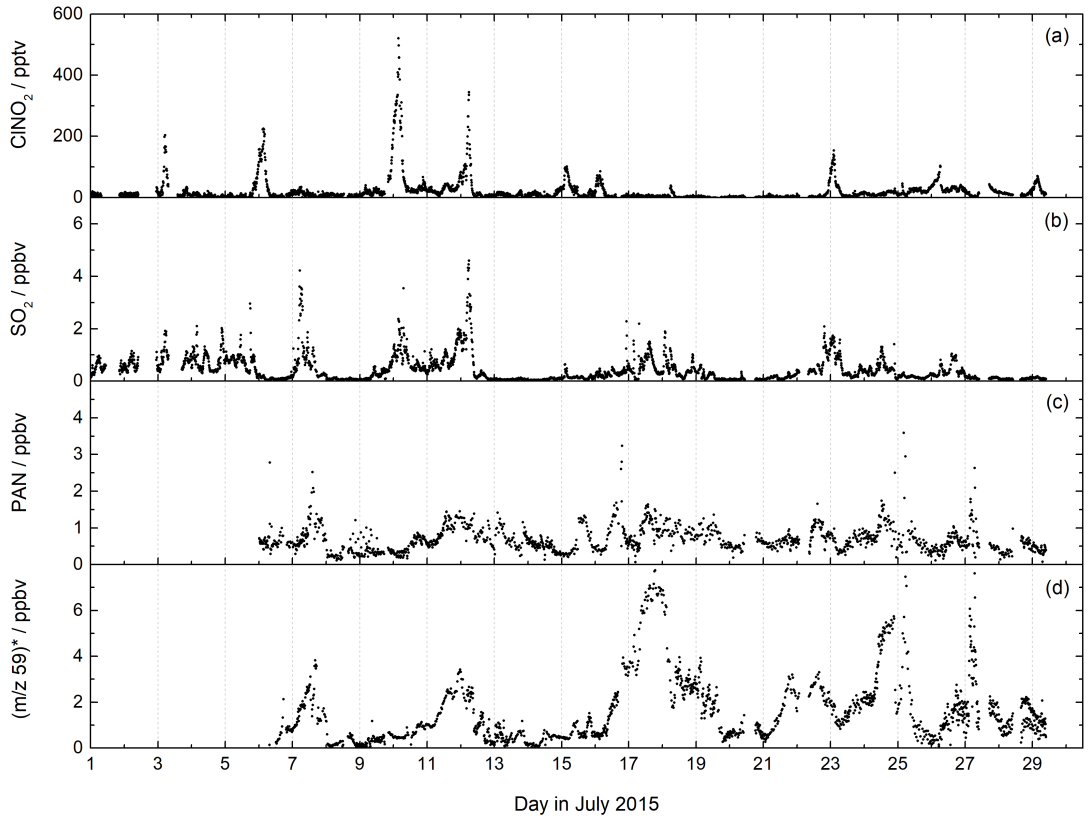

Figure 2.7: CI-QMS time series of $ClNO_2$, SO_2 and PAN mixing ratios and m/z 59 during the NOTOMO field campaign in Germany. The signal at m/z 59 was converted to ppbv, assuming that it consists only of acetic acid (no peracetic acid). The mixing ratios are therefore only an upper limit. For comparison with the PARADE campaign at the same location see Fig. B.7.

(see Fig. B.6). The SO_2 mixing ratios exceeded 1 ppbv on most days, with maximum values up to 5 ppbv. The likely origins of SO_2 at this site are emissions from coal-burning power plants in the local Rhine-Main urban conglomeration and the heavily industrialised Ruhr area to the north-west.

$ClNO_2$ was detected during NOTOMO as $ICl NO_2^-$ (m/z 208 and 210). Mixing ratios ranged from 0 to 500 pptv and were above 50 pptv during 10 out of 29 campaign nights. High levels of $ClNO_2$ were generally associated with mixed marine and continental air masses from the north-west which had passed over the English Channel and the polluted Ruhr area. The data are consistent with previous measurements (using the CI-QMS equipped with a ^{210}Po ioniser) at the same location and similar time of year (Phillips et al., 2012) whereby comparable $ClNO_2$ mixing ratios were observed (see Fig. B.7 of the supplement).

We measured PAN at m/z 59 and observed mixing ratios generally ranging between 0 and 2 ppbv throughout NOTOMO, occasionally reaching 3 ppbv. PAN levels predominantly peaked in the afternoon, when photochemical activity is usually highest. Compared with results from PARADE (see Fig. B.7 of the supplement)

in which PAN had been measured with a precursor version of this instrument with a ^{210}Po-ioniser, frequency and amplitude of the PAN mixing ratios throughout the campaign were very similar. However, due to the high and variable chemical background at m/z 59, as already pointed out in Sect. 2.4.1, the detection limit during NOTOMO was about an order of magnitude worse than in PARADE (see Table 2.2). As we did not require higher temporal resolution than a few minutes for analysis, this was not a key issue here. The measurements with the RF discharge ion source had adequate sensitivity towards PAN in this moderately polluted region and have the additional advantage over ^{210}Po of simultaneous detection of SO_2 and HCl. In contrast, the differentiation between PAA and acetic acid is problematic. During NOTOMO, we were unaware of the sensitivity towards acetic acid at m/z 59 and the signal without PAN (i.e. during titration of $CH_3C(O)O_2$ with NO) was measured with 20 V de-clustering only and therefore represents a combined signal of PAA and acetic acid. Although peracetic acid calibration was performed during the campaign, this is not considered reliable because the PAA diffusion source also contains significant amounts of acetic acid. For this reason, we present only an upper limit for acetic acid, ranging between 0 and 8 ppbv. From the PAN-to-PAA ratio calculated for PARADE (about 10) we would also expect several hundred pptv of PAA to be present (see Fig. B.7 of the supplement), which would lower this approximate acetic acid mixing ratio significantly.

2.7.3 IBAIRN 2016

The IBAIRN campaign (Influence of Biosphere–Atmosphere Interactions on the Reactive Nitrogen budget, summer 2016) took place in boreal forest in Hyytiälä, Finland, an area with large biogenic emissions and low-NO_x conditions (Liebmann et al., 2018). The CI-QMS inlet was located at about 6 m height within the canopy. A time series of SO_2, HCl, PAN, PAA and the signal at m/z 59 that has contributions from both acetic and peracetic acid is shown in Fig. 2.8.

During IBAIRN SO_2 was monitored by the CI-QMS as ISO_3^- (m/z 207) with mixing ratios up to 1 ppbv. SO_2 mixing ratios were largest when the air originated from the north-east (point sources like coal-burning power plants in northern Finland and Russia) but only occasionally exceeded 100 pptv in this remote, forested environment. Independent SO_2 measurements, using a TEI 43 CTL fluorescence analyser (SMEAR II station, University of Helsinki) were made on a tower at a 16 m height (5 m distant from the CI-QMS inlet but approximately at canopy height) and allow a direct comparison to be made. The datasets are generally in good agreement (Fig. 2.8a), although some SO_2 plumes were only observed at the higher inlet due to strong gradients in trace gas concentrations resulting from boundary layer dynamics.

HCl (Fig. 2.8b) was measured as $I(CN)Cl^-$ (m/z 188 and 190) with mixing ratios up to 300 pptv showing a distinct diurnal profile with a maximum in the afternoon, which reflects temperature-dependent changes in partitioning between the gas phase and particle phase in which HCl is converted into NH_4Cl.

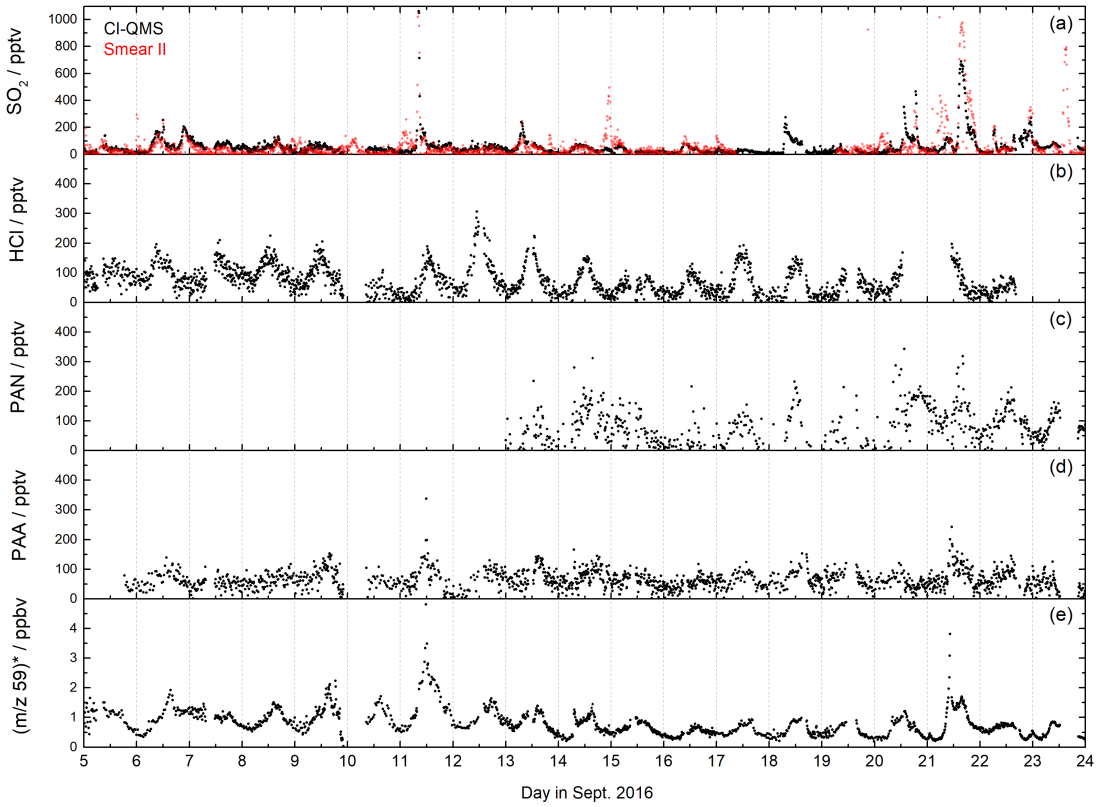

Figure 2.8: CI-QMS time series of SO_2, HCl, PAN and PAA mixing ratios and m/z 59 during the IBAIRN campaign, which was undertaken in boreal forest. The red SO_2 trace was obtained using a TEI 43 CTL fluorescence analyser (SMEAR II). The signal at m/z 59 was converted to ppbv assuming that it consists only of acetic acid (no peracetic acid). The mixing ratios are therefore only an upper limit.

The combined PAA and acetic acid signal at m/z 59 obtained with de-clustering at 20 V (Fig. 2.8e) displays the diurnal profile expected from photochemically generated trace gases with night-time depositional losses. However, as explained in Sect. 2.7.2, we cannot easily separate the contribution to the signal from PAA and acetic acid. When NO is added (see Fig. B.3), the signal at m/z 59 with low de-clustering is due to PAA only (Fig. 2.8d), but the PAA detection limit is poor due to a low sensitivity and elevated and variable background signal during zeroing. The PAA contribution to the total signal at m/z 59 is likely to be substantial but cannot be calculated as the sensitivity of the CI-QMS to PAA during de-clustering (Fig. 2.8e) is unknown, a result of the presence of unknown amounts of acetic acid in the PAA diffusion source. The use of a ^{210}Po-ioniser would have greatly improved the PAN (see Fig. 2.8c) and PAA data quality, as evidenced by the PAN and PAA measurements reported for the same location during 2010 (Phillips et al., 2013; Crowley et al., 2018).

2.8 Conclusions

The CI-QMS with an RF discharge ion source is a promising alternative to similar instruments using ^{210}Po-based ion sources and can be deployed in environments for which permission to use of ^{210}Po may be difficult or impossible to obtain or to which transportation is not feasible. The use of the RF discharge results in an extension of the established detection schemes (e.g. for $ClNO_2$ and PAN) using I^- ions, and we have identified ion schemes involving IO_x^- and $I(CN)_x^-$ primary ions that additionally enable detection of SO_2 and HCl. Detection limits ($2\,\sigma$, 1 s integration) are 56 pptv for SO_2, 135 pptv for HCl and 12 pptv for $ClNO_2$ which makes the CI-QMS a useful tool for investigation of atmospheric processes related to sulphur and chlorine chemistry. Application of the instrument with the RF discharge ion source for PAN detection is limited to polluted environments where mixing ratios usually exceed a hundred pptv and high temporal resolution is not needed. This restriction is mainly due to a background count rate that is higher by 1–2 orders of magnitude compared to the use of ^{210}Po and due to a strong dependence of the measurement uncertainty on the variability of the subtracted interpolated background signal (consisting of PAA and acetic acid). A PAN detection limit (in the absence of PAA and acetic acid) of 34 pptv in 1 s was obtained, though this value will rarely be reached in boundary layer air masses where acetic acid and peracetic acid are abundant. Similarly, while sensitive detection of PAA (requiring de-clustering) is precluded by the detection of acetic acid at the same m/z, the selective detection of acetic acid is uncertain due to the contribution of PAA.

The deployment of the CI-QMS with RF discharge and its advantages and disadvantages compared to instruments using ^{210}Po-based ionisation are illustrated in three campaign datasets, which demonstrate its potential to monitor trace gases at mixing ratios ranging from a few tens of pptv to a few ppbv. If the scientific focus is on PAA and PAN, the RF-discharge-based CI-QMS is clearly disadvantaged compared to the more selective and sensitive ^{210}Po-based ionisation. On the other hand, the potential to measure $ClNO_2$ without logistical obstacles related to transport and (mobile) operation of radioactive sources and the added benefit of simultaneous measurement of HCl and SO_2 may in some instances tip the balance in its favour.

Author contributions

Philipp Eger developed and tested the RF discharge ion source in the laboratory, deployed the CI-QMS during the NOTOMO and IBAIRN campaigns, evaluated the field data and wrote the paper. Frank Helleis and Gerhard Schuster helped to design and modify the CI-QMS for the constant pressure and RF discharge operations. John Crowley and Jos Lelieveld designed the field campaigns and contributed to the paper; Gavin Phillips operated the CI-QMS during CYPHEX and helped evaluate the data.

Acknowledgements

We thank the Cyprus Ministry of Defence for the use of the base of the Cypriot National Guard at Ineia and the generous assistance of the Lara Naval Observatory staff during the CYPHEX campaign. Our thanks also go to the Department of Labour Inspection of Cyprus for helping us set up the campaign. We thank Heinz Bingemer for logistical support and use of the facilities at the Taunus Observatory during the NOTOMO campaign. We are grateful to the technical staff of SMEAR II station for technical support and ENVRIplus for partial financial support of the IBAIRN campaign. We thank Jan Schuladen for his technical assistance with the CI-QMS and the design of the TDR. We thank Thomas Klüpfel and Jonathan Williams at the Max Planck Institute, Mainz, for the loan of a CO_2 detector (LI-COR).

Chapter 3

Pyruvic acid in the boreal forest: first measurements and impact on radical chemistry

Philipp G. Eger[1], Jan Schuladen[1], Nicolas Sobanski[1], Horst Fischer[1], Einar Karu[1], Jonathan Williams[1], Matthieu Riva[2,3], Qiaozhi Zha[2], Mikael Ehn[2], Lauriane L. J. Quéléver[2], Simon Schallhart[2], Jos Lelieveld[1], and John N. Crowley[1]

[1]Atmospheric Chemistry Department, Max-Planck-Institute for Chemistry, 55128 Mainz, Germany

[2]Institute for Atmospheric and Earth System Research / Physics, FI-00014 University of Helsinki, Finland

[3]University of Lyon, Université Claude Bernard Lyon 1, CNRS, IRCELYON, F-69626, Villeurbanne, France

This chapter is based on the manuscript "Pyruvic acid in the boreal forest: first measurements and impact on radical chemistry" published in Atmospheric Chemistry and Physics Discussions (ACPD) as Eger et al. (2019c). It focusses on the first measurements of pyruvic acid in a boreal forest environment during the IBAIRN campaign, for which SO_2, HCl, PAN and PAA / acetic acid mixing ratios have been reported in Sect. 2.7.3

Summary

Pyruvic acid, $CH_3C(O)C(O)OH$, is an organic acid of biogenic origin that plays a crucial role in plant metabolism, is present in tropospheric air in both gas-phase and aerosol-phase and is implicated in the formation of secondary organic aerosols (SOA). Up to now, only a few field studies have reported mixing ratios of gas-phase pyruvic acid and its tropospheric sources and sinks are poorly constrained. We present the first gas-phase measurements of pyruvic acid in the boreal forest as part of the IBAIRN (Influence of Biosphere–Atmosphere Interactions on the Reactive Nitrogen budget) field campaign in Hyytiälä, Finland, in September 2016. The mean pyruvic acid mixing ratio during IBAIRN was 96 pptv, with a maximum value of 327 pptv. From our measurements we derived the overall pyruvic acid source strength and quantified the contributions of isoprene oxidation and direct emissions from vegetation in this monoterpene-dominated, forested environment. Further, we discuss the relevance of gas-phase pyruvic acid for atmospheric chemistry by investigating the impact of its photolysis on acetaldehyde and peroxy radical production rates. Our results show that, based on our present understanding of its photo-chemistry, pyruvic acid is an important source of acetaldehyde in

the boreal environment, exceeding ethane/propane oxidation by factors of ≈ 10 and ≈ 20.

3.1 Introduction

Organic acids play a crucial role in tropospheric chemistry. They influence the acidity of aerosols and cloud droplets and are involved in the formation of secondary organic aerosol (SOA), thereby impacting air quality and climate (Kanakidou et al., 2005; Hallquist et al., 2009). Pyruvic acid ($CH_3C(O)C(O)OH$), the simplest α-keto-acid, is omnipresent in plants where it is central to the metabolism of isoprene, monoterpenes and sesquiterpenes (Magel et al., 2006; Jardine et al., 2010) and is also found in tropospheric air, especially in the boundary layer of vegetated regions (see Sect. 3.1.3).

The boreal forest is one of the largest terrestrial biomes on Earth covering about 10 % of its land surface and emitting large amounts of biogenic VOCs into the atmosphere (Kesselmeier and Staudt, 1999; Rinne et al., 2005; Hakola et al., 2012). It serves as an important global carbon reservoir (Bradshaw and Warkentin, 2015) and impacts the Earth's climate not only through forest-atmosphere carbon exchange but also via surface albedo, evapotranspiration and formation of cloud condensation nuclei and SOA from gaseous biogenic precursors (Kulmala et al., 2004; Bonan, 2008; Sihto et al., 2011). Our work focusses on the first measurement and chemical impact of pyruvic acid in a boreal forest environment.

3.1.1 Atmospheric sources of pyruvic acid

There are several known routes to the photochemical formation of pyruvic acid in the troposphere. In clean air, pyruvic acid is generated during the photo-oxidation of isoprene via the ozonolysis of methylvinylketone (MVK) and subsequent hydrolysis of the Criegee intermediates formed (Jacob and Wofsy, 1988; Grosjean et al., 1993; Paulot et al., 2009). Pyruvic acid is found in the photolysis (in air) of methylglyoxal (Raber and Moortgat, 1995), itself formed from the OH-initiated oxidation of several biogenic VOCs (Arey et al., 2009; Obermeyer et al., 2009) including monoterpenes (Yu et al., 1998; Fick et al., 2003). The aqueous-phase oxidation of methylglyoxal also leads to formation of pyruvic acid (Stefan and Bolton, 1999). In addition, pyruvic acid is found in anthropogenically influenced air masses where it is formed in the photo-oxidation of aromatics in the presence of NO_x (Grosjean, 1984; Praplan et al., 2014) and via the reactions of peroxy radicals generated in the oxidation of propane, acetone and hydroxyacetone (Jenkin et al., 1993; Warneck, 2005). It is also suggested to be formed in biomass burning plumes (Andreae et al., 1987; Helas et al., 1992). Finally, pyruvic acid is believed to be directly emitted by vegetation as indicated by measurements of very high mixing ratios under oxidation-free conditions in a tropical rain-forest biome (Jardine et al., 2010).

3.1.2 Atmospheric sinks of gas-phase pyruvic acid

Like other di-carbonyls, pyruvic acid has a UV-absorption spectrum that extends into the visible part of the electromagnetic spectrum (Horowitz et al., 2001) and is thus photolysed rapidly by actinic radiation. Experimental studies indicate that pyruvic acid has a lifetime with respect to photolysis of a few hours (Grosjean, 1983; Winterhalter et al., 2001). In contrast, the rate constant for reaction of pyruvic acid with OH is slow ($1.2 \times 10^{-13}\,\mathrm{cm^3\,molecule^{-1}\,s^{-1}}$, (IUPAC, 2019)) and this may be considered a negligible sink with a lifetime of ≈ 3 months (Mellouki and Mu, 2003). The photolysis of pyruvic acid proceeds mainly ($\approx 60\,\%$) via exothermic decarboxylation involving a 5-membered transition state that decomposes to CO_2 and methyl-hydroxycarbene (CH_3COH), the latter rearranging to acetaldehyde (IUPAC, 2019). Other product channels observed are CH_3CO + HOCO ($\approx 35\,\%$) and CO + $CH_3C(O)OH$ ($\approx 5\,\%$) (see Sect. 3.3.2 for more details). With a Henry's law solubility of $\approx 3 \times 10^5\,\mathrm{M\,atm^{-1}}$ (Staudinger and Roberts, 1996), pyruvic acid is highly soluble so that wet and dry deposition and partitioning into the aerosol-phase are expected to be important sinks, especially at high relative humidity, thus contributing to SOA formation (Carlton et al., 2006; Tan et al., 2012; Griffith et al., 2013; Reed Harris et al., 2014; Eugene and Guzman, 2017).

3.1.3 Observations of ambient gas-phase pyruvic acid

Pyruvic acid was first observed by Andreae et al. (1987) in the Amazonas region (Brazil) as well as in the southern US, with most (85–93 %) found in the gas-phase, where mixing ratios ranged from 10 to 400 pptv. Andreae et al. (1987) reported the highest mixing ratios for the Amazon forest near the top of the forest canopy, which was considered consistent with formation from the oxidation of isoprene in the boundary layer and removal by dry deposition. Similarly, average daytime mixing ratios of pyruvic acid over central Amazonia of (25 ± 15) pptv (forest canopy) and (15 ± 15) pptv (free troposphere) (Talbot et al., 1990) were consistent with model predictions (Jacob and Wofsy, 1988) of pyruvic acid formation from isoprene degradation. Helas et al. (1992) found pyruvic acid mixing ratios up to 800 pptv in and above the equatorial African rain forest which could not be attributed to isoprene oxidation, indicating additional sources. Pyruvic acid levels of up to 200 pptv in the rural continental atmosphere at a mountain top site over the Eastern U.S. were thought to originate from biogenic emissions and possibly photochemical production (Talbot et al., 1995). In regions influenced by anthropogenic emissions, pyruvic acid has been measured at mixing ratios of up to 500 pptv whereby the diurnal profiles indicated a dominant photochemical source (Mattila et al., 2018), and it was present in an urban air mass in the Los Angeles Basin and New York (Khwaja, 1995; Veres et al., 2008). Very low mixing ratios (≈ 1 pptv) of pyruvic acid were found in the marine boundary layer over the Atlantic Ocean (63 °N to 39 °S), confirming the importance of continental sources (Baboukas et al., 2000). The largest recorded ambient mixing ratios of pyruvic acid (up to 15 ppbv) were reported in an experimental tropical rain forest biome

(Jardine et al., 2010) and were accompanied by isoprene levels exceeding 100 ppbv with other terpenoids up to ≈ 10 ppbv. In the biome, photochemical production and loss of pyruvic acid are not important and the high pyruvic acid mixing ratios were attributed to direct emissions.

Pyruvic acid is a potentially important but unexplored atmospheric component which is present in the gas-phase as well as in the aerosol phase (Andreae et al., 1987) and, along with other di-carbonyls, has been proposed to be a potentially important source of $CH_3C(O)O_2$ and HO_2 radicals in areas dominated by biogenic emissions (Crowley et al., 2018). So far, elevated pyruvic acid mixing ratios have only been observed in temperate or equatorial forests where isoprene emissions were large. In the following, we present the first gas-phase measurements of pyruvic acid in the boreal forest where isoprene levels (in September) were generally low and investigate its impact on photochemical radical production in this environment.

3.2 Methods

The IBAIRN campaign (Influence of Biosphere–Atmosphere Interactions on the Reactive Nitrogen budget) took place in the boreal forest in Hyytiälä, Finland, in September 2016 during the summer–autumn transition. Measurements were performed at the "Station for Measuring Forest Ecosystem-Atmosphere Relations II" (SMEAR II) in Hyytiälä (61.846 °N, 24.295 °E, 180 m above sea level) in southern Finland (Hari and Kulmala, 2005), in a forested area which is characterised by large biogenic emissions and low NO_x concentrations (Williams et al., 2011; Crowley et al., 2018; Liebmann et al., 2018). The vegetation in the surrounding 50 km is dominated by Scots pine and Norway spruce and the site is only occasionally influenced by anthropogenic emissions, with the nearest city (Tampere) located ≈ 50 km to the south-west. A detailed description of the measurement site can be found elsewhere (Hari and Kulmala, 2005; Hari et al., 2013). Meteorological parameters including wind direction, wind speed, temperature, relative humidity and precipitation are continuously monitored at various heights on the 128 m SMEAR II tower and distributed via an on-line data exploration and visualisation tool for SMEAR stations (Junninen et al., 2009). Measurements of NO_3 radical reactivity, alkyl nitrates, highly oxygenated molecules (HOM) and meteorological parameters during the IBAIRN campaign have recently been reported (Liebmann et al., 2018; Zha et al., 2018; Liebmann et al., 2019). Unless stated otherwise, the trace-gases discussed in this paper were sampled from the centre of a high volume-flow inlet ($10\,m^3\,min^{-1}$, 0.15 m diameter, 0.2 s residence time) made of stainless steel, the top of which was located at a height of 8 m above the ground. The top of the canopy around the clearing was at ≈ 20 m.

3.2.1 CI-QMS measurement of pyruvic acid

Pyruvic acid was detected with a chemical ionisation quadrupole mass spectrometer (CI-QMS) equipped with an electrical, radio-frequency (RF) discharge ion

source, described in detail by (Eger et al., 2019a). The CI-QMS detected pyruvic acid as $CH_3C(O)C(O)O^-$ at a mass-to-charge ratio (m/z) of 87. The sensitivity was 4.8 Hz pptv^{-1} per 10^6 Hz of I^-, which resulted in a detection limit (LOD) of 15 pptv (10 s, 2σ) or 4 pptv (10 min). The detection scheme is believed to be similar to the one reported for acetic acid (Eger et al., 2019a) and involves the reaction of pyruvic acid with $I(CN)_2^-$ primary ions to initially form HCN + $I(CN)CH_3C(O)C(O)O^-$ (m/z 240) which then dissociates to $CH_3C(O)C(O)O^-$ (m/z 87) when a 20 V de-clustering voltage is applied in the collisional dissociation chamber. Laboratory experiments with the same instrument equipped with a ^{210}Po ioniser revealed that detection at m/z 87 is also possible with I^- (when a de-clustering voltage is applied), though the sensitivity was significantly lower.

As detection of pyruvic acid during IBAIRN was not expected, the instrument was calibrated post-campaign by simultaneously monitoring the output of a diffusion source (98 % pyruvic acid, Sigma-Aldrich) with the CI-QMS and an infrared absorption spectrometer measuring CO_2 (LI-COR) following the thermal oxidation of pyruvic acid to 3 CO_2 molecules (Veres et al., 2010). The CI-QMS sensitivity to pyruvic acid was found to be independent of relative humidity (RH) for RH >20 %. For dry air, however, the sensitivity drops to about 60 % of the sensitivity derived with humidified air reflecting the importance of water clusters in the reaction with the primary ion.

A flow of 2.5 L (standard temperature and pressure, STP) min^{-1} was drawn into the CI-QMS via a 3 m long 6.35 mm (outer diameter, OD) PFA tubing and then a 20 cm section of PFA that was heated to 200 °C, required for PAN detection (Eger et al., 2019a). A membrane filter (Pall Teflo, 2 μm pore) was placed between the high-volume inlet and CI-QMS sampling line to remove particles and was exchanged regularly to avoid accumulation of particulate matter. The ion molecule reactor was held at a pressure of 18 mbar and a de-clustering voltage of 20 V was applied in the collisional dissociation chamber. The background signal was determined by periodically passing ambient air (for 10 min) through a scrubber filled with steel wool where pyruvic acid was efficiently destroyed at the hot surfaces (120 °C). Due to pyruvic acid's high affinity for surfaces, it typically took 5–10 minutes to remove >90 % of the signal, which resulted in a background signal that co-varied with the ambient signal at m/z 87. In order to circumvent this, we corrected the data using a constant background signal derived from ambient measurements in which pyruvic acid mixing ratios were close to the detection limit or when the inlet was overflowed with synthetic air whilst calibrating other trace gases. We have increased the total uncertainty on the pyruvic acid mixing ratios to 30 % $\pm$ 10 pptv to account for this.

The sensitivity of the CI-QMS to pyruvic acid can be accurately derived from laboratory-based calibrations. However, m/z 87 is subject to potential interferences owing to the limited mass resolution ($\approx$1 atomic mass unit, amu) of our quadrupole mass spectrometer. In the following, we discuss potential contributions of other trace gases to m/z 87 and examine the evidence that supports the assignment to (predominantly) pyruvic acid.

Analogous to the detection of PAN ($CH_3C(O)O_2NO_2$) as the acetate anion at m/z 59, we would expect the CI-QMS to detect C4 nitric anhydrides (peroxy-isobutyric nitric anhydride, PiBN and peroxy-n-butyric nitric anhydride, PnBN) at m/z 87 following thermal dissociation to a peroxy radical, which reacts with I^- to form $C_4H_7O_2^-$. As the CI-QMS detects the peroxy-acids at the same m/z as the nitric anhydrides with the same carbon-backbone, we would also expect to detect peroxyisobutyric acid and peroxy-n-butyric acid (Phillips et al., 2013). The CI-QMS was set up to measure PAN during IBAIRN and we therefore regularly added NO to our heated inlet to zero the signal from PAN and thus also PiBN and PnBN. The lack of signal modulation at m/z 87 while adding NO enables us to conclude that the contribution of PiBN and PnBN was insignificant, which is consistent with the low mixing ratios of PAN (the dominant nitric-anhydride at this and most locations) observed during IBAIRN. Mixing ratios of PiBN and PnBN, generally associated with anthropogenically influenced air masses, are expected to be low at this site. Similarly, although differentiation between pyruvic acid and peroxyisobutyric / peroxy-n-butyric acid was not possible with our instrument, we expect the C4 peroxy-acids to be present at very low concentrations in this pristine environment as their organic backbone is derived from organics of mainly anthropogenic origin (Gaffney et al., 1999; Roberts et al., 2002, 2003). Similar arguments help us to rule out a significant contribution on m/z 87 from butanoic acid (which can react with $I(CN)_2^-$ in a similar manner to acetic and pyruvic acid), which accompanies anthropogenic activity (e.g. traffic emissions, see Mattila et al. (2018)) and would not acquire continuously high concentrations at this site. Assuming similar sensitivities for butanoic and acetic acid, i.e. $0.62\,\mathrm{Hz\,pptv^{-1}}$ (Eger et al., 2019a) concentrations of exceeding 2.5 ppbv would be required to account for the signal at m/z 87.

While the low resolution of the CI-QMS cannot differentiate between molecules of 87.008 amu with the formula $C_3H_3O_3^-$ (the anion from pyruvic acid) and 87.045 amu with the formula $C_4H_7O_2^-$ (the anion from PiBN, PnBN or butanoic acid), a second measurement of the exact mass of the anion detected at m/z 87 was provided by an Aerodyne high-resolution long time-of-flight chemical ionisation mass spectrometer (HR-L-ToF-CIMS), equipped with iodide (I^-) reagent ions (Lopez-Hilfiker et al., 2014; Riva et al., 2019). This instrument was located about 50 m away from the common inlet and sampled at a height of 1.5 m above the ground. Although neither the instrument nor its inlet transmission was calibrated for pyruvic acid, the signals at 214.921 amu ($C_3H_4O_3{\cdot}I^-$) and 87.008 amu ($C_3H_3O_3^-$) confirmed the assignment of m/z 87 to a molecule with three of each C- and O-atoms, and thus pyruvic acid. Figure C.1 of the supporting information shows that the dominant contribution to m/z 87 is an ion of formula $C_3H_3O_3^-$, which is a factor of ≈ 10 larger than that assigned to $C_4H_7O_2^-$. The HR-L-ToF-CIMS, which was operated under conditions that minimised de-clustering, also identified a signal at 214.921 amu that could be assigned to $C_3H_4O_3{\cdot}I^-$, which was about a factor of 10 higher than for the fragment at 87.008 amu. The correlation coefficient between both signals was 0.77, the deviation from unity likely being related to different

response to ambient relative humidity for formation and detection of the cluster and fragment. Pyruvic acid has been detected previously using a HR-L-ToF-CIMS (Lee et al., 2014) whereby a strong dependence of the sensitivity on the relative humidity was observed. If the same factors apply to the instrument used during IBAIRN, a significant change in sensitivity (up to a factor of 2) would have been observed over the course of the diel cycle when RH varied, for example, from 50 % at noon to 100 % at night. One might also expect a reduction in inlet transmission for this soluble, sticky trace gas at high relative humidity. As we have reported previously from the IBAIRN campaign (Liebmann et al., 2018), differences in mixing ratios of trace gases measured using the inlet at 8 m (e.g. CI-QMS) and that at 1.5 m (e.g. HR-L-ToF-CIMS) were great, and especially for soluble trace-gases, displayed different diel profiles due to the impact of ground-level fog in the evenings at the lower level. For these reasons, the uncalibrated HR-L-ToF-CIMS signal is used only to support the identification of pyruvic acid at m/z 87.

3.2.2 Other trace gases and meteorological parameters

Measurements of O_3, NO, NO_2, VOCs and meteorological parameters (T, RH, wind speed and direction, photolysis rate coefficients and UVB-radiation) during IBAIRN have recently been described in detail (Liebmann et al., 2018, 2019). Briefly, O_3 was measured by a commercial ozone monitor (2B-Technology, Model 202) based on optical absorption spectroscopy with a LOD of 3 ppbv (10 s) and a total uncertainty of 2 % $\pm$ 1 ppbv. NO was monitored using a chemiluminescence detector (CLD 790 SR, ECO Physics, Dürnten, Switzerland) with a LOD of 5 pptv (60 s) and a measurement uncertainty of 20 %. The NO_2 dataset was provided by a 5-channel, thermal dissociation cavity ring-down spectrometer (TD-CRDS) with a LOD of 60 pptv (60 s) and a total uncertainty of 6 % (Sobanski et al., 2016). CO was measured by a quantum cascade laser (QCL) spectrometer with a total uncertainty of < 20 %. VOC measurements (isoprene and monoterpenes) were performed with a gas chromatograph (Agilent 7890B GC) coupled to an atomic emission detector (JAS AEDIII, Moers, Germany) with an accuracy of 5 % (see supplement of Liebmann et al. (2018)). The GC-AED provides useful information on the contribution of α-pinene, β-pinene, Δ-3-carene, camphene and d-limonene to the sum of monoterpenes. Isoprene and total monoterpenes were additionally measured with a proton transfer reaction time of flight mass spectrometer (PTR-TOF 8000, Ionicon Analytic GmbH) (Jordan et al., 2009; Graus et al., 2010), which was located about 170 m away in dense forest, sampling at a height of 2.5 m above ground. As the PTR-ToF-MS provides a higher temporal resolution than the GC-AED ($\approx$ 1 data point per hour), we used this dataset to investigate potential co-variations of pyruvic acid with isoprene and total monoterpenes, bearing in mind that the mixing ratios of monoterpenes observed at the two locations sometimes differ owing to an inhomogeneous distribution of sources and poor mixing within the canopy (Liebmann et al., 2018).

Temperature and relative humidity were measured at the common inlet as well as on the nearby SMEAR II tower at a height of 8 m above ground. Wind direction

and speed were measured on the SMEAR II tower (8 m) along with Ultraviolet-B radiation (UVB, 280–320 nm, Solar Light SL501A radiometer, 18 m); the data was provided via SMART-Smear (Junninen et al., 2009). Photolysis rate coefficients (J_{NO2}, J_{NO3} and J_{pyr}) were calculated from actinic flux measurements at 35 m height using a spectral radiometer (Metcon GmbH) and evaluated cross sections and quantum yields (Burkholder et al., 2015). OH radical concentrations were calculated from the correlation of ground-level OH-measurements with ultraviolet B radiation intensity (UVB, in units of $W\,m^{-2}$) at the Hyytiälä site (Rohrer and Berresheim, 2006; Petäjä et al., 2009; Hellén et al., 2018). To account for gradients in OH between ground-level and canopy height (Hens et al., 2014), the calculated, ground level OH concentrations (50 % uncertainty) were multiplied by a factor of 2.

3.3 Results and discussion

The IBAIRN campaign was characterised by relatively high day-time temperatures for September and frequent night-time temperature inversions which were accompanied by drastic losses of ozone and an increase in monoterpenes in a very shallow nocturnal boundary layer of ≈ 35 m compared to ≈ 570 m during daytime (Hellén et al., 2018; Liebmann et al., 2018; Zha et al., 2018; Liebmann et al., 2019). The high variability in the boundary layer height over the course of the diel cycle dictated the diel pattern of many of the trace gases. A time series of pyruvic acid mixing ratios together with isoprene, monoterpenes, NO_x, O_3 and meteorological parameters is presented in Fig. 3.1. Pyruvic acid was present at mixing ratios of 17–327 pptv, with a mean value of (96 ± 45) pptv and a median of 97 pptv (based on 1740 data points at 10 min temporal resolution). On several days the pyruvic acid mixing ratios co-vary with those of isoprene and monoterpenes, with night-time maxima resulting from emissions into the very shallow boundary layer, which is especially apparent in the period 9–15 September 2016.

In the following we focus briefly on data from two days (9–10 September, see Fig. 3.2) during which the local wind direction / speed and 48 h back-trajectories (HYSPLIT, Draxler and Rolph (2011)) indicated that the air had occasionally passed over a sawmill to the south-east before reaching the measurement site. As previously observed at this site (Eerdekens et al., 2009; Williams et al., 2011; Hakola et al., 2012) air impacted by the sawmill has greatly elevated monoterpene mixing ratios. In this case > 2 ppbv of monoterpenes were observed on 9 September, 21 UTC and also > 1 ppbv on 10 September, 19 UTC. For the latter event, pyruvic acid and monoterpene mixing ratios were strongly correlated with $R^2 = 0.83$ (Fig. C.2) between 14:00 and 20:00 UTC. Values of $R^2 > 0.75$ were also observed on other days (e.g. 13 September 12–23 UTC and 14 September, 6–20 UTC). We later show that, although isoprene mixing ratios were enhanced (up to ≈ 200 pptv) and co-varied with pyruvic acid as well (e.g. $R^2 = 0.89$ on 10 September, 14–22 UTC, see Fig. C.2, and $R^2 = 0.80$ on 13 September, 12–23 UTC), they were too low to contribute significantly to pyruvic acid formation via

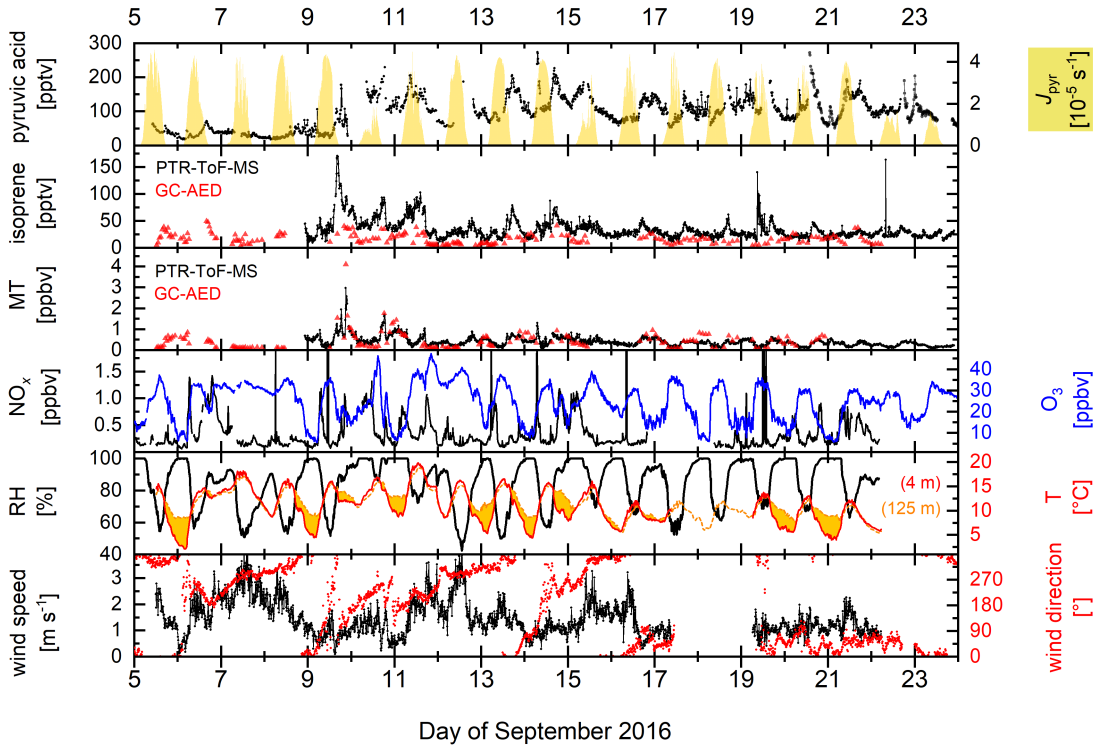

Figure 3.1: Time series of pyruvic acid mixing ratios, photolysis rate (J_{pyr}), isoprene and monoterpenes (PTR-ToF-MS, GC-AED), NO_x (NO_2 + NO), O_3, RH, temperature (at 4 and 125 m, with night-time inversions indicated by the coloured area) and wind speed and direction during the IBAIRN campaign.

reaction with OH or O_3. When considering the whole campaign, the correlation of pyruvic acid with isoprene and monoterpenes was much weaker (see Fig. C.2). Further, no correlation ($R^2 < 0.1$) was found between pyruvic acid mixing ratios and actinic flux, temperature or relative humidity and there was no indication of elevated pyruvic acid mixing ratios in anthropogenically influenced air masses, marked by high levels of NO_x. Below we show that known photochemical sources of pyruvic acid are insufficiently strong to account for the observed mixing ratios.

3.3.1 Sources and sinks of pyruvic acid

Figure 3.3 shows a diel profile of pyruvic acid, isoprene, monoterpenes, O_3, OH and photolysis rate coefficient (J_{pyr}) for the whole IBAIRN campaign. The diel profile of pyruvic acid neither follows the actinic flux (or OH) nor O_3 (markers of photochemical activity), but has features in common with isoprene and total monoterpenes including a rapid increase between 15 and 17 UTC prior to a decrease in mixing ratio towards midnight. The diel patterns observed are mainly determined by the interplay between production/emission rate (dependent on temperature and light), the boundary layer height and chemical and physical loss processes, such as dry deposition. On nights impacted by strong temperature inversions, the

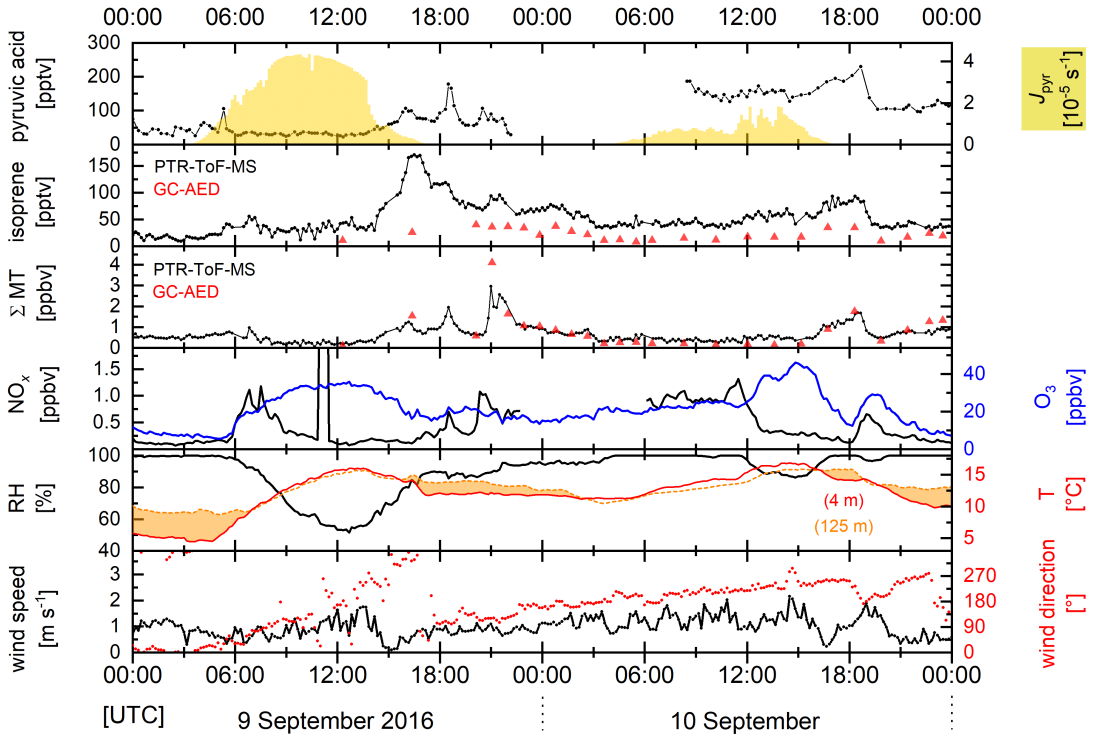

Figure 3.2: Time series of pyruvic acid, photolysis rate (J_{pyr}), isoprene, monoterpenes (MT), NO_x, O_3, RH, temperature and wind speed and direction for 9–10 of September 2016 where the measurements were impacted by emissions from the nearby sawmill (in particular on 9 September, 16–21 UTC and 10 September around 19 UTC).

17:30 UTC peak was more pronounced indicating the important role of boundary layer dynamics. The diel profile of pyruvic acid bears more resemblance to that of isoprene than to that of monoterpenes, which may indicate that the emission rate is sensitive to both temperature and levels of photosynthetically active radiation (PAR). It is also conceivable that pyruvic acid is not only emitted by the same vegetation as isoprene or monoterpenes but that fresh undergrowth and decaying vegetation may play a role. Enclosure experiments would be useful to clarify this.

Combining measurement of the mixing ratios of isoprene, monoterpenes and pyruvic acid with calculated loss rates of each enables rough estimation of the source strength of pyruvic acid relative to that of monoterpenes or isoprene. The rate constant for reaction with of OH with pyruvic acid is slow (Mellouki and Mu, 2003) so that its main chemical sink during the day is photolysis, with a photolysis rate coefficient of $J_{\mathrm{pyr}} \approx 4{\times}10^{-5}$ s^{-1} at solar noon ($\approx$ 10:00 UTC, see Fig. 3.3). The high solubility of pyruvic acid (see above) implies that dry deposition will be an important sink. To assess its impact on pyruvic acid lifetimes we use the day-time deposition velocity for H_2O_2 ($V_{\mathrm{dep}} = (8 \pm 4)$ cm s^{-1}) previously reported for this location (Crowley et al., 2018). The rationale for using the deposition velocity for H_2O_2 as surrogate for pyruvic acid is a similar solubility ($H_{\mathrm{H2O2}} \approx 1 \times 10^5$ Mol atm^{-1}). Using $k_{\mathrm{dep}} = V_{\mathrm{dep}}\, h^{-1}$ and a boundary layer height h of 570 m at

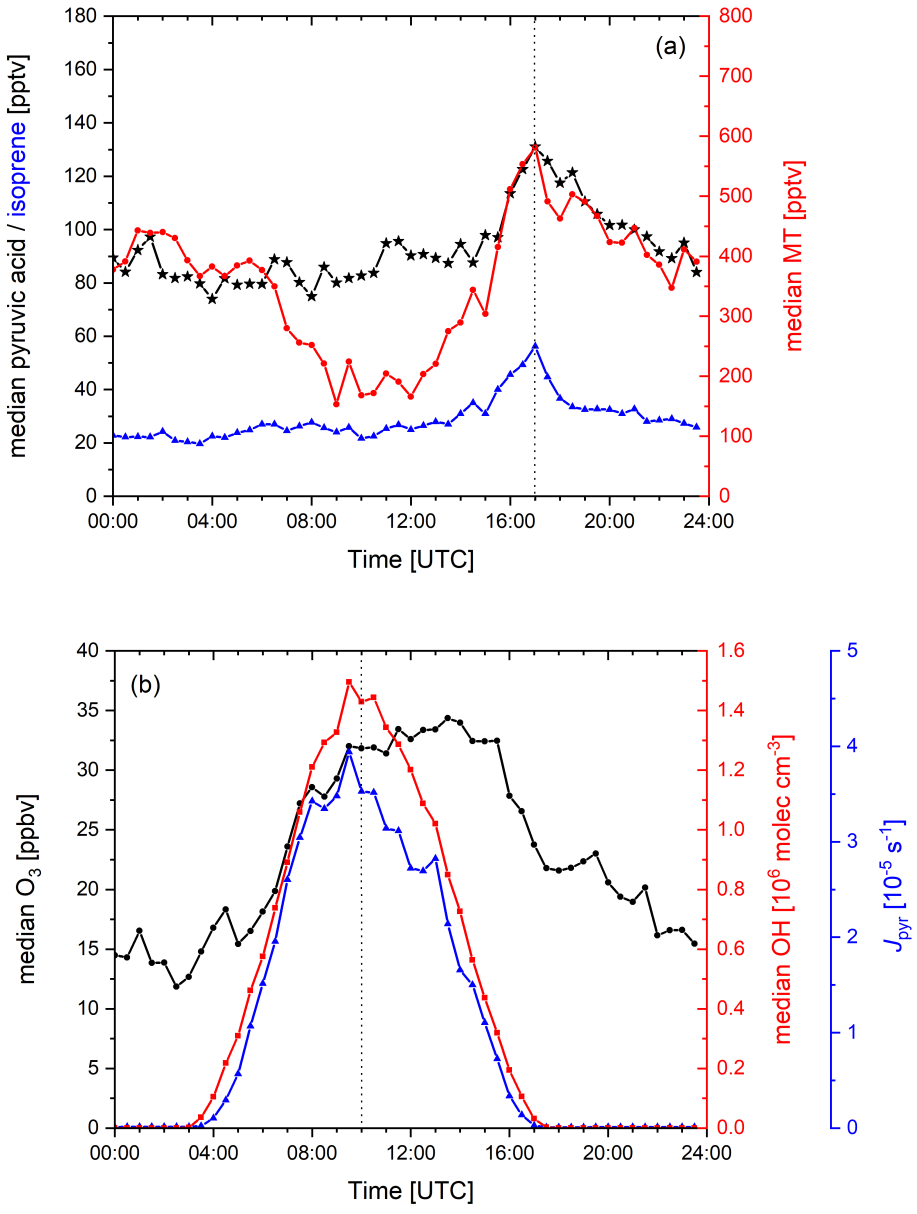

Figure 3.3: Diel profiles of median mixing ratios of (a) pyruvic acid, isoprene and monoterpenes (MT) as well as (b) O_3, calculated OH and photolysis rate coefficient (J_{pyr}, calculated with a quantum yield of 0.2) during the IBAIRN campaign. The dashed vertical line indicates (a) the characteristic maximum in observed pyruvic acid, isoprene and MT mixing ratios and (b) solar noon, respectively.

solar noon (Hellén et al., 2018) results in a loss rate constant for deposition of $k_{\mathrm{dep}} = 1.6 \times 10^{-4}$ s^{-1}. The overall loss rate (photolysis + deposition) of pyruvic acid is then $L_{\mathrm{pyr}} = 2.0 \times 10^{-4}$ s^{-1}, corresponding to a lifetime at solar noon of 1.4 h. We emphasise that the calculated lifetime (and thus the source strength we derive below) are very sensitive to the estimated deposition rate and are thus subject to major uncertainties.

To calculate the lifetime and the emission rates (at 10:00 UTC) of isoprene and monoterpenes, we assumed that reaction with OH (at 1.5×10^6 molecule cm^{-3}, see Fig. 3.3) and O_3 are the main loss processes and that dry deposition is insignificant. For isoprene, we used the rate coefficients evaluated by IUPAC (Atkinson et al., 2006; IUPAC, 2019), for the monoterpenes we used the rate coefficients (also from IUPAC) for α-pinene, which constituted, on average, more than 50 % of the overall monoterpene mixing ratio. This resulted in a loss rate constant for isoprene (L_{isop}) and monoterpenes (L_{MT}) of 1.4×10^{-4} s^{-1} for both trace gases, corresponding to a lifetime of ≈ 2 h.

Assuming steady state (ss) for all three trace gases, the source strength for pyruvic acid (S_{pyr}) relative to the emissions rates of isoprene (E_{isop}) or monoterpenes (E_{MT}) is given by Eq. (3.1) and (3.2) where [pyr], [isop] and [MT] are the measured mixing ratios of pyruvic acid, isoprene and monoterpenes.

$$\frac{S_{\mathrm{pyr}}}{E_{\mathrm{isop}}} = \frac{[\mathrm{pyr}]_{\mathrm{ss}}\, L_{\mathrm{pyr}}}{[\mathrm{isop}]_{\mathrm{ss}}\, L_{\mathrm{isop}}} \tag{3.1}$$

$$\frac{S_{\mathrm{pyr}}}{E_{\mathrm{MT}}} = \frac{[\mathrm{pyr}]_{\mathrm{ss}}\, L_{\mathrm{pyr}}}{[\mathrm{MT}]_{\mathrm{ss}}\, L_{\mathrm{MT}}} \tag{3.2}$$

Taking the diel averaged mixing ratios of pyruvic acid, isoprene and monoterpenes at 10:00 UTC (83, 22 and 168 pptv) and the loss terms calculated above, results in a pyruvic acid source strength relative to isoprene and monoterpenes (based on the PTR-ToF-MS measurements) of 5 and 0.6, respectively (Table 3.1). When using the (low time resolution) GC-AED dataset for isoprene and monoterpenes, these values increase to 10 and 0.9, respectively.

In steady-state, using $S_{\mathrm{pyr}} = [\mathrm{pyr}]_{\mathrm{ss}}\, L_{\mathrm{pyr}}$, the pyruvic acid source strength needed to account for the observed 10:00 UTC mixing ratios of ≈ 80 pptv is $S_{\mathrm{pyr}} = 60$ pptv h^{-1} (or 12 pptv h^{-1} when neglecting dry deposition, see Table 3.1). These values can be compared with the production rate of pyruvic acid from the photochemical oxidation of isoprene, which we calculate to be 0.02 pptv h^{-1}, orders of magnitude too small to explain the pyruvic acid mixing ratios observed. The basis for this calculation were measured isoprene and O_3 mixing ratios and the results from chamber experiments (Grosjean et al., 1993; Paulot et al., 2009) that report a pyruvic acid yield from isoprene oxidation of ≈ 2 %. Pyruvic acid is also a product of the ozonolysis of methyl vinyl ketone (MVK), with a yield of ≈ 5 % (Grosjean et al., 1993). In order to explain the observed pyruvic acid mixing ratios by the production rate from MVK alone would require 16 ppbv of MVK, which is a factor

Table 3.1: Calculated source strength of pyruvic acid (S_{pyr}), production rate from isoprene + O_3 ($S_{\mathrm{pyr\ (isop+O3)}}$) and emission rates of isoprene (E_{isop}) and monoterpenes (E_{MT}) at solar noon.

Source strength / emission rate [pptv h^{-1}]	$J_{\mathrm{pyr}} = 4 \times 10^{-5}$ s^{-1} $k_{\mathrm{dep}} = 16 \times 10^{-5}$ s^{-1}	$J_{\mathrm{pyr}} = 4 \times 10^{-5}$ s^{-1} $k_{\mathrm{dep}} = 0$
S_{pyr}	60	12
$S_{\mathrm{pyr\ (isop+O3)}}$	0.02	
	PTR-ToF-MS	GC-AED
E_{isop}	12	6
E_{MT}	94	65

Notes: S_{pyr} is the net source strength (emission rate + production rate) of pyruvic acid based on measured mixing ratios at solar noon, the assumption of steady-state and that photolysis (J_{pyr}) and deposition (k_{dep}) are the only significant loss processes. The net source strength is derived for two different values of k_{dep} as discussed in the text. $P_{\mathrm{pyr\ (isop+O3)}}$ is the rate of photochemical production of pyruvic acid from isoprene oxidation. The net isoprene and net monoterpene emission rates (E_{isop} and E_{MT}) were calculated using their mixing ratios and considering the reactions with OH and O_3 as the only relevant loss terms. Emission rates are shown for both VOC datasets (PTR-ToF-MS and GC-AED).

≈ 60 more than observed at this site during September (Hakola et al., 2003) and clearly not feasible.

As the degradation of monoterpenes is not expected to generate pyruvic acid (Vereecken et al., 2007; IUPAC, 2019), we conclude that, in the boreal forest around Hyytiälä, the main source of pyruvic acid is direct emission from the biosphere and not photochemical production via reactions of OH or O_3. This is consistent with the measurements of (Jardine et al., 2010) who report high mixing ratios of pyruvic acid resulting from direct emission in an O_3 and OH-free environment. Measurements in different seasons and enclosure experiments would be useful to validate these conclusions.

3.3.2 Role of pyruvic acid in the troposphere

In this section, we assess the potential role of pyruvic acid as source of radicals and other reactive trace gases in the boreal forest. Figure 3.4 provides an overview of the sources and sinks of pyruvic acid. The dominant photochemical loss process of pyruvic acid is its photolysis. Experimental data on its UV-cross-sections and photodissociation quantum yields have recently been evaluated by the IUPAC panel (IUPAC, 2019). The thermodynamically accessible dissociation pathways are listed below (R 3.1–3.3).

$$\mathrm{CH_3C(O)C(O)OH} + h\nu \longrightarrow \mathrm{CH_3CHO} + \mathrm{CO_2} \quad \text{(R 3.1)}$$

$$\longrightarrow \mathrm{CH_3CO} + \mathrm{HOCO} \quad \text{(R 3.2)}$$

$$\longrightarrow \mathrm{CH_3C(O)OH} + \mathrm{CO} \quad \text{(R 3.3)}$$

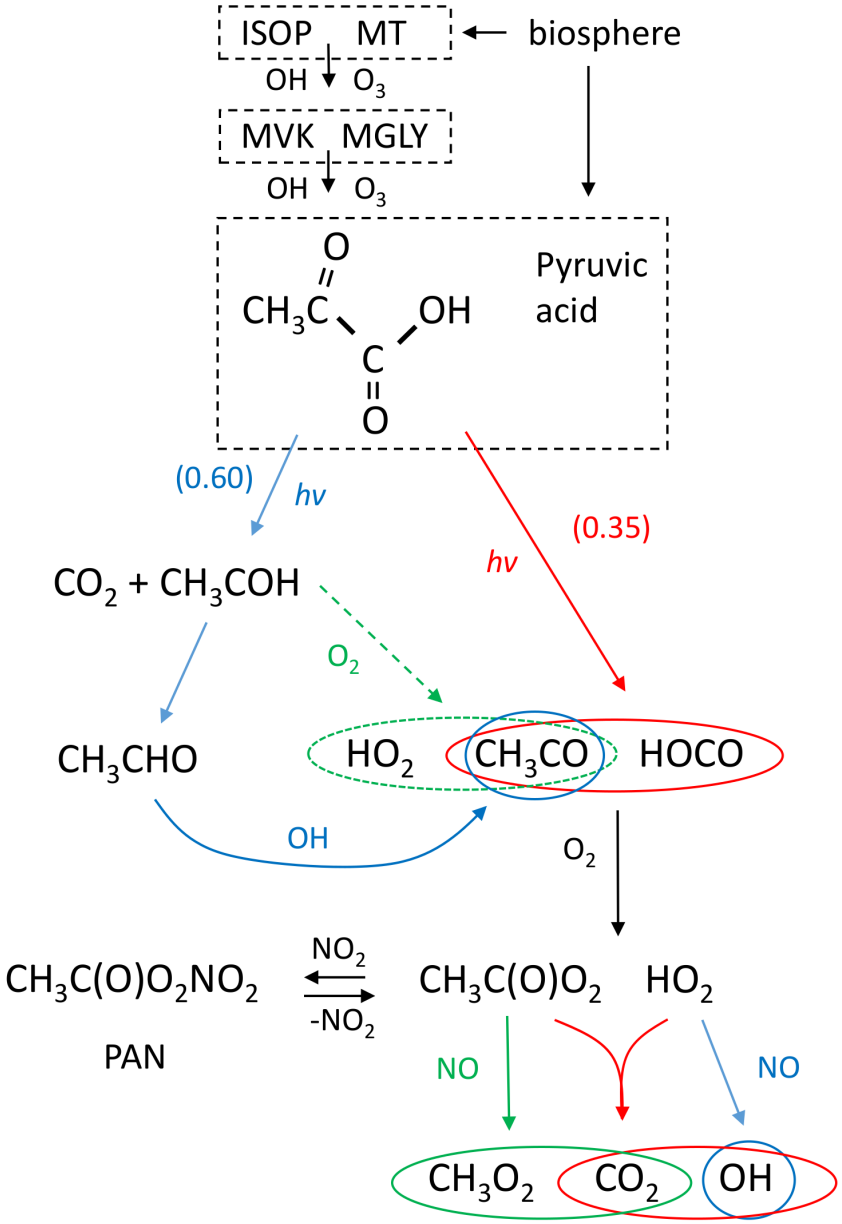

Figure 3.4: Sources of pyruvic acid and mechanism of formation of CH_3CHO, HO_2 and $CH_3C(O)O_2$ during its photolysis. ISOP = isoprene, MT = monoterpenes, MVK = methyl vinyl ketone, MGLY = methylglyoxal. Numbers in parentheses indicate branching ratios. CH_3COH is the methyl-hydroxycarbene that is believed to mainly rearrange to form CH_3CHO.

Table 3.2: Calculated production rates of acetaldehyde (CH_3CHO), HO_2 and $CH_3C(O)O_2$ from the photolysis of pyruvic acid at solar noon.

CH_3CHO production rate [pptv h^{-1}]	$J_{pyr} = 4 \times 10^{-5}$ s^{-1}	$J_{pyr} = 16 \times 10^{-5}$ s^{-1}
Pyruvic acid + $h\nu$	6.3	25.2
OH + ethane	0.6	0.6
OH + propane	0.3	0.3
OH + n-butane	1.3	1.3
HO_2 production rate [pptv h^{-1}]		
Pyruvic acid + $h\nu$	4	16
OH + O_3	12	12
OH + CO	100	100
$CH_3C(O)O_2$ production rate [pptv h^{-1}]		
Pyruvic acid + $h\nu$	4	16
CH_3CHO + $h\nu$	5	5

Notes: The production rates of CH_3CHO, HO_2 and $CH_3C(O)O_2$ from pyruvic acid photolysis are derived for two different values of J_{pyr} using quantum yields of 0.2 and 0.8 (see text). The production rates of CH_3CHO formation from alkanes are based on estimated mixing ratios (see text). The production rate of HO_2 from the reaction of OH with O_3 and CO is based on calculated OH and measurements of O_3 and CO during IBAIRN. The production rate of $CH_3C(O)O_2$ from CH_3CHO was calculated using a mixing ratio of 100 pptv of acetaldehyde.

Photolysis of pyruvic acid in the actinic region ($\lambda > 310$ nm) results mainly in the formation of acetaldehyde CH_3CHO + CO_2 (R 3.1) with a yield of 60 %. The second most important channel (R 3.2, with a yield of 35 %) leads to formation of organic radical fragments which react with O_2 to form the peroxy radicals $CH_3C(O)O_2$ and HO_2 (Reactions R 3.4 and R 3.5).

$$CH_3CO + O_2 + M \longrightarrow CH_3C(O)O_2 + M \quad \text{(R 3.4)}$$

$$HOCO + O_2 \longrightarrow HO_2 + CO_2 \quad \text{(R 3.5)}$$

Acetaldehyde (formed in Reaction R 3.1) is an air pollutant which plays an important role in tropospheric chemistry as a source of PAN (Roberts, 1990), PAA (Phillips et al., 2013; Crowley et al., 2018), HO_x radicals (Singh et al., 1995) and ultimately, via methyl peroxy radical oxidation, HCHO (Lightfoot et al., 1992). Based on campaign-median pyruvic acid mixing ratios and photolysis rates measured during IBAIRN (see Fig. 3.3), we calculate an acetaldehyde production rate of $P_{CH3CHO} = 0.6\, J_{pyr}\ [pyr] = 6.3$ pptv h^{-1} at local noon (Table 3.2, Fig. C.3).

On a global scale the main source of acetaldehyde is OH-initiated photochemical production from alkanes, alkenes, ethanol and isoprene with alkanes accounting for about one half of the total production of 128 Tg a^{-1} (Millet et al., 2010). Minor sources are direct biogenic emissions (23 Tg a^{-1}), anthropogenic emissions (2 Tg a^{-1}) and biomass burning (3 Tg a^{-1}). As alkanes were not measured during IBAIRN we estimate the mixing ratios of the three most abundant alkanes (ethane, propane and n-butane) from monthly averages measured at Pallas and Utö (both

Finland) for the years 1994-2003 (Hakola et al., 2006), which are consistent with measurements at Pallas in 2012 reported by Hellén et al. (2015). Combining mean (September) mixing ratios of 1000 pptv of ethane, 250 pptv of propane and 150 pptv of n-butane with OH rate coefficients of $k_{\mathrm{OH+ethane}} = 2.4 \times 10^{-13}$ cm^3 molecule^{-1} s^{-1}, $k_{\mathrm{OH+propane}} = 1.1 \times 10^{-12}$ cm^3 molecule^{-1} s^{-1} and $k_{\mathrm{OH+n\text{-}butane}} = 2.35 \times 10^{-12}$ cm^3 molecule^{-1} s^{-1} at 298 K (IUPAC, 2019) and acetaldehyde yields (at 0.1 ppbv of NO_x) of 0.50, 0.24 and 0.69 (Millet et al., 2010), results in a total CH_3CHO production rate from OH + alkanes of 2.2 pptv h^{-1} at local noon (Table 3.2). From these calculations we conclude that emission and subsequent photolysis of pyruvic acid is likely an important source of CH_3CHO in this environment and may impact our current understanding of the acetaldehyde budget (Millet et al., 2010) in forested regions in general.

The dominant sink of CH_3CHO is the reaction with OH (R 3.6) with a rate constant of 1.5×10^{-11} cm^3 molecule^{-1} s^{-1} (IUPAC, 2019) to form the CH_3CO radical. This then reacts in air (R 3.4) to form $CH_3C(O)O_2$, which is the precursor of PAN ($CH_3C(O)O_2NO_2$, R 3.7), peracetic acid ($CH_3C(O)OOH$, R 3.8), acetic acid ($CH_3C(O)OH$, R 3.9) and CH_3O_2 (R 3.10 and R 3.11), and which can recycle OH (R 3.10).

$$\mathrm{OH + CH_3CHO + O_2 \longrightarrow CH_3C(O)O_2 + H_2O} \quad \text{(R 3.6)}$$

$$\mathrm{CH_3C(O)O_2 + NO_2 + M \longrightarrow CH_3C(O)O_2NO_2 + M} \quad \text{(R 3.7)}$$

$$\mathrm{CH_3C(O)O_2 + HO_2 \longrightarrow CH_3C(O)OOH + O_2} \quad \text{(R 3.8)}$$

$$\mathrm{\longrightarrow CH_3C(O)OH + O_3} \quad \text{(R 3.9)}$$

$$\mathrm{\longrightarrow OH + CH_3O_2 + CO_2} \quad \text{(R 3.10)}$$

$$\mathrm{CH_3C(O)O_2 + NO + O_2 \longrightarrow CH_3O_2 + CO_2 + NO_2} \quad \text{(R 3.11)}$$

The second most important photolysis channel for pyruvic acid is Reaction (R 3.2), which leads to formation of HO_2 and $CH_3C(O)O_2$. These radicals play a crucial role in photochemical ozone production (Fishman and Crutzen, 1978), in the recycling of OH (in the presence and absence of NO_x) and, as described above, in PAN formation.

The production rate (10:00 UTC) of HO_2 and $CH_3C(O)O_2$ from pyruvic acid photolysis is given by $P_{\mathrm{HO2}} = P_{\mathrm{CH3CO3}} = 0.35 J_{\mathrm{pyr}} \times$ [pyr] and is equal to 4 pptv h^{-1}. This value is roughly equivalent to the production rate of $CH_3C(O)O_2$ from the OH-initiated acetaldehyde oxidation (the major source of this radical) assuming typical values of 100 pptv CH_3CHO and 1.5×10^6 OH molecules cm^{-3} and using $k_{\mathrm{OH+CH3CHO}} = 1.5 \times 10^{-11}$ cm^3 molecule^{-1} s^{-1} (IUPAC, 2019). We therefore conclude that pyruvic acid photolysis in this environment is an important source of the $CH_3C(O)O_2$ radical both directly (R 3.2 and R 3.4) and via acetaldehyde formation (R 3.1 and R 3.6).

Taking median O_3 and CO mixing ratios (at 10:00 UTC) found in IBAIRN, we can easily show that the rate of HO_2 formation (4 pptv h^{-1}) from pyruvic acid photolysis (reactions R 3.2 and R 3.5) is minor compared to that from OH + O_3 of 12 pptv h^{-1} (with $k_{\mathrm{OH+O3}} = 7.3 \times 10^{-14}$ cm^3 molecule^{-1} s^{-1}) and OH + CO of

100 pptv h^{-1} (with $k_{OH+CO} = 2.1 \times 10^{-13}$ cm^3 $molecule^{-1}$ s^{-1}) (IUPAC, 2019). It is also negligible compared to the total HO_2 production rate of 100–600 pptv h^{-1} previously derived in this environment (albeit in summer) via measurement of HO_x (Hens et al., 2014).

So far, to calculate the photo-dissociation rate constant for pyruvic acid (J_{pyr}) we have used the IUPAC recommendation of an overall quantum yield of 0.2 at atmospheric pressure. There are however several inconsistencies in the experimental data sets on pyruvic acid photolysis, with two groups reporting quantum yields that are a factor of ≈ 4 larger at this pressure (Berges and Warneck, 1992; Reed Harris et al., 2017). If these large quantum yields were to be correct, the calculated production rates of CH_3CHO and $CH_3C(O)O_2$ would increase by a factor of 4 (see Table 3.2) so that $P_{CH3CHO} = 28$ pptv h^{-1} (Table 3.2). Moreover, Reed Harris et al. (2017) report much lower yields of CH_3CHO, and suggest that other processes may compete with rearrangement of the methyl-hydroxycarbene (CH_3COH) necessary to form acetaldehyde. They propose that in air, initially formed methyl-hydroxycarbene may react with O_2 to form CH_3CO and HO_2. If this is correct, the intermediate step (R 3.6) in which OH reacts with acetaldehyde to form $CH_3C(O)O_2$ in air, is bypassed, so that pyruvic acid photolysis would be an even more important source of PAN. This alternative fate of the methyl-hydroxycarbene radical is depicted with the dashed line in Fig. 3.4.

3.4 Conclusions

Mixing ratios of pyruvic acid of 17–327 pptv (mean of (96 ± 45) pptv) were measured in the boreal forest in Hyytiälä, southern Finland, during a field study in late summer (September 2016). Campaign averaged, diel profiles of pyruvic acid displayed similar features to those of monoterpenes and isoprene. Combining the mixing ratios of pyruvic acid with its loss terms enabled calculation of the source strength at solar noon of ≈ 60 pptv h^{-1}. There appears to be no known photochemical mechanism to generate pyruvic acid at this rate and we suggest that pyruvic acid is, to a large extent, emitted directly from the biosphere. We show that pyruvic acid, at the mixing ratios observed in September, represents an important source of acetaldehyde and the acetyl peroxy radical, thus enhancing the formation of PAN, C_2-organic acids and CH_3O_2.

We conclude that, during late summer / autumn, pyruvic acid is an important biogenic VOC in the boreal forest which has previously received little attention. Further field and enclosure studies are necessary to quantify its emissions and role during other seasons and to better understand its sources and sinks (e.g. generation in OH / O_3 / NO_3 initiated oxidation of terpenes and dry deposition rates) in the boreal forest as well as in other environments. In addition, further laboratory studies are required to resolve discrepancies in the literature data on the pressure (and wavelength) dependence of both the overall photolysis quantum yield and the product distribution during pyruvic acid photolysis.

Author contributions

Philipp Eger performed the CI-QMS measurements of pyruvic acid during IBAIRN, analysed the data and, with contributions from John Crowley and Jos Lelieveld, wrote the manuscript. Nicolas Sobanski was responsible for the CRDS measurements of NO_2. Jan Schuladen was responsible for the O_3 and photolysis rate coefficient measurements. Horst Fischer was responsible for the NO and CO measurements. Matthieu Riva and Qiaozhi Zha were responsible for the HR-L-ToF-CIMS measurements of pyruvic acid. Einar Karu and Jonathan Williams provided the GC-AED measurements of isoprene and individual monoterpenes. Lauriane Quéléver and Simon Schallhart contributed the PTR-ToF-MS measurements of isoprene and monoterpenes. The IBAIRN campaign was conceived and organised by John Crowley and Michael Ehn. All authors contributed to the manuscript.

Acknowledgements

We would like to thank Uwe Parchatka for the provision of NO measurements and Janne Levula and the team at Hyytiälä for the excellent technical support.

Chapter 4

Shipborne measurements of $ClNO_2$ in the Mediterranean Sea and around the Arabian Peninsula during summer

Philipp G. Eger[1], Nils Friedrich[1], Jan Schuladen[1], Justin Shenolikar[1], Horst Fischer[1], Ivan Tadic[1], Hartwig Harder[1], Monica Martinez[1], Roland Rohloff[1], Sebastian Tauer[1], Frank Drewnick[2], Friederike Fachinger[2], James Brooks[3], Eoghan Darbyshire[3], Jean Sciare[4], Michael Pikridas[4], Jos Lelieveld[1], and John N. Crowley[1]

[1]Atmospheric Chemistry Department, Max-Planck-Institute for Chemistry, 55128 Mainz, Germany

[2]Particle Chemistry Department, Max-Planck-Institute for Chemistry, 55128 Mainz, Germany

[3]Centre for Atmospheric Science, University of Manchester, UK

[4]Energy, Environment and Water Research Center, The Cyprus Institute, Nicosia 1645, Cyprus

This chapter is based on the manuscript "Shipborne measurements of $ClNO_2$ in the Mediterranean Sea and around the Arabian Peninsula during summer" published in Atmospheric Chemistry and Physics Discussions (ACPD) as Eger et al. (2019b) and accepted for final publication in ACP. Here results from the AQABA ship campaign are presented with a focus on $ClNO_2$ production efficiency and its impact on radical chemistry.

Summary

Shipborne measurements of nitryl chloride ($ClNO_2$), hydrogen chloride (HCl) and sulphur dioxide (SO_2) were made during the AQABA (Air Quality and climate change in the Arabian BAsin) ship campaign in summer 2017. The dataset includes measurements over the Mediterranean Sea, the Suez Canal, the Red Sea, the Gulf of Aden, the Arabian Sea, the Gulf of Oman and the Arabian Gulf (also known as Persian Gulf) with observed $ClNO_2$ mixing ratios ranging from the limit of detection to ≈ 600 pptv. We examined the regional variability in the generation of $ClNO_2$ via the uptake of dinitrogen pentoxide (N_2O_5) to Cl-containing aerosol and its importance for Cl-atom generation in a marine boundary layer under the (variable) influence of emissions from shipping and oil industry. The yield of $ClNO_2$ formation per NO_3 radical generated was generally low (median of ≈ 1–$5\,\%$ depending on the region), mainly as a result of gas-phase loss of NO_3 dominating over heterogeneous loss of N_2O_5, the latter being disfavoured by the high temperatures found throughout the campaign. The contributions of $ClNO_2$

photolysis and OH-induced HCl oxidation to Cl-radical formation were derived and their relative contributions over the diel cycle compared. The results indicate that over the northern Red Sea, the Gulf of Suez and the Gulf of Oman the formation of Cl-atoms will enhance the oxidation rates of some VOCs, especially in the early morning.

4.1 Introduction

The AQABA (Air Quality and climate change in the Arabian BAsin) campaign was designed to study air quality and climate in a region (Eastern Mediterranean and Middle East) that is likely to be heavily impacted by future climate change with increasing frequency and intensity of droughts, heatwaves and associated Aeolian dust and pollution emissions (Lelieveld et al., 2012). As the Arabian Gulf already suffers from some of the most polluted air on Earth with O_3 levels regularly greater than 100 ppbv (Lelieveld et al., 2009), one aspect of the campaign was to investigate the factors that contribute to high levels of air pollution in the region. This includes the impact of reactive chlorine chemistry resulting from the interactions of pollutant emissions from ships and petrochemical activity with sea-salt, under conditions influenced by intense photochemistry and high temperatures during summer.

The heterogeneous uptake of gaseous N_2O_5 to the aerosol phase represents an important atmospheric sink for NO_x ($NO + NO_2$) via conversion to nitric acid (HNO_3), which is efficiently removed from the boundary layer via deposition (Lelieveld and Crutzen, 1990; Dentener and Crutzen, 1993; Macintyre and Evans, 2010). In the presence of aerosol chloride, nitryl chloride ($ClNO_2$) can also be formed along with HNO_3 (NO_3^-) as shown in Reaction (R 4.1) (Finlayson-Pitts et al., 1989; Behnke et al., 1997).

$$N_2O_5 + (H_2O \text{ or } Cl^-) \longrightarrow (2\text{-}f) \times {NO_3}^- + f \times ClNO_2 \quad (0 \leq f \leq 1) \quad \text{(R 4.1)}$$

$$ClNO_2 + h\nu \longrightarrow Cl + NO_2 \quad \text{(R 4.2)}$$

$ClNO_2$ has a lifetime of more than 30 hours in the nocturnal marine boundary layer (Osthoff et al., 2008) but is rapidly photolysed after sunrise (Reaction R 4.2), releasing nitrogen dioxide (NO_2) and chlorine atoms.

The formation of $ClNO_2$ can have a significant impact on regional NO_x cycling and radical chemistry especially in the polluted coastal and marine boundary layer (Simon et al., 2009; Riedel et al., 2014; Sarwar et al., 2014). The Cl-atoms formed in Reaction (R 4.2) can enhance oxidation rates of several volatile organic compounds (VOCs) especially during early morning hours (Phillips et al., 2012; Riedel et al., 2012a; Young et al., 2012) thus contributing to photochemical ozone production (Simon et al., 2009; Riedel et al., 2014; Sarwar et al., 2014; Faxon et al., 2015; Wang et al., 2019).

The chemical processes involved in the formation of $ClNO_2$ are complex and, as outlined in Fig. 4.1, involve the sequential oxidation of NO_x to N_2O_5 via NO_3 (Reactions R 4.3–4.5). During the day NO_3 is rapidly photolysed via Reaction

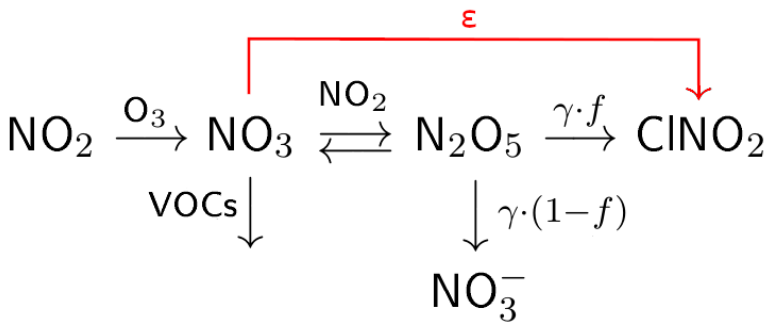

Figure 4.1: Simplified scheme of chemical reactions and parameters involved in the formation of $ClNO_2$. The $ClNO_2$ production efficiency per NO_3 formed is denoted as ϵ. The uptake coefficient to the particle phase is represented by γ and the $ClNO_2$ yield (per N_2O_5 taken up) by f.

(R 4.6 and R 4.7) or reacts with nitrogen oxide (NO) via Reaction (R 4.8) so that N_2O_5 formation is supressed. The heterogeneous reaction of N_2O_5 with particles is thus, to a good approximation, limited to the night-time. The equilibrium between NO_3 and N_2O_5 (Reactions R 4.4 and R 4.5) is strongly temperature-dependent, with N_2O_5 formation favoured by high NO_2 mixing ratios and low temperatures. NO_3 can also react with volatile organic compounds (VOCs) (R 4.9) forming e.g. alkyl nitrates, which also reduces the rate of formation of N_2O_5.

$$NO_2 + O_3 \longrightarrow NO_3 + O_2 \quad \text{(R 4.3)}$$
$$NO_3 + NO_2 \longrightarrow N_2O_5 \quad \text{(R 4.4)}$$
$$N_2O_5 + M \longrightarrow NO_3 + NO_2 + M \quad \text{(R 4.5)}$$
$$NO_3 + h\nu \longrightarrow NO + O_2 \quad \text{(R 4.6)}$$
$$NO_3 + h\nu \longrightarrow NO_2 + O \quad \text{(R 4.7)}$$
$$NO_3 + NO \longrightarrow 2\,NO_2 \quad \text{(R 4.8)}$$
$$NO_3 + VOCs \longrightarrow products \quad \text{(R 4.9)}$$

The N_2O_5 loss rate via heterogeneous uptake to particles is described by Eq. (4.1) where $\bar{c}$ is the average molecular velocity of N_2O_5, A is the particle surface area concentration and γ is the uptake coefficient.

$$\frac{d[N_2O_5]}{dt} = -\frac{\gamma \bar{c} A}{4}\,[N_2O_5] \quad (4.1)$$

The uptake coefficient, γ, has been characterised in several laboratory investigations (see Bertram and Thornton (2009); Chang et al. (2011); Ammann et al. (2013) for summaries) and in numerous field studies where it has been found to be highly variable (between 5×10^{-4} and 0.11) and dependent on temperature, relative humidity (RH) and aerosol composition (Brown et al., 2006; Bertram et al., 2009; Brown et al., 2009; Riedel et al., 2012b; Wagner et al., 2013; Morgan et al., 2015; Brown et al., 2016; Phillips et al., 2016). A value of $\gamma \approx 0.03$ has been

derived from measurements in the polluted marine environment (Aldener et al., 2006).

The $ClNO_2$ yield, f, which controls the relative formation rates of NO_3^- and $ClNO_2$ in Reaction (R 4.1), is determined by the $[Cl^-]$ to $[H_2O]$ ratio in the aerosol phase (Behnke et al., 1997; Bertram and Thornton, 2009; Ammann et al., 2013), and can vary between zero to unity (Thornton et al., 2010; Wagner et al., 2012; Riedel et al., 2013; Phillips et al., 2016; Wang et al., 2016; McDuffie et al., 2018a). In Fig. 4.1 we introduce the $ClNO_2$ production efficiency ϵ, which is the yield of $ClNO_2$ per NO_3 molecule formed in Reaction (R 4.3) and will be discussed in detail in Sect. 4.3.2.

The established method to measure atmospheric $ClNO_2$ mixing ratios from a few tens of pptv (part per trillion by volume) to several ppbv (parts per billion by volume) is Chemical Ionisation Mass Spectrometry (CIMS) using iodide ions to generate $I{\cdot}ClNO_2^-$ which can be detected at a mass-to-charge ratio (m/z) of 208 and 210 (McNeill et al., 2006). The first measurement highlighting the importance of $ClNO_2$ in the polluted marine boundary layer was performed by Osthoff et al. (2008) who detected mixing ratios exceeding 1 ppbv along the coast of Houston, Texas, originating from ship-plumes and urban and industrial NO_x sources. This was the starting point for numerous measurements of $ClNO_2$ in various locations around the globe with an initial focus on coastal areas in the United States (U.S.), e.g. the Los Angeles Basin in California (Riedel et al., 2012a; Wagner et al., 2012; Young et al., 2012). Other studies included coastal sites in Canada (Osthoff et al., 2018) and coastal / urban sites in the United Kingdom (Bannan et al., 2015, 2017; Priestley et al., 2018; Sommariva et al., 2018). Whereas $ClNO_2$ was initially believed to play a significant role only in areas with marine influence (Behnke et al., 1997; Keene et al., 1999), mid-continental measurements in the U.S. (Thornton et al., 2010; Riedel et al., 2013; Faxon et al., 2015) revealed the importance of anthropogenic sources (e.g. industrial combustion, cooling towers, natural gas extraction and suspension of road salt) and sea salt chloride transported inland. Further studies reported significant mixing ratios of $ClNO_2$ at a semi-rural site in continental Germany (Phillips et al., 2012, 2016) and at a mid-continental urban site in Canada (Mielke et al., 2011, 2016). Observations at continental sites could be reproduced by a global model (Wang et al., 2019) when considering the transport of HCl (aq) which had been initially formed in the gas-phase through acid displacement in coastal regions. More recently, $ClNO_2$ at the >1 ppbv level has been observed in the heavily industrialised North China Plain (Tham et al., 2016; Liu et al., 2017; Wang et al., 2017a; Tham et al., 2018), with even larger mixing ratios measured in Beijing (Le Breton et al., 2018; Zhou et al., 2018) and Hong Kong (Wang et al., 2016).

The great variability seen in $ClNO_2$ mixing ratios in different locations reflects regional variability in its efficiency of production, which, as described above involves a complex set of chemical reactions, both in the gas- and particle phase and which will vary over time and space. Most measurements of $ClNO_2$ to date have been measurements at single locations, though some data from mobile platforms

such as aircraft (Mielke et al., 2013; Lee et al., 2018; McDuffie et al., 2018a,b) and ships (Kercher et al., 2009; Riedel et al., 2012a) are available. With respect to understanding the formation and role of $ClNO_2$, much of the atmospheric boundary layer remains unexplored.

Here we present shipborne measurements of $ClNO_2$ in the marine boundary layer of the Mediterranean Sea and around the Arabian Peninsula, including the Red Sea and the Arabian Gulf. With a ship track from southern France to Kuwait we provide a unique marine $ClNO_2$ dataset with a large spatial coverage. This allows us to investigate the $ClNO_2$ production efficiency ϵ and its regional impact under various atmospheric conditions ranging from polluted marine and coastal environment to low-NO_x conditions in chemically aged air masses.

4.2 Methods

4.2.1 AQABA campaign

The measurements presented in this study were performed during the AQABA campaign which took place along the sea route between southern France and Kuwait in summer 2017. Five air-conditioned measurement containers with a variety of gas-phase and aerosol instrumentation were set up on-board the research vessel *Kommander Iona* which departed from Southern France on 24 June 2017 and passed various regions including the Mediterranean Sea, the Suez Canal, the Red Sea, the Gulf of Aden, the Arabian Sea, the Gulf of Oman and the Arabian Gulf (see Fig. 4.2), reaching its destination Kuwait on 31 July 2017 (first leg) and covering a latitude / longitude span of 12–43 °N and 6–60 °E. After a short break in Kuwait the ship returned via the same route to southern France, arriving on 2 September 2017 (second leg). The trace-gases described in this paper were sampled from the centre of a common, high volume-flow inlet ($10\,m^3\,min^{-1}$, 0.15 m in diameter, 0.2 s residence time) made of stainless steel, which was located on a measurement container at the front of the ship at a height of approximately 5.5 m above the foredeck.

Depending on the wind direction relative to the movement of the vessel, measurements were occasionally impacted by emissions from the stack of our own ship. Especially on the first leg, the relative wind direction was frequently from behind where the chimney was located. All datasets were filtered prior to analysis for periods where the measurements were contaminated by stack emissions to avoid a potential bias in the results. The filter is based on short-term variation in NO and SO_2 signals and relative wind direction and reduces the useful data coverage to 58 % on the first leg and 95 % on the second leg.

4.2.2 Measurement of $ClNO_2$, HCl and SO_2

Nitryl chloride ($ClNO_2$), hydrogen chloride (HCl) and sulphur dioxide (SO_2) were detected with a Chemical Ionisation Quadrupole Mass Spectrometer (CI-QMS) using an electrical, radio-frequency (RF) discharge ion-source. The instrument and

the ion-molecule-reactions involved in the detection of the above-mentioned trace gases are described in detail by Eger et al. (2019a). Briefly, $ClNO_2$ was monitored as $I{\cdot}ClNO_2^-$ at a mass-to-charge ratio (m/z) of 208 and 210 subsequent to the reaction of $ClNO_2$ with I^- (McNeill et al., 2006; Osthoff et al., 2008; Thornton et al., 2010). $I{\cdot}ClNO_2^-$ is more specific than ICl^- (m/z 162 and 164) and has a lower background signal, providing a sensitivity of $0.61\,\mathrm{Hz\,pptv^{-1}}$ per 10^6 Hz of I^- at m/z 208 (and $0.20\,\mathrm{Hz\,pptv^{-1}}$ at m/z 210), a limit of detection (LOD) (2σ, 5 min) of 12 pptv and a total measurement uncertainty of $30\,\% \pm 6$ pptv. We chose the signal at m/z 208 for its higher signal-to-noise (S/N) ratio to calculate the $ClNO_2$ mixing ratios reported. For the whole campaign dataset, the ratio between m/z 208 and 210 was 3.08 (with $R^2 = 0.96$, see Fig. D.1a), which is very close to the expected value of 3.13 derived from the natural abundance of the ^{35}Cl and ^{37}Cl isotopes. In addition, correlation plots from different regions (Fig. D.1b–f) indicate the absence of significant interferences at either of the two m/z.

HCl was observed as $I(CN)Cl^-$ (m/z 188 and 190) (Eger et al., 2019a) with a sensitivity of $0.17\,\mathrm{Hz\,pptv^{-1}}$ per 10^6 Hz of I^- at m/z 188 (and $0.05\,\mathrm{Hz\,pptv^{-1}}$ at m/z 190), a detection limit of 98 pptv and a total measurement uncertainty of $20\,\% \pm 72$ pptv. As m/z 190 suffers from known interferences (e.g. $I{\cdot}HNO_3^-$) and has a lower S/N ratio, we used m/z 188 to calculate the HCl mixing ratios reported. SO_2 was detected as ISO_3^- (m/z 207) with a sensitivity of $0.10\,\mathrm{Hz\,pptv^{-1}}$ per 10^6 Hz of I^-, a detection limit of 38 pptv and a total uncertainty of $20\,\% \pm 23$ pptv.

A flow of 2.5 slm (standard litres per minute) was drawn into the CI-QMS instrument via a ≈ 3 m long 6.35 mm (OD) PFA tubing while a 20 cm section of the inlet line in front of the IMR (ion molecule reactor) was heated to 200 °C to enable detection of peroxyacetyl nitrate (PAN) which is not reported here. The IMR region was held at a pressure of (18.00 ± 0.05) mbar by a dry vacuum scroll pump. The background signal was determined by periodically bypassing ambient air through a scrubber filled with steel wool where the trace gases of interest are efficiently destroyed at the hot surfaces (120 °C). To avoid condensation of water in the inlet lines in the containers, the pressure in the sampling line was reduced to $\approx$ 700–800 mbar with a bypass flow of ≈ 5 slm and by including an additional ≈ 50 cm long (coiled) piece of 3.18 mm (OD) PFA tubing. A 2 μm pore size membrane filter (Pall Teflo) was placed between high volume-flow inlet and CI-QMS sampling line to remove particles and was exchanged regularly to avoid accumulation of particulate matter. No indication for $ClNO_2$ formation via N_2O_5 reactions on salty surfaces in the inlet line was observed during AQABA, i.e. whenever we changed the particle filter or the inlet line, no change in signal was observed. Further the $ClNO_2$-to-N_2O_5 ratio was highly variable during AQABA (range of 0.35–59 with a median of 3.2) and $ClNO_2$ was occasionally measured in periods where no N_2O_5 was present.

$ClNO_2$ was calibrated twice during the campaign by simultaneously sampling a source of $ClNO_2$ via the CI-QMS and by a thermal dissociation cavity ring-down spectrometer (Sobanski et al., 2016). $ClNO_2$ was generated by passing Cl_2 over $NaNO_2$ as described previously (Thaler et al., 2011; Eger et al., 2019a). HCl

was calibrated four times throughout the campaign by adding a small flow over a permeation source to the main flow and monitoring the CI-QMS signal at m/z 188 and 190. SO_2 calibrations were performed seven times during the AQABA campaign by addition of a known flow of SO_2 from a gas cylinder (1 ppmv in synthetic air, Air Liquide). In contrast to $ClNO_2$ and HCl, correction of the SO_2 signal for its relative humidity (RH) dependence was necessary, which we derived from calibrations during AQABA where the RH was actively varied between 1 and 80 %.

The CI-QMS was operated in selected ion monitoring mode measuring mainly $ClNO_2$, HCl, SO_2, PAN and peracetic / acetic acid with a temporal resolution of approximately 15 s for each molecule. Changes in sensitivity were captured by permanently monitoring the primary ion signal (I^- and its water cluster) during ambient measurements and a background signal was recorded every 100 minutes. For further analysis, all data sets were averaged to 5 min temporal resolution. Our $ClNO_2$, HCl and SO_2 datasets provide about 12 500 data points distributed over 61.4 days with interruptions due to background determinations, calibrations, filter and gas bottle changes and instrument power-down at the harbours of Jeddah and Kuwait. For periods where the ship was in motion, the data coverage for all three trace gases was about 80 %.

4.2.3 Other trace gases

O_3 was measured by a commercial ozone monitor (2B Technologies, Model 202) based on optical absorption at 254 nm with a detection limit of 3 ppbv (10 s) and a total uncertainty of 2 % ± 1 ppbv. Mixing ratios of NO_x and NO_y (NO_y = NO_x + reactive nitrogen trace gases + particulate nitrate) were monitored via thermal dissociation cavity ring-down spectroscopy (TD-CRDS) using a modified version of the instrument described by Thieser et al. (2016). The difference between the NO_y and the NO_x signal is referred to as NO_z, which includes organic nitrates (peroxyacetyl nitrates and alkyl nitrates), NO_3, N_2O_5, $ClNO_2$, HNO_3 and particulate nitrate. In contrast to Thieser et al. (2016), the TD-unit was operated at 850 °C to ensure detection of HNO_3 and nitrate in the particle phase. The detection limits for NO_x and NO_y were 80 and 160 pptv, respectively, with total uncertainties of 9 % ± 30 pptv. NO_z was calculated from measured NO_x and NO_y with a detection limit of 160 pptv and a total uncertainty of 13 % ± 42 pptv. NO_2 (LOD = 52 pptv (1 s), total uncertainty = 7 %) and N_2O_5 (LOD = 6 pptv (1 s), total uncertainty = 15 %) were measured by a five-channel TD-CRDS described by Sobanski et al. (2016). NO and NO_2 were measured by a chemiluminescence detector (CLD 790 SR, ECO Physics, Duernten, Switzerland) (Fontijn et al., 1970; Li et al., 2015). The LOD (5 s) was 21 pptv for NO and 52 pptv for NO_2 and the total uncertainty 6 % respectively 7 %. The NO_2 data was in good agreement with the CRDS dataset ($R^2 = 0.95$) with a mean deviation of 6 %. The hydroxyl radical (OH) was measured using a Laser-Induced-Fluorescence method (Martinez et al., 2010; Novelli et al., 2014).

4.2.4 Meteorological parameter and actinic flux

Photolysis rates ($J_{O(1D)}$, J_{ClNO2} and J_{NO3}) were calculated from wavelength resolved actinic flux measured by a spectral radiometer (Metcon GmbH; Meusel et al. (2016)) located close to the common trace-gas inlet. Cross sections and quantum yields were taken from Burkholder et al. (2015). J-values were not corrected for upwelling UV radiation and are estimated to have an overall uncertainty of $\approx 10\,\%$. A commercial NEPTUNE weather-station (Sterela) monitored various parameters such as temperature, relative humidity, wind speed and direction, speed of the vessel and GPS position.

4.2.5 Aerosols

An Aerosol Mass Spectrometer (Aerodyne HR-ToF-AMS, DeCarlo et al. (2006)) measured PM_1 non-refractory aerosol composition (30 s time resolution), including sulphate, nitrate, ammonium, chloride and total organics with an overall uncertainty of 35 %. An Optical Particle Spectrometer (OPC, Grimm model 1.109) measured the size distribution from 250 nm to 32 μm (6 s time resolution) with a total uncertainty of 25 %. A Fast Mobility Particle Spectrometer (FMPS, TSI model 3091) provided particle size distributions from 5.6 nm up to 560 nm (1 s time resolution). The particle surface area concentrations for PM_1 and PM_{10} were calculated from the OPC and FMPS datasets, the overall uncertainty of these variables is estimated to be 30 %. The inlet for the aerosol instrumentation was located at the top of a measurement container at a distance of ≈ 5 m to the common, trace-gas inlet described above. In order to avoid condensation in inlet lines, aerosol samples were passed through a drying system which reduced ambient relative humidity to an average value of $\approx 40\,\%$ in the measurement container. We calculated the ambient PM_1 particle surface area concentration (A) from the measured surface area concentration using a hygroscopic growth factor (on average 1.32 ± 0.24) based on ambient RH and aerosol composition. The calculation of the growth-factor is described in the appendix (Fig. D.2–D.5). The water soluble fraction of total suspended particles (TSP) was monitored with hourly resolution using a Monitor for AeRosols and Gases in Ambient Air, MARGA (Metrohm Applikon Model S2), sampling at a distance of ≈ 5 m from the common gas-phase inlet. In this work only results from Na^+ and Cl^- measurements (TSP), with detection limits equal to 0.05 and 0.01 μg m^{-3}, will be used.

4.3 Results and discussion

In the following, we use only data (5 min averages) which were free from contamination by the ship's own exhaust (see Sect. 4.2.1).

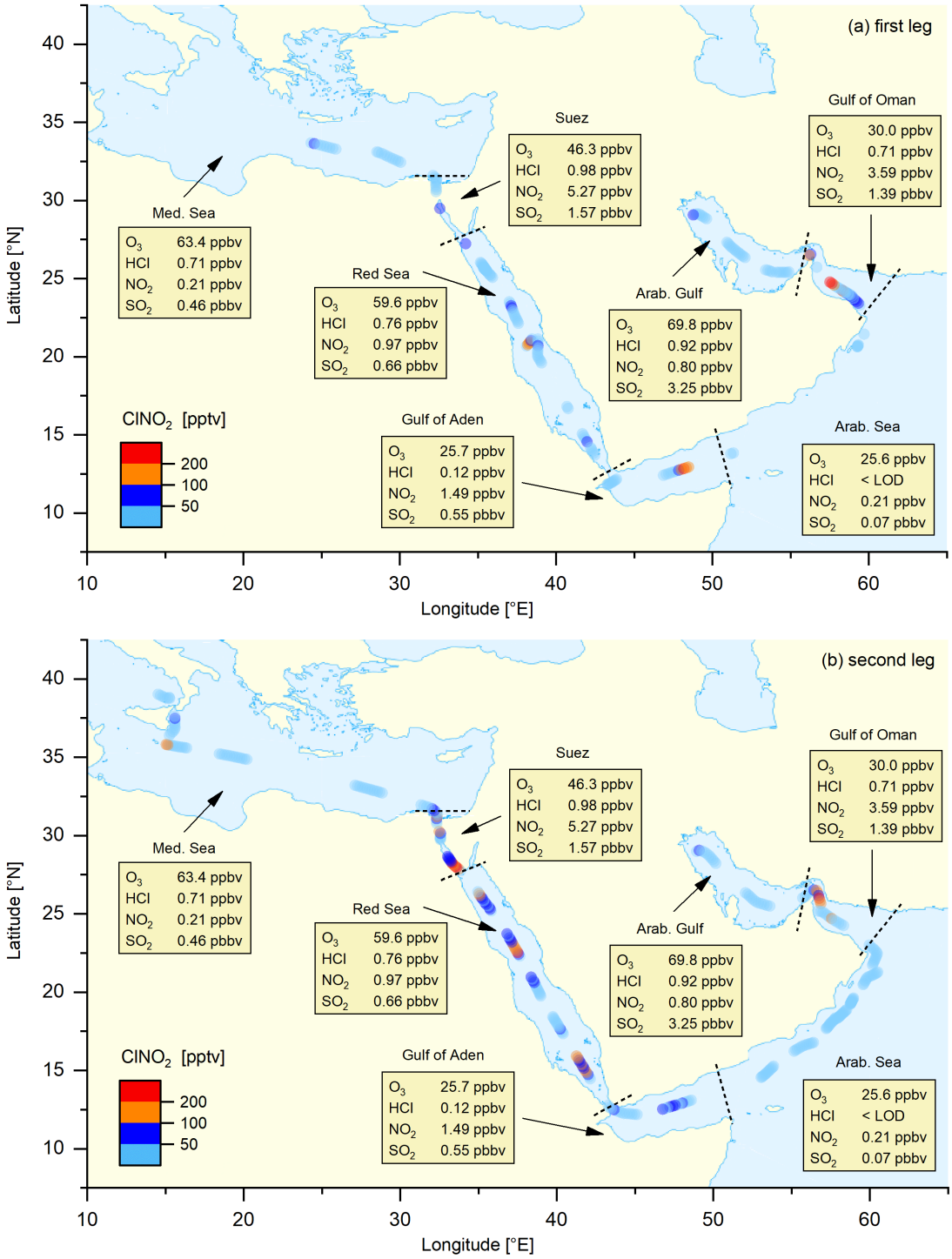

Figure 4.2: Map of nocturnal $ClNO_2$ mixing ratios (1-hour averages) for (a) first and (b) second leg, together with (median) night-time mixing ratios of O_3, HCl, NO_2 and SO_2 for different regions (data from both legs combined) demarked by the dashed lines. Maps are based on geospatial data from Kartverket.

4.3.1 Overview of measurement regions and $ClNO_2$ mixing ratios observed

Figure 4.2 illustrates the ship's track during AQABA, divided into seven regions demarked by dashed black lines: The Mediterranean Sea (Med. Sea, 30 June – 01 July and 24–30 August 2017), the Suez Canal including the Gulf of Suez (Suez, 02–03 July and 22–23 August), the Red Sea (03–15 July and 17–21 August), the Gulf of Aden (16–18 July and 15–16 August), the Arabian Sea (Arab. Sea, 19–23 July and 07–14 August), the Gulf of Oman (24–27 July and 05–06 August) and the Arabian Gulf (Arab. Gulf, 28 July – 04 August). On the first leg, the CI-QMS measurements started south of Crete; on the second leg measurements terminated close to Sicily after two months of almost continuous measurement. Maximum $ClNO_2$ mixing ratios observed during each night ranged from the limit of detection to 586 pptv (see Fig. D.6 for details). Figure 4.2 shows 1-hour averaged $ClNO_2$ mixing ratios along the ship track during (a) first and (b) second leg. Text boxes indicate the median night-time mixing ratios of O_3, HCl, NO_2 and SO_2 for the different regions where data from the first and second leg datasets have been combined. The night-time mean, median and range of the mixing ratios of these trace gases (and also of NO_2, temperature, relative humidity, NO_3 production rate and PM_1 particle surface area concentration) are listed in Table 4.1; a time-series of measured $ClNO_2$, HCl, SO_2 and O_3 is provided in Fig. D.7 in the appendix. The predominant air-mass origin for each night was derived from 48 h back-trajectories calculated with HYSPLIT (Stein et al., 2015; Rolph et al., 2017) and is illustrated for both legs in Fig. D.8. While Fig. 4.2 provides an overview of the measurements during both legs, Fig. 4.3 highlights two 9-day periods indicating features that characterised the transition from one region to the next. Based on these two figures, we will discuss observed $ClNO_2$ mixing ratios and related parameters for the seven regions defined above.

Over the Mediterranean Sea, during periods when the CIMS was operational, we encountered mainly aged air masses, which had passed over Italy, Greece or Turkey (Fig. D.8), characterised by relatively high O_3 levels but low NO_2-to-NO_y ratios. As illustrated in Fig. 4.1 the formation of $ClNO_2$ is initiated by NO_3 production which will depend on O_3 levels and availability of NO_2. For the Mediterranean Sea the low NO_2 mixing ratios resulted in a weak NO_3 production term (Table 4.1 and low $ClNO_2$ mixing ratios. The only exceptions are two nights south of Sicily on the second leg where $ClNO_2$ mixing ratios up to 439 pptv were observed, which coincided with an increase in NO_2 originating from industrial sources on the mainland (Sicily and Italy). There are no previous measurements of $ClNO_2$ over the Mediterranean Sea but our data can be compared to the output of a regional model (Li et al., 2019) which predicts monthly average $ClNO_2$ mixing ratios up to 100 pptv in the south-eastern Mediterranean Sea and around Sicily, in broad agreement with our observations.

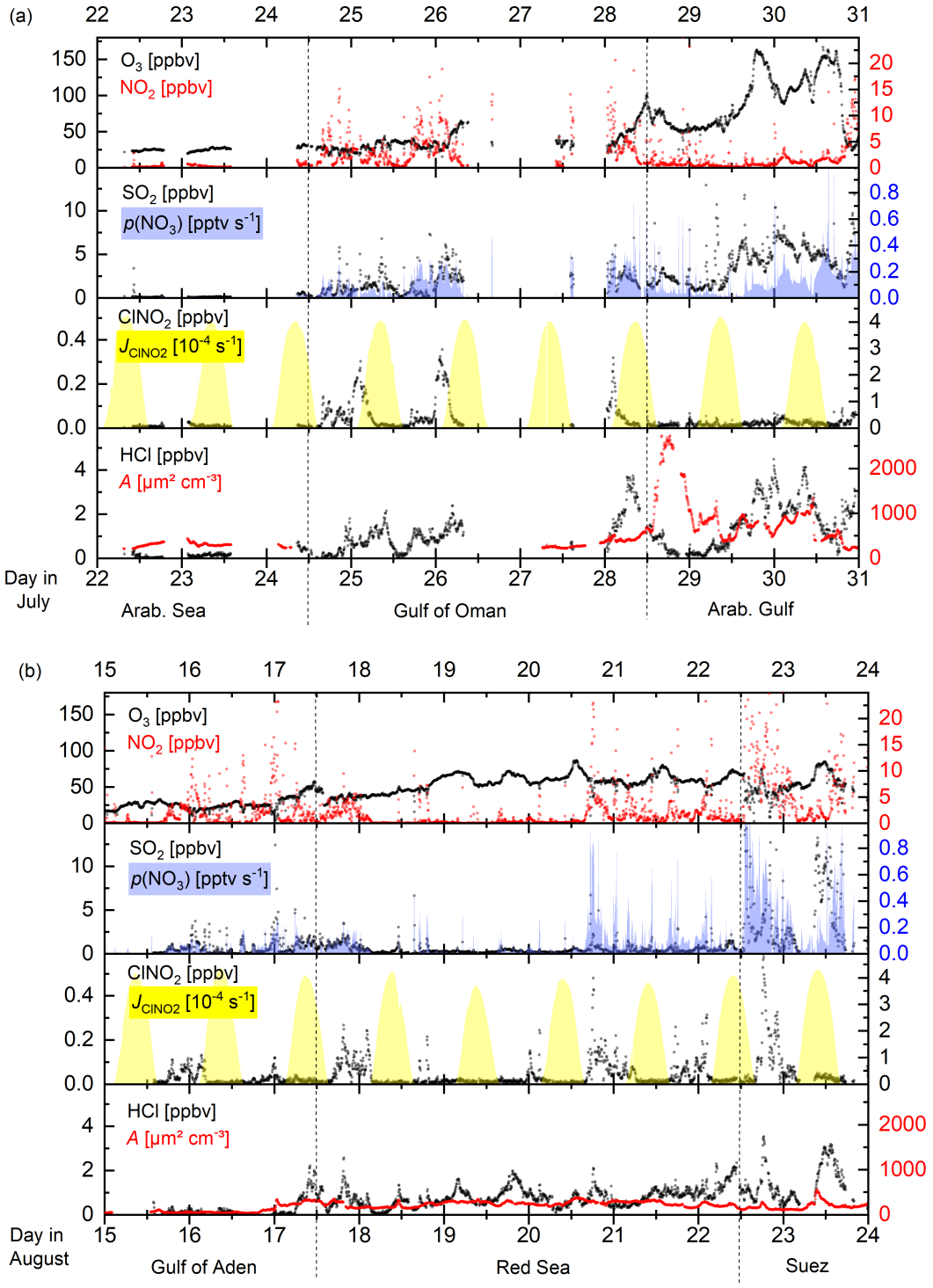

Figure 4.3: Time series of $ClNO_2$ and trace gases related to its production (NO_2 and O_3) as well as the NO_3 production rate, $p(NO_3)$, $ClNO_2$ photolysis rate (J_{ClNO2}), PM_1 particle surface area concentration (A) and HCl mixing ratio in different regions (separated by the dashed lines) for 9-day periods in the (a) first and (b) second leg.

Table 4.1: Measured trace gases and other parameters (5 min, night-time only) for different regions in Fig. 4.2.

Parameter	Med. Sea	Suez	Red Sea	Gulf of Aden	Arab. Sea	Gulf of Oman	Arab. Gulf
$ClNO_2$ [pptv]	N = 751	N = 376	N = 1247	N = 451	N = 918	N = 475	N = 500
Mean ± STD	20 ± 39	75 ± 101	47 ± 55	41 ± 56	7 ± 8	67 ± 71	21 ± 18
median	9	36	22	19	6	39	18
range	LOD–439	LOD–586	LOD–480	LOD–379	LOD–56	LOD–376	LOD–126
HCl [ppbv]	N = 749	N = 375	N = 1245	N = 449	N = 918	N = 473	N = 498
Mean ± STD	0.68 ± 0.52	0.94 ± 0.63	0.81 ± 0.36	0.28 ± 0.46	0.00 ± 0.13	0.86 ± 0.70	1.20 ± 0.99
median	0.71	0.98	0.76	0.12	LOD	0.71	0.92
range	LOD–3.09	LOD–3.54	LOD–2.58	LOD–1.98	LOD–0.38	LOD–3.23	LOD–4.49
SO_2 [ppbv]	N = 751	N = 376	N = 1247	N = 451	N = 918	N = 475	N = 500
Mean ± STD	0.64 ± 0.65	2.84 ± 3.87	0.81 ± 0.77	1.26 ± 2.89	0.18 ± 0.65	2.38 ± 2.26	3.71 ± 2.01
median	0.46	1.57	0.66	0.55	0.07	1.39	3.25
range	0.06–7.24	0.06–34.98	0.04–9.75	LOD–30.34	LOD–12.33	0.12–12.34	0.80–14.85
O_3 [ppbv]	N = 751	N = 376	N = 1247	N = 451	N = 800	N = 475	N = 500
Mean ± STD	61.6 ± 10.2	45.4 ± 16.1	58.1 ± 13.8	28.0 ± 10.9	24.4 ± 3.4	36.0 ± 16.4	83.9 ± 36.2
median	63.4	46.3	59.6	25.7	25.6	30.0	69.8
range	37.8–82.8	1.7–88.1	10.6–90.3	3.1–55.3	1.3–29.6	10.2–83.0	24.2–163.3
NO_2 [ppbv]	N = 547	N = 288	N = 1217	N = 449	N = 898	N = 470	N = 500
Mean ± STD	0.80 ± 1.57	7.37 ± 7.56	1.97 ± 3.50	2.94 ± 4.11	0.63 ± 1.57	4.57 ± 3.93	1.59 ± 2.34
median	0.21	5.27	0.97	1.49	0.21	3.59	0.80
range	0.01–14.45	0.24–44.03	0.01–56.81	0.07–25.87	0.01–20.88	0.12–30.38	0.16–23.22
pNO_3 [pptv s^{-1}]	N = 547	N = 288	N = 1138	N = 449	N = 783	N = 470	N = 500
Mean ± STD	0.04 ± 0.07	0.27 ± 0.21	0.10 ± 0.13	0.06 ± 0.05	0.01 ± 0.02	0.16 ± 0.14	0.12 ± 0.13
median	0.01	0.23	0.05	0.04	0.004	0.13	0.08
range	0.00–0.82	0.01–1.01	0.00–1.23	0.00–0.25	0.00–0.18	0.00–0.91	0.01–1.19
T [°C]	N = 751	N = 376	N = 1247	N = 451	N = 918	N = 475	N = 500
Mean ± STD	26.7 ± 0.6	27.2 ± 1.7	31.3 ± 1.7	31.3 ± 1.1	25.4 ± 0.9	32.7 ± 1.3	34.4 ± 0.6
median	26.8	27.5	31.8	31.1	25.5	33.0	34.4
range	25.5–29.1	21.6–31.7	27.7–34.1	29.3–35.6	23.5–31.2	29.6–35.8	33.2–36.4
RH [%]	N = 751	N = 376	N = 1247	N = 451	N = 918	N = 475	N = 500
Mean ± STD	79.0 ± 5.6	72.4 ± 9.1	73.2 ± 6.3	74.6 ± 10.2	88.8 ± 2.9	79.8 ± 8.9	76.5 ± 7.9
median	79.5	71.6	72.7	75.6	89.1	81.5	77.8
range	63.2–89.3	40.6–93.2	58.7–88.4	27.2–90.0	79.3–94.7	51.9–95.1	53.3–91.6
A [μm^2 cm^{-3}]	N = 690	N = 373	N = 1101	N = 440	N = 899	N = 222	N = 393
Mean ± STD	202 ± 61	240 ± 200	243 ± 62	111 ± 64	81 ± 62	363 ± 317	1010 ± 600
median	178	166	257	107	77	275	809
range	114–466	90–1134	111–376	35–338	23–426	101–1244	179–2726

Notes: STD = standard deviation; RH = relative humidity; A = ambient PM_1 particle surface area concentration (see section 4.2.5); p denotes a production rate; N = number of data points; LOD = Limit of detection (see Sect. 4.2.2).

The Suez Canal and the Gulf of Suez were impacted by fresh emissions from ships, industry and urban centres with high NO_2, SO_2, HCl and $ClNO_2$ mixing ratios. On the night 22–23 August 2017 we measured the highest $ClNO_2$ mixing ratio of the whole campaign (586 pptv) due to exceptionally high NO_2 levels and NO_3 production rates.

Over the Red Sea, O_3 levels were elevated with the highest NO_3 production rates (up to 0.7 pptv s^{-1}) observed when approaching the Gulf of Suez with NO_x transported south from the region around the Suez Canal, the city of Cairo and the Sinai Peninsula (see back-trajectories in Fig. D.8). $ClNO_2$ mixing ratios exceeded 200 pptv on most of the nights (with a maximum of 480 pptv) whereby elevated PM_1 particle surface area concentration and HCl mixing ratios indicated increased heterogeneous uptake and chloride availability.

Over the Gulf of Aden, with air mainly originating from Somalia, O_3 levels were close to 25 ppbv and NO_2 mixing ratios regularly exceeding 5 ppbv resulted in a NO_3 production rate up to ≈ 0.2 pptv s^{-1}. However, the PM_1 particle surface area concentration remained low and $ClNO_2$ was detected only occasionally (maximum of 379 pptv).

Over the Arabian Sea we experienced strong winds from the south with 48 h back-trajectories touching the coast of Somalia. $ClNO_2$ was generally below the detection limit (maximum 56 pptv) and NO_2, HCl and PM_1 particle surface area concentration were very low. Missing local sources of NO_x and low O_3 mixing ratios resulted in a weak NO_3 production term, partially responsible for the lack of $ClNO_2$. Low mixing ratios of $ClNO_2$ were occasionally detected that originated from single ships or point sources on the mainland.

Upon entering the Gulf of Oman, which marks the transition between remote marine environment and increased emissions from petrochemical industry and shipping lanes, NO_3 production rates increased significantly due to higher NO_x and O_3 levels. $ClNO_2$ mixing ratios exceeded 200 pptv during two consecutive nights with a maximum value in this region of 376 pptv.

The Arabian Gulf was characterised by very high ozone levels (sometimes exceeding 150 ppbv) and SO_2 mixing ratios that generally exceeded 5 ppbv. For the first leg (sailing into the Arabian Gulf), the air-mass passed over Kuwait whereas for the second leg (sailing out of the Arabian Gulf) it mainly passed over Iran. In the Gulf region, which was heavily polluted by emissions from shipping and petrochemical industry, we also observed the highest HCl and PM_1 particle surface area concentration throughout the whole campaign. However, despite high NO_3 production rates (≈ 0.4 pptv s^{-1}) due to NO_x emissions from oil and gas refineries as well as emissions from shipping and urban areas, we only observed relatively low $ClNO_2$ mixing ratios with a maximum value of 126 pptv close to Kuwait.

Consistent with Osthoff et al. (2008) we find significant amounts of nocturnal $ClNO_2$ in aged ship-plumes that could be identified by a defined peak-shape (Fig. D.9) and covariance of NO_2 and SO_2 indicative of upwind point sources. As SO_2 and NO_2 are co-emitted from the combustion of ship fuel, it is not surprising that they show a co-variance. The consequence of the co-emission of NO_2 and SO_2

is that $ClNO_2$ is generally observed in the presence of both whereby high $ClNO_2$ mixing ratios were associated with aged ship-plumes.

Figure 4.4 shows diel profiles of nitryl chloride for the Red Sea and the Gulf of Oman together with the photolysis rate constant J_{ClNO2} illustrating that mixing ratios generally decreased at sunrise with a $ClNO_2$ lifetime of a few hours. Diel $ClNO_2$ profiles for other regions (Fig. D.10 in the appendix) look generally similar but with a varying maximum mixing ratio. Over the Red Sea $ClNO_2$ was often observed in plumes, whereas mixing ratios over the Gulf of Oman increased continuously after sunset indicating that we sampled a more homogeneously polluted air mass in which $ClNO_2$ accumulated over the course of the night. The median mixing ratio in the afternoon was still around 10 pptv, which we attribute to an HCl interference at m/z 208 and 210 described by Eger et al. (2019a) rather than to the presence of $ClNO_2$ during the day when its production rate is close to zero and its lifetime is short due to photolysis. The magnitude of the HCl interference at the m/z used to monitor $ClNO_2$ was derived during HCl calibrations on-board the ship and found to be 0.006 Hz (pptv of HCl)$^{-1}$ which is about 1 % of the $ClNO_2$ count rate of 0.61 Hz (pptv of $ClNO_2$)$^{-1}$ at 10^6 Hz of I^-. However, during ambient air measurements the interfering signal was variable with a campaign average of (0.008 ± 0.005) Hz pptv^{-1}, which implies that a correction based on the HCl signal alone is not sufficient. The variable offset at the $ClNO_2$ mass contributes to the total measurement uncertainty and can be significant when analysing data close to the detection limit. Although on occasions several hundred pptv of $ClNO_2$ were observed, below we show that the $ClNO_2$ production efficiency was generally low. Reasons for this are examined in the following sections.

4.3.2 $ClNO_2$ yield per NO_3 molecule formed

We define the $ClNO_2$ production efficiency (ϵ) during AQABA as the number of $ClNO_2$ molecules generated per NO_3 molecule formed from the reaction of NO_2 with O_3 (Reaction R 4.3). The instantaneous production rate of NO_3 is given by $k_1[NO_2][O_3]$ and the total number of NO_3 molecules formed over the course of the night is derived using a rate coefficient of $k_1 = 1.4 \times 10^{-13} \exp(-2470/T)$ cm^3 molecule^{-1} s^{-1} (IUPAC, 2019) and integrating the NO_3 production term from the beginning of the night (t_0) to the time of the measurement (t) according to Eq. (4.2). In this calculation we assume that $[NO_2]$ changes over time but $[O_3]$ stays constant in good approximation.

$$[NO_3]_{int} = \int_{t_0}^{t} k_1[O_3][NO_2](t)\,dt \tag{4.2}$$

In order to account for the pre-sunset production of NO_3 at high solar zenith angles where N_2O_5 could already be detected, t_0 was defined as the point in time at which J_{NO3} was below 0.017 s^{-1} (about 10 % of maximum value during day). This was typically 30–50 minutes prior to sunset. All data points before sunset were however excluded from the analysis due to the increased uncertainty in the reaction time. The NO_2 mixing ratio at the beginning of the night, $[NO_2]_0$, was

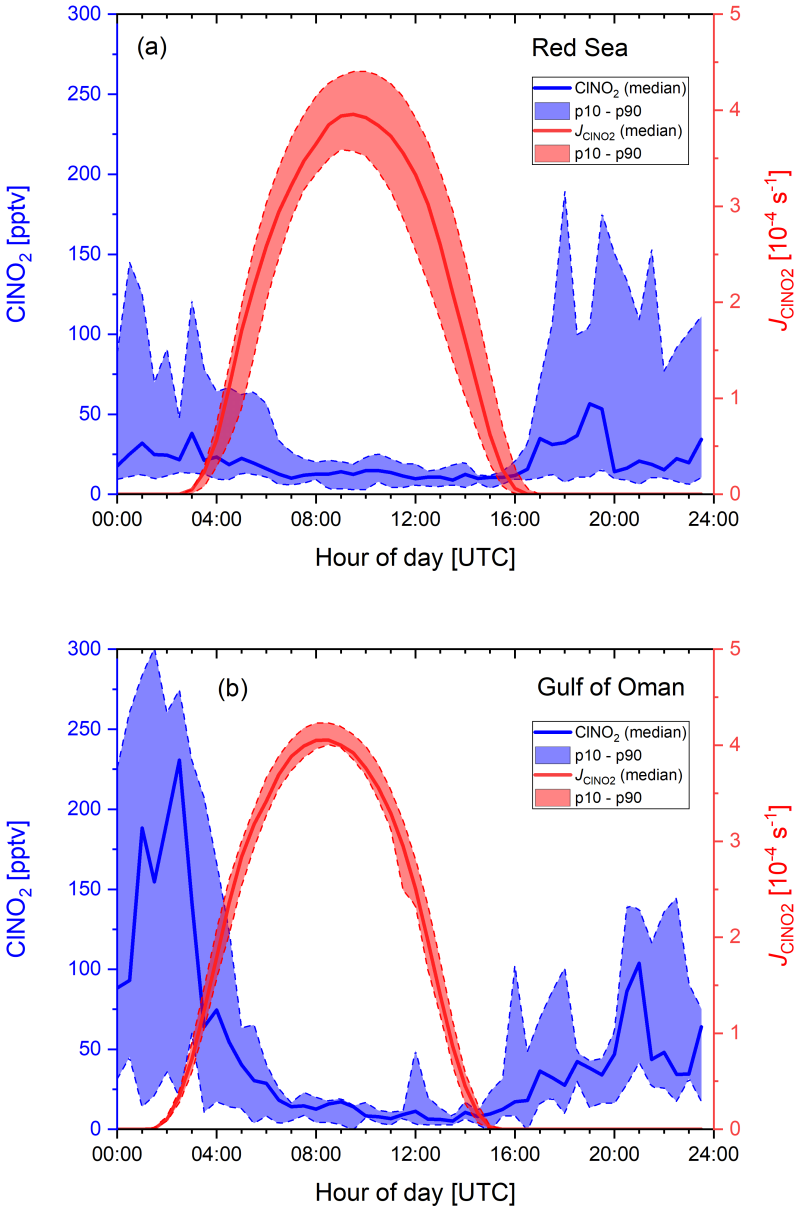

Figure 4.4: Diurnal profiles of $ClNO_2$ and its photolysis rate constant, J_{ClNO2}, for (a) the Red Sea and (b) the Gulf of Oman. The solid lines represent the median values, the shaded areas correspond to the 10 th and 90 th percentiles.

derived from the measured NO_2 mixing ratio at time t via Eq. (4.3) by assuming that NO_2 had been consumed by reaction with O_3 but the O_3 mixing ratio did not change significantly. Consequently, the amount of NO_3 produced along the air mass trajectory is equal to the difference between calculated $[NO_2]_0$ and measured $[NO_2](t)$.

$$[NO_2](t) = [NO_2]_0 \exp(-k_1[O_3]t) \tag{4.3}$$

The $ClNO_2$ production efficiency ϵ can be determined by inserting the integrated NO_3 production over the course of the night and the measured $ClNO_2$ mixing ratio (assuming no losses) into Eq. (4.4).

$$\epsilon = \frac{[ClNO_2]}{[NO_3]_{\text{int}}} \tag{4.4}$$

To account for fresh emissions of NO (e.g. by passing ships), the reaction time t' was calculated from Eq. (4.5) according to McDuffie et al. (2018b), where s represents the number of NO_2 molecules required to make NO_y and is 1 when NO_3 reacts directly with VOCs and 2 when NO_3 reacts with NO_2 to form N_2O_5, which subsequently hydrolyses to HNO_3.

$$t' = (k_1[O3]s) \ln\left(\frac{[NO_y]}{[NO_2]}\right) \tag{4.5}$$

As discussed later, the direct NO_3 losses are dominant throughout the campaign compared to the heterogeneous N_2O_5 production, so to a good approximation, $s \approx 1$. As discussed by McDuffie et al. (2018b), inherent to the use of this expression is the assumption that NO_y is conserved during the night; any losses of NO_y (e.g. via deposition of HNO_3) lead to an underestimation of the true reaction time. As the calculated, night-time air mass age depends on the ratio between $[NO_2]$ and $[NO_y]$, the calculation breaks down whenever a fresh NO emission (e.g. from a nearby ship) is injected into an air-mass and unreacted NO is still present. To avoid this, we only analyse $ClNO_2$ data when NO is below the detection limit. In addition, we only consider data points where the calculated age of the air mass is equal to or exceeds the time elapsed since sunset as these air masses are unlikely to have been impacted by recent emissions. As the loss of NO_z via deposition will result in an air mass age that is shorter than the true one, we relax the criterion for equality of reaction times by also including calculated air mass ages that are up to 25 % shorter. The reduced dataset provides 1742 data points with a median value of $\epsilon = 2.7\,\%$ for the whole campaign. The data reduction is described in more detail in the appendix (all the data shown in the manuscript corresponds to the application of method C), where the sensitivity of ϵ to these limitations and additional constraints is discussed. Here, we emphasise that even when limiting the dataset to $ClNO_2$ mixing ratios exceeding 100 pptv (see Table D.1), the $ClNO_2$ production efficiency still remains relatively low ($\epsilon = 6.4\,\%$, Fig. D.11). Although the median values would be modified (Fig. D.12), the relative differences between the regions and especially the low ϵ observed over the Arabian Gulf persist.

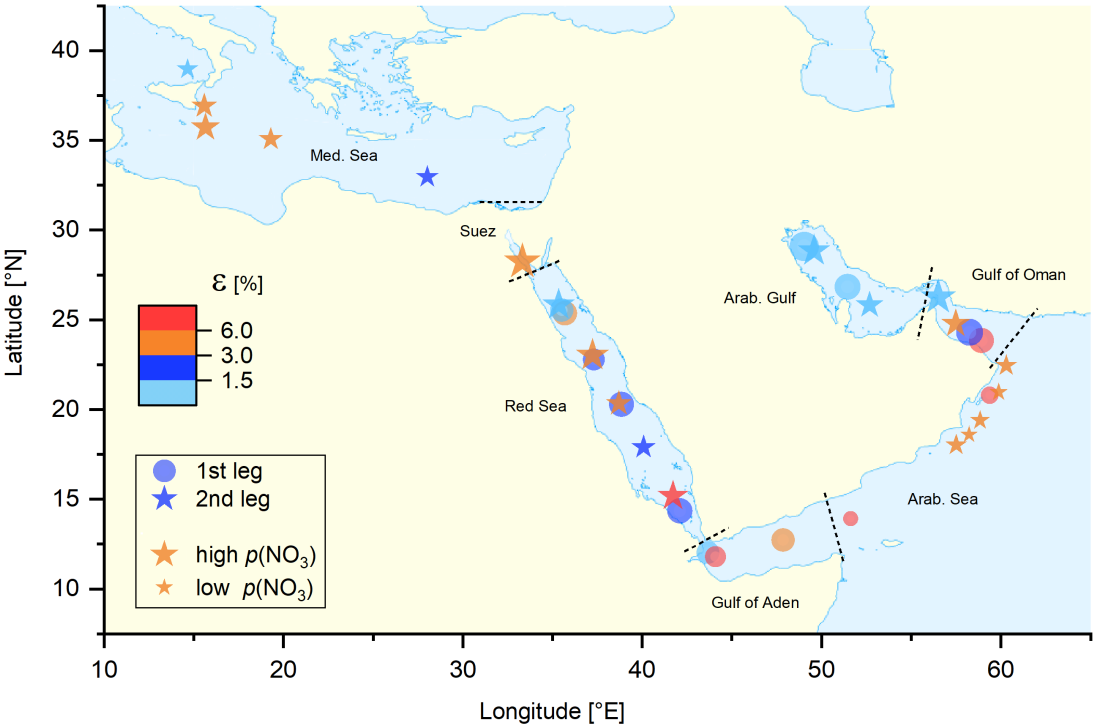

Figure 4.5: Median night-time values of ϵ (the $ClNO_2$ yield per NO_3 molecule formed) calculated via Eq. (4.4). The size of the symbols represents (logarithmic scale) the median NO_3 production rate, $p(NO_3)$, ranging from 0.001 pptv s^{-1} in the Arabian Sea to 1.2 pptv s^{-1} in the Suez Canal. Different regions are separated by the dashed black lines.

4.3.3 Temporal and regional variability in ϵ

To compare the efficiency of $ClNO_2$ formation in different regions, a median value for ϵ was derived for each individual night with the results illustrated in Fig. 4.5 in which the size of the circles (first leg) and stars (second leg) scales with the median NO_3 production rate (for a more detailed plot with 1-hour averaged data points see Fig. D.13). Despite high NO_3 production rates (high O_3 and NO_2 levels), the lowest values of ϵ were observed over the Arabian Gulf, whereas elevated values of ϵ were found e.g. over the Arabian Sea, where NO_3 production was lowest.

Fig. 4.6 displays box-plots of ϵ for each region, calculated from between 41 and 546 data points per region. The median $ClNO_2$ production efficiency ϵ displays large night-to-night variability and interregional variability with the highest value found over the Gulf of Aden and the Arabian Sea (median = 4.7 %) and the lowest value found over the Arabian Gulf (median = 0.8 %). Median values of ϵ (in %) derived for the Mediterranean Sea, the Suez Canal, the Red Sea and the Gulf of Oman were 2.9, 2.7, 2.1 and 2.0. In the following, we examine the factors that cause the generally low efficiency in $ClNO_2$ production and also the regional variability in ϵ.

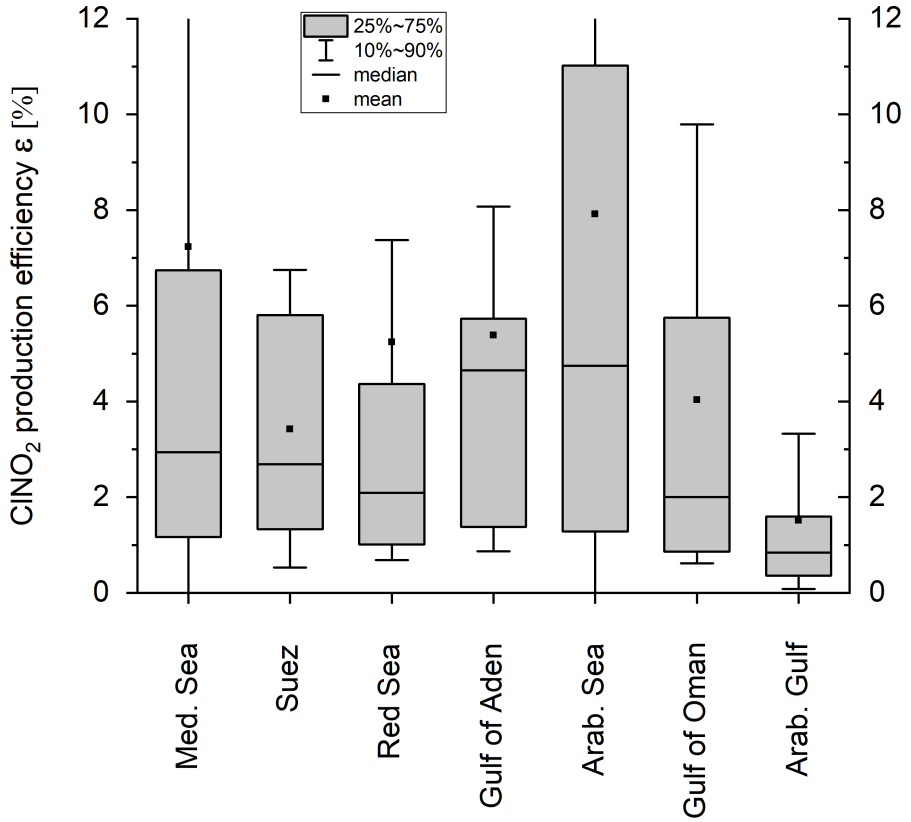

Figure 4.6: Box plots of ϵ ($ClNO_2$ production efficiency) for different regions, based on all corresponding individual night-time values calculated from Eq. (4.4).

4.3.4 Factors influencing the $ClNO_2$ production efficiency

The uptake of N_2O_5 to aerosol particles can proceed via hydrolysis to HNO_3 as well as formation of $ClNO_2$, with yield f (see Fig. 4.1). Assuming no night-time losses, the concentration of $ClNO_2$ is given by Eq. (4.6).

$$[ClNO_2] = \epsilon\,[NO_3]_{int} = f\left(\frac{k_{het}}{k_{het}+k_{dir}}\right)[NO_3]_{int} \tag{4.6}$$

$$k_{dir} = \sum_i (k_{VOC})_i\,[VOC]_i + k_{NO+NO3}\,[NO] \tag{4.7}$$

$$k_{het} = \gamma\left(\frac{A\bar{c}}{4}\right)K_{eq}\,[NO_2] \tag{4.8}$$

The overall $ClNO_2$ production efficiency ϵ as derived in Sect. 4.3.2 is dependent on f and on the relative rates of direct NO_3 loss (k_{dir}, Eq. 4.7) and indirect

NO_3 loss (k_{het}, Eq. 4.8) where A is the particle surface area concentration, $\bar{c}$ is the mean molecular velocity of N_2O_5 ($(24400 \pm 160)\,cm\,s^{-1}$ during AQABA) and $K_{eq} = \frac{[N_2O_5]}{[NO_2][NO3]} = 2.8 \times 10^{-27}(T/300)^{-0.6} \exp(11000/T)$ cm^3 molecule^{-1} (IUPAC, 2019) is the temperature-dependent equilibrium constant (Reactions R 4.4 and R 4.5). During night-time, k_{dir} is determined by the NO_3 reactivity towards VOCs and NO, k_{het} by the rate of heterogeneous uptake of N_2O_5 to aerosol particles. In the following we calculate f and γ from our measurements, compare the values with the literature and quantify the contributions of k_{het} and k_{dir} to the overall NO_3 loss rate.

If no particulate chloride is available, f is zero and two NO_3^- ions are produced according to Reaction (R 4.1) whereas if the particulate chloride concentration is large, f approaches unity and one NO_3^- anion plus one $ClNO_2$ molecule are formed. As particulate nitrate (NO_3^-) can leave the particle as HNO_3 we can derive f from Eq. (4.9), where p signifies a production rate.

$$f = 2\left(\frac{p[NO_3^-] + p[HNO_3]}{p[ClNO_2]} + 1\right)^{-1} \tag{4.9}$$

Equation (4.9) assumes that N_2O_5 uptake is the sole mechanism for the night-time production of HNO_3. In principal, as demonstrated by Phillips et al. (2016), f can be derived from field data using measured production rates (or concentrations) of inorganic nitrate (NO_3^- + HNO_3) and $ClNO_2$ according to Eq. (4.9). For AQABA, we derived the mixing ratio of total inorganic nitrate from measurements of NO_z (corrected for $ClNO_2$ and N_2O_5) assuming that, for this marine environment the contribution of organic nitrate in both gas- and particle phases is small compared to inorganic nitrate. f could be derived using Eq. (4.9) whenever there was a significant correlation (over a period of several hours) between $ClNO_2$ and inorganic nitrate, as illustrated in Fig. D.14 for data obtained in the Gulf of Oman (25–26 July 2017) for which $f = 0.60 \pm 0.04$. The spatially and temporally variable sources of pollution during AQABA meant that requirement of a homogeneous fetch over periods of hours was rarely fulfilled and only a handful of values for f could be derived this way. Further values derived are 0.42 ± 0.06 (Red Sea, 15 July 2017), 0.84 ± 0.09 (Gulf of Oman, 24–25 July 2017) and 0.65 ± 0.05 (Mediterranean Sea, 29 August 2017.), indicating that the values of f were generally large whenever $ClNO_2$ was observed.

$$f = \left(\frac{k_{Cl\text{-}}[Cl^-]}{k_{Cl\text{-}}[Cl^-] + k_{H2O}[H_2O]}\right) = \left(1 + \frac{[H_2O]}{\frac{k_{Cl\text{-}}}{k_{H2O}}[Cl^-]}\right)^{-1} \tag{4.10}$$

f can also be calculated (Eq. 4.10) if the relative concentrations of particulate chloride and water are known (Behnke et al., 1997; Bertram and Thornton, 2009), where $\left(\frac{k_{Cl\text{-}}}{k_{H2O}}\right) = 450$ is the ratio of rate constants (Ammann et al., 2013) for reaction of NO_2^+ (formed along with NO_3^- upon dissociation of N_2O_5 in the aqueous-phase) with either Cl^- or H_2O. The aerosol liquid water content $[H_2O]$ and chloride ion

Table 4.2: Regional variability in $ClNO_2$ production efficiency (ϵ), $ClNO_2$ yield (f), N_2O_5 uptake coefficient (γ) and heterogeneous NO_3 loss rate (k_{het}).

Region	ϵ [%]	f	γ	k_{het} [10^{-5} s^{-1}]
Med. Sea	2.9	0.53	0.034	4.4
Suez	2.7	0.90	0.031	69.7
Red Sea	2.1	0.86	0.031	12.9
Gulf of Aden	4.7	0.76	0.031	8.5
Arab. Sea	4.7	0.87	0.036	1.8
Gulf of Oman	2.0	0.50	0.033	64.8
Arab. Gulf	0.8	0.17	0.036	34.3

Notes: f was alculated from Eq. (4.10); γ was calculated from Eq. (4.11).

concentration [Cl^-] were calculated using the E-AIM model (Clegg et al., 1998; Friese and Ebel, 2010) and the ambient temperature and relative humidity along with PM_1 nitrate, sulphate, ammonium and chloride mass concentrations ($\mu g\,m^{-3}$) as reported by the AMS. From the median aerosol composition (PM_1) in the seven different regions we calculated median values of f, which are shown in Table 4.2. The values of f obtained via Eq. (4.10) were variable between regions, with medians of 0.53 in the Mediterranean Sea, 0.90 in the Suez Canal, 0.86 in the Red Sea, 0.76 in the Gulf of Aden, 0.87 in the Indian Ocean, 0.50 in the Gulf of Oman and 0.17 in the Arabian Gulf. To put these numbers in context, a value of $f = 0.9$ corresponds to a $\approx 1.1\,mol\,L^{-1}$ Cl^- solution. MARGA measurements of Cl^- and Na^+ (total suspended particles, TSP) also indicated sea salt concentrations up to $20\,\mu g\,m^{-3}$ in the coarse mode over the Arabian Sea. A comparison of the [Cl^-] (TSP) from the MARGA (which detects NaCl as well as NH_4Cl) with the (largely) non-refractory [Cl^-] reported by the AMS reveals a strong co-variance. The AMS concentrations (PM_1) were on average $\approx 1\%$ of those reported by the MARGA (TSP) with the correlation between them indicating that the AMS chloride (PM_1) is mainly due to sea-salt rather than NH_4Cl. If we assume that $\approx 10\,\%$ of the sea salt mass (TSP) is associated with the fine mode (PM_1) as previously derived (Sommariva et al., 2018), we can use the MARGA (TSP) [Cl^-] to estimate that the true PM_1 [Cl^-] would be about an order of magnitude higher than measured by the AMS. Under the assumption that this is true, f is > 0.67 in all seven regions implying that a lack of Cl^- is not the reason for low values of ϵ, as may be expected for a marine environment.

Previous derivations of f in a marine environment (Texas coast) yield values between 0.1 and 0.65 (Osthoff et al., 2008) whereas even larger values (up to 0.9) have been reported for inland sites impacted by anthropogenic emissions (Young et al., 2013) or by long-range transport of sea-salt ($0.035 < f < 1$) (Phillips et al., 2016). A median value of 0.138 ($0.003 < f < 1$) was derived for airborne

measurements in a coastal region during winter (McDuffie et al., 2018a).

$$\gamma = B\,k\,\left(1 - \left(a\,\frac{[\mathrm{H_2O}(l)]}{[\mathrm{NO_3^-}]} + 1 + b\,\frac{[\mathrm{Cl^-}]}{[\mathrm{NO_3^-}]}\right)^{-1}\right) \tag{4.11}$$

The uptake coefficient, γ, can be estimated using the parameterisation in Eq. (4.11) (Bertram and Thornton, 2009), where $B = 3.2 \times 10^{-8}$ s, $k = (1.15 \times 10^6 - 1.15{\times}10^6\exp(-0.13[\mathrm{H_2O}(l)]))$ $\mathrm{s^{-1}}$ is the rate constant for the reaction $\mathrm{N_2O_5(aq)}$ + $\mathrm{H_2O(l)}$, $a = 0.06$ denotes the ratio of rate constants for reactions $\mathrm{H_2NO_3^+(aq)}$ + $\mathrm{H_2O(l)}$ and $\mathrm{H_2NO_3^+(aq)}$ + $\mathrm{NO_3^-(aq)}$ and $b = 29$ denotes the ratio of rate constants for reactions $\mathrm{H_2NO_3^+(aq)}$ + $\mathrm{Cl^-}$ and $\mathrm{H_2NO_3^+(aq)}$ + $\mathrm{NO_3^-(aq)}$. Using AMS data for $[\mathrm{NO_3^-}]$ and $[\mathrm{Cl^-}]$ we derive $\gamma = 0.033 \pm 0.003$ where the standard deviation encompasses the weak inter-regional variation (see Table 4.2). This value is consistent with $\gamma = 0.03 \pm 0.02$ reported by Aldener et al. (2006) for a polluted marine environment. The large values of γ reflect the low $\mathrm{PM_1}$ particulate nitrate concentrations observed during AQABA where the high temperatures favour the partitioning of particulate nitrate and $\mathrm{HNO_3(g)}$ to the gas-phase. A suppression of γ through the presence of organics in the particle phase has been reported (Bertram et al., 2009), though the low (generally < 2) organic-to-sulphate ratio in particles observed during AQABA suggest that this is not likely to be important for the present analysis.

The campaign averaged, fractional contribution of coarse mode particles ($\mathrm{PM_{10}}$ minus $\mathrm{PM_1}$) to the total particle surface area concentration A was only (14 ± 14) % so that the uncertainty incurred when using the $\mathrm{PM_1}$ particle surface area concentration to derive the heterogeneous $\mathrm{NO_3}$ loss rate (k_{het}, Table 4.2) from Eq. (4.8) is negligible. However, during two periods (of 2–5 days duration) when the ship was sailing through the Gulf of Aden / Arabian Sea / southern Red Sea and air masses originated from the deserts of Eritrea, Djibouti and Ethiopia, the contribution from the coarse mode particles to the aerosol surface area increased to about 60 % mainly due to dust (and sea-salt). The relative contribution of dust and sea-salt to the coarse mode was estimated using MARGA measurements of $\mathrm{Ca^{2+}}$ and $\mathrm{Na^+}$ in TSP. The dust loading was calculated by assuming that the dust aerosols of Saharan origin consist of 10 % calcium (Molinaroli et al., 1993). Freshly generated dust particles do not contain chloride and the uptake of $\mathrm{N_2O_5}$ to them ($\gamma = 0.02 \pm 0.01$ for Saharan dust, Tang et al. (2012)) does not result in $\mathrm{ClNO_2}$ formation ($f = 0$) but contributes to k_{het} through the additional aerosol surface area, thus lowering the $\mathrm{ClNO_2}$ production efficiency. In contrast, the uptake of $\mathrm{N_2O_5}$ to coarse mode sea-salt particles has a $\mathrm{ClNO_2}$ yield f close to unity (Ammann et al., 2013), and can therefore enhance formation of $\mathrm{ClNO_2}$. Throughout the whole campaign, the contribution of dust to the uptake of $\mathrm{N_2O_5}$ to coarse mode particles was much larger than that of sea-salt (on average (13 ± 10) % with a range of 0–40 %). A close examination of the periods (14–19 July and 15–17 August 2017) strongly influenced by dust particles did not reveal any (anti)correlation between elevated dust concentration and $\mathrm{ClNO_2}$ mixing ratios. This is also reflected by the relatively high median value of ϵ over the Gulf of Aden where the highest concentrations of

coarse mode particles were observed.

Using a campaign average of $\epsilon = 2.7\,\%$ and a maximum value of $f = 1$ we can show that, with 97.3 %, the direct (gas-phase) loss of NO_3 (k_{dir}) is much more important than indirect losses via N_2O_5 uptake (k_{het}), which contribute the remaining 2.7 %. Assuming a very conservative estimate of $f = 0.5$ would still result in a contribution of 94.6 respectively 5.4 %. To put this into context, over the Gulf of Oman we calculated a median value of $k_{het} = 6.5 \times 10^{-4}$ s^{-1} (Table 4.2) which would result (assuming $\epsilon = 2.0\,\%$ and $f = 0.5$) in a direct NO_3 loss term towards VOCs of $k_{dir} = 1.6 \times 10^{-2}$ s^{-1}. The relatively small contribution of the heterogeneous loss term is readily explained by high mean night-time temperatures of 25–35 °C during AQABA, which favour the existence of NO_3 rather than N_2O_5. To illustrate this, we calculate that a nocturnal temperature of 20 °C (rather than 30 °C) would increase the contribution of k_{het} to 21 % of the total NO_3 loss and lead to 3 times higher $ClNO_2$ mixing ratios assuming that the rate constants for reaction between NO_3 and reactive trace gases are not strongly temperature-dependent. A further reduction in temperature to 10 °C would lead to equality in k_{het} and k_{dir} and result in a factor of seven more $ClNO_2$ than observed.

The direct (gas-phase) loss rate of NO_3 can also be calculated from Eq. (4.7) if the concentrations of all VOCs contributing to its reactivity are known. However, for a large fraction of each night NO_3 was below the detection limit (ca. 5 pptv) despite a high production rate (large mixing ratios of NO_2 and O_3). A steady-state analysis of NO_3 production and loss indicated a high total reactivity which could not be attributed to measured trace gases (k_{dir}) or heterogeneous losses of N_2O_5 (k_{het}). A detailed analysis of the NO_3 lifetime and the role of VOCs is beyond the scope of the present manuscript and will be described in detail in a separate publication.

4.3.5 Comparison with literature

In the following, we compare the generally low values of ϵ derived during AQABA with previous determinations. Mielke et al. (2013) report a yield of $ClNO_2$ relative to the total amount of NO_3 formed at night of 0.7 % to 62 % with a median of 12 % in the polluted coastal boundary layer in Pasadena, California. In contrast, $ClNO_2$ production efficiencies derived for the urban boundary layer of Calgary, Canada (Mielke et al., 2016), were significantly lower, ranging from 0.1 % to 4.5 % (10^{th} and 90^{th} percentiles, median 1.0 %). Osthoff et al. (2018) report very low efficiencies with a median of 0.17 % and a maximum of 5.4 % for the Lower Fraser Valley of British Columbia, Canada, potentially due to a lack of available aerosol chloride. For AQABA we derive a region-dependent median efficiency of 1–5 % with a campaign median of 2.8 %, despite similar conditions to Mielke et al. (2013), i.e. mostly polluted marine environment. The difference can be attributed to exceptionally high nocturnal temperatures during AQABA with a median of 25–35 °C for different regions, shifting the equilibrium from N_2O_5 towards NO_3 and favouring direct NO_3 losses. For comparison, daily minimum temperatures during the study reported by Mielke et al. (2013) were 10–20 °C (Ryerson et al., 2013)

whereas the lowest temperature measured during the whole AQABA cruise was 22 °C. Based on the $ClNO_2$ dataset reported by Phillips et al. (2012) for continental Germany, where $ClNO_2$ mixing ratios up to 800 pptv were reported, we calculate values of ϵ that range from 0.4 % to 12.3 % (10^{th} and 90^{th} percentiles) with a median of 2.6 %. On nights where $ClNO_2$ mixing ratios above 100 pptv were observed, range and median increase to 5.0–24.1 % and 10.6 % respectively. Compared to AQABA the yield per NO_3 molecule formed on nights where $ClNO_2$ was present at levels > 100 pptv is about a factor of 2 higher for this dataset, again most likely a result of the lower nocturnal temperatures.

4.3.6 Cl atom generation from $ClNO_2$ and HCl

In this section we assess the role of two gas-phase chlorine reservoirs, $ClNO_2$ and HCl as sources of Cl atoms during AQABA. Other potential Cl sources (e.g. Cl_2 photolysis) are not considered here as we do not have experimental data to quantify their impact. Compared to the complex route to $ClNO_2$ formation described above (Fig. 4.1), the formation of HCl in the polluted marine environment can be traced back to its displacement from sea-salt particles by stronger acids, such as H_2SO_4 and HNO_3 (Keene et al., 1999). The high emission rates of NO_x and SO_2 by ship traffic resulted in enhanced concentrations of both NO_2 and SO_2 (see Fig. D.9) during parts of the AQABA campaign. Both NO_2 and SO_2 are oxidised via OH to form HNO_3 and H_2SO_4, both of which can be taken up by sea-salt containing aerosol releasing HCl. The release of HCl through acid displacement leads to a deficit in particulate Cl^- concentrations which can be expressed in terms of a chloride depletion factor (Eq. 4.12) where $[Na^+]$ and $[Cl^-]$ represent the concentrations in mol m^{-2} and 1.174 is the molar ratio of Cl^- to Na^+ found in sea-water (Zhuang et al., 1999).

$$\text{Cl depletion } [\%] = 100 \left(\frac{1.174\,[Na^+] - [Cl^-]}{1.174\,[Na^+]} \right) \tag{4.12}$$

In Fig. 4.7 we present a time series (Gulf of Oman / Arabian Gulf) in which significant differences in particulate Na^+ and Cl^-concentrations coincide with high mixing ratios of NO_2, SO_2 and HCl (chloride depletion up to 90 %) indicating efficient HCl acid displacement by HNO_3 and H_2SO_4 in this region.

The instantaneous production rate of Cl atoms from the photolysis of $ClNO_2$ ($p\mathrm{Cl}_{\mathrm{ClNO2}}$) is given by the photolysis rate constant for $ClNO_2$ (J_{ClNO2}) and its concentration (Eq. 4.13) whereas the instantaneous Cl production rate from HCl ($p\mathrm{Cl}_{\mathrm{HCl}}$) requires knowledge of the OH concentration (Eq. 4.14) and the rate coefficient for reaction between OH and HCl ($k_{\mathrm{OH+HCl}} = 1.7 \times 10^{-12} \exp(-230/T)$ cm^3 molecule^{-1} s^{-1} (Atkinson et al., 2007; IUPAC, 2019)).

$$p\mathrm{Cl}_{\mathrm{ClNO2}} = J_{\mathrm{ClNO2}}\,[ClNO_2] \tag{4.13}$$

$$p\mathrm{Cl}_{\mathrm{HCl}} = k_{\mathrm{OH+HCl}}\,[OH][HCl] \tag{4.14}$$

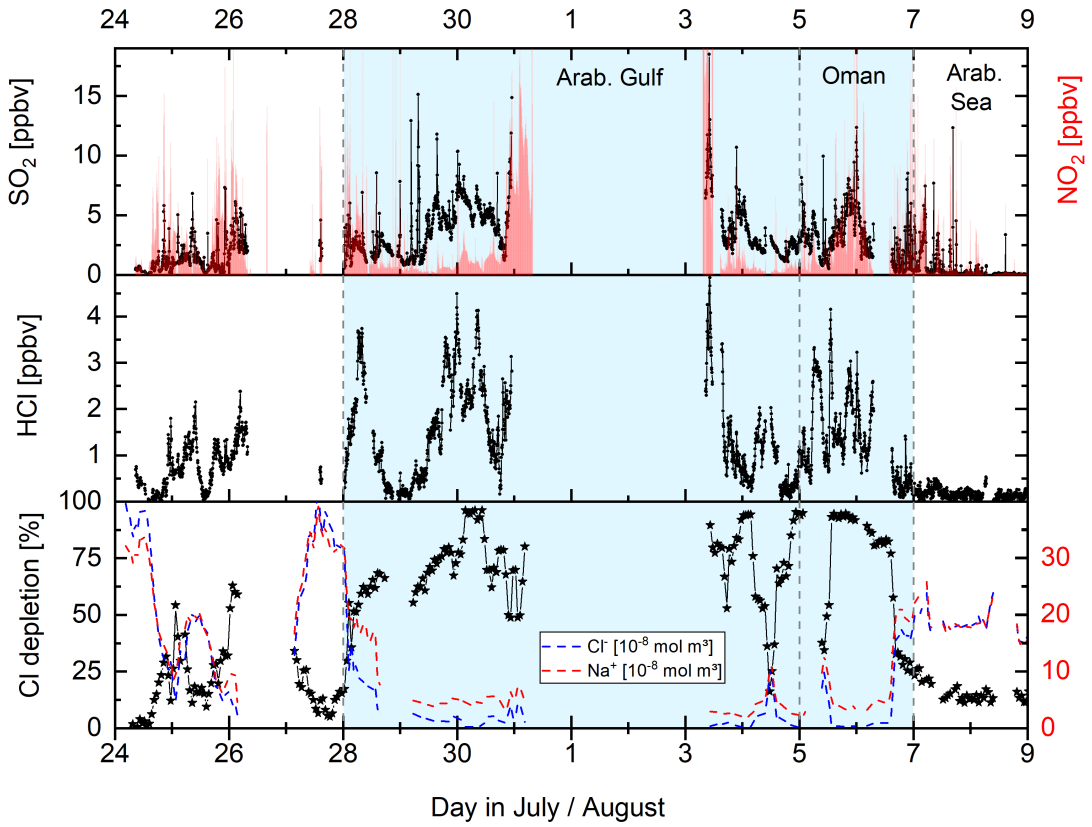

Figure 4.7: Co-variance between mixing ratios of SO_2, NO_2 and HCl and particulate chloride depletion (calculated from Eq. 4.12) illustrated by the difference in Cl^- and Na^+ (PM_1) measured. Chloride depletion of up to 90 % indicates effective acid displacement of HCl by HNO_3 and H_2SO_4 in this region.

In the following analysis, we focus on two consecutive nights in the Gulf of Oman region (Fig. 4.8) where we observed a monotonous increase of $ClNO_2$ mixing ratios up to ≈300 pptv during the second half of the night followed by a decrease over a 4-hour period starting at sunrise (upper panel). The corresponding Cl production rate from $ClNO_2$ photolysis reaches a maximum of 0.8×10^6 molecule cm^{-3} s^{-1} on the first night and 0.7×10^6 molecule cm^{-3} s^{-1} on the second night.

$$pOH_{O3} = \frac{2J_{O1D}[O_3]\, k_{H2O}[H_2O]}{k_{H2O}[H_2O] + k_{N2}[N_2] + k_{O2}[O_2]} \tag{4.15}$$

To place this in context, we also make a rough estimate (lower limit) to the rate of OH radical production (pOH_{O3}) from the photolysis of O_3 in the presence of H_2O (Eq. 4.15), where J_{O1D} is the photolysis rate constant for O_3, $k_{H2O} = 2.4 \times 10^{-11}$ cm^3 $molecule^{-1}$ s^{-1}, $k_{N2} = 2.15 \times 10^{-11}$ $\exp(110/T)$ cm^3 $molecule^{-1}$ s^{-1} and $k_{O2} = 3.2 \times 10^{-11}$ $\exp(67/T)$ cm^3 $molecule^{-1}$ s^{-1} (IUPAC, 2019) refer to reactions of $O(^1D)$ with H_2O, N_2 and O_2, respectively. As we do not consider other OH production channels (e.g. photolysis of HONO or HO_2 + NO), which can be of importance under more polluted conditions, pOH_{O3} represents a lower limit of

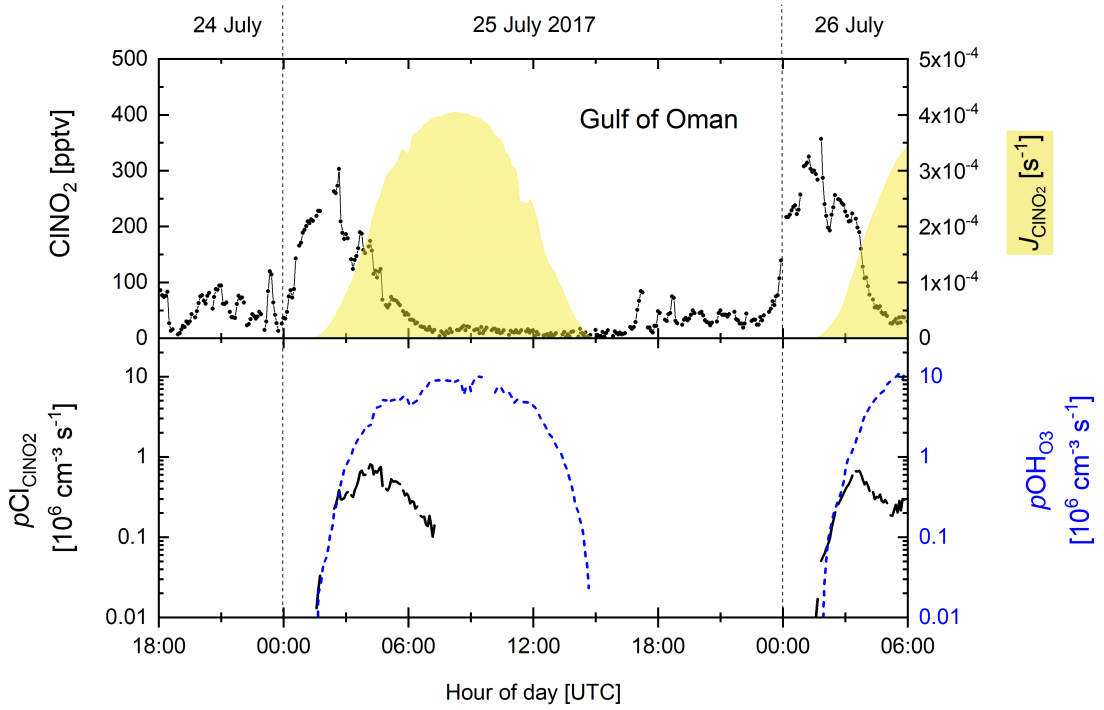

Figure 4.8: Time series of $ClNO_2$ mixing ratios, J_{ClNO2} photolysis rates and production of Cl-radicals from $ClNO_2$ photolysis ($p\mathrm{Cl}_{ClNO2}$) and OH-radicals from O_3 photolysis in the presence of H_2O ($p\mathrm{OH}_{O3}$) for two consecutive nights in the Gulf of Oman.

pOH. Although the maximum, midday OH production rates from O_3 photolysis ($\approx 1 \times 10^7$ OH molecules cm^{-3} s^{-1}) are about an order of magnitude higher than Cl atom production rates, during the first $\approx$2 hours after sunrise, $p\mathrm{Cl}_{ClNO2}$ and $p\mathrm{OH}_{O3}$ are roughly equal for this particular case-study.

In order to examine the regional dependence of Cl formation we calculated the $ClNO_2$ production rate from the regional median values of ϵ, the NO_3 production rate and the length of the night as described previously. As $ClNO_2$ is completely photolysed to Cl during daytime, the total Cl-production from $ClNO_2$ photolysis ($\Sigma\mathrm{Cl}_{ClNO2}$) is equal to the median amount of $ClNO_2$ formed during the night. The total Cl-production from HCl + OH ($\Sigma\mathrm{Cl}_{HCl}$) was calculated by integrating the production rate $p\mathrm{Cl}_{HCl}$ (based on [HCl] and [OH] measurements, Eq. 4.14) over the median diurnal profile. To calculate the contribution of O_3 photolysis to the OH production ($\Sigma\mathrm{OH}_{O3}$), we integrated $p\mathrm{OH}_{O3}$ (calculated via Eq. 4.15) over the median diel profile. In Table 4.3 we summarise the average, total daytime production of OH and Cl in the seven regions. The median radical production over one diurnal cycle calculated for the Suez region is exemplified in Fig. 4.9, whereby we assume an initial 363 pptv of $ClNO_2$ at sunrise (Table 4.3), which is subsequently photolysed according to J_{ClNO2}. Considering the entire campaign, we conclude that Cl-atom formation via $ClNO_2$ photolysis and OH-initiated HCl oxidation are of similar magnitude, though their relative contributions show large regional variability. For example, Cl formation from OH + HCl ($\Sigma\mathrm{Cl}_{HCl}$) is a factor $\approx$10 more

Table 4.3: Regional variability in ϵ and pNO_3 as well as OH and Cl radical production integrated over one diel cycle.

Region	ϵ [%]	[1]pNO_3	[2]ΣCl_{ClNO2}	[2]ΣCl_{HCl}	[2]ΣOH_{O3}	[3]$\Sigma Cl_{total}/\Sigma OH_{O3}$
Med. Sea	2.9	0.012	18	234	12 364	2.0
Suez	2.7	0.231	363	170	13 216	4.0
Red Sea	2.1	0.053	48	53	12 411	0.8
Gulf of Aden	4.7	0.043	96	24	5 608	2.1
Arab. Sea	4.7	0.004	11	3	4 639	0.3
Gulf of Oman	2.0	0.130	155	127	12 649	2.2
Arab. Gulf	0.8	0.077	25	50	10 985	0.7

Notes: ΣCl_{ClNO2} and ΣCl_{HCl} are the integrated formation of Cl atoms from $ClNO_2$ and HCl respectively. ΣOH_{O3} is the integrated formation of OH from O_3 photolysis. [1]Unit: [pptv s^{-1}]; [2]unit: [pptv]; [3]unit: [%].

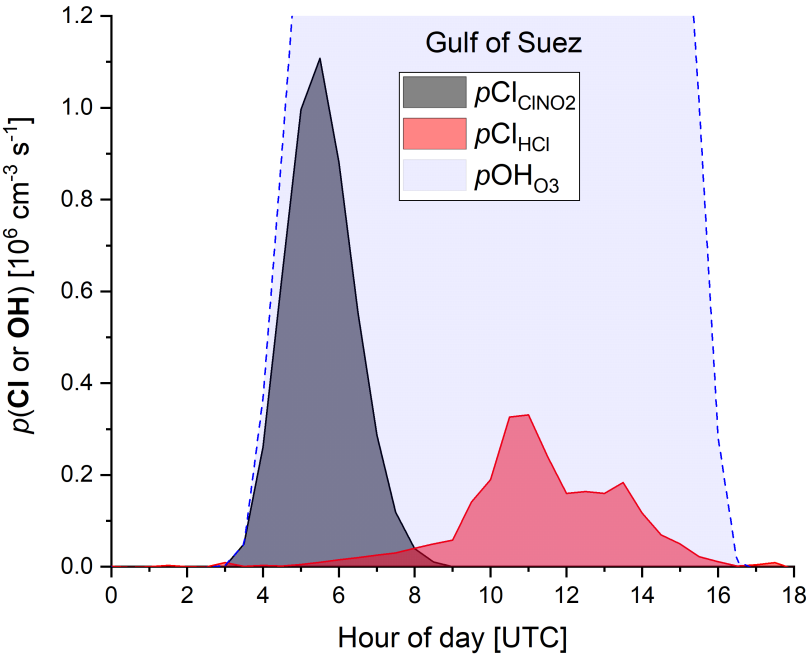

Figure 4.9: Production of Cl-atoms (from $ClNO_2$ photolysis and HCl + OH) and OH-radicals (from O_3 photolysis) over one diurnal cycle in the Suez Canal / Gulf of Suez.

important than $ClNO_2$ photolysis (ΣCl_{ClNO2}) over the Mediterranean Sea where the NO_3 (and thus $ClNO_2$) production rate was low owing to low NO_x levels and where the OH concentrations were highest. This is consistent with Li et al. (2019) who indicate the importance of HCl over the eastern Mediterranean Sea for which monthly average mixing ratios of 0.5–1.5 ppbv were predicted by a regional model. ΣCl_{HCl} is also a factor ≈ 2 higher than ΣCl_{ClNO2} over the Arabian Gulf where the $ClNO_2$ production efficiency, ϵ, was low. In all other regions ΣCl_{ClNO2} was about equal to ΣCl_{HCl} or higher by factors between ≈ 1 and 4. This in in broad agreement with Riedel et al. (2012a) who report roughly equal importance of $ClNO_2$ and HCl as chlorine atom sources in the polluted marine boundary layer of the Los Angeles region. They also report a maximum midday Cl production rate from $ClNO_2$ photolysis of 0.6×10^6 molecule cm^{-3} s^{-1}, which is similar to the production rates we obtained over the Gulf of Oman (Fig. 4.8).

When comparing the total number of chlorine atoms generated during the day ($\Sigma Cl_{total} = \Sigma Cl_{ClNO2} + \Sigma Cl_{HCl}$) with the total number of OH formed from O_3 photolysis (ΣOH_{O3}) over the same period, we find the expected domination of OH for all regions. The largest contribution of Cl to the total radical production (4 %) was observed over the Suez Canal where the Cl production was highest (about 32 % from HCl and 68 % from $ClNO_2$). The lowest ratio of Cl-to-OH production was observed over the Arabian Sea, reflecting the low levels of NO_x and very low rates of NO_3 generation. Although only (at maximum) ≈ 4 % of the radicals generated are Cl atoms, they react more rapidly than OH with some classes of hydrocarbons, especially saturated hydrocarbons and small oxygenates. For example, the relative, room temperature rate coefficients (k_{Cl} / k_{OH}) are 16, 61, 127 and 242 for reaction with CH_4, CH_3OH, C_3H_8 and C_2H_6, respectively (Atkinson et al., 2004; IUPAC, 2019). The impact of chlorine atoms is thus mainly seen in the oxidation rates of unsaturated hydrocarbons, the relative concentrations of which may be modified according to the relative abundance of OH and Cl and the relative reaction rate constants. For the AQABA campaign, evidence for such effects has been reported by Bourtsoukidis et al. (2019), and for the global scale Wang et al. (2019) conclude that oxidation by Cl atoms accounts for 1.0 % of methane loss with larger impacts on ethane (20 %), propane (14 %), and methanol (4 %).

4.4 Summary and conclusion

The AQABA campaign, which took place in summer 2017 along the sea route from southern France to Kuwait provided the first $ClNO_2$ measurements in the marine boundary layer of the Mediterranean Sea, the Suez Canal, the Red Sea, the Gulf of Aden, the Arabian Sea, the Gulf of Oman and the Arabian Gulf. Along the ship track we observed a large variability in $ClNO_2$ mixing ratios with nocturnal maxima ranging from below the detection limit over the Indian Ocean to a few hundred pptv over the Gulf of Oman, the northern part of the Red Sea, the Gulf of Suez and the Mediterranean Sea close to Sicily / Italy with a campaign maximum of ≈ 600 pptv observed over the Gulf of Suez.

The overall $ClNO_2$ production efficiency, i.e. the yield of $ClNO_2$ per NO_3 molecule formed in the reaction of NO_2 with O_3, was generally low (median of 2.7 % for the whole campaign) and highly variable within individual nights and between different regions with values (in percent) of 2.9, 2.7, 2.1, 4.7, 4.7, 2.0, and 0.8 over the Mediterranean Sea, the Suez Canal, the Red Sea, the Gulf of Aden, the Arabian Sea, the Gulf of Oman and the Arabian Gulf, respectively. The relatively low $ClNO_2$ production efficiency compared to previous measurements in the polluted marine boundary layer or at continental sites was attributed to high nocturnal temperatures during AQABA (25–35 °C), which significantly shifted the equilibrium between NO_3 and N_2O_5 towards NO_3 and lowered the importance of N_2O_5 uptake to particles relative to direct NO_3 losses. The low $ClNO_2$ production efficiency in the Arabian Gulf (< 1 %) results from a combination of high temperatures, enhanced NO_3 reactivity and lowered chloride availability. The photolysis of $ClNO_2$ was found to represent an important source of chlorine radicals in the early morning in areas where efficient night-time production was observed, and was augmented (and sometimes exceeded) by Cl atoms formation from the reaction of OH with HCl, especially in areas where ppbv levels of HCl were observed such as the Mediterranean Sea or the Arabian Gulf. Although the amount of Cl atoms generated were found to be a factor 25 to 300 less than the amount of OH molecules generated from O_3 photolysis, the high rate coefficients ratio for Cl compared to OH reactions towards some hydrocarbons imply that Cl may enhance hydrocarbon oxidation, especially in the early morning.

Author contributions

Philipp Eger performed the CI-QMS measurements of $ClNO_2$, HCl and SO_2 during the AQABA campaign, evaluated the field data and wrote the manuscript. John Crowley operated the CI-QMS and CRDS during parts of the first leg and supervised the study. NO_2 and N_2O_5 data were provided by Justin Shenolikar. NO_x, NO_y and NO_z data were provided by Nils Friedrich. J-values were measured by Jan Schuladen. Ivan Tadic and Horst Fischer contributed the NO and NO_2 data. AMS, OPC and FMPS measurements and analysis were performed by James Brooks, Eoghan Darbyshire, Friederike Fachinger and Frank Drewnick. MARGA data was provided by Michael Pikridas and Jean Sciare. Roland Rohloff, Sebastian Tauer, Monica Martinez and Hartwig Harder provided the OH dataset. Jos Lelieveld designed the campaign. All authors contributed to the manuscript.

Acknowledgements

We acknowledge the co-operation with the Cyprus Institute (CyI), the King Abdullah University of Science and Technology (KAUST) and the Kuwait Institute for Scientific Research (KISR). We are grateful for the support of Hays Ships Ltd, the captain and his crew on-board *Kommandor Iona*. We would like to thank the whole AQABA team, particularly Marcel Dorf and Claus Koeppel for logistical support.

Chapter 5

Conclusions and Outlook

Within the scope of this thesis a chemical ionisation quadrupole mass spectrometer (CI-QMS) with an electrical discharge ion source was characterised and deployed in three field studies under variable atmospheric conditions, measuring the trace gases $ClNO_2$, SO_2, HCl, PAN, PAA, acetic acid and pyruvic acid.

5.1 Characterisation of the instrument

Chemical ionisation mass spectrometers (CIMS) equipped with a ^{210}Po ioniser to generate I^- primary ions from a mixture of CH_3I and N_2 are frequently used devices for atmospheric trace gas measurement with a broad field of application. The CI-QMS described in this thesis is a technical evolution of a former instrument equipped with a radioactive ion source (^{210}Po), which focussed on the measurement of PAN, PAA and $ClNO_2$ (Phillips et al., 2012, 2013). By replacing ^{210}Po by an electrical discharge ion source (see Chapter 2), the CI-QMS was successfully modified for measurements in environments where permission for ^{210}Po is difficult to obtain or transport is not feasible. Extensive characterisation in laboratory experiments was necessary to identify newly discovered ions and detection schemes and to reveal potential sources of the generally elevated background signals across large parts of the mass spectrum. In addition to the well-established detection of $ClNO_2$, PAN and PAA via I^- primary ions, the instrument turned out to be capable of measuring SO_2, HCl, acetic acid and pyruvic acid through additional ion-molecule-reactions involving IO_x^- and $I(CN)_x^-$ primary ions, unique for the RF discharge ion source (see Chapter 2).

Limits of detection (LOD, 2σ, 1 s, see Table 5.1) for the trace gases reported in this thesis are 12 pptv for $ClNO_2$, 56 pptv for SO_2, 135 pptv for HCl, 15 pptv for pyruvic acid, 34 pptv for PAN (in the absence of PAA and acetic acid), 194 pptv for PAA (in the absence of acetic acid) and 57 pptv for acetic acid (in the absence of PAA). When averaging datasets to 5 minutes temporal resolution, which is usually adequate for the analysis of data obtained from stationary or slow-moving platforms, LODs can be enhanced by a factor of 3–4. The LOD for $ClNO_2$ is thus comparable to the use of ^{210}Po, and furthermore, the additional benefit of detecting SO_2, HCl, acetic acid and pyruvic acid provides various scopes of application. The instrumental sensitivity to different trace gases ranges from $0.1\,\mathrm{Hz\,pptv^{-1}}$ for SO_2 at m/z 207 (relatively low due to multiple product ions) to $4.8\,\mathrm{Hz\,pptv^{-1}}$ for pyruvic acid at m/z 87.

Due to its compact design and easy handling the CI-QMS can be applied in

Table 5.1: Sensitivity and limit of detection (LOD) of the CI-QMS with electrical discharge ion source for measurable trace gases ($ClNO_2$, SO_2, HCl, pyruvic acid, PAN, peracetic acid and acetic acid).

Trace gas	Product ion	m/z	S [Hz pptv^{-1}]	LOD [pptv]
$ClNO_2$	$I^{35}ClNO_2^-$	208	0.60	12
SO_2	ISO_3^-	207	0.09	56
HCl	$I(CN)^{35}Cl^-$	188	0.14	135
Pyruvic acid	$CH_3(C)OC(O)O^-$	87	4.80	15
PAN	$CH_3C(O)O^-$	59	1.04	34[a]
PAA	$CH_3C(O)O^-$	59	0.22[b]	194[b]
Acetic acid	$CH_3C(O)O^-$	59	0.62	57[c]

Notes: Parameters are reported for the CI-QMS with RF discharge ion source. Sensitivity S at 50 % RH (25 °C), normalised to 10^6 Hz I^- and de-clustering set to 20 V. Limit of detection (LOD) for 2σ and 1 s integration time. [a]LOD in the absence of PAA and acetic acid. [b]Without de-clustering applied. [c]LOD in the absence of PAA.

both stationary measurements (see NOTOMO and IBAIRN campaigns, Chapters 2 and 3) and on moving platforms like aircraft or ship (see AQABA campaign, Chapter 4). The instrument was successfully operated under difficult conditions onboard a research vessel for more than eight weeks and is thus well-suited for long-term operation with minimal maintenance (exchanging gas bottles and particle filters), which was also confirmed by measurements during NOTOMO and IBAIRN.

The CI-QMS was proved to be particularly useful when the main focus is on sulphur- and chlorine-related chemistry, which applies, for example, to the polluted marine boundary layer (see AQABA, Chapter 4). Though the simultaneous measurement of $ClNO_2$, HCl and SO_2 the CI-QMS has advantages over similar instruments equipped with a ^{210}Po ioniser, its application as a PAN detector is accompanied by a high background signal and chemical interferences, and is thus limited to polluted regions (see NOTOMO, Chapter 2) or low temporal resolution. This represents a major disadvantage compared to the use of ^{210}Po, especially for aircraft measurements, where a high temporal resolution is crucial. A further disadvantage is that differentiation between PAA and acetic acid, which are detected at the same m/z, is only feasible by modifying de-clustering potentials, which results in a strongly increased LOD for PAA.

To overcome problems with the limited mass resolution of the applied quadrupole analyser, it would be useful to equip a time-of-flight analyser (CIMS-ToF-MS) with a similar discharge ion source to that described in this thesis. In this way individual contributions to a certain m/z and thus chemical interferences could be potentially identified. Further, more details of the ion chemistry involved in SO_2, HCl, acetic acid and pyruvic acid detection could be revealed, resulting in a potential extension of the reported detection scheme.

5.2 Results from field studies

The CI-QMS has been applied in three different field studies (NOTOMO 2015, IBAIRN 2016 and AQABA 2017) from remote to polluted and continental to marine environment, for which the results are summarised in Table 5.2. Depending on the overarching question, a different set of trace gases was measured and various aspects of atmospheric chemistry were investigated.

5.2.1 NOTOMO campaign at a forested mountain-site

The NOTOMO (NOcturnal chemistry at the Taunus Observatory: insights into Mechanisms of Oxidation) campaign took place at a rural (forested) mountain-site in south-western Germany with significant urban influence in July 2015. It was characterised by generally high NO_x, O_3, SO_2 and PAN mixing ratios throughout the whole campaign, which reflected the influence of nearby urban conglomerations and industry on local air quality. Mixing ratios of SO_2 regularly exceeded 1 ppbv (occasionally up to 5 ppbv), with a likely origin from coal-burning power plants in the Rhine-Main urban conglomeration and the heavily industrialised Ruhr area. $ClNO_2$ above > 50 pptv was also observed during 10 out of 29 campaign nights with a maximum value of 500 pptv, which is comparable to polluted coastal environments. High levels were associated with mixed marine and continental air masses from the north-west, which had passed over the English Channel and the polluted Ruhr area. The observed $ClNO_2$ mixing ratios are consistent with previous measurements at the same location and similar time of the year (Phillips et al., 2012, 2016) and indicate the importance of fine mode particulate chloride transported inland, which has probably been formed by acid displacement in polluted coastal regions and subsequent partitioning of HCl to the particle phase. Due to a high photochemical activity and the presence of both NO_x and VOCs (from anthropogenic and biogenic sources), PAN mixing ratios sometimes approached 3 ppbv, with a range of observations from a few hundred pptv to a few ppbv. The observed diurnal profile was similar to that of O_3 with a characteristic maximum in the afternoon where the actinic flux and thus photochemical activity was highest. Although differentiation between PAA and acetic acid was not possible during NOTOMO, the generally high combined signal indicated the importance of biogenic acids at this site, with acetic acid probably being directly emitted by the surrounding vegetation and peracetic acid being photochemically generated from organic peroxy radicals reacting with HO_2.

5.2.2 IBAIRN campaign in the boreal forest

The IBAIRN (Influence of Biosphere–Atmosphere Interactions on the Reactive Nitrogen budget) campaign took place in Hyytiälä, Finland, in a boreal forest environment, in September 2016. It was characterised by large biogenic emissions and low-NO_x conditions, with much lower O_3 levels than during NOTOMO and observed mixing ratios of SO_2 and PAN close to the detection limit. Only occa-

Table 5.2: Overview of field campaigns and trace gases measured.

Trace gas	**NOTOMO**	**IBAIRN**	**AQABA**
Location	south-west Germany	southern Finland	Med. Sea and Arab. Peninsula
Time period	July 2015	September 2016	June–August 2017
Conditions	mixed urban / rural (stationary)	remote forested (stationary)	mostly polluted marine (shipborne)
NO_x [ppbv]			
Mean ± STD	2.1 ± 1.5	0.4 ± 0.4	4.2 ± 8.7
10–90th percentiles	0.8–4.0	0.1–0.7	0.1–10.6
maximum	10.5	7.6	78.0
O_3 [ppbv]			
Mean ± STD	50 ± 23	24 ± 9	51 ± 24
10–90th percentiles	25–84	11–35	23–75
maximum	144	46	167
$ClNO_2$ [pptv]			
Mean ± STD	20 ± 43	$<$ LOD	40 ± 60
10–90th percentiles	0–41	$<$ LOD	0–91
maximum	520	$<$ LOD	600
SO_2 [ppbv]			
Mean ± STD	0.4 ± 0.5	0.05 ± 0.08	1.4 ± 2.2
10–90th percentiles	0.1–1.0	0.01–0.11	0.1–3.7
maximum	4.6	1.06	35.0
HCl [ppbv]			
Mean ± STD	-	0.07 ± 0.05	0.8 ± 0.8
10–90th percentiles	-	0.02–0.14	0.0–1.8
maximum	-	0.31	5.5
PAN [ppbv]			
Mean ± STD	0.7 ± 0.4	0.06 ± 0.08	0.03 ± 0.16
10–90th percentiles	0.3–1.2	0.00–0.16	0.00–0.15
maximum	3.5	0.34	1.90
Pyruvic acid [pptv]			
Mean ± STD	-	95 ± 45	-
10–90th percentiles	-	35–155	-
maximum	-	330	-
T [°C]			
Mean ± STD	16.9 ± 5.7	10.6 ± 3.9	30.4 ± 4.0
10–90th percentiles	9.7–25.0	5.3–15.6	25.8–35.2
maximum	31.5	20.0	46.2

Notes: STD = standard deviation. NO_x, O_3 and T were measured by instruments other than the CI-QMS. For details on NOTOMO, IBAIRN and AQABA see Chapters 2–4, respectively.

sionally SO_2 plumes up to 1 ppbv were registered when the air originated from the north-east, most likely from point sources (e.g. coal-burning power plants) in northern Finland and Russia. PAN levels now and then increased to ≈ 200 pptv, reflecting an incidental increase in photochemical activity and the presence of NO_x at this remote site. However, a more detailed analysis of PAN and PAA was precluded by the (above-mentioned) instrumental limitations. $ClNO_2$ remained below the detection limit during the whole campaign, most probably due to a lack of N_2O_5 because of the high nocturnal NO_3 reactivity reported by Liebmann et al. (2018), which prevented N_2O_5 and thus $ClNO_2$ formation. In addition, a lack of particulate chloride could also play a role, as the site was rarely impacted by marine air masses from the south. In contrast, biogenic emissions from the boreal forest in late summer / autumn were still large and mixing ratios of pyruvic acid regularly exceeded 100 pptv.

Pyruvic acid and its impact on radical chemistry

Pyruvic acid is a largely unexplored organic acid of biogenic origin that plays a crucial role in plant metabolism, is present in tropospheric air in both gas-phase and aerosol phase and is implicated in SOA formation. During IBAIRN the first gas-phase measurements in the boreal forest were performed, with observed mixing ratios ranging between 20 and 330 pptv. By assuming steady-state and estimating the pyruvic acid loss rate through photolysis and deposition, the source strength (at local noon) was estimated as ≈ 60 pptv h^{-1}, which could not be explained by photochemical production from isoprene, as commonly suggested in the literature. Similarities with the diurnal profile of isoprene and monoterpenes (as well as occasional co-variations when air had passed over a sawmill), revealed that pyruvic acid is most likely emitted directly from the biosphere. With the mixing ratios observed in September, pyruvic acid represents an important source of acetaldehyde and acetyl peroxy radicals, enhancing the formation of PAN, C_2-organic acids and CH_3O_2. To quantify its source strength and role during other seasons and to better understand its sources and sinks in the boreal forest, further field and enclosure studies will be necessary. Also, model calculations using the IBAIRN dataset could help to more accurately define its role. Measurements in other environments would be useful to constrain the role of pyruvic acid in the troposphere in general.

5.2.3 AQABA ship campaign around the Arabian Peninsula

The AQABA (Air Quality and climate change in the Arabian BAsin) ship campaign took place along the sea route between southern France and Kuwait in summer 2017. The aim was to study air quality and climate in a (largely unexplored) region (Eastern Mediterranean and Middle East) that suffers from severe air pollution and is likely to be heavily impacted by future climate change. After departure from southern France the research vessel passed various regions including the Mediterranean Sea, the Suez Canal, the Red Sea, the Gulf of Aden, the Arabian Sea, the Gulf of Oman and the Arabian Gulf. During AQABA, a spatio-

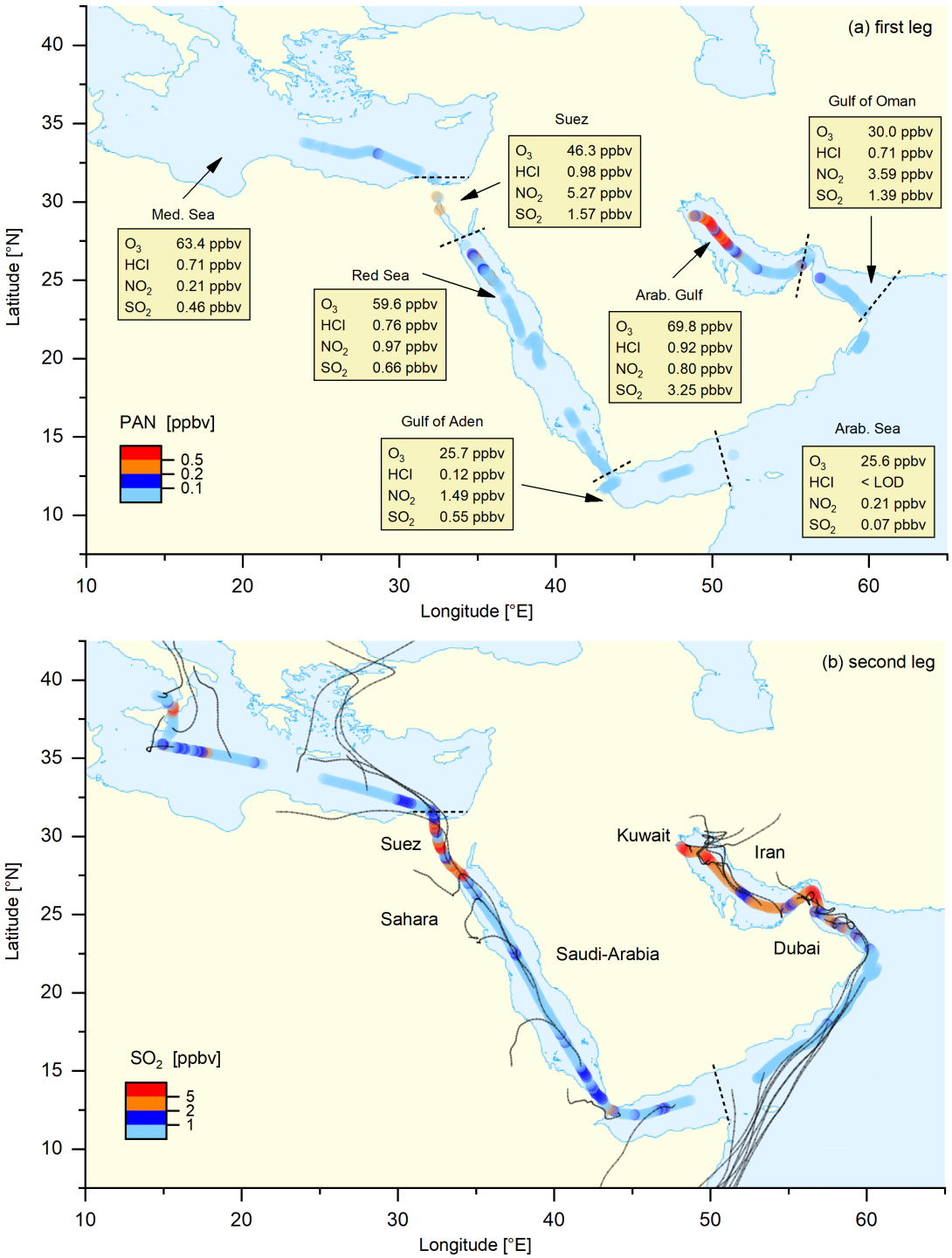

Figure 5.1: Map of (a) PAN mixing ratios (1-hour averages) for the first leg, together with (median) night-time mixing ratios of O_3, HCl, NO_2 and SO_2 for different regions (data from both legs combined) demarked by the dashed lines. (b) SO_2 mixing ratios (1-hour averages) for the second leg, together with 48 h back-trajectories calculated with HYSPLIT (Stein et al., 2015; Rolph et al., 2017).

temporally variable mix of anthropogenic (mainly petrochemical) and biogenic (mainly DMS) emissions, dust particles and maritime aerosols was sampled. For a substantial fraction of the campaign the measurements were also impacted by emissions from other ships (especially in the narrow and crowded shipping lanes in the Suez Canal and the Arabian Gulf), characterised by a distinct peak shape and the co-variance of SO_2 and NO_2 signals.

Along the ship track a high variability of SO_2 mixing ratios was observed, with the lowest values detected in the Arabian Sea due to missing sources, and high mixing ratios (several ppbv) found in the Arabian Gulf, the Gulf of Suez and the Suez Canal (see Fig. 5.1 and Appendix A). In particular over the Arabian Gulf, SO_2 levels regularly exceeded 5 ppbv and even approached 20 ppbv close to Kuwait where emissions from oil and gas industry were strongest (originating from Kuwait, Iran and offshore platforms). Further, ship traffic represented a major source of SO_2 emissions in this region and the SO_2 dataset has been used to calculate emission factors from different types of vessels (Celik et al., in preparation) and to estimate the sulphur content of the ship diesel used (which is, in contrast to European waters, not regulated). In addition, Pfannerstill et al. (2019) reported that, in narrow sea-way regions during AQABA, SO_2 and CO from ship exhaust accounted for 4–6 % of the observed OH reactivity. The CI-QMS observations of SO_2 underline that the Arabian Gulf region is subject to major air pollution and are in broad agreement with OMI satellite data (see Fig. 1.13), which also indicate several SO_2 hotspots in this region. The large SO_2 emissions are also reflected in the dominance of sulphate in the aerosol phase, which can have a significant impact on cloud properties and climate.

In contrast, elevated PAN mixing ratios >100 pptv were only occasionally observed during the AQABA campaign (see Fig. 5.1 and Appendix A), as the high average temperatures in summer (usually $>30\,^{\circ}$C) resulted in a thermal lifetime of typically less than one hour. Thus transport of PAN over longer distances was precluded and only very local sources could be detected, for example in the Arabian Gulf, which was characterised by remarkably strong photochemical activity with O_3 mixing ratios exceeding 150 ppbv. Here PAN levels up to 2 ppbv were measured when approaching or leaving the harbour of Kuwait. However, models predict much higher PAN levels in the Gulf region during winter when thermal decomposition is minimised and transport might play a more important role. It would thus be of interest to perform further PAN measurements around the Arabian Peninsula during other seasons to verify these predictions and to quantify the importance of PAN for the Middle East region.

$ClNO_2$ and its impact on radical chemistry

$ClNO_2$ mixing ratios observed along the ship track ranged from below the detection limit over the Arabian Sea to a few hundred pptv over the Gulf of Oman, the northern part of the Red Sea, the Gulf of Suez and the Mediterranean Sea close to Sicily and Italy (see Fig. 5.2). The largest value of ≈ 600 pptv was registered over the Gulf of Suez, due to both high NO_x concentrations and particulate chloride

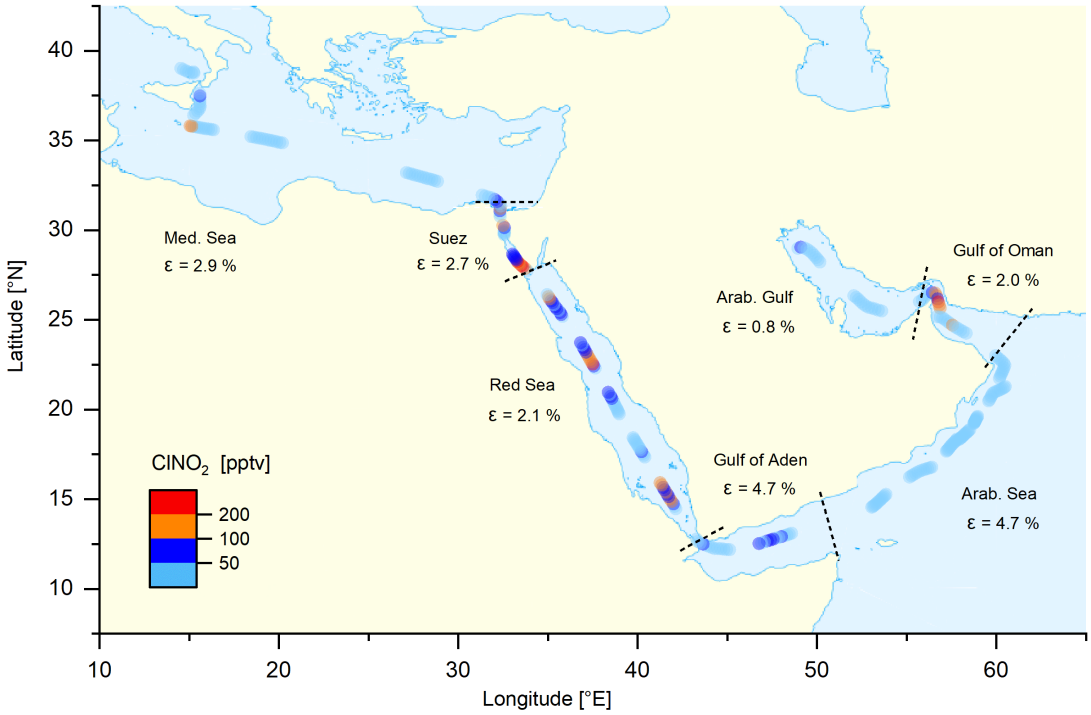

Figure 5.2: Map of nocturnal $ClNO_2$ mixing ratios (1-hour averages) for the second leg, together with (median) $ClNO_2$ production efficiencies ϵ (see Chapter 4) calculated for different regions (data from both legs combined).

availability. The overall $ClNO_2$ production efficiency ϵ, i.e. the yield of $ClNO_2$ per NO_3 molecule formed in the reaction of NO_2 with O_3 (see Sect. 4.3.2), was generally low with a campaign median of 2.7 % and the lowest efficiencies found in the Arabian Gulf (Fig. 5.2), where NO_3 reactivity and temperatures were highest. Despite high sea salt concentrations, ϵ remained relatively low compared to previous measurements in the polluted marine boundary layer or at continental sites, which can be explained by exceptionally high nocturnal temperatures during AQABA, shifting the equilibrium from N_2O_5 towards NO_3 and lowering the importance of N_2O_5 uptake to the particle phase relative to direct NO_3 losses. Nevertheless, the photolysis of $ClNO_2$ as well as the oxidation of HCl, which had been released from acid displacement by H_2SO_4 and HNO_3, were found to represent important sources of chlorine radicals in the polluted marine boundary layer (with variable fractional contributions). Although OH formation rates were about two orders of magnitude larger than for Cl, the high rate coefficient ratio for reactions of Cl compared to OH towards some hydrocarbons (e.g. propane) suggests a potentially enhanced hydrocarbon oxidation in some areas.

The AQABA campaign confirmed that the CI-QMS is well-suited for future measurements of $ClNO_2$ in areas where $ClNO_2$, HCl and SO_2 play an important role and transport of ^{210}Po might not be feasible. In this way the instrument can contribute to the closure of observational gaps in understudied regions, as

$ClNO_2$ measurements are mainly available for North America, Europe and China. It would also be of interest to conduct measurements over a longer time period in certain regions around the Arabian Peninsula or to realise additional measurements along the coast to draw a more detailed picture of the importance of $ClNO_2$ in the whole area. Further measurements in other seasons would help to investigate if lower temperatures in winter would lead to higher $ClNO_2$ mixing ratios than observed during AQABA. Measured $ClNO_2$, HCl, SO_2 and PAN are also valuable for improving regional and global chemistry models in order to contribute to a better understanding and prediction of atmospheric processes in the Middle East region.

References

Abdelkader, M., Metzger, S., Mamouri, R. E., Astitha, M., Barrie, L., Levin, Z., and Lelieveld, J. Dust-air pollution dynamics over the eastern Mediterranean. *Atmospheric Chemistry and Physics*, 15(16):9173–9189, 2015. 10.5194/acp-15-9173-2015.

Aldener, M., Brown, S. S., Stark, H., Williams, E. J., Lerner, B. M., Kuster, W. C., Goldan, P. D., Quinn, P. K., Bates, T. S., Fehsenfeld, F. C., and Ravishankara, A. R. Reactivity and loss mechanisms of NO3 and N2O5 in a polluted marine environment: Results from in situ measurements during New England Air Quality Study 2002. *Journal of Geophysical Research-Atmospheres*, 111, art. D23S73(D23), 2006. https://doi.org/10.1029/2006JD007252.

Ammann, M., Cox, R. A., Crowley, J. N., Jenkin, M. E., Mellouki, A., Rossi, M. J., Troe, J., and Wallington, T. J. Evaluated kinetic and photochemical data for atmospheric chemistry: Volume VI - heterogeneous reactions with liquid substrates. *Atmospheric Chemistry and Physics*, 13(16):8045–8228, 2013. ISSN 1680-7324. https://doi.org/10.5194/acp-13-8045-2013.

Andreae, M. O., Talbot, R. W., and Li, S. M. Atmospheric measurements of pyruvic and formic acid. *Journal of Geophysical Research-Atmospheres*, 92(D6):6635–6641, 1987. ISSN 2169-897X. https://doi.org/10.1029/JD092iD06p06635.

Arey, J., Obermeyer, G., Aschmann, S. M., Chattopadhyay, S., Cusick, R. D., and Atkinson, R. Dicarbonyl products of the OH radical-initiated reaction of a series of aromatic hydrocarbons. *Environmental Science & Technology*, 43(3):683–689, 2009. ISSN 0013-936X. https://doi.org/10.1021/es8019098.

Atkinson, R. Atmospheric chemistry of VOCs and NOx. *Atmospheric environment*, 34 (12-14):2063–2101, 2000.

Atkinson, R. and Arey, J. Gas-phase tropospheric chemistry of biogenic volatile organic compounds: a review. *Atmospheric Environment*, 37:197–219, 2003. https://doi.org/10.1016/S1352-2310(03)00391-1.

Atkinson, R., Baulch, D. L., Cox, R. A., Crowley, J. N., Hampson, R. F., Hynes, R. G., Jenkin, M. E., Rossi, M. J., and Troe, J. Evaluated kinetic and photochemical data for atmospheric chemistry: Volume I - gas phase reactions of Ox, HOx, NOx and SOx species. *Atmospheric Chemistry and Physics*, 4:1461–1738, 2004. ISSN 1680-7324. https://doi.org/10.5194/acp-4-1461-2004.

Atkinson, R., Baulch, D., Cox, R., Crowley, J., Hampson, R., Hynes, R., Jenkin, M., Rossi, M., and Troe, J. Evaluated kinetic and photochemical data for atmospheric chemistry: Volume II - reactions of organic species. *Atmospheric Chemistry and Physics*, pages 3625–4055, 2006. https://doi.org/10.5194/acp-6-3625-2006.

Atkinson, R., Baulch, D., Cox, R., Crowley, J., Hampson, R., Hynes, R., Jenkin, M., Rossi, M., and Troe, J. Evaluated kinetic and photochemical data for atmospheric chemistry: Volume III - gas phase reactions of inorganic halogens. *Atmospheric Chemistry and Physics*, 7:981–1191, 2007. https://doi.org/10.5194/acp-7-981-2007.

Aufmhoff, H., Schäuble, D., Roiger, A., Arnold, F., Jurkat, T., Voigt, C., and Schlager, H. Chemical ionization mass spectrometric measurements of atmospheric trace gases. In *Atmospheric Physics*, pages 277–296. Springer, 2012.

Awtrey, A. D. and Connick, R. E. The absorption spectra of I2, I3-, I-, IO3-, S4O6- and S2O3-. heat of the reaction I3- = I2 + I-. *Journal of the American Chemical Society*, 73(4):1842–1843, 1951. ISSN 0002-7863. https://doi.org/10.1021/ja01148a504.

Baboukas, E. D., Kanakidou, M., and Mihalopoulos, N. Carboxylic acids in gas and particulate phase above the Atlantic Ocean. *Journal of Geophysical Research-Atmospheres*, 105(D11):14459–14471, 2000. ISSN 2169-897X. https://doi.org/10.1029/1999jd900977.

Bahou, M., Chung, C. Y., Lee, Y. P., Cheng, B. M., Yung, Y. L., and Lee, L. C. Absorption cross sections of HCl and DCl at 135–232 nanometers: Implications for photodissociation on Venus. *Astrophysical Journal*, 559(2):L179–L182, 2001.

Bannan, T. J., Booth, A. M., Bacak, A., Muller, J. B. A., Leather, K. E., Le Breton, M., Jones, B., Young, D., Coe, H., Allan, J., Visser, S., Slowik, J. G., Furger, M., Prevot, A. S. H., Lee, J., Dunmore, R. E., Hopkins, J. R., Hamilton, J. F., Lewis, A. C., Whalley, L. K., Sharp, T., Stone, D., Heard, D. E., Fleming, Z. L., Leigh, R., Shallcross, D. E., and Percival, C. J. The first UK measurements of nitryl chloride using a chemical ionization mass spectrometer in central London in the summer of 2012, and an investigation of the role of Cl atom oxidation. *Journal of Geophysical Research-Atmospheres*, 120(11):5638–5657, 2015. ISSN 2169-897X. https://doi.org/10.1002/2014JD022629.

Bannan, T. J., Bacak, A., Le Breton, M., Flynn, M., Ouyang, B., McLeod, M., Jones, R., Malkin, T. L., Whalley, L. K., and Heard, D. E. Ground and airborne UK measurements of nitryl chloride: An investigation of the role of Cl atom oxidation at Weybourne Atmospheric Observatory. *Journal of Geophysical Research: Atmospheres*, 122 (20):11,154–11,165, 2017. ISSN 2169-8996. https://doi.org/10.1002/2017JD026624.

Bardouki, H., Berresheim, H., Vrekoussis, M., Sciare, J., Kouvarakis, G., Oikonomou, K., Schneider, J., and Mihalopoulos, N. Gaseous (DMS, MSA, SO2, H2SO4 and DMSO) and particulate (sulfate and methanesulfonate) sulfur species over the northeastern coast of Crete. *Atmospheric Chemistry and Physics*, 3:1871–1886, 2003. ISSN 1680-7316. https://doi.org/10.5194/acp-3-1871-2003.

Bayram, S. B. and Freamat, M. V. Vibrational spectra of N-2: An advanced undergraduate laboratory in atomic and molecular spectroscopy. *American Journal of Physics*, 80(8):664–669, 2012. ISSN 0002-9505. https://doi.org/10.1119/1.4722793.

Behnke, W., George, C., Scheer, V., and Zetzsch, C. Production and decay of ClNO2 from the reaction of gaseous N2O5 with NaCl solution: Bulk and aerosol experiments. *Journal of Geophysical Research: Atmospheres*, 102(D3):3795–3804, 1997.

Beirle, S., Platt, U., Wenig, M., and Wagner, T. Weekly cycle of NO2 by GOME measurements: A signature of anthropogenic sources. *Atmospheric Chemistry and Physics*, 3(6):2225–2232, 2003.

Berges, M. G. M. and Warneck, P. Product quantum yields for the 350 nm photodecomposition of pyruvic-acid in air. *Berichte Der Bunsen-Gesellschaft-Physical Chemistry Chemical Physics*, 96(3):413–416, 1992. ISSN 0005-9021. https://doi.org/10.1002/bbpc.19920960334.

Bertram, T. H. and Thornton, J. A. Toward a general parameterization of N2O5 reactivity on aqueous particles: the competing effects of particle liquid water, nitrate and chloride. *Atmospheric Chemistry and Physics*, 9(21):8351–8363, 2009. ISSN 1680-7316. https://doi.org/10.5194/acp-9-8351-2009.

Bertram, T. H., Thornton, J. A., Riedel, T. P., Middlebrook, A. M., Bahreini, R., Bates, T. S., Quinn, P. K., and Coffman, D. J. Direct observations of N2O5 reactivity on ambient aerosol particles. *Geophysical Research Letters*, 36, L19803, doi:10.1029/2009GL040248, 2009.

Bogumil, K., Orphal, J., Homann, T., Voigt, S., Spietz, P., Fleischmann, O. C., Vogel, A., Hartmann, M., Kromminga, H., Bovensmann, H., Frerick, J., and Burrows, J. P. Measurements of molecular absorption spectra with the SCIAMACHY pre-flight model: instrument characterization and reference data for atmospheric remote-sensing in the 230–2380 nm region. *Journal of Photochemistry and Photobiology a-Chemistry*, 157 (2-3):167–184, 2003. ISSN 1010-6030. https://doi.org/10.1016/s1010-6030(03)00062-5.

Bonan, G. B. Forests and climate change: forcings, feedbacks, and the climate benefits of forests. *science*, 320(5882):1444–1449, 2008. ISSN 0036-8075. https://doi.org/10.1126/science.1155121.

Bourtsoukidis, E., Ernle, L., Crowley, J. N., Lelieveld, J., Paris, J. D., Pozzer, A., Walter, D., and Williams, J. Non Methane Hydrocarbon (C2-C8) sources and sinks around the Arabian Peninsula. *Atmos. Chem. Phys. Discuss.*, 2019:1–45, 2019. ISSN 1680-7375. https://doi.org/10.5194/acp-2019-92.

Bradshaw, C. J. and Warkentin, I. G. Global estimates of boreal forest carbon stocks and flux. *Global and Planetary Change*, 128:24–30, 2015. ISSN 0921-8181. https://doi.org/10.1016/j.gloplacha.2015.02.004.

Brown, S. S., Stark, H., and Ravishankara, A. Applicability of the steady state approximation to the interpretation of atmospheric observations of NO3 and n2o5. *Journal of Geophysical Research: Atmospheres*, 108(D17), 2003. https://doi.org/10.1029/2003JD003407.

Brown, S. S., Ryerson, T. B., Wollny, A. G., Brock, C. A., Peltier, R., Sullivan, A. P., Weber, R. J., Dube, W. P., Trainer, M., Meagher, J. F., Fehsenfeld, F. C., and Ravishankara, A. R. Variability in nocturnal nitrogen oxide processing and its role in regional air quality. *Science*, 311(5757):67–70, 2006. https://doi.org/10.1126/science.1120120.

Brown, S. S., Dube, W. P., Fuchs, H., Ryerson, T. B., Wollny, A. G., Brock, C. A., Bahreini, R., Middlebrook, A. M., Neuman, J. A., Atlas, E., Roberts, J. M., Osthoff, H. D., Trainer, M., Fehsenfeld, F. C., and Ravishankara, A. R. Reactive uptake coefficients for N2O5 determined from aircraft measurements during the second texas air quality study: Comparison to current model parameterizations. *Journal of Geophysical Research-Atmospheres*, 114, art. D00F10, 2009. https://doi.org/10.1029/2008JD011679.

Brown, S. S., Dube, W. P., Tham, Y. J., Zha, Q. Z., Xue, L. K., Poon, S., Wang, Z., Blake, D. R., Tsui, W., Parrish, D. D., and Wang, T. Nighttime chemistry at a high altitude site above Hong Kong. *Journal of Geophysical Research-Atmospheres*, 121(5): 2457–2475, 2016. ISSN 2169-897X. https://doi.org/10.1002/2015jd024566.

Burkholder, J. B., Sander, S. P., Abbatt, J., Barker, J. R., Huie, R. E., Kolb, C. E., Kurylo, M. J., Orkin, V. L., Wilmouth, D. M., and Wine, P. H. Chemical kinetics and photochemical data for use in atmospheric studies, evaluation no. 18, JPL Publication 15-10, Jet Propulsion Laboratory, Pasadena, http://jpldataeval.jpl.nasa.gov. Report, 2015.

Butchart, S. H., Walpole, M., Collen, B., Van Strien, A., Scharlemann, J. P., Almond, R. E., Baillie, J. E., Bomhard, B., Brown, C., Bruno, J., et al. Global biodiversity: indicators of recent declines. *Science*, 328(5982):1164–1168, 2010.

Carlton, A. G., Turpin, B. J., Lim, H. J., Altieri, K. E., and Seitzinger, S. Link between isoprene and secondary organic aerosol (SOA): Pyruvic acid oxidation yields low volatility organic acids in clouds. *Geophysical Research Letters*, 33(6), 2006. https://doi.org/10.1029/2005GL025374.

Celik, S., Drewnick, F., Fachinger, F., Brooks, J., Darbyshire, E., Coe, H., Paris, J.-D., Eger, P. G., Schuladen, J., Tadic, I., Friedrich, N., Dienhart, D., Hottmann, B., Fischer, H., Crowley, J. N., Harder, H., and Borrmann, S. Influence of vessel characteristics and atmospheric processes on the gas and particle phase of ship emission: In-situ measurements in the Mediterranean Sea and around the Arabian Peninsula. Work submitted for publication in ACP.

Chadwick, B. M., Long, D. A., and Qureshi, S. U. The Raman and infra-red spectra of the dicyanoiodate(I) ion. *Journal of Raman Spectroscopy*, 9(1):1–4, 1980. ISSN 0377-0486. https://doi.org/10.1002/jrs.1250090103.

Chang, W. L., Bhave, P. V., Brown, S. S., Riemer, N., Stutz, J., and Dabdub, D. Heterogeneous atmospheric chemistry, ambient measurements, and model calculations of N2O5: A review. *Aerosol Science and Technology*, 45(6):665–695, 2011. https://doi.org/10.1080/02786826.2010.551672.

Chapman, S. XXXV. On ozone and atomic oxygen in the upper atmosphere. *The London, Edinburgh, and Dublin Philosophical Magazine and Journal of Science*, 10 (64):369–383, 1930.

Chase, M.W., J. NIST-JANAF Themochemical Tables, fourth edition. *J. Phys. Chem. Ref. Data*, Monograph 9:1–1951, 1998.

Ciais, P., Sabine, C., Bala, G., Bopp, L., Brovkin, V., Canadell, J., Chhabra, A., DeFries, R., Galloway, J., Heimann, M., et al. Carbon and other biogeochemical cycles. Climate change 2013: the physical science basis. contribution of Working Group I to the Fifth Assessment Report of the Intergovernmental Panel on Climate Change. *Cambridge University Press Cambridge United Kingdom and New York NY USA*, pages 465–570, 2013.

Clegg, S. L., Brimblecombe, P., and Wexler, A. S. Thermodynamic model of the system h+-nh4+-na+-so42–no3–cl–h2o at 298.15 k. *Journal of Physical Chemistry A*, 102 (12):2155–2171, 1998. ISSN 1089-5639. https://doi.org/10.1021/jp973043j.

Coggon, M., Sorooshian, A., Wang, Z., Metcalf, A., Frossard, A., Lin, J., Craven, J., Nenes, A., Jonsson, H., Russell, L., et al. Ship impacts on the marine atmosphere: insights into the contribution of shipping emissions to the properties of marine aerosol and clouds. *Atmospheric Chemistry and Physics*, 12(18):8439–8458, 2012.

Corbett, J. J. and Fischbeck, P. Emissions from ships. *Science*, 278(5339):823–824, 1997.

Crowley, J., Schuster, G., Pouvesle, N., Parchatka, U., Fischer, H., Bonn, B., Bingemer, H., and Lelieveld, J. Nocturnal nitrogen oxides at a rural mountain-site in south-western Germany. *Atmos. Chem. Phys*, 10(6):2795–2812, 2010. https://doi.org/10.5194/acp-10-2795-2010.

Crowley, J. N., Pouvesle, N., Phillips, G. J., Axinte, R., Fischer, H., Petäjä, T., Nölscher, A., Williams, J., Hens, K., Harder, H., et al. Insights into HOx and ROx chemistry in the boreal forest via measurement of peroxyacetic acid, peroxyacetic nitric anhydride (PAN) and hydrogen peroxide. *Atmospheric Chemistry and Physics*, 18(18):13457–13479, 2018.

Crutzen, P. J. The influence of nitrogen oxides on the atmospheric ozone content. *Quarterly Journal of the Royal Meteorological Society*, 96(408):320–325, 1970. https://doi.org/10.1002/qj.49709640815.

Crutzen, P. J. The "anthropocene". In *Earth system science in the anthropocene*, pages 13–18. Springer, 2006.

Dawson, P. Quadrupole mass analyzers: performance, design and some recent applications. *Mass Spectrometry Reviews*, 5(1):1–37, 1986.

Dawson, P. H. Quadrupole mass spectrometry and its applications. *Eisevier, New York*, page 2, 1976.

Dayan, U., Ricaud, P., Zbinden, R., and Dulac, F. Atmospheric pollution over the eastern Mediterranean during summer – a review. *Atmospheric Chemistry and Physics*, 17 (21):13233–13263, 2017. https://doi.org/10.5194/acp-17-13233-2017.

DeCarlo, P. F., Kimmel, J. R., Trimborn, A., Northway, M. J., Jayne, J. T., Aiken, A. C., Gonin, M., Fuhrer, K., Horvath, T., Docherty, K. S., Worsnop, D. R., and Jimenez, J. L. Field-deployable, high-resolution, time-of-flight aerosol mass spectrometer. *Analytical Chemistry*, 78(24):8281–8289, 2006. ISSN 0003-2700. https://doi.org/10.1021/ac061249n.

Dentener, F. J. and Crutzen, P. J. Reaction of N2O5 on tropospheric aerosols: Impact on the global distributions of NOx, O3, and OH. *Journal of Geophysical Research: Atmospheres*, 98(D4):7149–7163, 1993. https://doi.org/10.1029/92JD02979.

Derstroff, B., Huser, I., Bourtsoukidis, E., Crowley, J. N., Fischer, H., Gromov, S., Harder, H., Janssen, R. H. H., Kesselmeier, J., Lelieveld, J., Mallik, C., Martinez, M., Novelli, A., Parchatka, U., Phillips, G. J., Sander, R., Sauvage, C., Schuladen, J., Stonner, C., Tomsche, L., and Williams, J. Volatile organic compounds (VOCs) in photochemically aged air from the eastern and western Mediterranean. *Atmospheric Chemistry and Physics*, 17(15):9547–9566, 2017. ISSN 1680-7316.

Douglas, D. Linear quadrupoles in mass spectrometry. *Mass spectrometry reviews*, 28 (6):937–960, 2009.

Draxler, R. and Rolph, G. HYSPLIT (HYbrid Single-Particle Lagrangian Integrated Trajectory) Model access via NOAA ARL READY Website (http://ready.arl.noaa.gov/hysplit.php). NOAA Air Resources Laboratory, Silver Spring, MD. 2011.

Eerdekens, G., Yassaa, N., Sinha, V., Aalto, P. P., Aufmhoff, H., Arnold, F., Fiedler, V., Kulmala, M., and Williams, J. VOC measurements within a boreal forest during spring 2005: on the occurrence of elevated monoterpene concentrations during night time intense particle concentration events. *Atmos. Chem. Phys.*, 9(21):8331–8350, 2009. ISSN 1680-7324. https://doi.org/10.5194/acp-9-8331-2009.

Eger, P. G., Helleis, F., Schuster, G., Phillips, G. J., Lelieveld, J., and Crowley, J. N. Chemical ionization quadrupole mass spectrometer with an electrical discharge ion source for atmospheric trace gas measurement. *Atmospheric Measurement Techniques*, 12(3):1935–1954, 2019a. https://doi.org/10.5194/amt-12-1935-2019.

Eger, P. G., Friedrich, N., Schuladen, J., Shenolikar, J., Fischer, H., Tadic, I., Harder, H., Martinez, M., Rohloff, R., Tauer, S., Fachinger, F., Drewnick, F., Brooks, J., Darbyshire, E., Sciare, J., Pikridas, M., Lelieveld, J., and Crowley, J. N. Shipborne measurements of ClNO2 in the Mediterranean Sea and around the Arabian Peninsula during summer. *Atmospheric Chemistry and Physics Discussions*, 2019:1–37, 2019b. https://doi.org/10.5194/acp-2019-531.

Eger, P. G., Schuladen, J., Sobanski, N., Fischer, H., Karu, E., Williams, J., Riva, M., Zha, Q., Ehn, M., Quéléver, L. L. J., Schallhart, S., Lelieveld, J., and Crowley, J. N. Pyruvic acid in the boreal forest: first measurements and impact on radical chemistry. *Atmospheric Chemistry and Physics Discussions*, 2019:1–24, 2019c. https://doi.org/10.5194/acp-2019-768.

Eugene, A. J. and Guzman, M. I. Reactivity of ketyl and acetyl radicals from direct solar actinic photolysis of aqueous pyruvic acid. *The journal of physical chemistry. A*, 2017. https://doi.org/10.1021/acs.jpca.6b11916.

Faxon, C. B., Bean, J. K., and Hildebrandt Ruiz, L. Inland concentrations of Cl2 and ClNO2 in Southeast Texas suggest chlorine chemistry significantly contributes to atmospheric reactivity. *Atmosphere*, 6(10):1487–1506, 2015. ISSN 2073-4433. https://doi.org/10.3390/atmos6101487.

Fick, J., Pommer, L., Nilsson, C., and Andersson, B. Effect of OH radicals, relative humidity, and time on the composition of the products formed in the ozonolysis of alpha-pinene. *Atmospheric Environment*, 37(29):4087–4096, 2003. ISSN 1352-2310. https://doi.org/10.1016/s1352-2310(03)00522-3.

Finlayson-Pitts, B., Ezell, M., and Pitts Jr, J. Formation of chemically active chlorine compounds by reactions of atmospheric nacl particles with gaseous N2O5 and clono2. *Nature*, 337(6204):241, 1989.

Finlayson-Pitts, B. J. and Pitts Jr, J. N. *Chemistry of the upper and lower atmosphere: theory, experiments, and applications*. Elsevier, 1999.

Fishman, J. and Crutzen, P. J. The origin of ozone in the troposphere. *Nature*, 274 (5674):855, 1978. ISSN 1476-4687. https://doi.org/10.1038/274855a0.

Flocke, F. M., Weinheimer, A. J., Swanson, A. L., Roberts, J. M., Schmitt, R., and Shertz, S. On the measurement of PANs by gas chromatography and electron capture detection. *Journal of Atmospheric Chemistry*, 52(1):19–43, 2005.

Fontijn, A., Sabadell, A. J., and Ronco, R. J. Homogeneous chemiluminescent measurement of nitric oxide with ozone - implications for continuous selective monitoring of gaseous air pollutants. *Analytical Chemistry*, 42(6):575–579, 1970. https://doi.org/10.1021/ac60288a034.

Friedrich, N. *Development and characterisation of two methods for the wet-chemical calibration of peracetic acid for chemical ionisation mass-spectrometry (in German)*. Thesis, 2015.

Friese, E. and Ebel, A. Temperature dependent thermodynamic model of the system H+ - NH4+ - Na+ - SO42- - NO3- - Cl- - H2O. *The Journal of Physical Chemistry A*, 114(43):11595–11631, 2010. ISSN 1089-5639. https://doi.org/10.1021/jp101041j.

Furgeson, A., Mielke, L. H., Paul, D., and Osthoff, H. D. A photochemical source of peroxypropionic and peroxyisobutanoic nitric anhydride. *Atmospheric Environment*, 45(28):5025–5032, 2011. ISSN 1352-2310. https://doi.org/10.1016/j.atmosenv.2011.03.072.

Gaffney, J., Marley, N., Cunningham, M., and Doskey, P. Measurements of peroxyacyl nitrates (PANs) in Mexico City: implications for megacity air quality impacts on regional scales. *Atmospheric Environment*, 33(30):5003–5012, 1999. ISSN 1352-2310. https://doi.org/10.1016/S1352-2310(99)00263-0.

Galloway, J. N., Dentener, F. J., Capone, D. G., Boyer, E. W., Howarth, R. W., Seitzinger, S. P., Asner, G. P., Cleveland, C. C., Green, P., Holland, E. A., et al. Nitrogen cycles: past, present, and future. *Biogeochemistry*, 70(2):153–226, 2004.

Goldstein, A. H. and Galbally, I. E. Known and unexplored organic constituents in the earth's atmosphere, 2007.

Goos, E., Burcat, A., and Ruscic, B. Extended third millennium ideal gas and condensed phase thermochemical database for combustion with updates from active thermochemical tables: Update of "third millennium ideal gas and condensed phase thermochemical database for combustion with updates from active thermochemical tables by Alexander Burcat and Branko Ruscic, Report ANL 05/20 and TAE 960 Technion-IIT, Aerospace Engineering, and Argonne National Laboratory, Chemistry Division, September 2005. Report, 2005.

Graus, M., Muller, M., and Hansel, A. High resolution PTR-TOF: Quantification and formula confirmation of VOC in real time. *Journal of the American Society for Mass Spectrometry*, 21(6):1037–1044, 2010. ISSN 1044-0305. https://doi.org/10.1016/j.jasms.2010.02.006.

Griffith, E. C., Carpenter, B. K., Shoemaker, R. K., and Vaida, V. Photochemistry of aqueous pyruvic acid. *Proceedings of the National Academy of Sciences of the United States of America*, 110(29):11714–11719, 2013. ISSN 0027-8424. https://doi.org/10.1073/pnas.1303206110.

Grosjean, D. Atmospheric reactions of pyruvic acid. *Atmospheric Environment (1967)*, 17(11):2379–2382, 1983. ISSN 0004-6981. https://doi.org/10.1016/0004-6981(83)90242-1.

Grosjean, D. Atmospheric reactions of ortho cresol: gas phase and aerosol products. *Atmospheric Environment (1967)*, 18(8):1641–1652, 1984. ISSN 0004-6981. https://doi.org/10.1016/0004-6981(84)90386-X.

Grosjean, D., Williams, E. L., and Grosjean, E. Atmospheric chemistry of isoprene and of its carbonyl products. *Environmental science & technology*, 27(5):830–840, 1993. ISSN 0013-936X. https://doi.org/10.1021/es00042a004.

Gross, J. H. *Mass spectrometry: a textbook*. Springer Science & Business Media, 2nd edition, 2011.

Guenther, A., Hewitt, C. N., Erickson, D., Fall, R., Geron, C., Graedel, T., Harley, P., Klinger, L., Lerdau, M., McKay, W., et al. A global model of natural volatile organic compound emissions. *Journal of Geophysical Research: Atmospheres*, 100 (D5):8873–8892, 1995. https://doi.org/10.1029/94JD02950.

Gurjar, B., Ravindra, K., and Nagpure, A. S. Air pollution trends over Indian megacities and their local-to-global implications. *Atmospheric Environment*, 142:475–495, 2016.

Gysel, M., Crosier, J., Topping, D., Whitehead, J., Bower, K., Cubison, M., Williams, P., Flynn, M., McFiggans, G., and Coe, H. Closure study between chemical composition and hygroscopic growth of aerosol particles during TORCH2. *Atmospheric Chemistry and Physics*, 7(24):6131–6144, 2007. ISSN 1680-7316.

Haagen-Smit, A. J. Chemistry and physiology of Los Angeles smog. *Industrial & Engineering Chemistry*, 44(6):1342–1346, 1952.

Hakola, H., Tarvainen, V., Laurila, T., Hiltunen, V., Hellén, H., and Keronen, P. Seasonal variation of VOC concentrations above a boreal coniferous forest. *Atmospheric Environment*, 37(12):1623–1634, 2003. ISSN 1352-2310. https://doi.org/10.1016/S1352-2310(03)00014-1.

Hakola, H., Hellén, H., and Laurila, T. Ten years of light hydrocarbons (C2-C6) concentration measurements in background air in Finland. *Atmospheric Environment*, 40(19):3621–3630, 2006. ISSN 1352-2310. https://doi.org/10.1016/j.atmosenv.2005.08.019.

Hakola, H., Hellén, H., Hemmilä, M., Rinne, J., and Kulmala, M. In situ measurements of volatile organic compounds in a boreal forest. *Atmos. Chem. Phys.*, 12(23):11665–11678, 2012. ISSN 1680-7324. https://doi.org/10.5194/acp-12-11665-2012.

Hallquist, M., Wenger, J. C., Baltensperger, U., Rudich, Y., Simpson, D., Claeys, M., Dommen, J., Donahue, N., George, C., Goldstein, A., et al. The formation, properties and impact of secondary organic aerosol: current and emerging issues. *Atmospheric chemistry and physics*, 9(14):5155–5236, 2009. https://doi.org/10.5194/acp-9-5155-2009.

Hao, C. T., Gilbert, T. M., and Sunderlin, L. S. The bond dissociation energies of SO3-X- (X = F, Cl, Br, and I). *Canadian Journal of Chemistry*, 83(11):2013–2019, 2005. ISSN 0008-4042. https://doi.org/10.1139/v05-216.

Hari, P. and Kulmala, M. Station for Measuring Ecosystem-Atmosphere Relations (SMEAR II). *Boreal Env. Res.*, 10:315–322, 2005. https://doi.org/10.1007/978-94-007-5603-8_9.

Hari, P., Heliövaara, K., and Kulmala, L. *Physical and Physiological Forest Ecology.* Springer, 2013.

Hartmann, D. L., Tank, A. M. K., Rusticucci, M., Alexander, L. V., Brönnimann, S., Charabi, Y. A. R., Dentener, F. J., Dlugokencky, E. J., Easterling, D. R., Kaplan, A., et al. Observations: atmosphere and surface. In *Climate change 2013 the physical science basis: Working group I contribution to the fifth assessment report of the intergovernmental panel on climate change*, pages 159–254. Cambridge University Press, 2013.

Helas, G., Bingemer, H., and Andreae, M. O. Organic acids over equatorial Africa: Results from DECAFE 88. *Journal of Geophysical Research: Atmospheres*, 97(D6): 6187–6193, 1992. ISSN 0148-0227. https://doi.org/10.1029/91jd01438.

Hellén, H., Kouznetsov, R., Anttila, P., and Hakola, H. Increasing influence of easterly air masses on NMHC concentrations at the Pallas-Sodankylä GAW station. 2015. ISSN 1797-2469.

Hellén, H., Praplan, A. P., Tykkä, T., Ylivinkka, I., Vakkari, V., Bäck, J., Petäjä, T., Kulmala, M., and Hakola, H. Long-term measurements of volatile organic compounds highlight the importance of sesquiterpenes for the atmospheric chemistry of a boreal forest. *Atmos. Chem. Phys.*, 18(19):13839–13863, 2018. ISSN 1680-7324. https://doi.org/10.5194/acp-18-13839-2018.

Hens, K., Novelli, A., Martinez, M., Auld, J., Axinte, R., Bohn, B., Fischer, H., Keronen, P., Kubistin, D., Nolscher, A. C., Oswald, R., Paasonen, P., Petaja, T., Regelin, E., Sander, R., Sinha, V., Sipila, M., Taraborrelli, D., Ernest, C. T., Williams, J., Lelieveld, J., and Harder, H. Observation and modelling of HOx radicals in a boreal forest. *Atmospheric Chemistry and Physics*, 14(16):8723–8747, 2014. ISSN 1680-7316. https://doi.org/10.5194/acp-14-8723-2014.

Hoor, P., Wernli, H., Hegglin, M. I., and Bönisch, H. Transport timescales and tracer properties in the extratropical UTLS. *Atmospheric Chemistry and Physics*, 10(16): 7929–7944, 2010. https://doi.org/10.5194/acp-10-7929-2010.

Horowitz, A., Meller, R., and Moortgat, G. K. The UV-VIS absorption cross sections of the alpha-dicarbonyl compounds: Pyruvic acid, biacetyl and glyoxal. *Journal of Photochemistry and Photobiology a-Chemistry*, 146(1-2):19–27, 2001. ISSN 1010-6030. https://doi.org/10.1016/s1010-6030(01)00601-3.

Huey, L. G. Measurement of trace atmospheric species by chemical ionization mass spectrometry: Speciation of reactive nitrogen and future directions. *Mass spectrometry reviews*, 26(2):166–184, 2007.

Huey, L. G., Hanson, D. R., and Howard, C. J. Reactions of $sf6$-and i- with atmospheric trace gases. *The Journal of Physical Chemistry*, 99(14):5001–5008, 1995.

IUPAC. Task Group on Atmospheric Chemical Kinetic Data Evaluation, (Ammann, M., Cox, R.A., Crowley, J.N., Herrmann, H., Jenkin, M.E., McNeill, V.F., Mellouki, A., Rossi, M. J., Troe, J. and Wallington, T. J.). http://iupac.pole-ether.fr/index.html. 2019.

Jacob, D. J. and Wofsy, S. C. Photochemistry of biogenic emissions over the Amazon forest. *Journal of Geophysical Research-Atmospheres*, 93(D2):1477–1486, 1988. https://doi.org/10.1029/JD093iD02p01477.

Jardine, K. J., Sommer, E. D., Saleska, S. R., Huxman, T. E., Harley, P. C., and Abrell, L. Gas phase measurements of pyruvic acid and its volatile metabolites. *Environmental Science & Technology*, 44(7):2454–2460, 2010. ISSN 0013-936X. https://doi.org/10.1021/es903544p.

Jenkin, M., Cox, R., Emrich, M., and Moortgat, G. Mechanism of the Cl-atom initiated oxidation of acetone and hydroxyacetone in air. *JCSFT*, 89:2983–2991, 1993. https://doi.org/10.1039/FT9938902983.

Jordan, A., Haidacher, S., Hanel, G., Hartungen, E., Mark, L., Seehauser, H., Schottkowsky, R., Sulzer, P., and Mark, T. D. A high resolution and high sensitivity proton-transfer-reaction time-of-flight mass spectrometer (PTR-TOF-MS). *International Journal of Mass Spectrometry*, 286(2-3):122–128, 2009. ISSN 1387-3806. https://doi.org/10.1016/j.ijms.2009.07.005.

Jost, C., Sprung, D., Kenntner, T., and Reiner, T. Atmospheric pressure chemical ionization mass spectrometry for the detection of tropospheric trace gases: the influence of clustering on sensitivity and precision. *International Journal of Mass Spec-*

trometry, 223(1-3):771–782, 2003. ISSN 1387-3806. https://doi.org/10.1016/S1387-3806(02)00963-6.

Junninen, H., Lauri, A., Keronen, P., Aalto, P., Hiltunen, V., Hari, P., and Kulmala, M. Smart-SMEAR: on-line data exploration and visualization tool for SMEAR stations. 2009. ISSN 1797-2469.

Kampa, M. and Castanas, E. Human health effects of air pollution. *Environmental pollution*, 151(2):362–367, 2008.

Kanakidou, M., Seinfeld, J., Pandis, S., Barnes, I., Dentener, F., Facchini, M., Dingenen, R. V., Ervens, B., Nenes, A., and Nielsen, C. Organic aerosol and global climate modelling: a review. *Atmospheric Chemistry and Physics*, 5(4):1053–1123, 2005. ISSN 1680-7316. https://doi.org/10.5194/acp-5-1053-2005.

Kanakidou, M., Mihalopoulos, N., Kindap, T., Im, U., Vrekoussis, M., Gerasopoulos, E., Dermitzaki, E., Unal, A., Kocak, M., Markakis, K., Melas, D., Kouvarakis, G., Youssef, A. F., Richter, A., Hatzianastassiou, N., Hilboll, A., Ebojie, F., Wittrock, F., von Savigny, C., Burrows, J. P., Ladstaetter-Weissenmayer, A., and Moubasher, H. Megacities as hot spots of air pollution in the East Mediterranean. *Atmospheric Environment*, 45(6):1223–1235, 2011. ISSN 1352-2310. https://doi.org/10.1016/j.atmosenv.2010.11.048.

Keene, W. C., Khalil, M. A. K., Erickson, D. J., McCulloch, A., Graedel, T. E., Lobert, J. M., Aucott, M. L., Gong, S. L., Harper, D. B., Kleiman, G., Midgley, P., Moore, R. M., Seuzaret, C., Sturges, W. T., Benkovitz, C. M., Koropalov, V., Barrie, L. A., and Li, Y. F. Composite global emissions of reactive chlorine from anthropogenic and natural sources: Reactive chlorine emissions inventory. *Journal of Geophysical Research-Atmospheres*, 104(D7):8429–8440, 1999. ISSN 0148-0227. https://doi.org/10.1029/1998jd100084.

Keene, W. C., Stutz, J., Pszenny, A. A. P., Maben, J. R., Fischer, E. V., Smith, A. M., von Glasow, R., Pechtl, S., Sive, B. C., and Varner, R. K. Inorganic chlorine and bromine in coastal New England air during summer. *Journal of Geophysical Research-Atmospheres*, 112(D10), 2007. ISSN 2169-897X. https://doi.org/10.1029/2006jd007689.

Keene, W. C., Long, M. S., Pszenny, A. A. P., Sander, R., Maben, J. R., Wall, A. J., O'Halloran, T. L., Kerkweg, A., Fischer, E. V., and Schrems, O. Latitudinal variation in the multiphase chemical processing of inorganic halogens and related species over the eastern North and South Atlantic Oceans. *Atmospheric Chemistry and Physics*, 9(19):7361–7385, 2009. ISSN 1680-7316. https://doi.org/10.5194/acp-9-7361-2009.

Kercher, J. P., Riedel, T. P., and Thornton, J. A. Chlorine activation by N2O5: simultaneous, in situ detection of ClNO2 and N2O5 by chemical ionization mass spectrometry. *Atmospheric measurement techniques*, 2(1):193–204, 2009. ISSN 1867-1381. https://doi.org/10.5194/amt-2-193-2009.

Kesselmeier, J. and Staudt, M. Biogenic volatile organic compounds (VOC): an overview on emission, physiology and ecology. *Journal of atmospheric chemistry*, 33(1):23–88, 1999. https://doi.org/10.1023/A:1006127516791.

Kharol, S. K., McLinden, C. A., Sioris, C. E., Shephard, M. W., Fioletov, V., van Donkelaar, A., Sajeev, P., and Martin, R. V. OMI satellite observations of decadal changes in ground-level sulfur dioxide over North America. *Atmospheric Chemistry and Physics*, 17(9):5921, 2017.

Khatib, H. Oil and natural gas prospects: Middle East and North Africa. *Energy Policy*, 64:71–77, 2014. https://doi.org/10.1016/j.enpol.2013.07.091.

Khwaja, H. A. Atmospheric concentrations of carboxylic acids and related compounds at a semiurban site. *Atmospheric Environment*, 29(1):127–139, 1995. ISSN 1352-2310. https://doi.org/10.1016/1352-2310(94)00211-3.

Klimont, Z., Smith, S. J., and Cofala, J. The last decade of global anthropogenic sulfur dioxide: 2000–2011 emissions. *Environmental Research Letters*, 8(1):014003, 2013.

Krotkov, N. A., McLinden, C. A., Li, C., Lamsal, L. N., Celarier, E. A., Marchenko, S. V., Swartz, W. H., Bucsela, E. J., Joiner, J., Duncan, B. N., et al. Aura OMI observations of regional SO2 and NO2 pollution changes from 2005 to 2015. *Atmospheric Chemistry and Physics*, 16(7):4605–4629, 2016.

Kulmala, M., Suni, T., Lehtinen, K., Maso, M. D., Boy, M., Reissell, A., Rannik, u., Aalto, P., Keronen, P., and Hakola, H. A new feedback mechanism linking forests, aerosols, and climate. *Atmospheric Chemistry and Physics*, 4(2):557–562, 2004. ISSN 1680-7316. https://doi.org/10.5194/acp-4-557-2004.

Kürten, A., Rondo, L., Ehrhart, S., and Curtius, J. Performance of a corona ion source for measurement of sulfuric acid by chemical ionization mass spectrometry. *Atmospheric Measurement Techniques*, 4(3):437–443, 2011. ISSN 1867-1381. https://doi.org/10.5194/amt-4-437-2011.

LaFranchi, B. W., Wolfe, G. M., Thornton, J. A., Harrold, S. A., Browne, E. C., Min, K. E., Wooldridge, P. J., Gilman, J. B., Kuster, W. C., Goldan, P. D., de Gouw, J. A., McKay, M., Goldstein, A. H., Ren, X., Mao, J., and Cohen, R. C. Closing the peroxy acetyl nitrate budget: observations of acyl peroxy nitrates (PAN, PPN, and MPAN) during BEARPEX 2007. *Atmospheric Chemistry and Physics*, 9(19):7623–7641, 2009. doi:10.5194/acp-9-7623-2009.

Lazrus, A. L., Kok, G. L., Lind, J. A., Gitlin, S. N., Heikes, B. G., and Shetter, R. E. Automated fluorometric method for hydrogen-peroxide in air. *Analytical Chemistry*, 58(3):594–597, 1986. ISSN 0003-2700. https://doi.org/10.1021/ac00281a031.

Le Breton, M., McGillen, M. R., Muller, J. B. A., Bacak, A., Shallcross, D. E., Xiao, P., Huey, L. G., Tanner, D., Coe, H., and Percival, C. J. Airborne observations of formic acid using a chemical ionization mass spectrometer. *Atmospheric Measurement Techniques*, 5(12):3029–3039, 2012. ISSN 1867-1381. https://doi.org/10.5194/amt-5-3029-2012.

Le Breton, M., Hallquist, A. M., Pathak, R. K., Simpson, D., Wang, Y., Johansson, J., Zheng, J., Yang, Y., Shang, D., and Wang, H. Chlorine oxidation of VOCs at a semi-rural site in beijing: significant chlorine liberation from ClNO2 and subsequent

gas-and particle-phase Cl-VOC production. *Atmospheric Chemistry and Physics*, 18 (17):13013–13030, 2018. ISSN 1680-7316. https://doi.org/10.5194/acp-18-13013-2018.

Lee, B. H., Lopez-Hilfiker, F. D., Mohr, C., Kurtén, T., Worsnop, D. R., and Thornton, J. A. An iodide-adduct high-resolution time-of-flight chemical-ionization mass spectrometer: Application to atmospheric inorganic and organic compounds. *Environmental science & technology*, 48(11):6309–6317, 2014. https://doi.org/10.1021/es500362a.

Lee, B. H., Lopez-Hilfiker, F. D., Schroder, J. C., Campuzano-Jost, P., Jimenez, J. L., McDuffie, E. E., Fibiger, D. L., Veres, P. R., Brown, S. S., Campos, T. L., et al. Airborne observations of reactive inorganic chlorine and bromine species in the exhaust of coal-fired power plants. *Journal of Geophysical Research: Atmospheres*, 123(19): 11–225, 2018. https://doi.org/10.1029/2018JD029284.

Leighton, P. *Photochemistry of air pollution*. Academic Press, 1961.

Lelieveld, J. and Crutzen, P. Influences of cloud photochemical processes on tropospheric ozone. *Nature*, 343(6255):227, 1990. https://doi.org/10.1038/343227a0.

Lelieveld, J. and Dentener, F. J. What controls tropospheric ozone? *Journal of Geophysical Research: Atmospheres*, 105(D3):3531–3551, 2000.

Lelieveld, J., Berresheim, H., Borrmann, S., Crutzen, P., Dentener, F., Fischer, H., Feichter, J., Flatau, P., Heland, J., Holzinger, R., et al. Global air pollution crossroads over the Mediterranean. *Science*, 298(5594):794–799, 2002.

Lelieveld, J., Dentener, F. J., Peters, W., and Krol, M. C. On the role of hydroxyl radicals in the self-cleansing capacity of the troposphere. *Atmospheric Chemistry and Physics*, 4(9/10):2337–2344, 2004. https://doi.org/10.5194/acp-4-2337-2004.

Lelieveld, J., Hoor, P., Jöckel, P., Pozzer, A., Hadjinicolaou, P., Cammas, J.-P., and Beirle, S. Severe ozone air pollution in the Persian Gulf region. *Atmospheric Chemistry and Physics*, 9(4), 2009. ISSN 1680-7316. https://doi.org/10.5194/acp-9-1393-2009.

Lelieveld, J., Hadjinicolaou, P., Kostopoulou, E., Chenoweth, J., El Maayar, M., Giannakopoulos, C., Hannides, C., Lange, M. A., Tanarhte, M., Tyrlis, E., and Xoplaki, E. Climate change and impacts in the Eastern Mediterranean and the Middle East. *Climatic Change*, 114(3):667–687, 2012. ISSN 1573-1480. https://doi.org/10.1007/s10584-012-0418-4.

Lelieveld, J., Evans, J. S., Fnais, M., Giannadaki, D., and Pozzer, A. The contribution of outdoor air pollution sources to premature mortality on a global scale. *Nature*, 525 (7569):367, 2015.

Lelieveld, J., Gromov, S., Pozzer, A., and Taraborrelli, D. Global tropospheric hydroxyl distribution, budget and reactivity. *Atmospheric Chemistry and Physics*, 16 (19):12477–12493, 2016.

Lewis, E. R. An examination of Köhler theory resulting in an accurate expression for the equilibrium radius ratio of a hygroscopic aerosol particle valid up to and including relative humidity 100 %. *Journal of Geophysical Research: Atmospheres*, 113(D3), 2008. ISSN 2156-2202.

Li, J., Reiffs, A., Parchatka, U., and Fischer, H. In situ measurements of atmospheric CO and its correlation with NOx and O3 at a rural mountain site. *Metrol. Meas. Sys.*, XXII:25–38, 2015. https://doi.org/10.1515/mms-2015-0001.

Li, Q., Borge, R., Sarwar, G., de la Paz, D., Gantt, B., Domingo, J., Cuevas, C. A., and Saiz-Lopez, A. Impact of halogen chemistry on air quality in coastal and continental Europe: application of CMAQ model and implication for regulation. *Atmos. Chem. Phys. Discuss.*, 2019:1–31, 2019. ISSN 1680-7375. https://doi.org/10.5194/acp-2019-171.

Liebmann, J., Karu, E., Sobanski, N., Schuladen, J., Ehn, M., Schallhart, S., Quéléver, L., Hellen, H., Hakola, H., Hoffmann, T., Williams, J., Fischer, H., Lelieveld, J., and Crowley, J. N. Direct measurement of NO3 radical reactivity in a boreal forest. *Atmospheric Chemistry and Physics*, 2018(18):3799–3815, 2018. ISSN 1680-7375. https://doi.org/10.5194/acp-18-3799-2018.

Liebmann, J., Sobanski, N., Schuladen, J., Karu, E., Hellén, H., Hakola, H., Zha, Q., Ehn, M., Riva, M., Heikkinen, L., Williams, J., Fische, H., Lelieveld, J., and Crowley, J. N. Alkyl nitrates in the boreal forest: formation via the NO3-, OH- and O3-induced oxidation of biogenic volatile organic compounds and ambient lifetimes. *Atmos. Chem. Phys.*, 19(15):10391–10403, 2019. ISSN 1680-7324. https://doi.org/10.5194/acp-19-10391-2019.

Lightfoot, P. D., Cox, R. A., Crowley, J. N., Destriau, M., Hayman, G. D., Jenkin, M. E., Moortgat, G. K., and Zabel, F. Organic peroxy radicals - kinetics, spectroscopy and tropospheric chemistry. *Atmospheric Environment, Part A: General Topics*, 26(10): 1805–1961, 1992.

Liu, X., Qu, H., Huey, L. G., Wang, Y., Sjostedt, S., Zeng, L., Lu, K., Wu, Y., Hu, M., and Shao, M. High levels of daytime molecular chlorine and nitryl chloride at a rural site on the North China Plain. *Environmental science & technology*, 51(17): 9588–9595, 2017. ISSN 0013-936X.

Lofthus, A. and Krupenie, P. H. Spectrum of molecular nitrogen. *Journal of Physical and Chemical Reference Data*, 6(1):113–307, 1977. ISSN 0047-2689. https://doi.org/10.1063/1.555546.

Logan, J. A. Nitrogen oxides in the troposphere: Global and regional budgets. *Journal of Geophysical Research: Oceans*, 88(C15):10785–10807, 1983. https://doi.org/10.1029/JC088iC15p10785.

Lopez-Hilfiker, F. D., Mohr, C., Ehn, M., Rubach, F., Kleist, E., Wildt, J., Mentel, T. F., Lutz, A., Hallquist, M., Worsnop, D., and Thornton, J. A. A novel method for online analysis of gas and particle composition: description and evaluation of a filter inlet for gases and aerosols (figaero). *Atmospheric Measurement Techniques*, 7 (4):983–1001, 2014. ISSN 1867-1381. https://doi.org/10.5194/amt-7-983-2014.

Macintyre, H. L. and Evans, M. J. Sensitivity of a global model to the uptake of N2O5 by tropospheric aerosol. *Atmospheric Chemistry and Physics*, 10(15):7409–7414, 2010. ISSN 1680-7324. https://doi.org/10.5194/acp-10-7409-2010.

Magel, E., Mayrhofer, S., Müller, A., Zimmer, I., Hampp, R., and Schnitzler, J.-P. Photosynthesis and substrate supply for isoprene biosynthesis in poplar leaves. *Atmospheric Environment*, 40:138–151, 2006. ISSN 1352-2310. https://doi.org/10.1016/j.atmosenv.2005.09.091.

Martinez, M., Harder, H., Kubistin, D., Rudolf, M., Bozem, H., Eerdekens, G., Fischer, H., Kluepfel, T., Gurk, C., Koenigstedt, R., Parchatka, U., Schiller, C. L., Stickler, A., Williams, J., and Lelieveld, J. Hydroxyl radicals in the tropical troposphere over the Suriname rainforest: airborne measurements. *Atmospheric Chemistry and Physics*, 10(8):3759–3773, 2010. ISSN 1680-7316. https://doi.org/10.5194/acp-10-3759-2010.

Mathieu, É. Mémoire sur le mouvement vibratoire d'une membrane de forme elliptique. *Journal de mathématiques pures et appliquées*, 13:137–203, 1868.

Mattila, J. M., Brophy, P., Kirkland, J., Hall, S., Ullmann, K., Fischer, E. V., Brown, S., McDuffie, E., Tevlin, A., and Farmer, D. K. Tropospheric sources and sinks of gas-phase acids in the colorado front range. *Atmospheric Chemistry and Physics*, 18(16): 12315–12327, 2018. ISSN 1680-7316. https://doi.org/10.5194/acp-18-12315-2018.

McDuffie, E. E., Fibiger, D. L., Dubé, W. P., Lopez-Hilfiker, F., Lee, B. H., Jaeglé, L., Guo, H., Weber, R. J., Reeves, J. M., and Weinheimer, A. J. ClNO2 yields from aircraft measurements during the 2015 WINTER campaign and critical evaluation of the current parameterization. *Journal of Geophysical Research: Atmospheres*, 123 (22):12,994–13,015, 2018a. ISSN 2169-897X. https://doi.org/10.1029/2018JD029358.

McDuffie, E. E., Fibiger, D. L., Dubé, W. P., Lopez-Hilfiker, F., Lee, B. H., Thornton, J. A., Shah, V., Jaeglé, L., Guo, H., and Weber, R. J. Heterogeneous N2O5 uptake during winter: Aircraft measurements during the 2015 WINTER campaign and critical evaluation of current parameterizations. *Journal of Geophysical Research: Atmospheres*, 123(8):4345–4372, 2018b. ISSN 2169-897X. https://doi.org/10.1002/2018JD028336.

McNeill, V. F., Patterson, J., Wolfe, G. M., and Thornton, J. A. The effect of varying levels of surfactant on the reactive uptake of N2O5 to aqueous aerosol. *Atmospheric Chemistry and Physics*, 6:1635–1644, 2006. https://doi.org/10.5194/acp-6-1635-2006.

Mellouki, A. and Mu, Y. J. On the atmospheric degradation of pyruvic acid in the gas phase. *Journal of Photochemistry and Photobiology a-Chemistry*, 157(2-3):295–300, 2003. ISSN 1010-6030. https://doi.org/10.1016/s1010-6030(03)00070-4.

Meusel, H., Kuhn, U., Reiffs, A., Mallik, C., Harder, H., Martinez, M., Schuladen, J., Bohn, B., Parchatka, U., Crowley, J. N., Fischer, H., Tomsche, L., Novelli, A., Hoffmann, T., Janssen, R. H. H., Hartogensis, O., Pikridas, M., Vrekoussis, M., Bourtsoukidis, E., Weber, B., Lelieveld, J., Williams, J., Pöschl, U., Cheng, Y., and Su, H. Daytime formation of nitrous acid at a coastal remote site in Cyprus indicating a common ground source of atmospheric HONO and NO. *Atmospheric Chemistry and Physics*, 16(22):14475–14493, 2016. ISSN 1680-7324. https://doi.org/10.5194/acp-16-14475-2016.

Mielke, L. H. and Osthoff, H. D. On quantitative measurements of peroxycarboxylic nitric anhydride mixing ratios by thermal dissociation chemical ionization mass spectrometry. *International Journal of Mass Spectrometry*, 310:1–9, 2012. ISSN 1387-3806. doi:10.1016/j.ijms.2011.10.005.

Mielke, L. H., Furgeson, A., and Osthoff, H. D. Observation of ClNO2 in a mid-continental urban environment. *Environmental Science & Technology*, 45(20):8889–8896, 2011. ISSN 0013-936X. https://doi.org/10.1021/es201955u.

Mielke, L. H., Stutz, J., Tsai, C., Hurlock, S. C., Roberts, J. M., Veres, P. R., Froyd, K. D., Hayes, P. L., Cubison, M. J., Jimenez, J. L., Washenfelder, R. A., Young, C. J., Gilman, J. B., de Gouw, J. A., Flynn, J. H., Grossberg, N., Lefer, B. L., Liu, J., Weber, R. J., and Osthoff, H. D. Heterogeneous formation of nitryl chloride and its role as a nocturnal NOx reservoir species during CalNex-LA 2010. *Journal of Geophysical Research-Atmospheres*, 118(18):10638–10652, 2013. ISSN 2169-897X. https://doi.org/10.1002/jgrd.50783.

Mielke, L. H., Furgeson, A., Odame-Ankrah, C. A., and Osthoff, H. D. Ubiquity of ClNO2 in the urban boundary layer of Calgary, Alberta, Canada. *Canadian Journal of Chemistry*, 94(4):414–423, 2016. ISSN 0008-4042. https://doi.org/10.1139/cjc-2015-0426.

Miller, E. M., Sheps, L., Lu, Y. J., Case, A. S., McCoy, A. B., and Lineberger, W. C. New view of the ICN a continuum using photoelectron spectroscopy of ICN-. *Journal of Chemical Physics*, 136(4), 2012. ISSN 0021-9606. https://doi.org/10.1063/1.3679170.

Millet, D. B., Guenther, A., Siegel, D. A., Nelson, N. B., Singh, H. B., de Gouw, J. A., Warneke, C., Williams, J., Eerdekens, G., and Sinha, V. Global atmospheric budget of acetaldehyde: 3-D model analysis and constraints from in-situ and satellite observations. *Atmospheric Chemistry and Physics*, 10(7):3405–3425, 2010. ISSN 1680-7316. https://doi.org/10.5194/acp-10-3405-2010.

Miyazaki, K., Eskes, H., Sudo, K., Boersma, K. F., Bowman, K., and Kanaya, Y. Decadal changes in global surface NOx emissions from multi-constituent satellite data assimilation. *Atmos. Chem. Phys*, 17(2):807–837, 2017.

Molina, M. J., Tso, T.-L., Molina, L. T., and Wang, F. C.-Y. Antarctic stratospheric chemistry of chlorine nitrate, hydrogen chloride, and ice: Release of active chlorine. *Science*, 238(4831):1253–1257, 1987.

Molinaroli, E., Guerzoni, S., and Rampazzo, G. Contribution of Saharan dust to the Central Mediterranean Basin. *Geological Society of America*, Special Paper 284:303–312, 1993.

Morgan, W. T., Ouyang, B., Allan, J. D., Aruffo, E., Di Carlo, P., Kennedy, O. J., Lowe, D., Flynn, M. J., Rosenberg, P. D., Williams, P. I., Jones, R., McFiggans, G. B., and Coe, H. Influence of aerosol chemical composition on N2O5 uptake: airborne regional measurements in northwestern Europe. *Atmospheric Chemistry and Physics*, 15(2):973–990, 2015. ISSN 1680-7316. https://doi.org/10.5194/acp-15-973-2015.

Moxim, W. J., Levy, H., and Kasibhatla, P. S. Simulated global tropospheric PAN: Its transport and impact on NOx. *Journal of Geophysical Research-atmospheres*, 101 (D7):12621–12638, 1996. https://doi.org/10.1029/96JD00338.

Munson, M. S. and Field, F.-H. Chemical ionization mass spectrometry. I. General introduction. *Journal of the American Chemical Society*, 88(12):2621–2630, 1966.

Myhre, G., Shindell, D., Bréon, F.-M., Collins, W., Fuglestvedt, J., Huang, J., Koch, D., Lamarque, J.-F., Lee, D., Mendoza, B., et al. Anthropogenic and natural radiative forcing. *Climate change*, 423:658–740, 2013.

Neuman, J., Trainer, M., Brown, S., Min, K.-E., Nowak, J., Parrish, D., Peischl, J., Pollack, I., Roberts, J., Ryerson, T., et al. HONO emission and production determined from airborne measurements over the Southeast US. *Journal of Geophysical Research: Atmospheres*, 121(15):9237–9250, 2016.

Ng, N. L., Brown, S. S., Archibald, A. T., Atlas, E., Cohen, R. C., Crowley, J. N., Day, D. A., Donahue, N. M., Fry, J. L., Fuchs, H., et al. Nitrate radicals and biogenic volatile organic compounds: oxidation, mechanisms, and organic aerosol. *Atmospheric chemistry and physics*, 17(3):2103–2162, 2017.

NIST. NIST Chemistry WebBook, NIST Standard Reference Database Number 69, National Institute of Standards and Technology, eds. Linstrom, P.J and Mallard, W.G. http://webbook.nist.gov/chemistry/, Gaithersburg MD, 20899, 2016.

Novelli, A., Hens, K., Ernest, C. T., Kubistin, D., Regelin, E., Elste, T., Plass-Duelmer, C., Martinez, M., Lelieveld, J., and Harder, H. Characterisation of an inlet pre-injector laser-induced fluorescence instrument for the measurement of atmospheric hydroxyl radicals. *Atmospheric measurement techniques*, 7(10):3413–3430, 2014. ISSN 1867-1381. https://doi.org/10.5194/amt-7-3413-2014.

Obermeyer, G., Aschmann, S. M., Atkinson, R., and Arey, J. Carbonyl atmospheric reaction products of aromatic hydrocarbons in ambient air. *Atmospheric Environment*, 43(24):3736–3744, 2009. ISSN 1352-2310. https://doi.org/10.1016/j.atmosenv.2009.04.015.

Osthoff, H. D., Roberts, J. M., Ravishankara, A. R., Williams, E. J., Lerner, B. M., Sommariva, R., Bates, T. S., Coffman, D., Quinn, P. K., Dibb, J. E., Stark, H., Burkholder, J. B., Talukdar, R. K., Meagher, J., Fehsenfeld, F. C., and Brown, S. S. High levels of nitryl chloride in the polluted subtropical marine boundary layer. *Nature Geoscience*, 1(5):324–328, 2008. https://doi.org/10.1038/ngeo177.

Osthoff, H. D., Odame-Ankrah, C. A., Taha, Y. M., Tokarek, T. W., Schiller, C. L., Haga, D., Jones, K., and Vingarzan, R. Low levels of nitryl chloride at ground level: nocturnal nitrogen oxides in the Lower Fraser Valley of British Columbia. *Atmospheric Chemistry and Physics*, 18(9):6293–6315, 2018. ISSN 1680-7316. https://doi.org/10.5194/acp-18-6293-2018.

Paul, W. and Steinwedel, H. A new mass spectrometer without a magnetic field. *Zeitschrift fuer Naturforschung (West Germany) Divided into Z. Nautrforsch., A, and Z. Naturforsch., B: Anorg. Chem., Org. Chem., Biochem., Biophys.,*, 8, 1953.

Paulot, F., Crounse, J. D., Kjaergaard, H. G., Kroll, J. H., Seinfeld, J. H., and Wennberg, P. O. Isoprene photooxidation: new insights into the production of acids and organic nitrates. *Atmospheric Chemistry and Physics*, 9(4):1479–1501, 2009. https://doi.org/10.5194/acp-9-1479-2009.

Petäjä, T., Mauldin, I. R. L., Kosciuch, E., McGrath, J., Nieminen, T., Paasonen, P., Boy, M., Adamov, A., Kotiaho, T., and Kulmala, M. Sulfuric acid and OH concentrations in a boreal forest site. *Atmos. Chem. Phys.*, 9(19):7435–7448, 2009. ISSN 1680-7324. https://doi.org/10.5194/acp-9-7435-2009.

Pfannerstill, E. Y., Wang, N., Edtbauer, A., Bourtsoukidis, E., Crowley, J. N., Dienhart, D., Eger, P. G., Ernle, L., Fischer, H., Hottmann, B., Paris, J.-D., Stönner, C., Tadic, I., Walter, D., Lelieveld, J., and Williams, J. Shipborne measurements of total OH reactivity around the Arabian Peninsula and its role in ozone chemistry. *Atmospheric Chemistry and Physics*, 19(17):11501–11523, 2019. https://doi.org/10.5194/acp-19-11501-2019.

Phillips, G., Tang, M., Thieser, J., Brickwedde, B., Schuster, G., Bohn, B., Lelieveld, J., and Crowley, J. Significant concentrations of nitryl chloride observed in rural continental europe associated with the influence of sea salt chloride and anthropogenic emissions. *Geophysical research letters*, 39(10), 2012.

Phillips, G., Pouvesle, N., Thieser, J., Schuster, G., Axinte, R., Fischer, H., Williams, J., Lelieveld, J., and Crowley, J. Peroxyacetyl nitrate (PAN) and peroxyacetic acid (PAA) measurements by iodide chemical ionisation mass spectrometry: first analysis of results in the boreal forest and implications for the measurement of PAN fluxes. *Atmospheric Chemistry and Physics*, 13(3):1129–1139, 2013.

Phillips, G. J., Thieser, J., Tang, M., Sobanski, N., Schuster, G., Fachinger, J., Drewnick, F., Borrmann, S., Bingemer, H., Lelieveld, J., et al. Estimating N2O5 uptake coefficients using ambient measurements of NO3, N2O5, ClNO2 and particle-phase nitrate. *Atmospheric Chemistry and Physics*, 16(20):13231–13249, 2016.

Platt, U., Perner, D., Winer, A. M., Harris, G. W., and Pitts Jr, J. N. Detection of NO3 in the polluted troposphere by differential optical absorption. *Geophysical Research Letters*, 7(1):89–92, 1980.

Praplan, A. P., Hegyi-Gaeggeler, K., Barmet, P., Pfaffenberger, L., Dommen, J., and Baltensperger, U. Online measurements of water-soluble organic acids in the gas and aerosol phase from the photooxidation of 1, 3, 5-trimethylbenzene. *Atmospheric Chemistry and Physics*, 14(16):8665–8677, 2014. ISSN 1680-7316. https://doi.org/10.5194/acp-14-8665-2014.

Priestley, M., Breton, M. l., Bannan, T. J., Worrall, S. D., Bacak, A., Smedley, A. R., Reyes-Villegas, E., Mehra, A., Allan, J., Webb, A. R., et al. Observations of organic and inorganic chlorinated compounds and their contribution to chlorine radical concentrations in an urban environment in northern europe during the wintertime. *Atmospheric Chemistry and Physics*, 18(18):13481–13493, 2018.

Raber, W. H. and Moortgat, G. K. Photooxidation of selected carbonyl compounds in air: methyl ethyl ketone, methyl vinyl ketone, methacrolein and methylglyoxal. *Progress and problems in atmospheric chemistry, edited by: Barker, JR, World Scientific Publishing, Singapore*, pages 318–373, 1995.

Reed Harris, A. E., Ervens, B., Shoemaker, R. K., Kroll, J. A., Rapf, R. J., Griffith, E. C., Monod, A., and Vaida, V. Photochemical kinetics of pyruvic acid in aqueous solution. *The Journal of Physical Chemistry A*, 118(37):8505–8516, 2014. ISSN 1089-5639. https://doi.org/10.1021/jp502186q.

Reed Harris, A. E., Cazaunau, M., Gratien, A., Pangui, E., Doussin, J. F., and Vaida, V. Atmospheric simulation chamber studies of the gas-phase photolysis of pyruvic acid. *Journal of Physical Chemistry A*, 121(44):8348–8358, 2017. ISSN 1089-5639. https://doi.org/10.1021/acs.jpca.7b05139.

Refaey, K. M. A. and Franklin, J. L. Endoergic ion-molecule collision processes of negative ions. 6. Collisions of I- on (CN)2 and NOCl. *International Journal of Mass Spectrometry and Ion Processes*, 23(1):13–20, 1977. ISSN 0168-1176. https://doi.org/10.1016/0020-7381(77)80002-8.

Reimann, S. and Lewis, A. C. Anthropogenic VOCs. *Volatile organic compounds in the atmosphere*, pages 33–70, 2007.

Riedel, T. P., Bertram, T. H., Crisp, T. A., Williams, E. J., Lerner, B. M., Vlasenko, A., Li, S. M., Gilman, J., de Gouw, J., Bon, D. M., Wagner, N. L., Brown, S. S., and Thornton, J. A. Nitryl chloride and molecular chlorine in the coastal marine boundary layer. *Environmental Science & Technology*, 46(19):10463–10470, 2012a. ISSN 0013-936X. https://doi.org/10.1021/es204632r.

Riedel, T. P., Bertram, T. H., Ryder, O. S., Liu, S., Day, D. A., Russell, L. M., Gaston, C. J., Prather, K. A., and Thornton, J. A. Direct N2O5 reactivity measurements at a polluted coastal site. *Atmos. Chem. Phys.*, 12(6):2959–2968, 2012b. ISSN 1680-7324. https://doi.org/10.5194/acp-12-2959-2012.

Riedel, T. P., Wagner, N. L., Dube, W. P., Middlebrook, A. M., Young, C. J., Ozturk, F., Bahreini, R., VandenBoer, T. C., Wolfe, D. E., Williams, E. J., Roberts, J. M., Brown, S. S., and Thornton, J. A. Chlorine activation within urban or power plant plumes: Vertically resolved ClNO2 and Cl2 measurements from a tall tower in a polluted continental setting. *Journal of Geophysical Research-Atmospheres*, 118(15): 8702–8715, 2013. ISSN 2169-897X. https://doi.org/10.1002/jgrd.50637.

Riedel, T. P., Wolfe, G. M., Danas, K. T., Gilman, J. B., Kuster, W. C., Bon, D. M., Vlasenko, A., Li, S. M., Williams, E. J., Lerner, B. M., Veres, P. R., Roberts, J. M., Holloway, J. S., Lefer, B., Brown, S. S., and Thornton, J. A. An MCM modeling study of nitryl chloride (clno2) impacts on oxidation, ozone production and nitrogen oxide partitioning in polluted continental outflow. *Atmos. Chem. Phys.*, 14(8):3789–3800, 2014. ISSN 1680-7324. https://doi.org/10.5194/acp-14-3789-2014.

Rinne, J., Ruuskanen, T. M., Reissell, A., Taipale, R., Hakola, H., and Kulmala, M. On-line PTR-MS measurements of atmospheric concentrations of volatile organic compounds in a European boreal forest ecosystem. *Boreal Environmental Research*, 10 (5):425–436, 2005. ISSN ISSN 1239-6095.

Riva, M., Heikkinen, L., Bell, D. M., Peräkylä, O., Zha, Q., Schallhart, S., Rissanen, M. P., Imre, D., Petäjä, T., Thornton, J. A., Zelenyuk, A., and Ehn, M. Chemical transformations in monoterpene-derived organic aerosol enhanced by inorganic composition. *npj Climate and Atmospheric Science*, 2(1):2, 2019. ISSN 2397-3722. https://doi.org/10.1038/s41612-018-0058-0.

Roberts, J. M. The atmospheric chemistry of organic nitrates. *Atmospheric Environment. Part A. General Topics*, 24(2):243–287, 1990.

Roberts, J. M., Flocke, F., Stroud, C. A., Hereid, D., Williams, E., Fehsenfeld, F., Brune, W., Martinez, M., and Harder, H. Ground-based measurements of peroxycarboxylic nitric anhydrides (PANs) during the 1999 Southern Oxidants Study Nashville Intensive. *Journal of Geophysical Research-Atmospheres*, 107(D21):4554, 2002. ISSN 0747-7309. https://doi.org/10.1029/2001jd000947.

Roberts, J. M., Jobson, B. T., Kuster, W., Goldan, P., Murphy, P., Williams, E., Frost, G., Riemer, D., Apel, E., Stroud, C., Wiedinmyer, C., and Fehsenfeld, F. An examination of the chemistry of peroxycarboxylic nitric anhydrides and related volatile organic compounds during Texas Air Quality Study 2000 using ground-based measurements. *Journal of Geophysical Research-Atmospheres*, 108(D16), 2003. ISSN 0148-0227. 4495, doi:10.1029/2003jd003383.

Roedel, W. *Physik unserer Umwelt: Die Atmosphäre*. Springer-Verlag, 3rd edition, 2000.

Rohrer, F. and Berresheim, H. Strong correlation between levels of tropospheric hydroxyl radicals and solar ultraviolet radiation. *Nature*, 442(7099):184–187, 2006. ISSN 1476-4687. https://doi.org/10.1038/nature04924.

Roiger, A., Aufmhoff, H., Stock, P., Arnold, F., and Schlager, H. An aircraft-borne chemical ionization - ion trap mass spectrometer (CI-ITMS) for fast PAN and PPN measurements. *Atmospheric measurement techniques*, 4(2):173–188, 2011. ISSN 1867-1381. doi:10.5194/amt-4-173-2011.

Rolph, G., Stein, A., and Stunder, B. Real-time environmental applications and display system: READY. *Environmental Modelling & Software*, 95:210–228, 2017. ISSN 1364-8152. https://doi.org/10.1016/j.envsoft.2017.06.025.

Ryerson, T. B., Andrews, A. E., Angevine, W. M., Bates, T. S., Brock, C. A., Cairns, B., Cohen, R. C., Cooper, O. R., de Gouw, J. A., Fehsenfeld, F. C., Ferrare, R. A., Fischer, M. L., Flagan, R. C., Goldstein, A. H., Hair, J. W., Hardesty, R. M., Hostetler, C. A., Jimenez, J. L., Langford, A. O., McCauley, E., McKeen, S. A., Molina, L. T., Nenes, A., Oltmans, S. J., Parrish, D. D., Pederson, J. R., Pierce, R. B., Prather, K., Quinn, P. K., Seinfeld, J. H., Senff, C. J., Sorooshian, A., Stutz, J., Surratt, J. D., Trainer, M., Volkamer, R., Williams, E. J., and Wofsy, S. C. The 2010 California Research at the Nexus of Air Quality and Climate Change (CalNex) field study.

Journal of Geophysical Research-Atmospheres, 118(11):5830–5866, 2013. ISSN 2169-897X. https://doi.org/10.1002/jgrd.50331.

Sarwar, G., Simon, H., Xing, J., and Mathur, R. Importance of tropospheric ClNO2 chemistry across the northern hemisphere. *Geophysical Research Letters*, 41(11):4050–4058, 2014. ISSN 0094-8276. https://doi.org/10.1002/2014GL059962.

Schembari, C., Cavalli, F., Cuccia, E., Hjorth, J., Calzolai, G., Perez, N., Pey, J., Prati, P., and Raes, F. Impact of a European directive on ship emissions on air quality in Mediterranean harbours. *Atmospheric Environment*, 61:661–669, 2012. ISSN 1352-2310. https://doi.org/10.1016/j.atmosenv.2012.06.047.

Schlager, H., Grewe, V., and Roiger, A. Chemical composition of the atmosphere. In *Atmospheric Physics*, pages 17–35. Springer, 2012.

Schneider, J., Hings, S. S., Hock, B. N., Weimer, S., Borrmann, S., Fiebig, M., Petzold, A., Busen, R., and Kärcher, B. Aircraft-based operation of an aerosol mass spectrometer: Measurements of tropospheric aerosol composition. *Journal of aerosol science*, 37(7):839–857, 2006. https://doi.org/10.1016/j.jaerosci.2005.07.002.

Seinfeld, J. H. and Pandis, S. N. *Atmospheric chemistry and physics: from air pollution to climate change*. John Wiley & Sons, Hoboken, New Jersey, 3rd edition, 2016.

Sihto, S.-L., Mikkilä, J., Vanhanen, J., Ehn, M., Liao, L., Lehtipalo, K., Aalto, P., Duplissy, J., Petäjä, T., and Kerminen, V.-M. Seasonal variation of CCN concentrations and aerosol activation properties in boreal forest. *Atmospheric Chemistry and Physics*, 11(24):13269–13285, 2011. ISSN 1680-7316. https://doi.org/10.5194/acp-11-13269-2011.

Simon, H., Kimura, Y., McGaughey, G., Allen, D. T., Brown, S. S., Osthoff, H. D., Roberts, J. M., Byun, D., and Lee, D. Modeling the impact of ClNO2 on ozone formation in the Houston area. *Journal of Geophysical Research-Atmospheres*, 114, 2009. https://doi.org/10.1029/2008JD010732.

Singh, A. and Agrawal, M. Acid rain and its ecological consequences. *Journal of Environmental Biology*, 29(1):15, 2007.

Singh, H. B. Reactive nitrogen in the troposphere. *Environmental science & technology*, 21(4):320–327, 1987.

Singh, H. B. and Hanst, P. L. Peroxyacetyl nitrate (pan) in the unpolluted atmosphere: An important reservoir for nitrogen oxides. *Geophysical Research Letters*, 8(8):941–944, 1981. https://doi.org/10.1029/GL008i008p00941.

Singh, H. B., Kanakidou, M., Crutzen, P., and Jacob, D. High concentrations and photochemical fate of oxygenated hydrocarbons in the global troposphere. *Nature*, 378:50–54, 1995. https://doi.org/10.1038/378050a0.

Skalny, J. D., Horvath, G., and Mason, N. L. Mass spectrometric analysis of small negative ions (e/m $<$ 100) produced by trichel pulse negative corona discharge fed by ozonised air. *Journal of Optoelectronics and Advanced Materials*, 9(4):887–893, 2007. ISSN 1454-4164.

Slusher, D. L., Huey, L. G., Tanner, D. J., Flocke, F. M., and Roberts, J. M. A thermal dissociation-chemical ionization mass spectrometry (TD-CIMS) technique for the simultaneous measurement of peroxyacyl nitrates and dinitrogen pentoxide. *Journal of Geophysical Research-Atmospheres*, 109, Art Nr. D19315, doi:10.1029/2004JD004670 (D19), 2004.

Sobanski, N., Schuladen, J., Schuster, G., Lelieveld, J., and Crowley, J. N. A five-channel cavity ring-down spectrometer for the detection of NO2, NO3, N2O5, total peroxy nitrates and total alkyl nitrates. *Atmospheric Measurement Techniques*, 9(10): 5103–5118, 2016. ISSN 1867-8548. https://doi.org/10.5194/amt-9-5103-2016.

Sobanski, N., Thieser, J., Schuladen, J., Sauvage, C., Song, W., Williams, J., lelieveld, J., and Crowley, J. Day- and night-time formation of organic nitrates at a forested mountain-site in south west germany. *Atmospheric Chemistry and Physics*, 17:4115–4130, 2017.

Solomon, S. The mystery of the antarctic ozone "hole". *Reviews of Geophysics*, 26(1): 131–148, 1988. https://doi.org/10.1029/RG026i001p00131.

Sommariva, R., Hollis, L. D., Sherwen, T., Baker, A. R., Ball, S. M., Bandy, B. J., Bell, T. G., Chowdhury, M. N., Cordell, R. L., and Evans, M. J. Seasonal and geographical variability of nitryl chloride and its precursors in Northern Europe. *Atmospheric Science Letters*, 19(8):e844, 2018. ISSN 1530-261X. https://doi.org/10.1002/asl.844.

Staudinger, J. and Roberts, P. V. A critical review of Henry's law constants for environmental applications. *Critical Reviews in Environmental Science and Technology*, 26(3):205–297, 1996. ISSN 1064-3389. https://doi.org/10.1080/10643389609388492.

Stefan, M. I. and Bolton, J. R. Reinvestigation of the acetone degradation mechanism in dilute aqueous solution by the UV/H2O2 process. *Environmental science & technology*, 33(6):870–873, 1999. ISSN 0013-936X. https://doi.org/10.1021/es9808548.

Stein, A. F., Draxler, R. R., Rolph, G. D., Stunder, B. J. B., Cohen, M. D., and Ngan, F. NOAA'S HYSPLIT atmospheric transport and dispersion modeling system. *Bulletin of the American Meteorological Society*, 96(12):2059–2077, 2015. ISSN 0003-0007. https://doi.org/10.1175/bams-d-14-00110.1.

Stocker, T. F., Qin, D., Plattner, G.-K., Tignor, M., Allen, S. K., Boschung, J., Nauels, A., Xia, Y., Bex, V., Midgley, P. M., et al. Climate change 2013: The physical science basis, 2013.

Stull, R. B. *An introduction to boundary layer meteorology*. Kluwer Academic Publishers, 1988.

Svarnas, P. Vibrational temperature of excited nitrogen molecules detected in a 13.56 MHz electrical discharge by sheath-side optical emission spectroscopy. *Plasma Science & Technology*, 15(9):891–895, 2013. ISSN 1009-0630. https://doi.org/10.1088/1009-0630/15/9/11.

Talbot, R., Andreae, M., Berresheim, H., Jacob, D. J., and Beecher, K. Sources and sinks of formic, acetic, and pyruvic acids over Central Amazonia: 2. Wet season. *Journal of Geophysical Research: Atmospheres*, 95(D10):16799–16811, 1990. ISSN 2156-2202. https://doi.org/10.1029/JD095iD10p16799.

Talbot, R. W., Mosher, B. W., Heikes, B. G., Jacob, D. J., Munger, J. W., Daube, B. C., Keene, W. C., Maben, J. R., and Artz, R. S. Carboxylic acids in the rural continental atmosphere over the eastern United States during the Shenandoah Cloud and Photochemistry Experiment. *Journal of Geophysical Research: Atmospheres*, 100 (D5):9335–9343, 1995. ISSN 2156-2202. https://doi.org/10.1029/95jd00507.

Tan, Y., Lim, Y. B., Altieri, K. E., Seitzinger, S. P., and Turpin, B. J. Mechanisms leading to oligomers and SOA through aqueous photooxidation: insights from OH radical oxidation of acetic acid and methylglyoxal. *Atmospheric Chemistry and Physics*, 12 (2):801–813, 2012. ISSN 1680-7324. https://doi.org/10.5194/acp-12-801-2012.

Tang, M. J., Thieser, J., Schuster, G., and Crowley, J. Kinetics and mechanism of the heterogeneous reaction of N2O5 with mineral dust particles. *Phys. Chem. Chem. Phys*, 14:8551–8561, 2012. https://doi.org/10.1039/C2CP40805H.

Taylor, O. Importance of peroxyacetyl nitrate (PAN) as a phytotoxic air pollutant. *Journal of the Air Pollution Control Association*, 19(5):347–351, 1969.

Thaler, R. D., Mielke, L. H., and Osthoff, H. D. Quantification of nitryl chloride at part per trillion mixing ratios by thermal dissociation cavity ring-down spectroscopy. *Analytical Chemistry*, 83(7):2761–2766, 2011. ISSN 0003-2700. https://doi.org/10.1021/ac200055z.

Tham, Y. J., Wang, Z., Li, Q. Y., Yun, H., Wang, W. H., Wang, X. F., Xue, L. K., Lu, K. D., Ma, N., Bohn, B., Li, X., Kecorius, S., Gross, J., Shao, M., Wiedensohler, A., Zhang, Y. H., and Wang, T. Significant concentrations of nitryl chloride sustained in the morning: investigations of the causes and impacts on ozone production in a polluted region of northern China. *Atmospheric Chemistry and Physics*, 16(23): 14959–14977, 2016. ISSN 1680-7316. https://doi.org/10.5194/acp-16-14959-2016.

Tham, Y. J., Wang, Z., Li, Q., Wang, W., Wang, X., Lu, K., Ma, N., Yan, C., Kecorius, S., and Wiedensohler, A. Heterogeneous N2O5 uptake coefficient and production yield of ClNO2 in polluted northern China: roles of aerosol water content and chemical composition. *Atmospheric Chemistry and Physics*, 18(17):13155–13171, 2018. ISSN 1680-7316. https://doi.org/10.5194/acp-18-13155-2018.

Thieser, J., Schuster, G., Phillips, G., Reiffs, A., Parchatka, U., Pöhler, D., Lelieveld, J., and Crowley, J. A two-channel, thermal dissociation cavity-ringdown spectrometer for the detection of ambient NO2, RO2NO2 and RONO2. *Atmos. Meas. Tech.*, 9: 553–576, 2016. https://doi.org/10.5194/amt-9-553-2016.

Thornton, J. A., Kercher, J. P., Riedel, T. P., Wagner, N. L., Cozic, J., Holloway, J. S., Dube, W. P., Wolfe, G. M., Quinn, P. K., Middlebrook, A. M., Alexander, B., and Brown, S. S. A large atomic chlorine source inferred from mid-continental reactive nitrogen chemistry. *Nature*, 464(7286):271–274, 2010. ISSN 0028-0836. https://doi.org/10.1038/nature08905.

Turnipseed, A. A., Huey, L. G., Nemitz, E., Stickel, R., Higgs, J., Tanner, D. J., Slusher, D. L., Sparks, J. P., Flocke, F., and Guenther, A. Eddy covariance fluxes of peroxyacetyl nitrates (PANs) and NOy to a coniferous forest. *Journal of Geophysical Research-atmospheres*, 111(D9):D09304, 2006. https://doi.org/10.1029/2005JD006631.

Vereecken, L., Muller, J. F., and Peeters, J. Low-volatility poly-oxygenates in the OH-initiated atmospheric oxidation of alpha-pinene: impact of non-traditional peroxyl radical chemistry. *Physical Chemistry Chemical Physics*, 9(38):5241–5248, 2007. ISSN 1463-9076. https://doi.org/10.1039/b708023a.

Veres, P., Roberts, J. M., Warneke, C., Welsh-Bon, D., Zahniser, M., Herndon, S., Fall, R., and de Gouw, J. Development of negative-ion proton-transfer chemical-ionization mass spectrometry (NI-PT-CIMS) for the measurement of gas-phase organic acids in the atmosphere. *International Journal of Mass Spectrometry*, 274(1-3):48–55, 2008. https://doi.org/10.1016/j.ijms.2008.04.032.

Veres, P., Gilman, J. B., Roberts, J. M., Kuster, W. C., Warneke, C., Burling, I. R., and de Gouw, J. Development and validation of a portable gas phase standard generation and calibration system for volatile organic compounds. *Atmospheric Measurement Techniques*, 3(3):683–691, 2010. ISSN 1867-1381. https://doi.org/10.5194/amt-3-683-2010.

Veres, P. R., Roberts, J. M., Wild, R. J., Edwards, P. M., Brown, S. S., Bates, T. S., Quinn, P. K., Johnson, J. E., Zamora, R. J., and de Gouw, J. Peroxynitric acid (HO2NO2) measurements during the UBWOS 2013 and 2014 studies using iodide ion chemical ionization mass spectrometry. *Atmos. Chem. Phys.*, 15(14):8101–8114, 2015. ISSN 1680-7324. https://doi.org/10.5194/acp-15-8101-2015.

Wagner, N. L., Riedel, T. P., Roberts, J. M., Thornton, J. A., Angevine, W. M., Williams, E. J., Lerner, B. M., Vlasenko, A., Li, S. M., Dube, W. P., Coffman, D. J., Bon, D. M., de Gouw, J. A., Kuster, W. C., Gilman, J. B., and Brown, S. S. The sea breeze/land breeze circulation in Los Angeles and its influence on nitryl chloride production in this region. *Journal of Geophysical Research-Atmospheres*, 117, Art. D00V24, 2012. ISSN 2169-897X. https://doi.org/10.1029/2012jd017810.

Wagner, N. L., Riedel, T. P., Young, C. J., Bahreini, R., Brock, C. A., Dube, W. P., Kim, S., Middlebrook, A. M., Ozturk, F., Roberts, J. M., Russo, R., Sive, B., Swarthout, R., Thornton, J. A., VandenBoer, T. C., Zhou, Y., and Brown, S. S. N2O5 uptake coefficients and nocturnal NO2 removal rates determined from ambient wintertime measurements. *Journal of Geophysical Research-Atmospheres*, 118(16):9331–9350, 2013. ISSN 2169-897X. https://doi.org/10.1002/jgrd.50653.

Wallace, J. M. and Hobbs, P. V. *Atmospheric science: an introductory survey.* Academic Press, Elsevier, 2nd edition, 2006.

Wang, T., Tham, Y. J., Xue, L., Li, Q., Zha, Q., Wang, Z., Poon, S. C. N., Dube, W. P., Blake, D. R., Louie, P. K. K., Luk, C. W. Y., Tsui, W., and Brown, S. S. Observations of nitryl chloride and modeling its source and effect on ozone in the planetary boundary

layer of southern china. *Journal of Geophysical Research-Atmospheres*, 121(5):2476–2489, 2016. ISSN 2169-897X. https://doi.org/10.1002/2015jd024556.

Wang, X., Wang, H., Xue, L., Wang, T., Wang, L., Gu, R., Wang, W., Tham, Y. J., Wang, Z., and Yang, L. Observations of N2O5 and ClNO2 at a polluted urban surface site in North China: High N2O5 uptake coefficients and low ClNO2 product yields. *Atmospheric environment*, 156:125–134, 2017a. ISSN 1352-2310. https://doi.org/10.1016/j.atmosenv.2017.02.035.

Wang, X., Wang, T., Xue, L. K., Nie, W., Xu, Z., Poon, S. C. N., and Wang, W. X. Peroxyacetyl nitrate measurements by thermal dissociation-chemical ionization mass spectrometry in an urban environment: performance and characterizations. *Frontiers of Environmental Science & Engineering*, 11(4), 2017b. ISSN 2095-2201. https://doi.org/10.1007/s11783-017-0925-7.

Wang, X., Jacob, D. J., Eastham, S. D., Sulprizio, M. P., Zhu, L., Chen, Q., Alexander, B., Sherwen, T., Evans, M. J., Lee, B. H., Haskins, J. D., Lopez-Hilfiker, F. D., Thornton, J. A., Huey, G. L., and Liao, H. The role of chlorine in global tropospheric chemistry. *Atmospheric Chemistry and Physics*, 19(6):3981–4003, 2019. https://doi.org/10.5194/acp-19-3981-2019.

Warneck, P. Multi-phase chemistry of C2 and C3 organic compounds in the marine atmosphere. *Journal of Atmospheric Chemistry*, 51(2):119–159, 2005. ISSN 0167-7764. https://doi.org/10.1007/s10874-005-5984-7.

Warneck, P. and Zerbach, T. Synthesis of peroxyacetyl nitrate in air by acetone photolysis. *Environmental Science & Technology*, 26(1):74–79, 1992.

Warneke, C., Trainer, M., de Gouw, J. A., Parrish, D. D., Fahey, D. W., Ravishankara, A., Middlebrook, A. M., Brock, C. A., Roberts, J. M., Brown, S. S., et al. Instrumentation and measurement strategy for the NOAA SENEX aircraft campaign as part of the Southeast Atmosphere Study 2013. *Atmospheric measurement techniques*, 9(7): 3063, 2016.

Wen, H., Hou, G. L., Huang, W., Govind, N., and Wang, X. B. Photoelectron spectroscopy of higher bromine and iodine oxide anions: Electron affinities and electronic structures of BrO2,3 and IO2-4 radicals. *Journal of Chemical Physics*, 135(18), 2011. ISSN 0021-9606.

Williams, J., Roberts, J., Fehsenfeld, F., Bertman, S., Buhr, M., Goldan, P., Hübler, G., Kuster, W., Ryerson, T., Trainer, M., et al. Regional ozone from biogenic hydrocarbons deduced from airborne measurements of PAN, PPN, and MPAN. *Geophysical Research Letters*, 24(9):1099–1102, 1997. https://doi.org/10.1029/97GL00548.

Williams, J., Crowley, J., Fischer, H., Harder, H., Martinez, M., Petaja, T., Rinne, J., Back, J., Boy, M., Dal Maso, M., Hakala, J., Kajos, M., Keronen, P., Rantala, P., Aalto, J., Aaltonen, H., Paatero, J., Vesala, T., Hakola, H., Levula, J., Pohja, T., Herrmann, F., Auld, J., Mesarchaki, E., Song, W., Yassaa, N., Nolscher, A., Johnson, A. M., Custer, T., Sinha, V., Thieser, J., Pouvesle, N., Taraborrelli, D., Tang, M. J., Bozem, H., Hosaynali-Beygi, Z., Axinte, R., Oswald, R., Novelli, A.,

Kubistin, D., Hens, K., Javed, U., Trawny, K., Breitenberger, C., Hidalgo, P. J., Ebben, C. J., Geiger, F. M., Corrigan, A. L., Russell, L. M., Ouwersloot, H. G., de Arellano, J. V. G., Ganzeveld, L., Vogel, A., Beck, M., Bayerle, A., Kampf, C. J., Bertelmann, M., Kollner, F., Hoffmann, T., Valverde, J., Gonzalez, D., Riekkola, M. L., Kulmala, M., and Lelieveld, J. The summertime boreal forest field measurement intensive (HUMPPA-COPEC-2010): an overview of meteorological and chemical influences. *Atmospheric Chemistry and Physics*, 11(20):10599–10618, 2011. ISSN 1680-7316. https://doi.org/10.5194/acp-11-10599-2011.

Winterhalter, R., Jensen, N., Magneron, I., Wirtz, K., Mellouki, W., Yuying, M., Tadic, J., Horowitz, A., Moortgat, G., and Hjorth, J. Studies of the photolysis of pyruvic acid: Products and mechanism. 2001.

Wolfe, G. M., Thornton, J. A., Yatavelli, R. L. N., McKay, M., Goldstein, A. H., LaFranchi, B., Min, K. E., and Cohen, R. C. Eddy covariance fluxes of acyl peroxy nitrates (PAN, PPN and MPAN) above a Ponderosa pine forest. *Atmospheric Chemistry and Physics*, 9(2):615–634, 2009. ISSN 1680-7316.

Wollenhaupt, M., Carl, S., Horowitz, A., and Crowley, J. Rate coefficients for reaction of OH with acetone between 202 and 395 K. *Journal of Physical Chemistry*, 104: 2695–2705, 2000. https://doi.org/10.1021/jp993738f.

Young, A. H., Keene, W. C., Pszenny, A. A. P., Sander, R., Thornton, J. A., Riedel, T. P., and Maben, J. R. Phase partitioning of soluble trace gases with size-resolved aerosols in near-surface continental air over northern Colorado, USA, during winter. *Journal of Geophysical Research-Atmospheres*, 118(16):9414–9427, 2013. ISSN 2169-897X. https://doi.org/10.1002/jgrd.50655.

Young, C. J., Washenfelder, R. A., Roberts, J. M., Mielke, L. H., Osthoff, H. D., Tsai, C., Pikelnaya, O., Stutz, J., Veres, P. R., Cochran, A. K., VandenBoer, T. C., Flynn, J., Grossberg, N., Haman, C. L., Lefer, B., Stark, H., Graus, M., de Gouw, J., Gilman, J. B., Kuster, W. C., and Brown, S. S. Vertically resolved measurements of nighttime radical reservoirs in Los Angeles and their contribution to the urban radical budget. *Environmental Science & Technology*, 46(20):10965–10973, 2012. ISSN 0013-936X. https://doi.org/10.1021/es302206a.

Yu, J. Z., Flagan, R. C., and Seinfeld, J. H. Identification of products containing -COOH, -OH, and -C=O in atmospheric oxidation of hydrocarbons. *Environmental Science & Technology*, 32(16):2357–2370, 1998. ISSN 0013-936X. https://doi.org/10.1021/es980129x.

Zeldovich, Y. B. and Raizer, Y. P. Physics of shock waves and high-temperature hydrodynamic phenomena. 1:11, 1966.

Zha, Q., Yan, C., Junninen, H., Riva, M., Sarnela, N., Aalto, J., Quéléver, L., Schallhart, S., Dada, L., Heikkinen, L., Peräkylä, O., Zou, J., Rose, C., Wang, Y., Mammarella, I., Katul, G., Vesala, T., Worsnop, D. R., Kulmala, M., Petäjä, T., Bianchi, F., and Ehn, M. Vertical characterization of highly oxygenated molecules (homs) below and above a boreal forest canopy. *Atmos. Chem. Phys.*, 18(23):17437–17450, 2018. ISSN 1680-7324. https://doi.org/10.5194/acp-18-17437-2018.

Zheng, J., Yang, D. S., Ma, Y., Chen, M. D., Cheng, J., Li, S. Z., and Wang, M. Development of a new corona discharge based ion source for high resolution time-of-flight chemical ionization mass spectrometer to measure gaseous H2SO4 and aerosol sulfate. *Atmospheric Environment*, 119:167–173, 2015. ISSN 1352-2310. https://doi.org/10.1016/j.atmosenv.2015.08.028.

Zheng, W., Flocke, F. M., Tyndall, G. S., Swanson, A., Orlando, J. J., Roberts, J. M., Huey, L. G., and Tanner, D. J. Characterization of a thermal decomposition chemical ionization mass spectrometer for the measurement of peroxy acyl nitrates (PANs) in the atmosphere. *Atmospheric Chemistry and Physics*, 11(13):6529–6547, 2011. ISSN 1680-7316. https://doi.org/10.5194/acp-11-6529-2011.

Zhou, W., Zhao, J., Ouyang, B., Mehra, A., Xu, W., Wang, Y., Bannan, T. J., Worrall, S. D., Priestley, M., Bacak, A., Chen, Q., Xie, C., Wang, Q., Wang, J., Du, W., Zhang, Y., Ge, X., Ye, P., Lee, J. D., Fu, P., Wang, Z., Worsnop, D., Jones, R., Percival, C. J., Coe, H., and Sun, Y. Production of N2O5 and ClNO2 in summer in urban Beijing, China. *Atmos. Chem. Phys.*, 18(16):11581–11597, 2018. ISSN 1680-7324. https://doi.org/10.5194/acp-18-11581-2018.

Zhuang, H., Chan, C. K., Fang, M., and Wexler, A. S. Formation of nitrate and non-sea-salt sulfate on coarse particles. *Atmospheric Environment*, 33(26):4223–4233, 1999. ISSN 1352-2310. https://doi.org/10.1016/s1352-2310(99)00186-7.

Zimmermann, S., Kippenberger, M., Schuster, G., and Crowley, J. N. Adsorption isotherms for hydrogen chloride (HCl) on ice surfaces between 190 and 220 K. *Physical Chemistry Chemical Physics*, 18(20):13799–13810, 2016. ISSN 1463-9076. https://doi.org/10.1039/c6cp01962e.

Zörner, J., Penning de Vries, M., Beirle, S., Sihler, H., Veres, P. R., Williams, J., and Wagner, T. Multi-satellite sensor study on precipitation-induced emission pulses of NOx from soils in semi-arid ecosystems. *Atmospheric Chemistry and Physics*, 16(14): 9457–9487, 2016.

Appendix A

Additional measurements during AQABA

A.1 SO_2 measurements

A high variability of SO_2 mixing ratios was observed along the ship track during AQABA with the lowest values detected in the Arabian Sea due to missing sources and high mixing ratios found in the Arabian Gulf, the Gulf of Suez and the Suez Canal. As illustrated in Fig. A.1, SO_2 mixing ratios over the Arabian Gulf region regularly exceeded 5 ppbv and even approached 20 ppbv close to Kuwait due to emissions from petrochemical industry and ship traffic. Large SO_2 signals were usually accompanied by the dominance of particulate sulphate in PM_1 aerosol composition, suggesting a significant impact on cloud properties and radiative forcing. Elevated SO_2 mixing ratios were also observed over the Gulf of Oman and over the northern part of the Red Sea / the Gulf of Suez where back-trajectories calculated with HYSPLIT (Stein et al., 2015; Rolph et al., 2017) indicated that air masses have passed over the polluted region around Cairo, the Suez Canal or the Sinai Peninsula. The transit through the Suez Canal was characterised by SO_2 levels greater than 10 ppbv from local industry and accumulation of ship exhaust. In the Mediterranean Sea, SO_2 mixing ratios only occasionally exceeded 1 ppbv, e.g. in chemically aged air masses transported from southern Europe or when passing the Strait of Messina between Italy and Sicily. For a substantial fraction of the campaign our measurements were impacted by emissions from nearby ships (especially in the narrow and crowded shipping lanes in the Suez Canal and the Arabian Gulf), whereby single ship plumes could be identified by their sharp peak shape and co-variance of SO_2 and NO_2 signals. In contrast to European waters where the sulphur content in ship diesel is regulated, for international shipping it can be very high, leading to increased SO_2 emissions.

Our measurements are in broad agreement with OMI satellite observations shown in Fig. 1.13 for the years 2013–2015 (Krotkov et al., 2016) where the whole Arabian Gulf region could be identified as SO_2 hotspot with local maxima found in Kuwait, at offshore oil and gas platforms and along the coast of Iran. The high values seen around Dschidda (west coast of Saudi-Arabia) are only partially reflected in the AQABA dataset due to the predominant wind patterns. The high SO_2 levels in the Arabian Gulf are also in line with preliminary EMAC model calculations (personal communication with Andrea Pozzer, MPIC Mainz) along the ship track predicting several ppbv of SO_2, although the observational data is characterised by much higher short-term variability due to poorly resolved point emission sources (ships and oil and gas platforms).

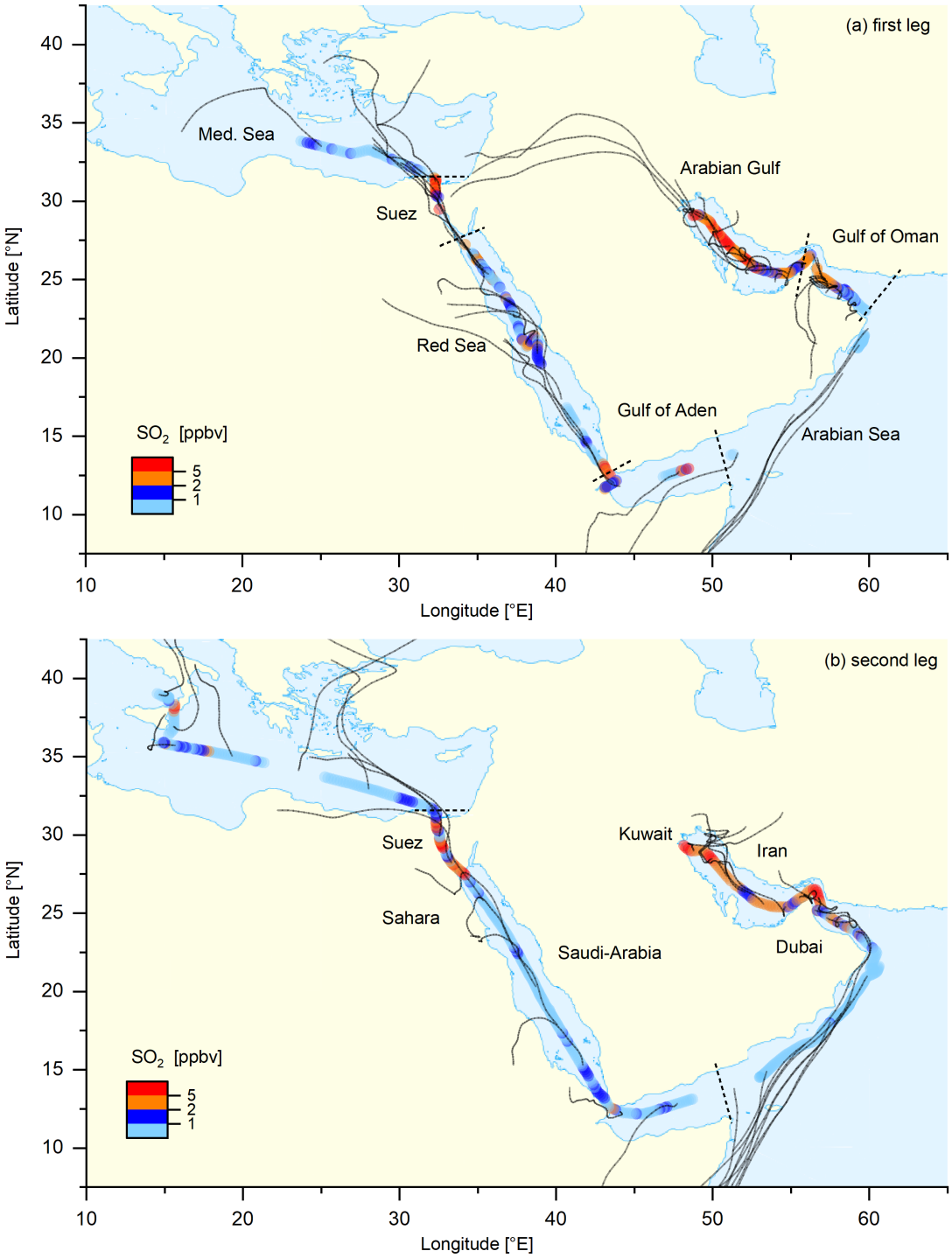

Figure A.1: Map of 1 h-averaged SO_2 mixing ratios during AQABA together with 48-h back-trajectories (HYSPLIT) for (a) first and (b) second leg.

A.2 PAN measurements

PAN mixing ratios > 100 pptv were only occasionally observed during the AQABA ship campaign due to high average temperatures (> 30 °C) resulting in a thermal lifetime of typically less than one hour. Thus transport of PAN over longer distances was precluded and only very local sources could be detected. In the Arabian Gulf, which was characterised by remarkably strong photochemical activity with O_3 mixing ratios exceeding 150 ppbv, PAN levels up to 2 ppbv were measured when approaching or leaving Kuwait harbour (Fig. A.2), indicating local sources of NO_x and NMHCs on the mainland (Kuwait city on the first leg and Iraq / Iran on the second leg). These high PAN mixing ratios measured in the western Arabian Gulf are in line with severe O_3 pollution reported by Lelieveld et al. (2009) with main NO_2 and VOC sources in this region being power generation, transport and industry. In addition, elevated mixing ratios of PAN were observed in the eastern part of the Arabian Gulf around Dubai and in the Gulf of Suez, where air masses originated from western Egypt. In this region PAN followed a typical diurnal pattern with a maximum around noon as expected for a photochemically produced species, whereas for major parts of the campaign we could rarely identify a diurnal pattern. High PAN levels were also detected in the narrow Suez Canal where industrial and urban sources are in close vicinity. In contrast, missing NO_x sources in the Arabian Sea, the Mediterranean Sea and in large parts of the Red Sea typically led to PAN mixing ratios below 100 pptv for most of the campaign.

Our observations are in broad agreement with Krotkov et al. (2016) who report elevated NO_2 column densities from OMI satellite data for the years 2013–2015 in the Arabian Gulf around Kuwait and Dubai and in the region around Cairo (Fig. 1.13). Elevated NO_2 levels are also seen for Jeddah and surroundings (Saudi-Arabia) but these were not reflected in the AQABA data as the predominant wind direction in this area was from the north-west. For the Central Gulf region (25–30 N, 45–55 °E) Lelieveld et al. (2009) report model calculated PAN mixing ratios of $\approx$ 200 pptv during summer, which are relatively low due to the thermal instability of PAN at high temperatures. For the winter months, however, values between 0.5 and 2.5 ppbv are predicted which suggests that PAN is of major importance during the latter season. This is in line with only sporadic observations of high mixing ratios in July / August where the AQABA campaign took place, and highlights the need for further measurements during the winter months.

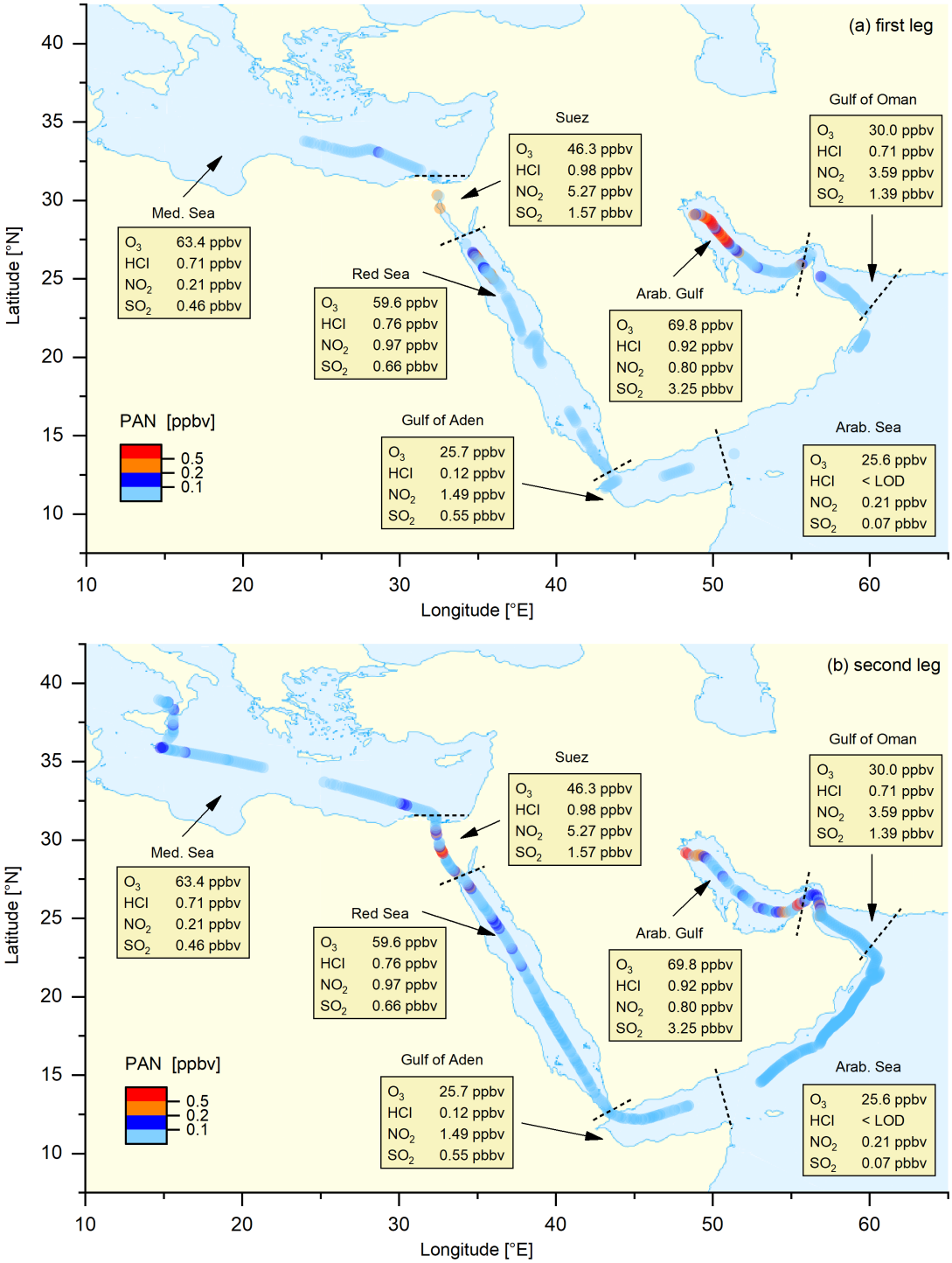

Figure A.2: Map of 1 h-averaged PAN mixing ratios during AQABA together with (median) night-time mixing ratios of O_3, HCl, NO_2 and SO_2 for different regions (data from both legs combined) for (a) first and (b) second leg.

Appendix B

Supplement of Chapter 2

This supplement provides additional figures and information on Chapter 2 “Characterisation of a chemical ionisation quadrupole mass spectrometer with an electrical discharge ion source and application in field studies”.

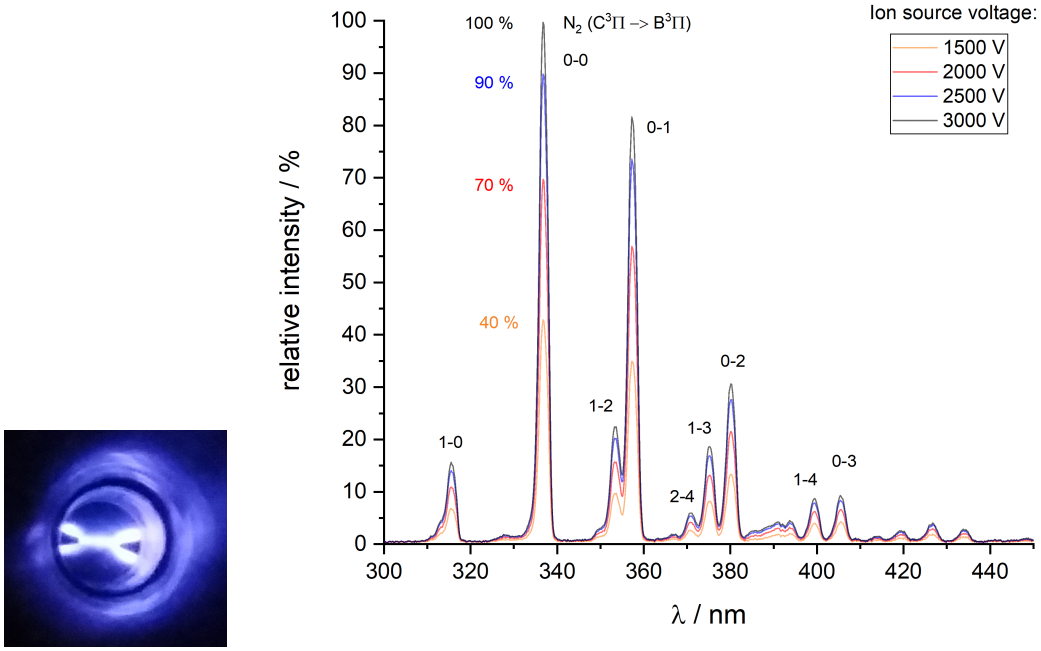

Figure B.1: Photo: N_2 emission observed between and around the pointed tungsten tips of the electrodes of the RF discharge source. Right: The emission spectrum was recorded with an Ocean-Optics USB-4000 spectrometer with optical fibre at various high-voltages. The strongest features (not fully resolved using the low-resolution ($\Delta\lambda \approx 1.5\,\mathrm{nm}$) spectrograph) can be assigned to transitions from the ground vibrational level of the electronically excited N_2 ($C^3\Pi_u$) state to the $B^3\Pi_g$ state.

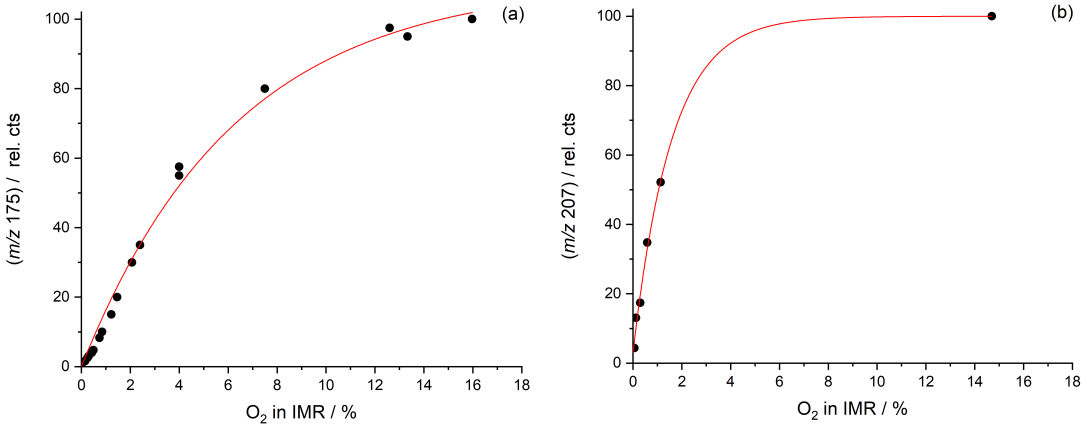

Figure B.2: (a): Dependence of IO_3^- signal (m/z 175) on the fractional pressure of O_2 in the IMR when adding 800 sccm N_2 / CH_3I through the RF discharge region. (b): Signal at m/z 207 (ISO_3^-) for a constant amount of SO_2 over the same range of O_2 partial pressures.

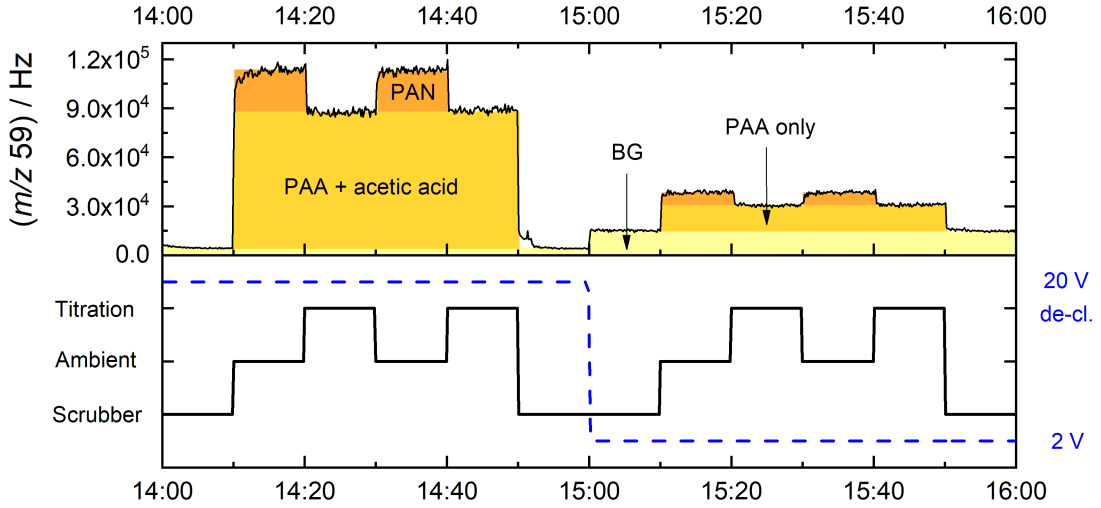

Figure B.3: Exemplary time series of the CI-QMS signal at m/z 59 when sampling from the photochemical PAN calibration source described in Sect. 2.2.7. The instrument periodically switches between the states "scrubber", "ambient" and "titration" (i.e. addition of NO). In ambient mode we measure the total signal of PAN, PAA and acetic acid. When adding NO to the inlet, the peroxyacyl radicals are titrated and the signal consists of PAA and acetic acid only. Changing the de-clustering voltage (at 15:00 UTC) from 20 V to 2 V results in the complete loss of sensitivity for acetic acid. During measurements of ambient air, the de-clustering voltage is usually changed more frequently, which means for each data point we firstly measure the signal at m/z 59 with high de-clustering and immediately afterwards with low de-clustering.

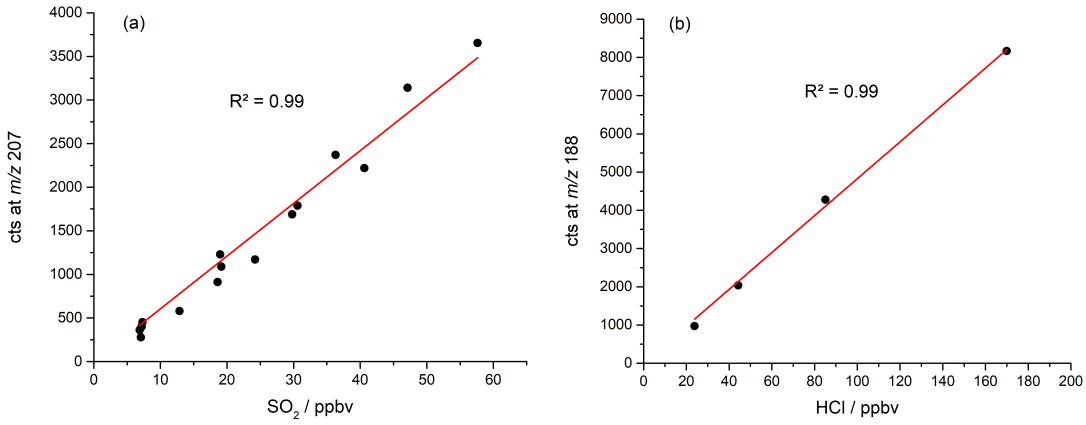

Figure B.4: (a) Linear dependence of count rate at m/z 207 (ISO_3^-) on the SO_2 mixing ratio of the sample measured. (b) Linear dependence of count rate at m/z 188 ($I(CN)Cl^-$) on the HCl mixing ratio.

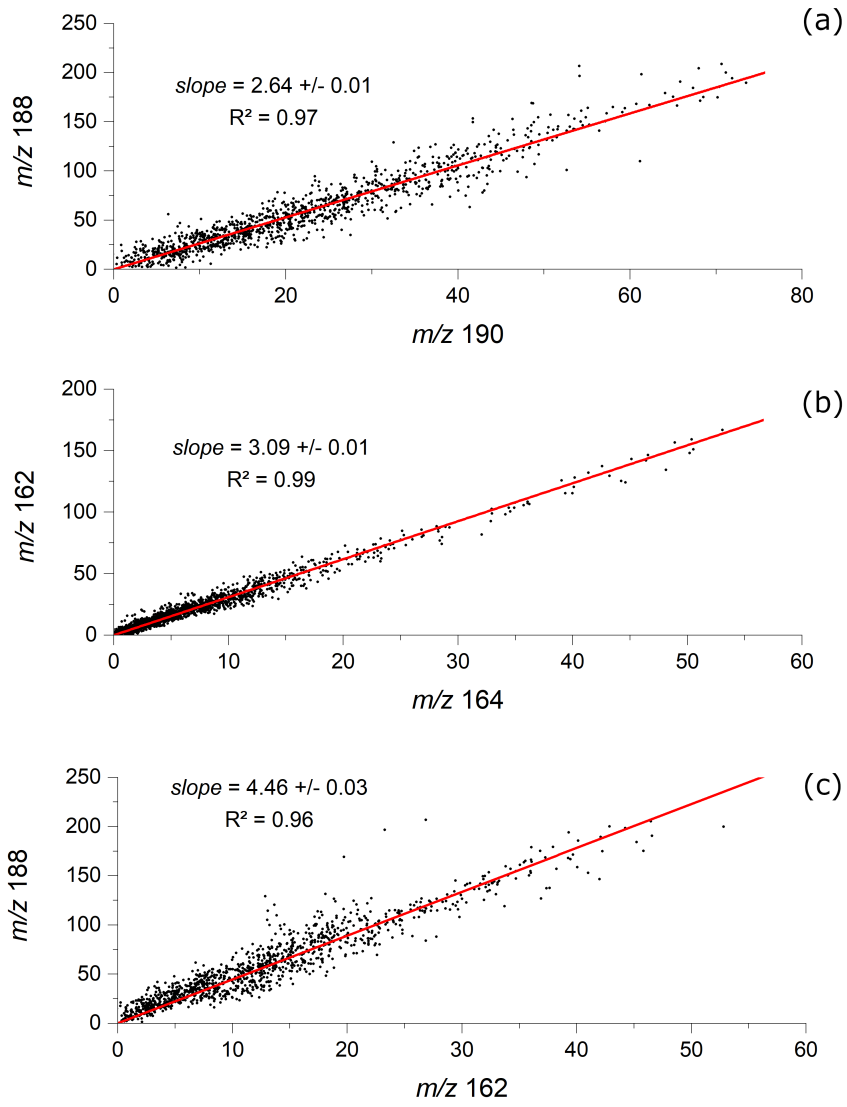

Figure B.5: (a) and (b): Correlation of ion signals at m/z 162 versus m/z 164 (ICl^-) and m/z 188 versus m/z 190 ($I(CN)Cl^-$) during CYPHEX. The expected slope resulting from the isotopic abundance of ^{35}Cl to ^{37}Cl is 3.13. (c) Signal at m/z 188 versus m/z 162. The linear correlation indicates that both ions are from the same trace gas, HCl.

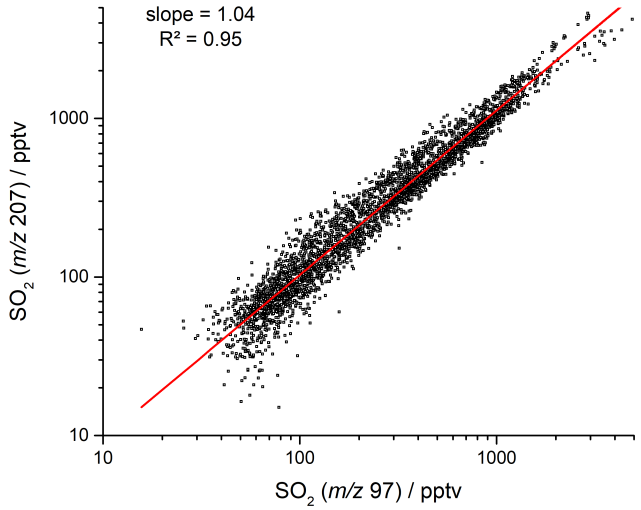

Figure B.6: Correlation between the CI-QMS measurement of SO_2 at m/z 207 (ISO_3^-) vs. m/z 97 (HSO_4^-) during NOTOMO.

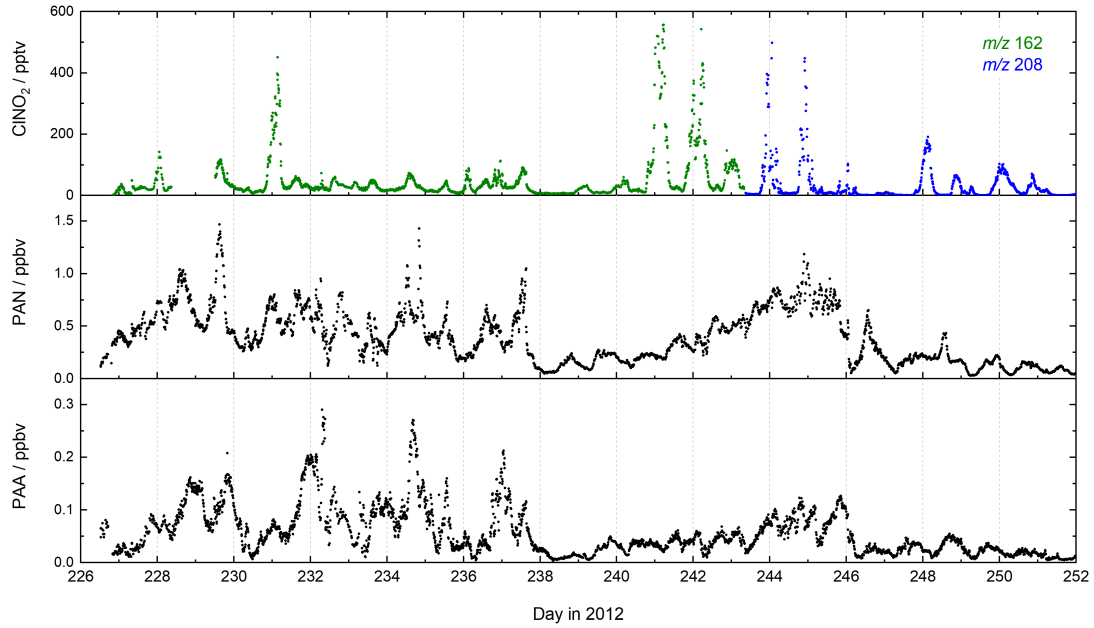

Figure B.7: Measurements of $ClNO_2$, PAN and PAA using CI-QMS with a ^{210}Po-ionisation source during the PARADE campaign, which took place at the same location and similar time of year as the NOTOMO campaign in which the RF discharge was deployed. The $ClNO_2$ data during PARADE has been reported by Phillips et al. (2012).

Appendix C

Supplement of Chapter 3

This supplement provides additional figures and information on Chapter 3 “Pyruvic acid in the boreal forest: first measurements and impact on radical chemistry”.

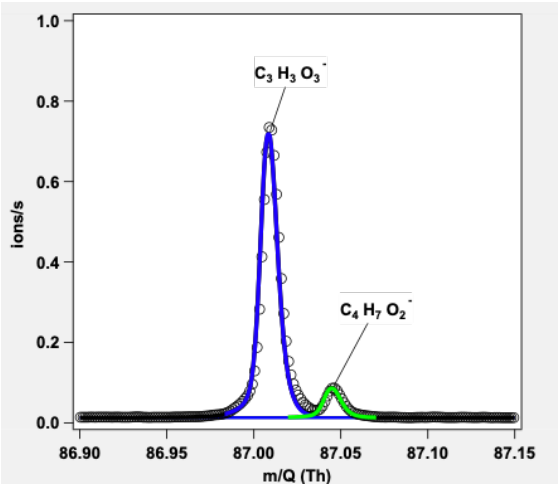

Figure C.1: Signals measured by the HR-L-ToF-CIMS for the ions detected at m/z 87.008 (assigned to pyruvic acid) and 87.045 (assigned to butanoic acid).

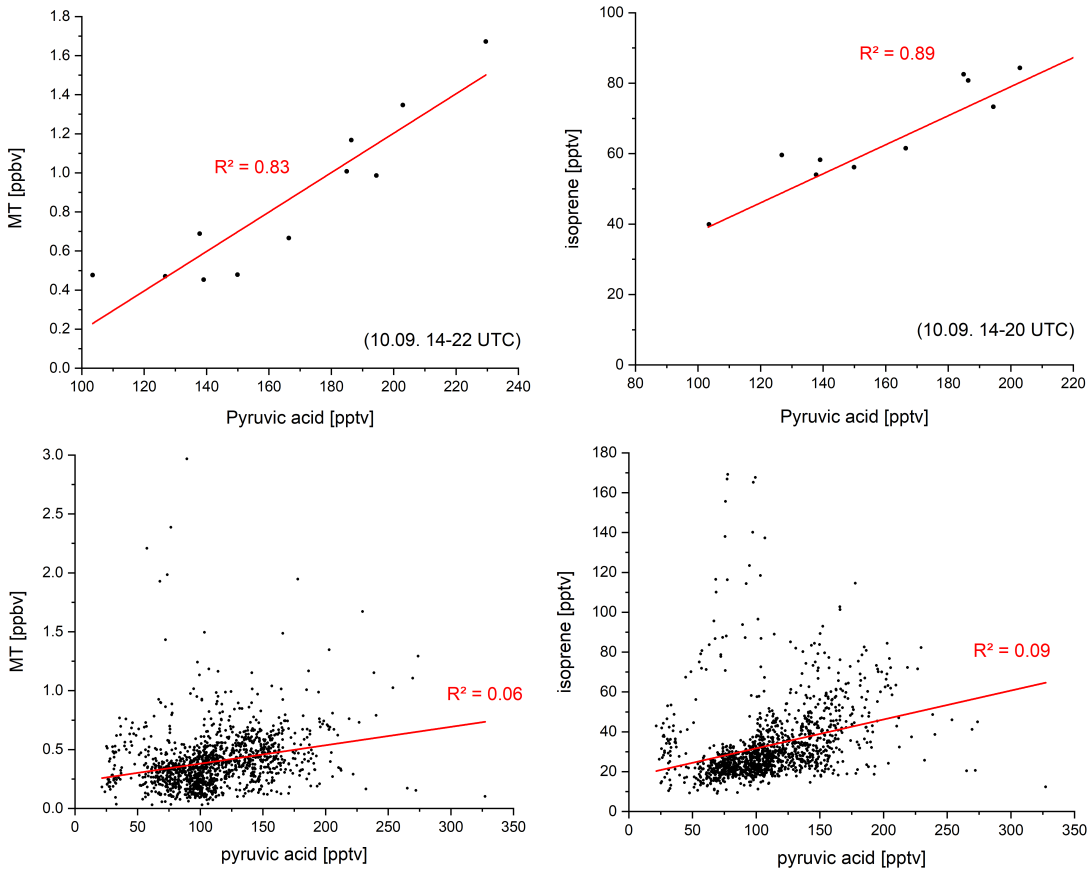

Figure C.2: Upper panel: Correlation plots of pyruvic acid and isoprene / monoterpenes (MT) for 10 September 2016 (air mass influenced by sawmill). Lower panel: Correlation plots of pyruvic acid and isoprene / MT for the whole IBAIRN campaign

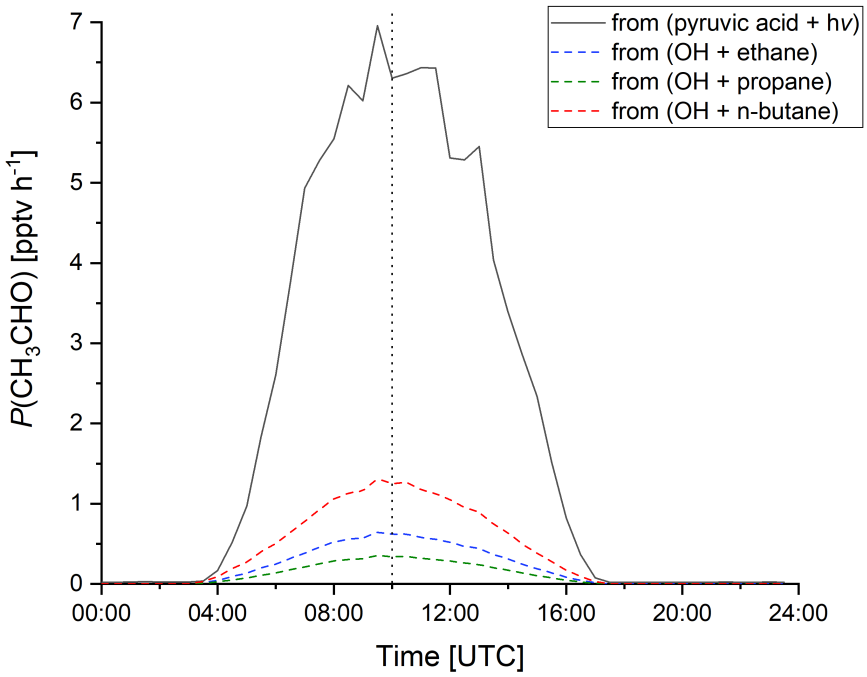

Figure C.3: Acetaldehyde (CH_3CHO) production rates over the diel cycle based on measurements (median diel profiles for IBAIRN) of pyruvic acid and Jpyr (assuming a photolysis yield of $\phi = 0.2$), calculated OH and estimated mixing ratios of alkanes from literature data (see manuscript). The dashed vertical line indicates solar noon.

Appendix D

Supplement of Chapter 4

This supplement provides additional figures and information on Chapter 4 “Ship-borne measurements of $ClNO_2$ in the Mediterranean Sea and around the Arabian Peninsula during summer”.

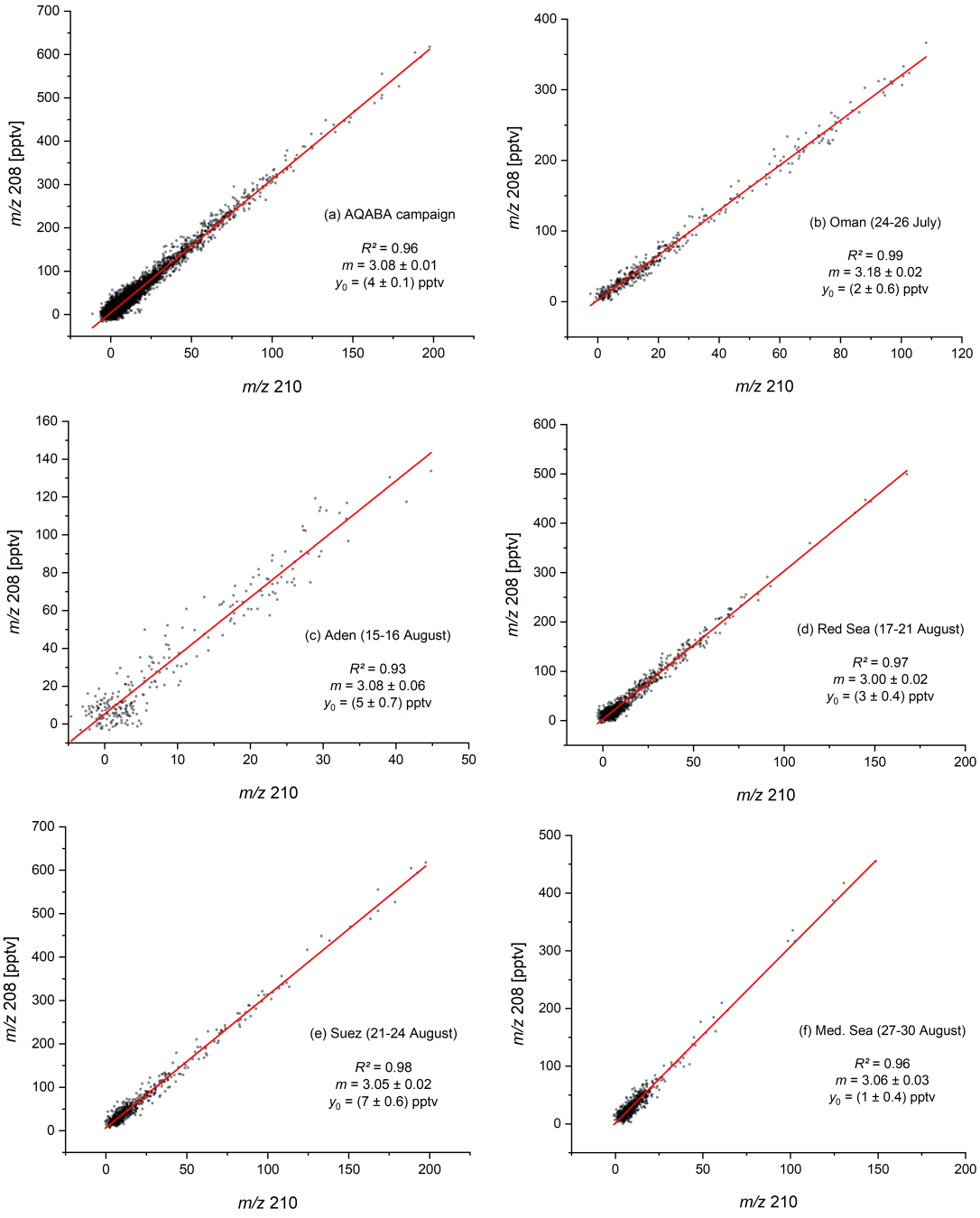

Figure D.1: Correlation between relative $ClNO_2$ signals measured at m/z 208 and 210 (with slope m and intercept y_0) for (a) the AQABA campaign and (b–f) selected periods in the Gulf of Oman, the Gulf of Aden, the Red Sea, the Suez Canal and the Mediterranean Sea.

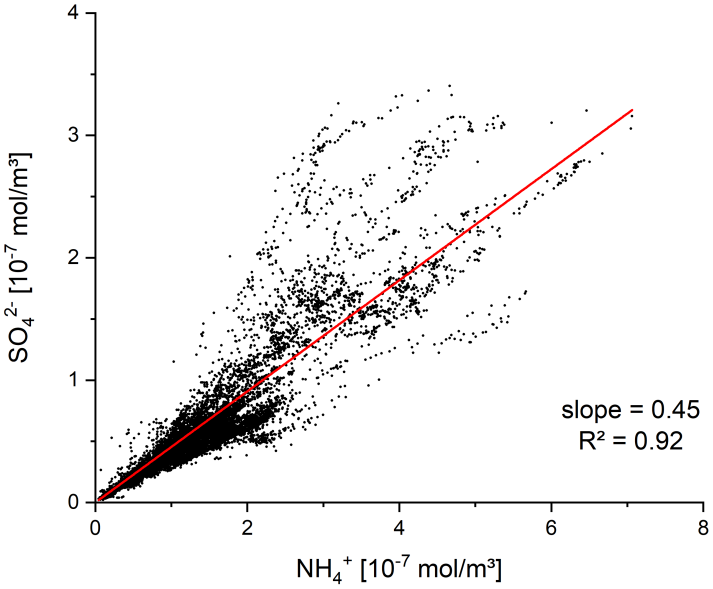

Figure D.2: Correlation between PM_1 (AMS) ammonium and sulphate (in $\mathrm{mol\,m^{-3}}$).

D.1 Corrections to the aerosol particle surface area concentration

To derive the ambient PM_1 particle surface area concentration A from the measured dry particle surface area concentration (AMS) we applied a hygroscopic growth factor based on ambient RH and PM_1 aerosol composition. From the AMS measurements we derived the molar ratio of sulphate to ammonium of ≈ 2.2 (see Fig. D.2), which is close to the ratio of ≈ 2 for completely neutralised ammonium-sulphate aerosol, indicating its dominance in the fine mode during AQABA. For most of the campaign $(NH_4^+)_2(SO_4^{2-})$ contributed 80–100 % to the total inorganic PM_1 aerosol mass (see Fig. D.3) while nitrate and chloride were less abundant. A relative humidity-dependent growth factor G_{amsu} for the particle diameter was calculated using the parameterisation (Eq. D.1) of Lewis (2008) for pure ammonium-sulphate drops with $a = 0.78$ and $b = 1.90$.

$$G_{\mathrm{amsu}} = a\left(b + \frac{1}{1-\mathrm{RH}}\right)^{1/3} \tag{D.1}$$

The growth factor was calculated considering the RH of the sample air after passing the aerosol dryer (see Sect. 4.2.5) which was usually in the range 40 ± 10 %. To account for the organic mass fraction we calculated the volume fraction v_{org} of organics using a typical density of 1400 kg $\mathrm{m^{-3}}$ for oxidised organics in aged atmospheric aerosol (Gysel et al., 2007) and the volume fraction v_{amsu} of $(NH_4^+)_2(SO_4^{2-})$, assuming that all NH_4^+ and SO_4^{2-} measured originated from ammonium-sulphate. In the next step we derived a combined growth factor by applying a mixing rule

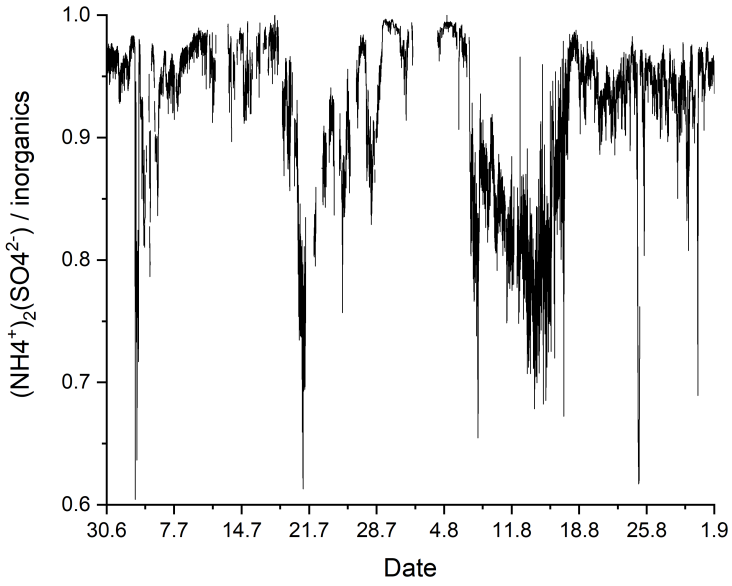

Figure D.3: Contribution of ammonium-sulphate to the total non-refractory inorganic PM_1 aerosol mass.

(Eq. D.2) where the water activity a_w was approximated by the relative humidity (Gysel et al., 2007).

$$G_{\text{mixed}} \approx \left(\sum_i v_i \, G_i^3 \right)^{1/3} \tag{D.2}$$

For the organic fraction a growth factor of $G_{\text{org}} = 1.20 \pm 0.10$ at $a_w = 0.9$ and a ratio of $\frac{G_{\text{org}}}{G_{\text{amsu}}} \approx \frac{1.2}{1.8}$ was reported by Gysel et al. (2007). Assuming a similar RH-dependence for G_{org} than for G_{amsu} results in Eq. (D.3) which can be inserted into Eq. (D.2) along with Eq. (D.1).

$$G_{\text{org}} \approx 1 + \frac{1}{4} \left(G_{\text{amsu}} - 1 \right) \tag{D.3}$$

The resulting surface area growth factor $G_A = (G_{\text{mixed}})^2$ as a function of RH is shown in Fig. D.4. The particle surface area concentration (PM_1) reported in Table 4.1 already includes this correction. The distribution of surface area growth factors for the whole AQABA campaign is shown in Fig. D.5 and has a campaign average of 1.32 ± 0.24.

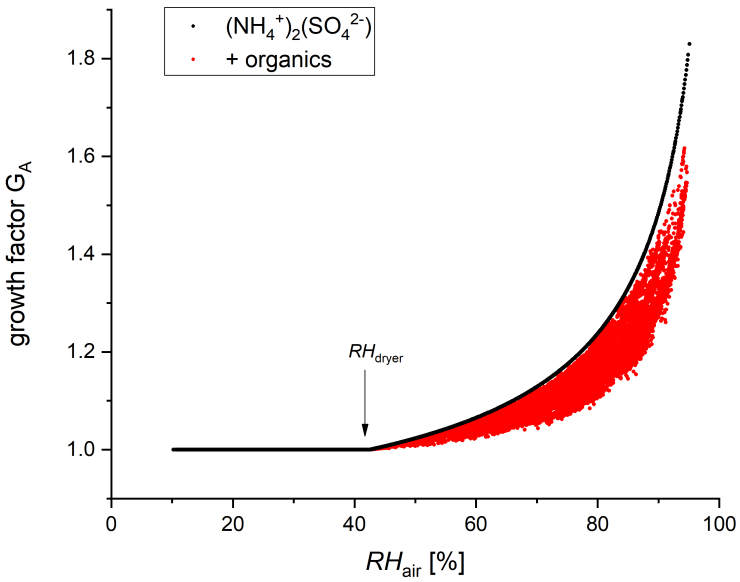

Figure D.4: Surface growth factors for pure ammonium-sulphate (black) and for a mixture with organics (red).

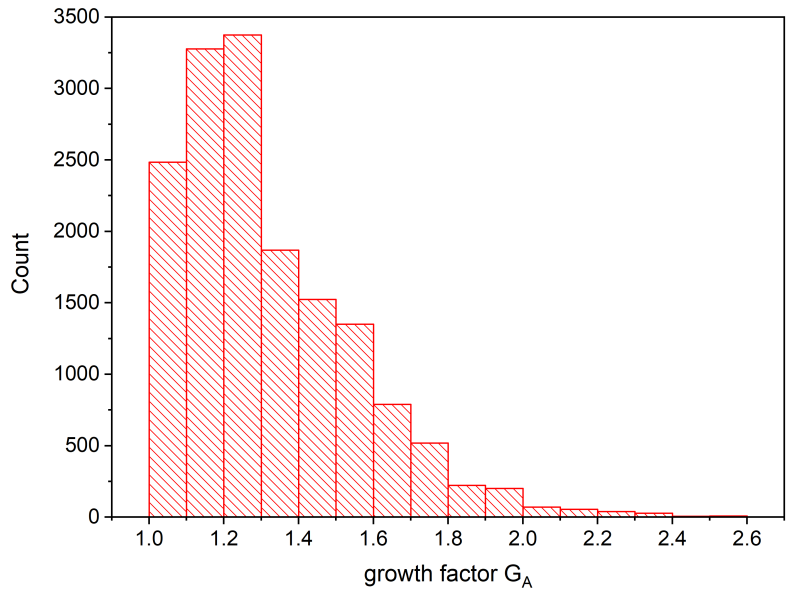

Figure D.5: Distribution of calculated surface area growth factors G_A for the whole AQABA campaign.

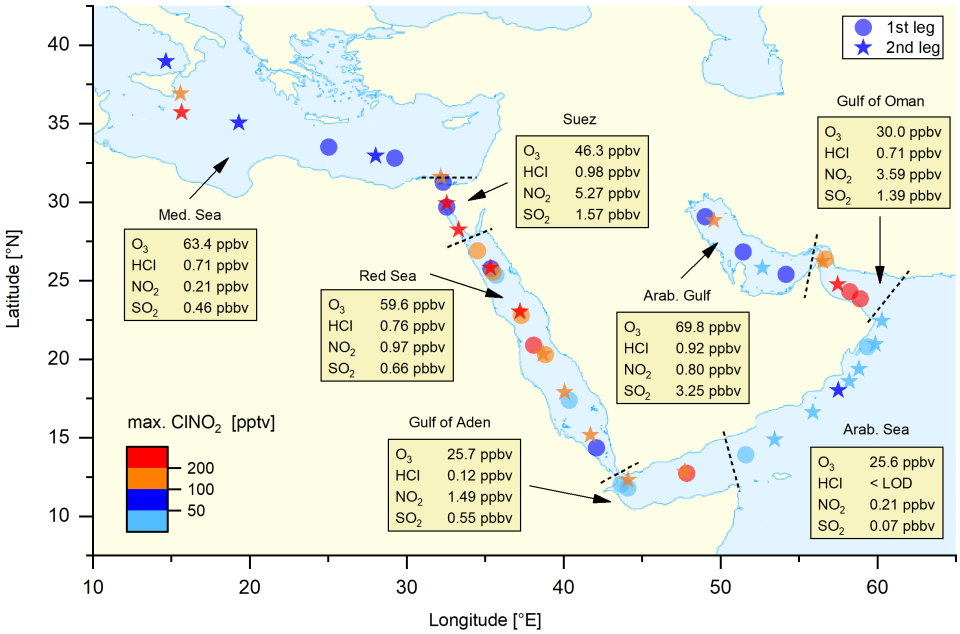

Figure D.6: Map of maximum $ClNO_2$ mixing ratios on individual nights together with (median) night-time mixing ratios of O_3, HCl, NO_2 and SO_2 for different regions demarked by dashed lines. Circles and stars represent data obtained on the first and second legs, respectively.

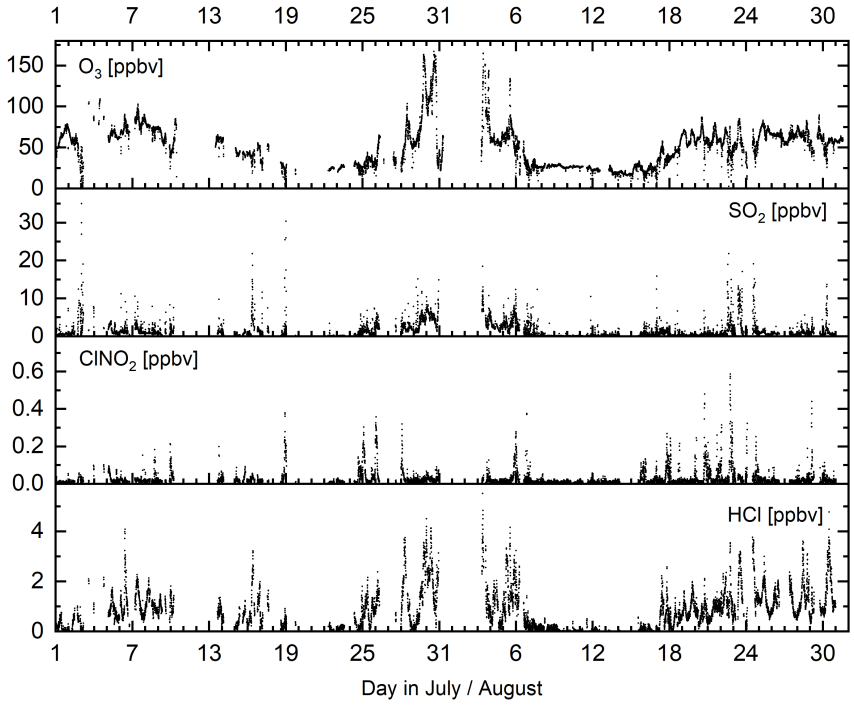

Figure D.7: Time series of O_3, SO_2, $ClNO_2$ and HCl mixing ratios during the AQABA campaign.

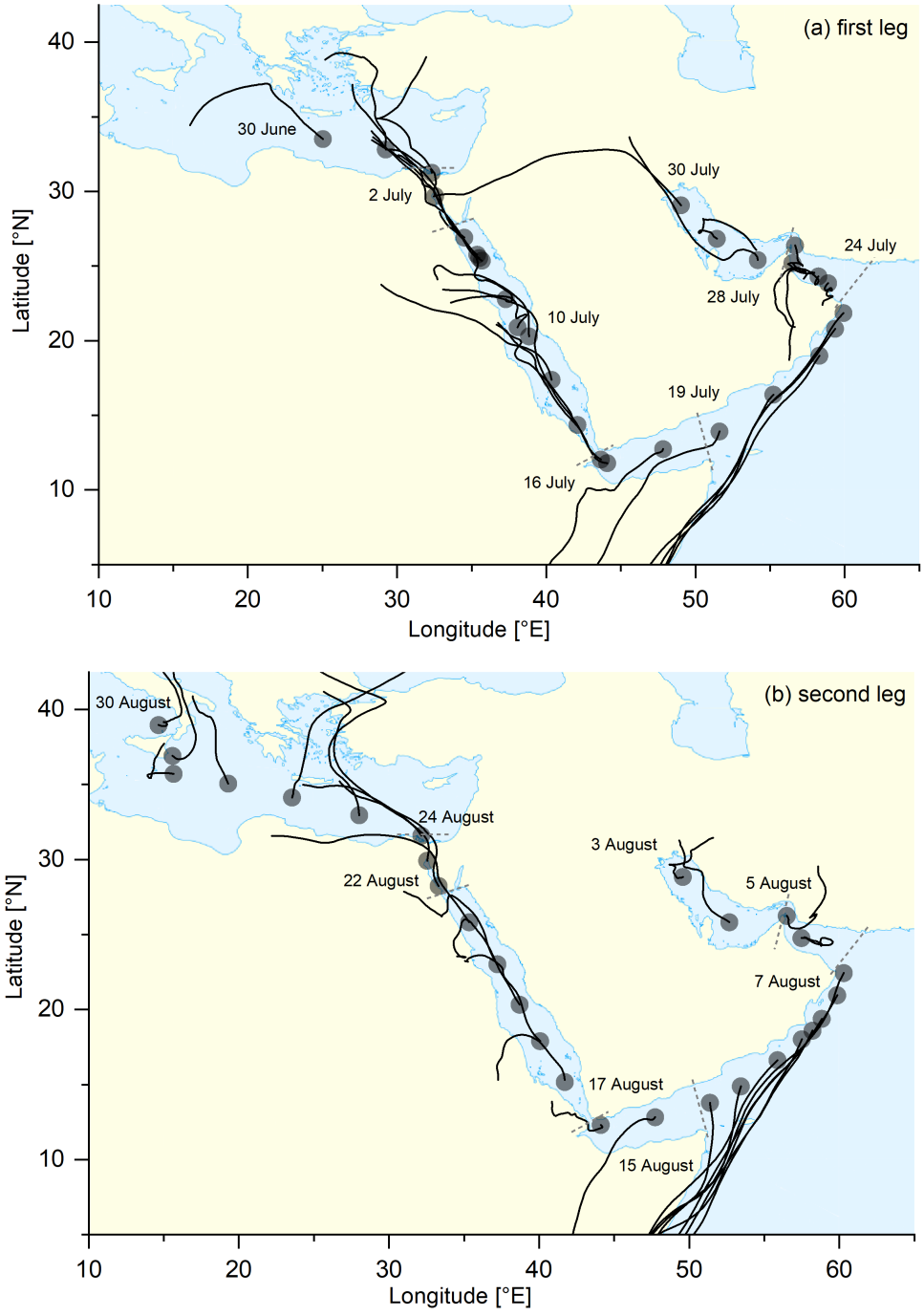

Figure D.8: 48-h back-trajectories calculated with HYSPLIT (Stein et al., 2015; Rolph et al., 2017) (at 100 m above sea-level) representative for the corresponding nights.

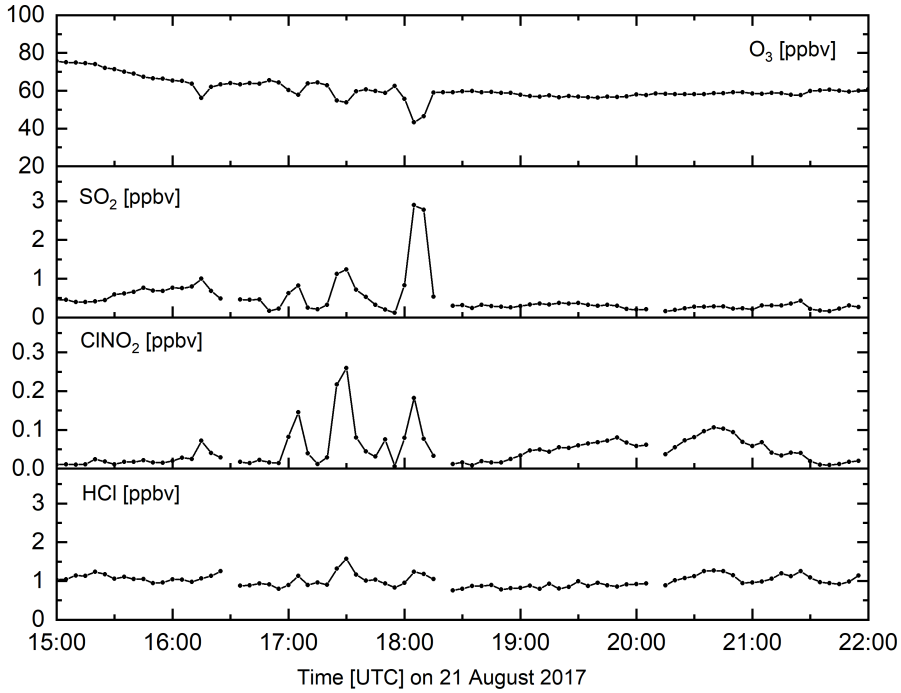

Figure D.9: Observation of $ClNO_2$ in distinct ship plumes between 16:30 and 18:30 UTC (indicated by increased SO_2 mixing ratios and O_3 titration due to NO) on 21 August in the Red Sea.

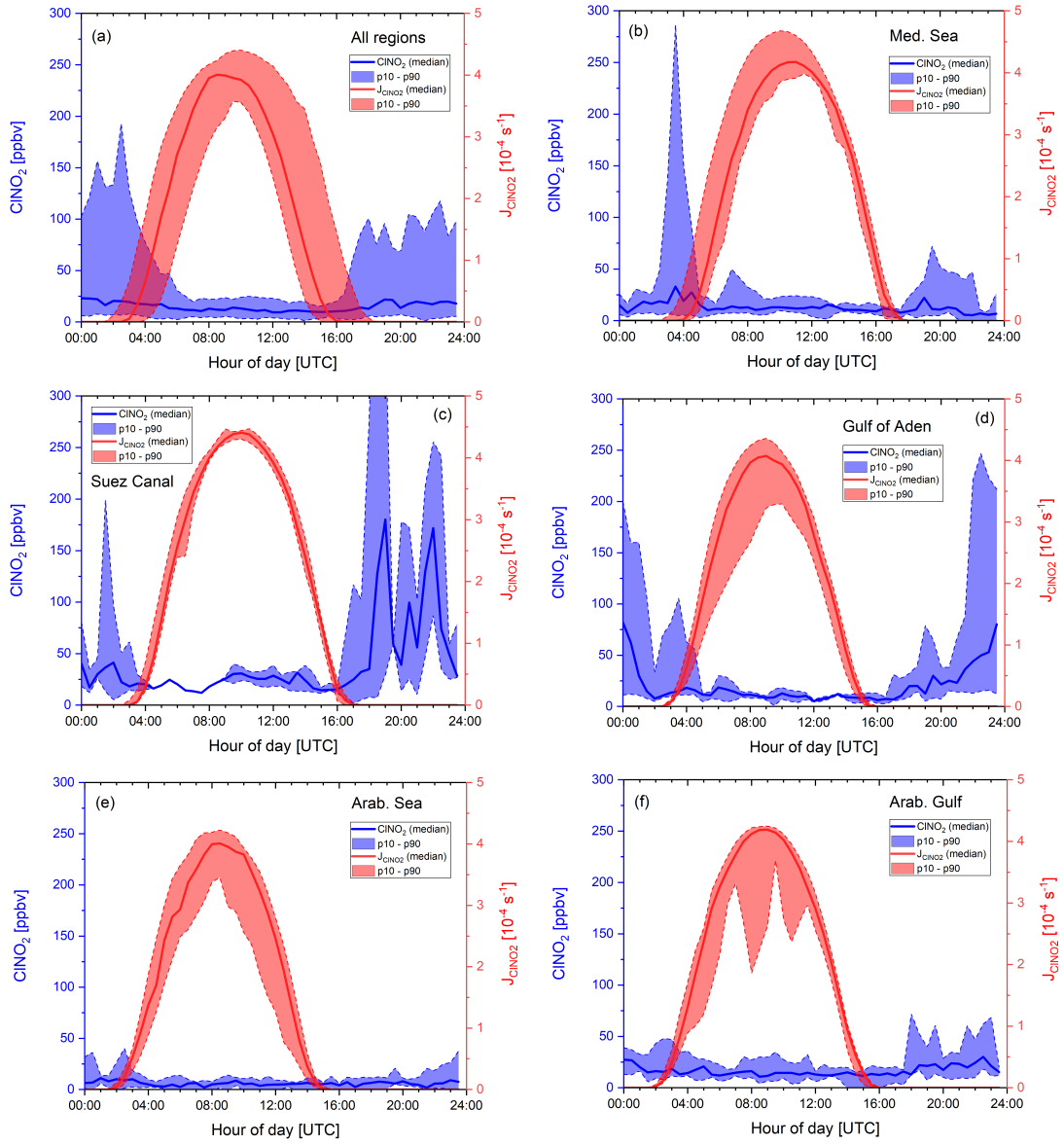

Figure D.10: Diurnal profiles of $ClNO_2$ for (a) all regions combined, (b) the Mediterranean Sea, (c) the Suez Canal and Gulf of Suez, (d) the Gulf of Aden, (e) the Arabian Sea, and (f) the Arabian Gulf. p10 and p90 correspond to the 10th and 90th percentiles.

D.2 Additional details to the derivation of the $ClNO_2$ production efficiency ϵ

To investigate the uncertainty related to assumptions made in the calculation of ϵ, we define five different methods A-E and compare them to each other by applying them to the whole AQABA dataset (Fig. D.11).

Method A: The starting point t_0 for NO_3 formation is set to sunset minus (40 ± 10) min as described in the manuscript but all data points before sunset were excluded from the analysis due to a large uncertainty in reaction time. This way $N_A = 4175$ values of ϵ were obtained throughout the campaign. In *Method A*, we inherently assume that the air mass we probe has not been influenced by fresh NO emissions since the beginning of the night. A fresh NO emission would mean that the air mass at the beginning of the night would have contained less NO_2 than calculated in Eq. (4.3) resulting in an overestimation of the integrated NO_3 production and thus values of ϵ calculated by *Method A* represent a lower limit.

Method B: To account for fresh emissions of NO (e.g. by passing ships), the reaction time t' was calculated from Eq. (4.5) where s represents the number of NO_2 molecules required to make NO_y and is 1 when NO_3 reacts directly with VOCs and 2 when NO_3 reacts with NO_2 to form N_2O_5, which subsequently hydrolyses to HNO_3. As discussed later, the direct NO_3 losses are dominant throughout the campaign compared to the heterogeneous N_2O_5 production, so to a good approximation, $s = 1$. As discussed by McDuffie et al. (2018b), inherent to the use of this expression is the assumption that NO_y is conserved during the night; any losses of NO_y (e.g. via deposition of HNO_3) leading to an underestimation of the true reaction time. Whenever t' is shorter than the time elapsed since sunset (see *Method A*), t' is used to integrate the NO_3 production term. As the calculated, night-time air mass age depends on the ratio between $[NO_2]$ and $[NO_y]$, the calculation breaks down whenever a fresh NO emission (e.g. from a nearby ship) is injected into an air-mass and unreacted NO is still present. In this case the NO_2 to NO_y ratio would be decreased and the age of the air-mass overestimated. To avoid this, we only use data where NO is below the detection limit, resulting in a total number of $N_B = 2987$ data points.

Method C: Here we only consider data points where the calculated age of the air mass (as derived in *Method B*) is equal to or exceeds the time elapsed since sunset as derived in *Method A*. These air masses are unlikely to have been impacted by recent emission. As loss of NO_z by deposition will result in an air mass age that is shorter than the true one, we relax the criterion for equality of reaction times by also including calculated air mass ages that are up to 25 % shorter (i.e. $t' \geq 0.75(t - t_0)$). The resulting dataset is reduced to $N_C = 1742$ data points. All values of ϵ discussed in the manuscript were derived using *Method C*.

Method D: $ClNO_2$ mixing ratios close to the limit of detection (LOD) result in a higher uncertainty and variability in ϵ, especially when the NO_3 production term is also small. In *Method D* we use only data in which the $ClNO_2$ mixing ratio is at least 25 pptv, which represents the LOD + the median, daytime HCl-interference

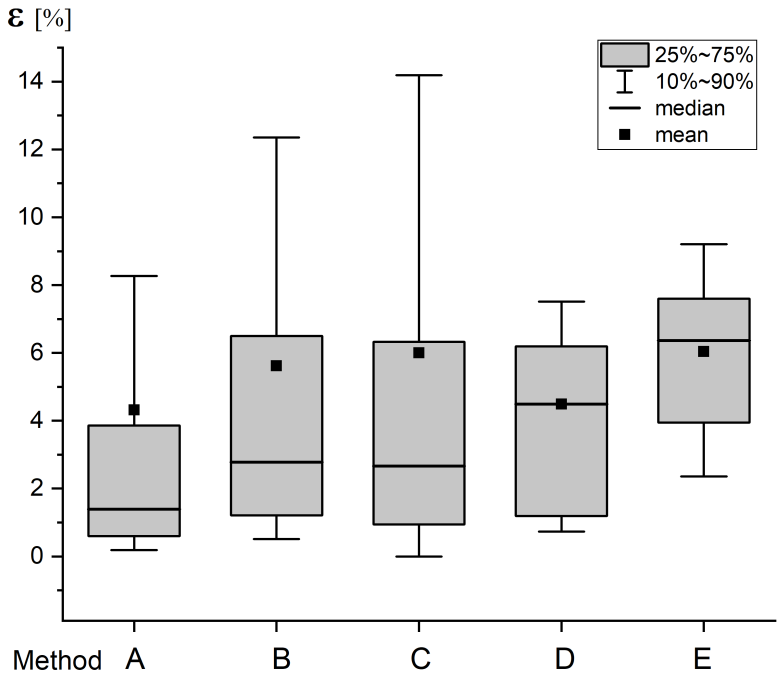

Figure D.11: Box plot of ϵ derived by the different methods A–E for the whole AQABA campaign. The whiskers represent the 10th and 90th percentiles.

(Sect. 4.3.1). This drastically reduces the size of the dataset to $N_D = 280$ data points.

Method E: Here we examine the efficiency of $ClNO_2$ formation only during a few nights when its mixing ratio exceeded 100 pptv. The intention here is not to derive e.g. a regional mean value, but to indicate that even when biasing the dataset to apparently efficient $ClNO_2$ generation, ϵ remains low. In *Method E*, only $N_E = 50$ data points remain (1.2 % of the dataset analysed in *Method A*).

We summarise values of ϵ as median and mean values for the entire campaign in Fig. D.11, segregated into the five different methods used to select data and derive the reaction time. As described earlier, *Method A* can be understood as a lower limit for ϵ providing a median efficiency of only 1.4 % with a range from 0–8 % (10th and 90th percentiles) and a large difference between mean and median values. More reliable median values of $\epsilon = 2.8\,\%$ and 2. % are provided by *Methods B and C*. *Method D*, results in identical median and mean values of $\epsilon = 4.5\,\%$, although a bias towards higher values is difficult to rule out as low $ClNO_2$ mixing ratios were excluded. For *Method E*, where we only consider data with $ClNO_2 >$ 100 pptv, we derive a larger median value of $\epsilon = 6.4\,\%$. If we consider only the individual maxima in the $ClNO_2$ mixing ratio (above 100 pptv) on any particular night, we derive 17 values of ϵ that vary between 1.1 and 11.2 % which are listed in Table D.1.

In Fig. 4.5 and 4.6 we exclusively report values of ϵ derived by *Method C*. In comparison to Fig. 4.6, Fig. D.12 illustrates how the box-plots for the seven regions

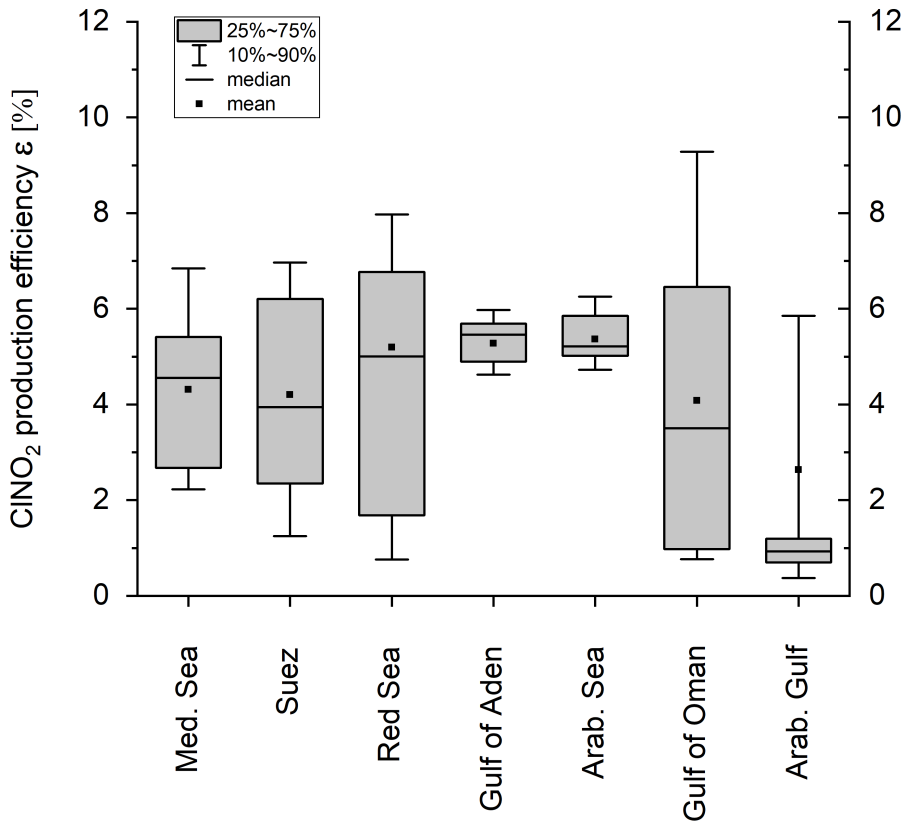

Figure D.12: Median values of ϵ ($ClNO_2$ production efficiency) for each region, calculated from individual night-time values (between 10 and 104 per region) based on Eq. (4.4) but using *Method D* instead of *Method C*.

would be altered when applying *Method D* instead of *Method C*. The variability is generally decreased and median values are shifted towards higher values, but the general picture and conclusions are not changed.

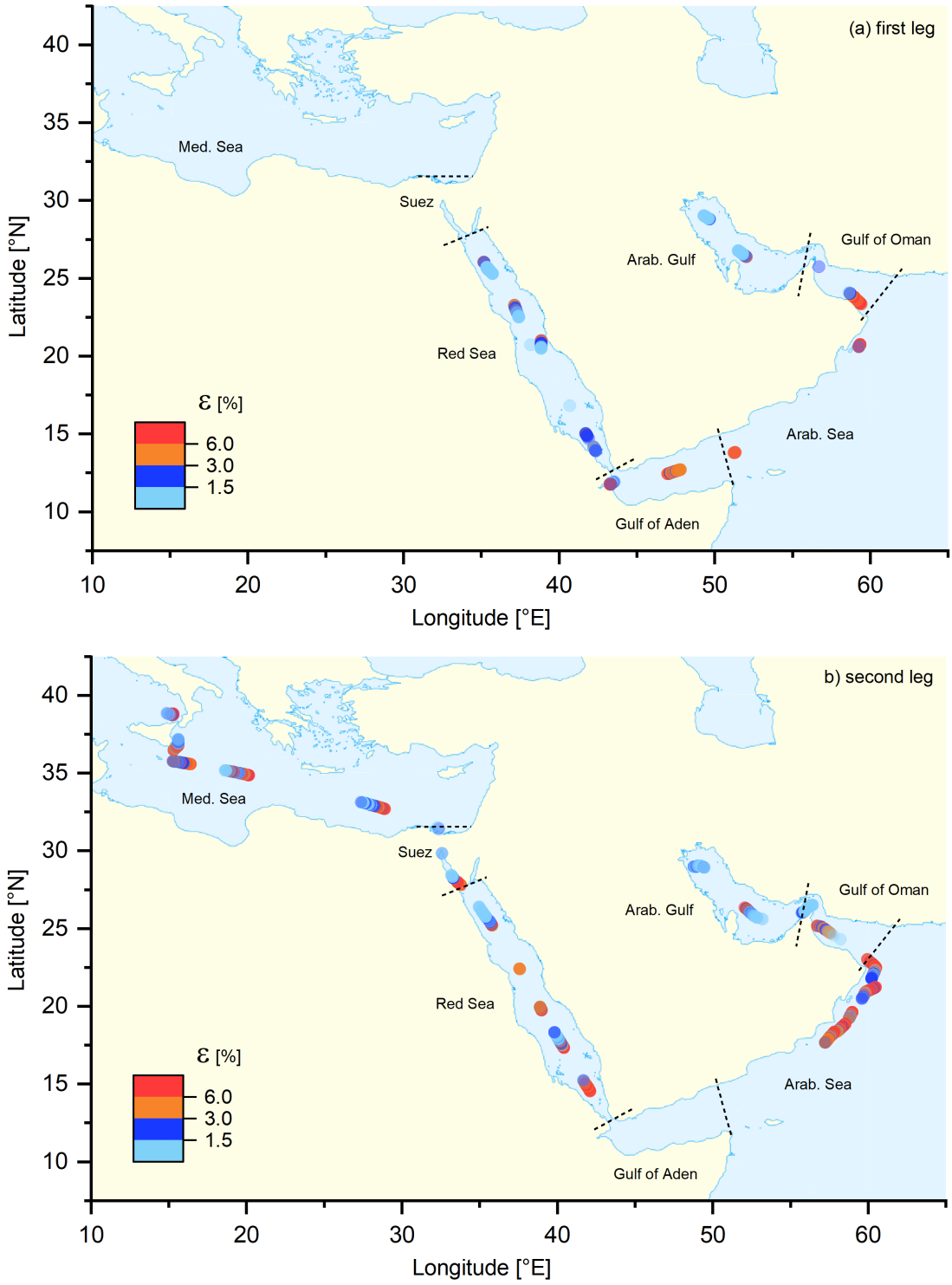

Figure D.13: Median values of ϵ (1-hour averaged) along the ship track for (a) first and (b) second leg, calculated via Eq. (4.4).

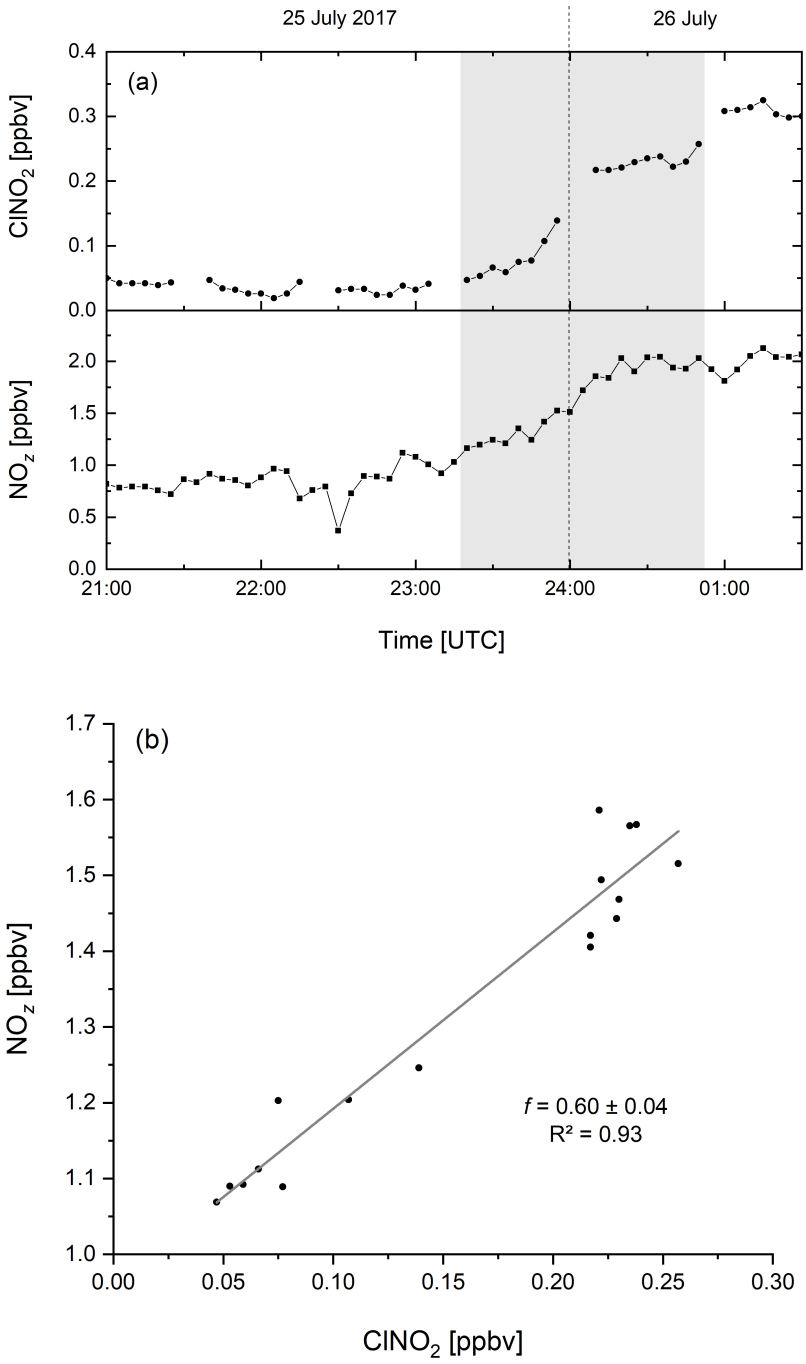

Figure D.14: (a) Time series of $ClNO_2$ and NO_z on 25–26 July 2017 in the Gulf of Oman. (b) The slope of NO_2 vs. $ClNO_2$ can be used (Eq. 4.9) to calculate $f = 0.60 \pm 0.04$ for the ≈ 2 h period (grey shaded area in Fig. D.14a).

Table D.1: Observed $ClNO_2$ plumes (typical duration of one to several hours) with mixing ratios above 100 pptv.

Date, time [UTC]	Region	t [h]	t' [h]	$ClNO_2$ [pptv]	N_2O_5 [pptv]	$NO_{3,int}$ [ppbv]	ϵ [%]	O_3 [ppbv]	SO_2 [ppbv]	HCl [ppbv]	NO_2 [ppbv]
08.07. 17:50	Red Sea	1.8	1.5	128	-	3.17	4.0	61.5	3.0	1.1	6.9
24.07. 16:05	Oman	1.8	2.3	143	-	1.28	1.1	25.7	1.1	0.3	7.0
03.08. 18:00	Arab. Gulf	2.9	2.6	115	53	9.65	1.2	78.8	3.0	1.8	6.7
06.08. 18:45	Oman	4.3	3.9	173	-	1.55	1.1	28.1	1.4	0.7	2.9
06.08. 20:35	Oman	6.1	6.9	159	-	2.86	5.6	20.0	4.0	0.6	5.2
17.08. 18:00	Red Sea	3.0	4.5	120	9	1.54	7.8	34.4	1.6	0.7	3.2
17.08. 19:25	Red Sea	4.4	3.6	212	14	3.03	7.0	34.7	2.1	1.8	3.9
17.08. 20:05	Red Sea	5.1	4.7	168	8	2.03	8.3	32.0	1.3	1.5	2.4
18.08. 17:00	Red Sea	1.8	1.5	106	23	1.49	7.1	42.9	0.9	0.6	4.6
20.08. 16:45	Red Sea	1.3	1.0	144	59	1.90	7.6	58.7	0.7	1.0	5.8
21.08. 17:05	Red Sea	1.5	1.4	145	53	2.13	6.8	57.9	0.8	1.1	5.9
21.08. 17:30	Red Sea	1.9	2.5	259	87	3.14	8.2	53.8	1.2	1.6	7.1
21.08. 23:40	Red Sea	8.1	8.5	103	27	9.78	1.1	58.0	0.7	1.1	2.3
22.08. 16:50	Suez	1.0	1.3	123	118	1.96	6.3	45.7	2.5	1.2	11.4
22.08. 18:20	Suez	2.5	2.1	586	355	7.09	8.3	56.4	4.6	3.5	11.3
22.08. 21:40	Suez	5.8	4.6	308	52	8.77	3.5	39.4	1.2	1.2	7.6
22.08. 22:30	Suez	6.7	6.1	222	47	9.45	2.3	43.0	1.0	1.1	5.9

Notes: Regions: Red Sea, Gulf of Oman (Oman), Arabian Gulf (Arab. Gulf) and Suez Canal / Gulf of Suez (Suez). t denotes the time since sunset; t' corresponds to the air mass age calculated from Eq. (4.5); $NO_{3,int}$ is the total amount of NO_3 produced over the course of the night and ϵ is the $ClNO_2$ production efficiency (Eq. 4.4).

List of Acronyms

AED . . . . . Atomic Emission Detector

AMS . . . . . Aerosol Mass Spectrometer

AP . . . . . Atmospheric Presure

APAN . . . . . Peeroxyacrylic nitric anhydride

AQABA . . . . . Air Quality and climate change in the Arabian BAsin

CDC . . . . . Collisional Dissociation Chamber

CI-QMS . . . . . Chemical Ionisation Quadrupole Mass Spectrometer

CPAN . . . . . Peroxycrotonyl nitric anhydride

CRDS . . . . . Cavity ring-down spectroscopy

CYPHEX . . . . CYprus PHotochemistry EXperiment

DET . . . . . Detector

DIS . . . . . Discharge Ion Source

DMS . . . . . Dimethylsulfid, CH_3SCH_3

E-AIM . . . . . Extended Aerosol Inorganics Model

EI . . . . . Electron ionisation

FMPS . . . . . Fast Particle Mass Spectrometer

FWHM . . . . . Full width at half maximum

GC . . . . . Gas Chromatograph

HALO . . . . . High Altitude and LOng range research aircraft

HOM . . . . . Highly Oxygenated Molecule

HR . . . . . High Resolution

HYSPLIT . . . . HYbrid Single-Particle Lagrangian Integrated Trajectory model

IBAIRN . . . . . Influence of Biosphere–Atmosphere Interactions on the Reactive Nitrogen budget

I-CIMS . . . . . Iodide Chemical Ionisation Mass Spectrometry

ID . . . . . Internal diameter

IMR . . . . . Ion Molecule Reactor

ISOP . . . . . Isoprene

IUPAC . . . . . International Union of Pure and Applied Chemistry

LOD . . . . . Limit Of Detection

m/z . . . . . Mass-to-charge ratio

MARGA . . . . Monitor for AeRosols and Gases in Ambient air

MGLY . . . . . Methylglyoxal

MPAN . . . . . Peroxymethacrylic nitric anhydride

MT . . . . . Monoterpenes

MVK . . . . . Methylvinylketone

NCI . . . . . Negative ion - Chemical Ionisation

NMHCs . . . . . Non-methane hydrocarbons

NO_x . . . . . NO + NO_2

NO_y . . . . . Sum of all reactive nitrogen oxides

NO_z . . . . . $NO_y - NO_x$

NOTOMO . . . NOcturnal chemistry at the Taunus Observatory: insights into Mechanisms of Oxidation

OCT . . . . . Octupole ion guide

OD . . . . . Outer diameter

OMI . . . . . Ozone Monitoring Instrument

OPC . . . . . Optical Particle Counter

PAA . . . . . Peracetic acid, $CH_3C(O)OOH$

PAN . . . . . Peroxy acetyl nitrate, $CH_3C(O)O_2NO_2$

PAR . . . . . Photosynthetically Active Radiation

PARADE . . . . PArticles and RAdicals, Diel observations of mEchanisms of oxidation

PBL . . . . . Planetary Boundary Layer

PFA . . . . . Perfluoroalkoxy

PiBN . . . . . Peroxyisobutyric nitric anhydride

PM . . . . . Particulate matter

PNA . . . . . Pernitric acid

PnBN . . . . . Peroxy-n-butyric nitric anhydride

PPN . . . . . Peroxypropionic nitric anhydride

PTR . . . . . Proton Transfer Reaction

PVDF . . . . . Polyvinylidene fluoride

QCL . . . . . Quantum Cascade Laser

QMF . . . . . Quadrupole Mass Filter

RF . . . . . Radio-frequency

RH . . . . . Relative humidity

S/N . . . . . Signal-to-noise ratio

slm . . . . . Standard litres per minute

SMEAR . . . . . Station for Measuring Ecosystem–Atmosphere Relations

SOA . . . . . Secondary Organic Aerosol

STD . . . . . Standard deviation

STP . . . . . Standard temperature and pressure

TDR . . . . . Thermal Dissociation Region

ToF . . . . . Time-of-Flight

TSP . . . . . Total Suspended Particles

UTC . . . . . Coordinated Universal Time

UV . . . . . Ultra-violet

VOCs . . . . . Volatile Organic Compounds

X-ray . . . . . X-radiation

List of Figures

List of Tables